

# **Molecular Level Interfacial Studies of Nanoemulsions: Surface Structure, Specific Ion Effects and Stability**

**Thèse N° 9037**

Présentée le 1<sup>ER</sup> MARS 2019

à la Faculté des sciences et techniques de l'ingénieur

Chaire Julia Jacobi de photomédecine - Laboratoire de biophotonique fondamentale

Programme doctoral en photonique

pour l'obtention du grade de Docteur ès Sciences

par

**EVANGELIA ZDRALI**

Acceptée sur proposition du jury

Prof. D. Psaltis, président du jury

Prof. S. Roke, directrice de thèse

Prof. E. Tyrode, rapporteur

Prof. N. Levinger, rapporteuse

Prof. F. Stellacci, rapporteur

2019



*To Bram*





# Acknowledgements

First of all I would like to thank my supervisor Professor Sylvie Roke for giving me the opportunity to work with her for the last 5 years, and conduct front line research. Thanks for all the scientific input and support, the time and the effort invested in my work.

I would also like to thank my committee, Prof. Tyrode, Prof. Levinger, Prof. Stellacci, and Prof. Psaltis for reading this thesis and giving me feedback on this work.

LBP group, thank you very much from the bottom of my heart! Orly, Jan, Nathan, Arianna, Marie B., Igor, Sergey, Maksim, David, Tereza, Cornelis, Rudi and Rebecca, I really appreciate the nice atmosphere and your support, any kind of it, over the years. Special thanks to Nikolay and Yixing, for introducing me to the science upon my arrival to the lab and for answering innumerable questions for years. Halil, a huge “thank you” goes to you; this work would not have been possible without your help. Last, Marie D., you will be greatly missed, not appearing out of the blue with crazy stories and unimaginable confusions.

My stay in Lausanne has brought me new good friends outside the lab as well. To them, and to my friends back in Greece, a big “thanks” for pulling me back to reality when academic “tragedies” overwhelmed me. The same applies to my sister and my parents, whom I miss a lot, but somehow always carry with me.

The last word is for Bram. This PhD has been our achievement; until the next one.

*Lausanne, December 2018*

Evangelia Zdrali



# Abstract

This thesis is a study on the molecular structure of the interface of nanometer-sized oil droplets dispersed in water, a system known as oil-in-water nanoemulsion. There are two motivations for this choice: First, nanoemulsions are important constituents of various food and medical products, and their interfacial structure determines the physicochemical properties of the systems, thus their efficient application. Secondly, the oil/water nanointerface is an appropriate model for the study of molecular interactions at a mixed hydrophobic / hydrophilic heterogeneous system that is confined to a sub-micron length scale, and in contact with aqueous electrolyte solutions. The latter resembles interfaces of biological systems crucial for human life, such as the cell membranes. However, despite its importance, the molecular level structure of aqueous nanointerfaces is still not fully understood, as they are difficult to probe experimentally. Here we apply the nonlinear optical techniques of sum frequency scattering and second harmonic scattering to study the stabilization mechanism of nanoemulsions, as well as specific ion effects at the nanoscale.

We begin with the study of the interfacial structure of oil nanodroplets stabilized with a positively charged, a negatively charged and a neutral surfactant, along with the stability of each system. We show that the surface density of charged surfactants on nanodroplets is an order of magnitude lower than on planar interfaces, due to repulsive interactions between like charges on opposing sides on the droplets surface through the oil phase, allowed by the small droplet size. Moreover, we find no experimental correlation between stability and surfactant surface density. Instead droplet stability is found to depend on the relative cooperativity between charge-charge, charge-dipole and hydrogen bonding interactions.

Then, we study the effect of the inversion of the oil and the water phases on the droplet stability for nanometer-sized and micrometer-sized droplets. We employ an oil-soluble neutral surfactant, a water-soluble anionic surfactant, and the combination of the two. We find that, while microdroplets and water-in-oil nanodroplets follow the widely accepted empirical rules, and are stabilized only with a surfactant soluble in the continuous phase, nanometer-sized oil-in-water emulsions can be stabilized with an oil-soluble surfactant. Moreover, the structure of the surfactant is different when it approaches the interface from the dispersed or the continuous phase.

Next, we study the interaction of four anions ( $\text{SCN}^-$ ,  $\text{NO}_3^-$ ,  $\text{Cl}^-$  and  $\text{SO}_4^{2-}$ ) with different molecular structure with the nanointerface of droplets stabilized with a surfactant with a positively charged headgroup (trimethylammonium) for different anionic concentrations. Our results reveal a unique adsorption pattern for each anion that changes with concentration, possibly involving reorientation of the anions and adsorption to different patches of the

interface. Interestingly, not only the weakly-hydrated  $\text{SCN}^-$  and  $\text{NO}_3^-$ , but also the well-hydrated  $\text{SO}_4^{2-}$  approaches the nanointerface, inducing strong interfacial water ordering.

Last, we further study the interaction of  $\text{SCN}^-$  with the positively charged nanointerface employing *ab-initio* molecular dynamics simulations. We find ion-pairing of  $\text{SCN}^-$  with the interfacial trimethylammonium groups at concentrations as low as 5 millimolar. Moreover, a variety of ion species emerge at different ionic strengths, with differently oriented  $\text{SCN}^-$  groups adsorbed on hydrophilic and/or hydrophobic parts of the surface. This diverse and heterogeneous chemical environment is surprisingly different from the behaviour at extended liquid planar interfaces, where ion pairing is typically detected at molar concentrations.

## Keywords

water, oil, nanoscale interfaces, droplets, stability, electrolytes, surface charge, specific ion effects, sum frequency generation, second harmonic generation, nonlinear light scattering

## Résumé

Dans cette thèse, nous présentons une étude de la structure moléculaire de l'interface de gouttelettes d'huile de taille nanométrique dispersées dans l'eau, un système connu sous le nom de nanoémulsion d'huile dans l'eau. Ce choix répond à deux motivations: premièrement, les nanoémulsions sont des composants importants que l'on trouve dans divers produits alimentaires et médicaux. Leur structure interfaciale est à l'origine des propriétés physicochimiques de ces produits, et détermine leur efficacité d'application. Deuxièmement, la nanointerface huile/eau est un modèle approprié pour l'étude des interactions moléculaires dans un système hétérogène mixte hydrophobe/hydrophile, confiné à une échelle sub-micrométrique, et dans un environnement de solutions électrolytiques aqueuses. Cette nanointerface huile/eau est similaire aux interfaces des systèmes biologiques cruciaux pour la vie humaine, telles que les membranes cellulaires. Néanmoins, malgré son importance, la structure des nanointerfaces d'eau au niveau moléculaire n'est pas encore complètement comprise, car ces nanointerfaces sont difficiles à sonder expérimentalement. Nous appliquons ici les techniques d'optique non linéaire telles que la technique de la diffusion de fréquences sommes et de la diffusion de seconde harmonique pour étudier les mécanismes de stabilisation des nanoémulsions, ainsi que les effets ioniques spécifiques à l'échelle nanométrique.

Premièrement, nous commençons par l'étude de la structure interfaciale de nanoparticules stabilisées avec un agent tensioactif chargé positivement, négativement et neutre, ainsi que la stabilité de chacun de ces systèmes. Nous montrons que la densité de surface des tensioactifs chargés sur les nanogouttelettes est inférieure d'un ordre de grandeur à celle des interfaces planaires. Ceci est dû à des interactions répulsives à travers la phase huileuse entre les charges similaires sur les côtés opposés des gouttelettes, interactions permises par la taille réduite des gouttelettes. En outre, nous ne trouvons aucune corrélation expérimentale entre la stabilité et la densité de surface du tensioactif. Au contraire, la stabilité des gouttelettes dépend de la coopérativité relative entre les interactions charge-charge, charge-dipôle et liaison hydrogène.

Ensuite, nous étudions l'effet de l'inversion des phases huileuse et aqueuse sur la stabilité des gouttelettes de tailles nanométrique et micrométrique. Nous utilisons un tensioactif neutre soluble dans l'huile, un tensioactif anionique soluble dans l'eau, ainsi qu'une combinaison des deux. Nous constatons que toutes les microgouttelettes, ainsi que les nanogouttelettes d'eau dans l'huile, suivent les règles empiriques largement acceptées et ne sont stabilisées que par un agent tensioactif soluble en phase continue. À l'inverse, les émulsions d'huile dans une solution aqueuse, à la taille nanométrique, ne peuvent être

stabilisées qu'avec un tensioactif soluble dans l'huile. De plus, la structure du tensioactif est différente lorsqu'il se rapproche de l'interface depuis la phase dispersée ou la phase continue.

Ensuite, nous étudions l'interaction de quatre anions ( $\text{SCN}^-$ ,  $\text{NO}_3^-$ ,  $\text{Cl}^-$  et  $\text{SO}_4^{2-}$ ), de structures moléculaires différentes, avec la nanointerface de gouttelettes stabilisées par un tensioactif (triméthylammonium) dont le groupe de tête est chargé positivement. Nous étudions ces interactions pour différentes concentrations anioniques. Nos résultats révèlent un modèle d'adsorption unique pour chaque anion qui varie selon la concentration, impliquant possiblement une réorientation des anions et une adsorption à différents endroits de l'interface. Il est intéressant de noter que non seulement les ions  $\text{SCN}^-$  et  $\text{NO}_3^-$  faiblement hydratés, mais aussi l'ion  $\text{SO}_4^{2-}$  fortement hydraté, s'approchent de l'interface nanométrique, induisant un fort réarrangement de l'eau interfaciale.

Finalement, nous étudions plus en détail l'interaction de l'ion  $\text{SCN}^-$  avec une nanointerface chargée positivement en utilisant des simulations de dynamiques moléculaires *ab-initio*. Nous obtenons un appariement ionique de l'entité moléculaire  $\text{SCN}^-$  avec les groupes interfaciaux triméthylammonium à des concentrations aussi faibles que 5 millimoles par litre. De plus, une variété d'espèces ioniques émergent à différentes forces ioniques, avec des groupes  $\text{SCN}^-$  orientés différemment, adsorbés sur des parties hydrophiles et / ou hydrophobes de la surface. Ce comportement diversifié et hétérogène est étonnamment différent du comportement aux interfaces planaires liquides étendues où l'appariement des ions est généralement détecté pour des concentrations de l'ordre de la mole par litre.

## Mots clés

eau, huile, interfaces à l'échelle nanométrique, gouttelettes, stabilité, électrolytes, charge de surface, effets ioniques spécifiques, génération de la fréquence somme, génération de seconde harmonique, diffusion non linéaire de la lumière

# Table of Contents

Acknowledgements.....	i
Abstract.....	iii
Résumé .....	v
Table of Contents.....	vii
List of Figures .....	xi
List of Tables .....	xiii
Chapter 1: Introduction.....	1
1.1    Nanoemulsions and the oil/water nanointerface.....	1
1.1.1    Stability of the nanointerface.....	1
1.1.2    Ions and specific ion effects at the nanointerface.....	4
1.2    Second order nonlinear spectroscopic techniques .....	8
1.2.1    Second order nonlinear light generation.....	8
1.2.2    Vibrational Sum Frequency Scattering (SFS).....	9
1.2.3    Second Harmonic Scattering (SHS).....	11
1.3    This thesis .....	12
1.4    References .....	13
Chapter 2: Experimental Details and Methodology.....	23
2.1    Introduction.....	24
2.2    Theoretical background .....	24
2.2.1    Vibrational Sum Frequency Scattering .....	24
2.2.2    Second Harmonic Scattering .....	30
2.2.3    Dynamic Light Scattering (DLS) measurements.....	31
2.2.4    Electrophoretic measurements and $\zeta$ -potential.....	32
2.3    Experimental Details .....	34
2.3.1    Experimental setup and measurements of SFS .....	34
2.3.2    SFS Spectral Analysis .....	38
2.3.3    Experimental setup and measurements of SHS.....	38
2.3.4    Raman hydration shell spectroscopy.....	40
2.4    Sample preparation.....	41
2.4.1    Chemicals.....	41
2.4.2    Production of nanometer-sized droplets.....	41

2.4.3	Production of micrometer-sized droplets .....	44
2.5	References .....	45
Chapter 3: The Molecular Mechanism of Nanodroplet Stability .....		49
3.1	Introduction.....	50
3.2	Results and Discussion .....	51
3.2.1	Stability .....	51
3.2.2	Surface density .....	52
3.2.3	Electrokinetic mobility.....	54
3.2.4	Molecular interfacial structure and bulk hydration.....	54
3.2.5	Stability and structure.....	56
3.2.6	Electrostatic interactions in charged systems .....	60
3.3	Conclusions.....	62
3.4	Appendix .....	64
3.4.1	Calculation of Interfacial Charge Density.....	64
3.4.2	DLVO theory predictions .....	66
3.5	References .....	71
Chapter 4: The interfacial structure of nanometer- and micrometer-sized oil and water droplets stabilized with SDS and Span80.....		75
4.1	Introduction.....	76
4.2	Results and discussion .....	77
4.2.1	Nanometer-sized oil-in-water emulsions.....	78
4.2.2	Micrometer-sized oil-in-water emulsions .....	80
4.2.3	Nanometer-sized water-in-oil emulsions.....	81
4.2.4	Micrometer-sized water-in-oil emulsions .....	83
4.2.5	Discussion.....	84
4.3	Conclusions.....	85
4.4	Appendix .....	87
4.4.1	Surface structure of SDS with and without the addition of Span80 in a system of nanometer-sized oil droplets in water.....	87
4.4.2	Surface structure of SDS and Span80 in a system of micrometer-sized oil droplets in water .....	88
4.5	References .....	89
Chapter 5: Specific ion effects at the interface of nanometer-sized oil droplets in water.....		93



5.1. Introduction .....	94
5.2. Results and discussion .....	95
5.2.1. Electrokinetic mobility .....	95
5.2.2. Interfacial water ordering .....	97
5.2.3. Surface density and structure of $\text{SCN}^-$ , $\text{NO}_3^-$ and $\text{SO}_4^{2-}$ .....	98
5.2.4. Discussion .....	101
5.3 Conclusions .....	104
5.4 Appendix .....	106
5.4.1 DLVO theory predictions .....	106
5.5 References .....	110
Chapter 6: The diverse nature of ion speciation at the nanoscale hydrophobic/water interface .....	113
6.1 Introduction .....	114
6.2 Results and Discussion .....	116
6.2.1 Electrokinetic mobility .....	116
6.2.2 Interfacial water ordering .....	117
6.2.3 Surface density and structure of $\text{SCN}^-$ .....	118
6.2.4 MD simulation results .....	119
6.2.5 Diverse ion speciation .....	122
6.3 Conclusions .....	125
6.4 Appendix .....	127
6.4.1 SFS measurements of the interfacial $\text{DTA}^+$ cations .....	127
6.4.2 Spectral Lorentzian fittings .....	128
6.4.3 Orientation of $\text{SCN}^-$ at the surface .....	129
6.4.4 Validation of QM/MM approach .....	130
6.5 References .....	133
Chapter 7: Summary and Outlook .....	139
7.1 Summary .....	139
7.2 Outlook .....	141
List of publications .....	143
Curriculum Vitae .....	145



# List of Figures

Figure 1.1: Rationale and aim. ....	3
Figure 1.2: Typical ordering of cations and anions in a Hofmeister series. ....	6
Figure 1.3: Interaction of different anions with the positively charged oil/water nanointerface. ....	7
Figure 1.4: Schematic illustration of the optical processes of SFG/SFS and SHG/SHS. ....	10
Figure 2.1: Top view of the SFS geometry (sketch). ....	25
Figure 2.2: Top view of the collinear SFS geometry (sketch). ....	30
Figure 2.3: Particle size distribution measured by DLS. ....	32
Figure 2.4: Ion distribution around a particle. ....	33
Figure 2.5: Illustration of the SFS experimental setup. ....	37
Figure 2.6: Illustration of the SHS experimental setup. ....	39
Figure 3.1: Stability and surface group density. ....	53
Figure 3.2: Interfacial structure and bulk hydration. ....	57
Figure 3.3: Sketch of interfacial ion-induced electric field. ....	60
Figure 3.4: Electrostatic interactions. ....	61
Figure 3.5: Geometry of Interest. ....	64
Figure 3.6: Surface Charge Densities on Sheet S. ....	66
Figure 3.7: Ion distribution around two approaching particles in solution. ....	68
Figure 3.8: DLVO pair potentials of surfactant stabilized hexadecane nanodroplets in water. ....	69
Figure 4.1: Surface structure of surfactants stabilizing nanometer-sized oil droplets in water. ....	79
Figure 4.2: Stability of micrometer-sized oil droplets in water. ....	81
Figure 4.3: Surface structure of surfactant stabilizing nanometer-sized water droplets in oil. ....	82
Figure 4.4: Stability of micrometer-sized water droplets in oil. ....	83
Figure 4.5: Interfacial structure of SDS with and without Span80 on nanometer-sized oil droplets. ....	87
Figure 4.6: Interfacial structure of SDS and Span80 on micrometer-sized oil droplets. ....	88
Figure 5.1: Electrokinetic potential and interfacial water ordering. ....	96
Figure 5.2: Normalized vibrational SFS spectra of $\text{SO}_4^{2-}$ , $\text{NO}_3^-$ and $\text{SCN}^-$ . ....	99
Figure 5.3: Integrated SFS intensity for $\text{SO}_4^{2-}$ , $\text{NO}_3^-$ and $\text{SCN}^-$ . ....	100
Figure 5.4: Interfacial structure of DTAB stabilized nanodroplets without added salt and with NaCl, NaSCN and $\text{NaNO}_3$ added. ....	103
Figure 5.5: DLVO pair potentials of DTAB stabilized hexadecane nanodroplets in water for the addition of different electrolytes. ....	109
Figure 6.1: Electrokinetic potential and interfacial water ordering. ....	117

Figure 6.2: Interfacial structure of SCN <sup>-</sup> .....	119
Figure 6.3: Vibrational modes from fitting and MD simulations. ....	120
Figure 6.4: Diverse and heterogeneous surface structures. ....	124
Figure 6.5: Surface structure of DTA <sup>+</sup> .....	127
Figure 6.6: Probability distribution of the CN-bond vector $\alpha$ with the surface normal. ....	130
Figure 6.7: Correlation between QM and QM/MM harmonic frequencies .....	131
Figure 6.8: Comparison of averaged harmonic spectra .....	131

## List of Tables

Table 3.1: Stability and interfacial structure of amphiphiles..	58
Table 3.2: Fitting parameters for DLVO pair potentials for nanodroplets stabilized with differently charged surfactants. ....	68
Table 5.1: Fitting parameters for DLVO pair potentials for DTAB stabilized nanodroplets with the addition of 100 mM of different sodium electrolytes.....	107
Table 5.2: Fitting parameters for DLVO pair potentials for DTAB stabilized nanodroplets with the addition of the critical coagulation concentration of different sodium electrolytes.....	107
Table 5.3: Fitting parameters for DLVO pair potentials for DTAB stabilized nanodroplets with the addition of different concentrations of NaSCN.....	107
Table 6.1: Fitting parameters for SCN <sup>-</sup> spectra.....	129



# Chapter 1: Introduction

The thesis that you hold in your hands is a molecular level study of the oil/water interface of nanoemulsions. Here, at the beginning of this work, we discuss the “why” and the “how”: We present the motivation behind studying nanoemulsions, especially their stability and the interaction of their interface with charged molecules/molecular groups, along with the techniques that make the molecular level approach feasible. We finish this introduction by a summary of the next chapters.

## 1.1 Nanoemulsions and the oil/water nanointerface

The oil/water nanoemulsions are dispersions of nanometer-sized oil droplets in water or water droplets in oil.<sup>1-3</sup> Apart from essential components of various industrial products, nanoemulsions are an ideal platform for the study of biologically relevant interactions at the nanoscale. While numerous studies have been conducted on (nano)emulsions for more than a century they have been mostly macroscopic. The possibility of direct access to the interface of nanodroplets in their natural environment, buried in solutions, has only recently become available. The previously unexpected discrepancies that were revealed between the interfacial structure at the nano- and the macro-scale raised many open questions still to be answered.

### 1.1.1 Stability of the nanointerface

Emulsions, in general, are systems that surround us in our daily life: If you are drinking a coffee with milk while reading this thesis, then you are holding an emulsion. If you have chosen the more healthy option of a salad, its dressing is also an emulsion. Apart from food, emulsions are fundamental constituents of industrial products that cover an impressively diverse range, from drugs and pharmaceutical products, to derivatives of the petrochemical industry. In the last decade, even additional applications of interest to biology came into play, with droplets in microfluidic systems employed as miniature reaction vessels to conduct, for example, biochemical reactions or to perform high throughput screening assays.<sup>4,5</sup>

In order for the emulsions to be used efficiently, they need to remain stable (that is, their properties should remain unchanged) over periods of time that, depending on the application, can range from minutes to years. However, the formation of an oil/water emulsion is energetically unfavourable, as the increase of the area of the oil/water interface increases the free energy of the system. As a result the system tends to minimize the oil/water interfacial area, and thus phase-separates into bulk water and bulk oil (Figure 1.1).<sup>6</sup>

This latter situation can be avoided by using amphiphilic molecules/surfactants to decrease the interfacial tension of the oil/water interface, and allows the creation of stable emulsions. In these emulsions the droplets are kinetically (but not thermodynamically) stable, which means that eventually the system will phase-separate into oil and water phases, even if this process can take months or, sometimes, years. This separation is driven by irreversible processes such as flocculation, coalescence, and Ostwald ripening.<sup>1</sup>

The first empirical ideas about droplet stability, as well as the importance of the interfacial region, and the balance of interactions thereat, were formulated already a century ago by Hardy,<sup>7</sup> Harkins,<sup>8</sup> and Langmuir.<sup>9</sup> Since then extensive research has been conducted on emulsion stability, however the fabrication process of emulsions remains mainly empirical until today. As such, a molecular level understanding of the droplet stabilization mechanism is still needed, for better control of the emulsion systems. Ideally, this requires understanding the correlation of molecular structural information of the droplets' interface with droplet stability data. A major hindrance to this approach is definitely the complexity of the liquid state and the liquid interface in the nano- and micro-scale, which is further reinforced by the absence of technology that can provide direct access to the molecular level structure of nanoscale liquid interfaces. It was only recently demonstrated that the nanodroplet interfaces can be directly probed with molecular level precision.<sup>10</sup> As such, typically the stability of droplets is explained<sup>6,11-13</sup> by correlating surface structural data from extended planar interfaces, such as that gathered from X-ray,<sup>14-16</sup> neutron scattering/reflection,<sup>17,18</sup> and sum frequency generation (SFG)<sup>19-24</sup> experiments, with stability data of droplets made of the same chemicals as the planar systems. With the term extended planar interfaces we refer to the interface of two continuous bulk phases that exceeds the nano-meter and micro-meter range, and, although is used as a model system, it does not resemble realistic conditions.

Despite the conventional approach described above, recent studies suggest that macroscopic effects cannot be simply translated to the nanoscale regime.<sup>25-33</sup> Specifically, in the case of the planar interface of bulk hexadecane in contact with bulk water, the surfactant sodium dodecyl sulfate (SDS) reduces the interfacial tension from 52mN/m (neat hexadecane-water) to 10mN/m, populating the interface with a surface density of  $\sim 50 \text{ \AA}^2/\text{molecule}$ .<sup>23,34-36</sup> About ten years ago, de Aguiar *et al.* showed that the same surfactant (SDS) populates the interface of hexadecane nanodroplets in water with a surface density an order of magnitude lower, hardly affecting the interfacial tension of the pristine/bare hexadecane/water nanodroplet interface.<sup>29</sup> Yet, the nanodroplets are still stable. Another discrepancy can be seen in the configuration of interfacial oil molecules that are oriented predominantly parallel to the nanodroplet interface,<sup>38</sup> in contrast to what is seen on most planar interfaces.<sup>39</sup>



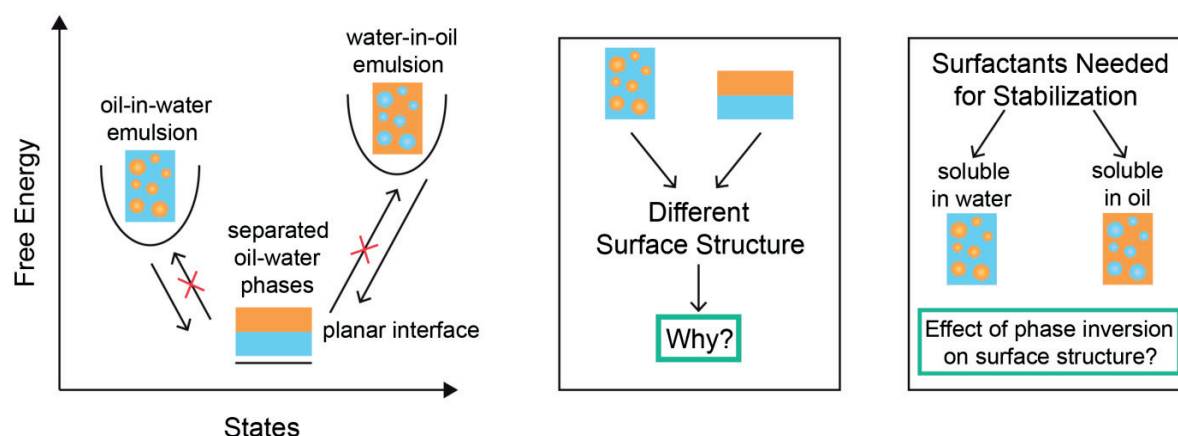


**Figure 1.1: Rationale and aim.** Qualitative free energy profiles (left) for three systems prepared: Droplets of oil in water, droplets of water in oil, and the planar interface of the separated oil-water phases, all prepared with the same chemicals. The free energy of each system is different, and generally one cannot reversibly transform into the other.<sup>3,37</sup> The red crosses indicate the energetically unfavourable transformations. In this thesis, the stabilization mechanism of oil/water nanoemulsions is studied (middle, discussed in Chapter 3), along with the effect of phase inversion to the droplet surface structure (right, discussed in Chapter 4).

Last, the interfacial structure of water on the nanoscale interface of fatty alcohol has been found to be much more ordered than on the equivalent macroscopic interface.<sup>33</sup> All these studies exemplify the fact that the system downscaling to nanometer sizes leads to substantial differences in the molecular structure of every component of the oil/water interface, namely the oil, the water, and the surfactant. As a result, the first topic of interest in this thesis is the following:

1. What is the stabilization mechanism by a charged (positive or negative) or neutral surfactant of an oil-in-water nanoemulsion? (Chapter 3)

### Inversion of the oil and water phases

Mayonnaise is an oil-in-water system, while butter is a water-in-oil system. Oil/water emulsions of both types are very common and extensively used in industry. What is of particular interest is that, despite the fact that the oil/water interface to be stabilized is identical in both types of emulsions, different surfactants are used for the stabilization of each system. Specifically, according to the widely accepted Bancroft rule,<sup>2</sup> and in agreement with the Hydrophile – Lipophile – Balance (HLB) scale,<sup>40</sup> a surfactant that is more soluble in the continuous phase can stabilize the emulsion (Fig. 1.1, right). The basic idea behind these two empirical classifications is that when two emulsion droplets come in close proximity, a thin film of the continuous phase will be formed between them, the stability of which is key to prevent merging of droplets.<sup>41</sup> Studies have shown that such films are more stable when the

surfactant is soluble predominantly in the film (continuous) phase,<sup>42</sup> but molecular level information about the stability of the nanointerface is missing. The phenomenological models available are based on macroscopic observation of the emulsion systems, including the number of phases present, and the partitioning of surfactants in each phase. Such information for the characterization of emulsion stability is typically gathered, among others, by phase inversion, phase separation, gravitational/ centrifugal sedimentation and optical microscopy studies.<sup>42-44</sup> As far as modelling is concerned, mean-field models exist for droplets with a continuum surface charge distribution, but not for a dilute, variable and heterogeneous charge distribution, as could be the case for nanoemulsions.<sup>45</sup> Moreover, the existing models require a well-defined dissociated electrolyte concentration, which is not necessarily the case for water droplets in non-conducting oil.<sup>13,46</sup>

If studies on planar oil/water systems could be used to characterize the interface of both water-in-oil and oil-in-water systems, then the empirical rules regarding emulsion stability should not hold, since the two systems would be of identical composition. Moreover, while the HLB scale is in general valid, it is not a rule without exceptions.<sup>3</sup> As such, the second topic of interest in this thesis is the following:

2. What is the effect of the inversion of the two phases on the interfacial structure of oil/water nanoemulsions? Are deviations from Bancroft rule observed? (Ch. 4)

### **1.1.2 Ions and specific ion effects at the nanointerface**

Life is a matter of interfaces and their interactions with the surrounding environment. Biologically important systems, such as cells, organelles, proteins and macromolecules, interact with their environment through complex interfaces. These interfaces are the ones that attribute to the systems the essential functionalities and allow vital processes, like signalling through a cell membrane, to occur.<sup>47</sup> What all of these systems have in common is a mixed hydrophobic/hydrophilic heterogeneous environment confined to a sub-micron length scale, or divided in micron-sized non-uniform structures<sup>2</sup> that interact with aqueous electrolyte solutions often constituting the environment. The stability of biological interfaces is crucial for a myriad of biological processes, and is controlled/ defined by a balance of interactions at the molecular level. Despite their importance the molecular level details of these interactions (of ions with ionic, hydrophilic and hydrophobic groups at the nanoscale and sub-micron-sized-domain liquid interfaces) have remained largely unexplored, due to the complexity of real biological systems. Nanoemulsions of oil nanodroplets in water stabilized with charged/uncharged surfactants, and the interaction of ions with the interfacial region

(both its hydrophobic and hydrophilic patches), serve as an appropriate simple model system for the study of biologically relevant interactions. The immense (3-4 order of magnitude larger) surface to volume ratio of a nanoemulsion, as compared to the respective planar oil/water interface, and its resulting resistance to impurities<sup>48</sup> makes it ideal for the study of interfacial phenomena.

As far as interactions of ions with interfaces are concerned, there is a category of phenomena that are omnipresent in nature and, hence, of special interest, known as specific ion or Hofmeister effects.<sup>49,50</sup> The term refers to effects for which differences are observed when the composition/structure of ions, ionic groups, or the charge of ionic species varies. Ionic specificity was first reported in the pioneering work of Franz Hofmeister in 1888,<sup>51</sup> who discovered that the solubility of egg white albumin in water changes with the addition of different salts. Since then, an enormous amount of studies has been conducted to elucidate the general rankings of ions at different systems, including both aqueous salt solutions<sup>52-60</sup> and aqueous interfaces,<sup>61</sup> such as with air,<sup>50,62-65</sup> macromolecules,<sup>60,66-71</sup> membranes(lipids)<sup>72-76</sup> and hydrophobic liquids<sup>16,17,77</sup>. (The references provided here are not meant to be comprehensive, as the bibliography on specific ion effects is enormous. They serve as indicative examples for the most studied types of interfaces.) By now it is clear that Hofmeister ordering is not unique: there are cases of inversion of the 'direct' (Figure 1.2) Hofmeister series,<sup>71</sup> it depends on the counterions present,<sup>66</sup> and generally smaller differences are observed between cations than between anions in their interactions with interfaces.<sup>78,79</sup> Still, the most usual ordering of ions is presented in Fig. 1.2.

Macroscopic studies are traditionally conducted for the interaction of ions with hydrophobic aqueous (oil/water) interfaces, and are still in use today. A usual method is the phase inversion study of colloidal systems for the addition of different electrolytes,<sup>80</sup> as well as the measurements of the interfacial tension of hydrocarbon (alkane)/aqueous electrolytes interfaces,<sup>81-84</sup> in combination with modelling and simulations.<sup>85</sup> Additionally, zeta potential measurements on emulsions are usual indicators for similarities/differences in the interactions of different salts with the nano- and micro-scopic hydrophobic interface: Beattie *et al.* did not observe any specific cation or anion effects on the zeta-potential of surfactant free hexadecane-in-water emulsions in pH 9 for various alkali-metal salts at salt concentrations below 10 mM.<sup>77</sup> Moreover, they found that dipolar anions (thiocyanate or acetate) are not preferentially attracted to the hexadecane/water of the same system.<sup>87</sup> In contrast, although little, anion dependence (NaBr, NaNO<sub>3</sub>, NaF and NaClO<sub>4</sub>) was actually found for the zeta potential values of CTAB-stabilized toluene-in-water emulsions.<sup>88</sup> These methods suggest differences in the interaction of different ions with the nanointerface, however no molecular level details have been provided.

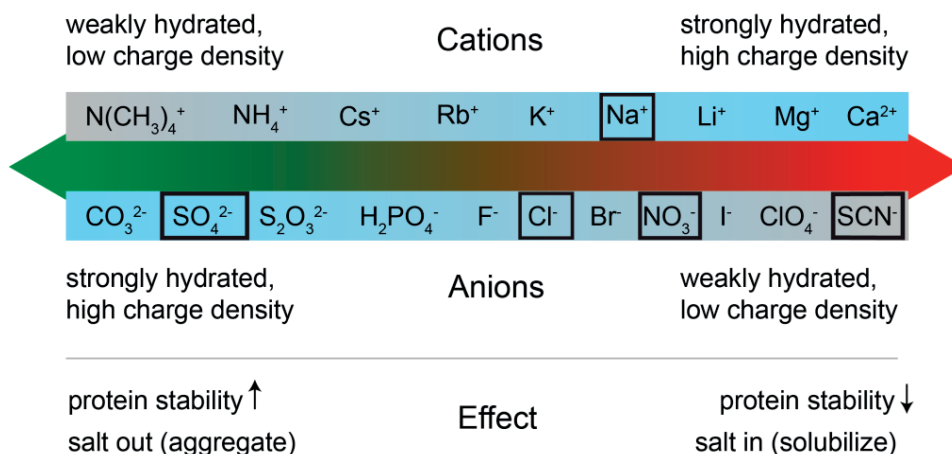


**Figure 1.2: Typical ordering of cations and anions in a Hofmeister series.** Adapted from Ref. <sup>71,86</sup>. The black boxes indicate the ions studied in this thesis

Access to molecular level details of the interfacial structure/interactions has been gained since the 1990's with the advancement of numerous computation and experimental (spectroscopic) methods, mostly focused on extended planar interfaces: The air/water interface has been thoroughly studied,<sup>50,62-65</sup> while membrane(lipid)/aqueous<sup>72-76</sup> and liquid-liquid<sup>16,17</sup> interfaces have also been reported.<sup>89,90</sup> The techniques can selectively report on different components of the interfaces, like the ions of interest (resonant UV-SHG)<sup>91</sup> as well as the configuration of the hydrophobic and the water interfacial layers (vibrational SFG).<sup>92</sup> However, differences between planar systems suggest that molecular level interactions are rather specific. Given the differences in the interfacial structure of an extended planar interface with a nanointerface with the same components,<sup>29</sup> one could expect that the specific ion interactions are also different at the nanointerface.

Despite extensive studies for more than 130 years, our knowledge on the molecular level details of ionic specificity is still not complete.<sup>71</sup> As suggested already by Hofmeister, and adopted for many years, specific ion effects were explained as a result of ion-induced changes to their hydrating water, which in turn affected the hydration of the solvated compound (proteins, macromolecules, liposomes, droplets, colloids).<sup>51,86,93</sup> The current accepted opinion is that the origin of ionic specificity is much more complex: The different polarization and hydration shell of every ion, the molecular structure of the interface that they adsorb to the molecular structure of the chemical groups at the interface that can interact with the ion, as well as the detailed molecular structure and hydrogen bonding of the water network (or other solvent if present) are crucial and should be taken into account.<sup>51,91,95-99</sup> As such, classical mean field models that handle ions as point charges, and simplified continuum models, such as the Debye-Hückel and other Poisson-Boltzmann-based

approaches, where water is only accounted for through its dielectric constant, cannot completely capture specific ion effects.

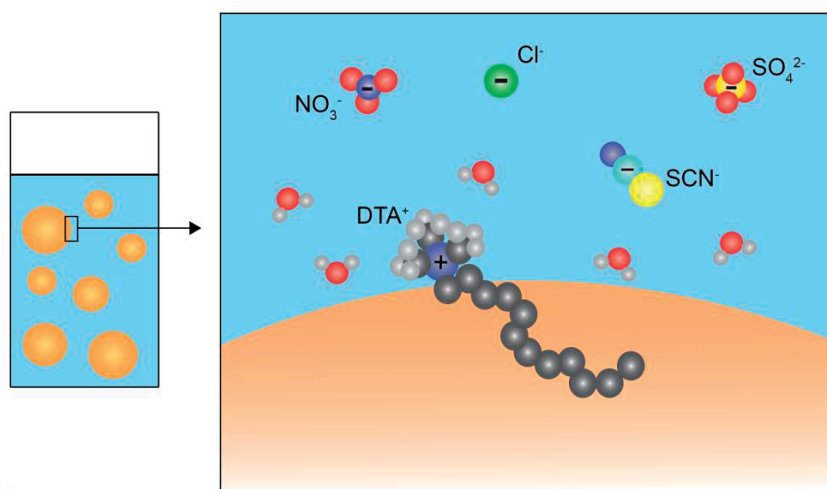


**Figure 1.3: Interaction of different anions with the positively charged oil/water nanointerface.** The interaction of thiocyanate ( $\text{SCN}^-$ ), nitrate ( $\text{NO}_3^-$ ), chloride ( $\text{Cl}^-$ ) and sulfate ( $\text{SO}_4^{2-}$ ) with the surface charges ( $\text{DTA}^+$ ), the hydrophobic interfacial patches, and the interfacial water molecules are compared (Chapters 5 and 6).

For the case of nanoemulsions, ion-specific interactions have already been observed for surfactants with different headgroups:<sup>94</sup> Anionic and cationic amphiphiles adopt strikingly different structures at liquid hydrophobic/water interfaces, linked to the different specific interactions between water and the amphiphile head groups, both at the interface and in the bulk. Specifically, the hydration-shell of a dodecyltrimethylammonium ( $\text{DTA}^+$ ) headgroup (similar to a hydrophobic solute) is very different from that of a dodecyl sulfate ( $\text{DS}^-$ ) headgroup (similar to a hydrophilic solute). This observation is in accordance with a Hofmeister-like ordering of charged headgroups.<sup>68</sup> It is suggested that specific interactions with water play a key role in driving the anionic head group ( $\text{DS}^-$ ) towards the water phase and the cationic headgroup ( $\text{DTA}^+$ ) towards the oil phase. As a consequence, these two opposite charges have quite different surface stabilization mechanisms. Moreover, specific ion effects are also found to depend on the concentration of the salt involved.<sup>78</sup>

Given the importance and complexity of such phenomena, in this thesis we further extend their study in nanoemulsions, and shed light on the molecular level interactions involved. While studying the system presented in Fig. 1.3, namely a positively charged nanointerface and its interaction with various anions, answers to the following questions were provided:

3. While keeping the surfactant headgroup the same, are specific ion effects observed at the oil/water nanointerface, and how do they vary with concentration? (Chapters 5 and 6)
4. What are the specific interactions that ions develop with the hydrophobic and hydrophilic patches of the nanointerface, and what is the resulting interfacial structure? (Chapters 5 and 6)

In order to address the questions raised above, which are all relevant to the structural properties of the nanointerface of droplets in an oil/water nanoemulsion and the interactions thereat, nonlinear second order spectroscopy was employed, presented in the following section.

## 1.2 Second order nonlinear spectroscopic techniques

In this study, we employ two different spectroscopic techniques based on the phenomenon of second-order nonlinear light generation. As is explained here and in Chapter 2, under specific conditions and approximations, light generation of second-order displays the characteristics of surface specificity and chemical specificity. It is, thus, suitable for the study of interfaces and their molecular level structure. The two techniques are introduced briefly here, while further information is provided in Ch. 2.

### 1.2.1 Second order nonlinear light generation

When electromagnetic fields interact with a medium, they can induce a molecular dipole  $\mathbf{p}_i$  in the molecule  $i$ , which can be expressed as<sup>95,96</sup>

$$\mathbf{p}_i = \mathbf{p}_i^{(1)} + \mathbf{p}_i^{(2)} + \mathbf{p}_i^{(3)} + \dots = \alpha^{(1)} \cdot \mathbf{E} + \frac{1}{2}\beta^{(2)} : \mathbf{E}\mathbf{E} + \frac{1}{6}\beta^{(3)} : \mathbf{E}\mathbf{E}\mathbf{E} + \dots \quad (1.1)$$

Here,  $\mathbf{p}_i^{(n)}$  is the molecular polarization component of  $n$ -th order,  $\alpha^{(1)}$  is the first-order polarizability,  $\beta^{(2)}$  the second-order polarizability (or first-order hyperpolarizability) and  $\beta^{(3)}$  the third-order polarizability (or second order hyperpolarizability). The symbols  $:$  and  $:$  designate tensorial products, while  $\mathbf{E}$  denotes any electric field present (one or several). The macroscopic polarization  $\mathbf{P}$  induced in the medium equals to the sum of the molecular dipoles per unit volume, and has components of different order, in correspondence to Eq. (1.1):

$$\mathbf{P} = \mathbf{P}^{(1)} + \mathbf{P}^{(2)} + \mathbf{P}^{(3)} + \dots \quad (1.2)$$

The techniques of Sum Frequency Scattering (SFS) and Second Harmonic Scattering (SHS) used in this thesis employ light originating from the second-order polarization  $\mathbf{P}^{(2)}$ . This choice is of fundamental importance for our study: Under the electric dipole approximation, second-order nonlinear optical processes are forbidden in media possessing inversion symmetry/centrosymmetry.<sup>97</sup> As such, SF and SH light cannot be generated in bulk phases (in this study, the oil and water phases of emulsions), but only at the interface between them, attributing to the two techniques the desired characteristic of surface sensitivity/specificity.  $\mathbf{P}^{(2)}$  can be expressed as

$$\mathbf{P}^{(2)} = \varepsilon_0 \chi^{(2)} : \mathbf{E}\mathbf{E} \quad (1.3)$$

where  $\varepsilon_0$  is the vacuum permittivity, and  $\chi^{(2)}$  is the second-order susceptibility of the medium, namely a third-order tensor with  $3^3 = 27$  elements.  $\chi^{(2)}$  describes the local second-order optical response, reflecting the configuration of the molecules at the interface, as will be discussed in detail in Ch.2.

### 1.2.2 Vibrational Sum Frequency Scattering (SFS)

In the case of vibrational sum frequency generation (SFG), two incident photons with different frequencies lead to the emission of a third photon at the sum of their frequencies ( $\omega_{SF}$ ). The frequency of one of the incident beams is in the visible regime ( $\omega_{VIS}$ ), while of the other one in the infrared ( $\omega_{IR}$ ). Figure 1.4A shows the energy diagram for the SFG process: The IR frequency is tuned to the frequency of a vibrational mode of the molecule, thus the incident IR photon causes the excitation of the molecular vibration. The VIS photon is nonresonant with any vibration and upconverts the molecule to a virtual state. Subsequently the molecule returns to the ground state with the emission of a photon with frequency  $\omega_{SF} = \omega_{IR} + \omega_{VIS}$ . The polarization of the emitted light is given by

$$P_i^{(2)}(\omega_{SF}) \propto \chi_{ijk}^{(2)} E_j(\omega_{VIS}) E_k(\omega_{IR}) \quad (1.4)$$

$i, j$  and  $k$  indices are with respect to the chosen coordinate system (see Ch. 2). The tuning of the IR frequency to a molecular vibrational mode attributes chemical specificity to SFG, allowing to target specific molecules of interest.



The development of SFG theory started in 1962,<sup>98</sup> while the first experiments were reported in 1987.<sup>99,100</sup> Since then, SFG has been extensively used in the reflection configuration (Fig. 1.4B) for the study of various planar interfaces.<sup>24,101-103</sup> However, in this configuration it is not possible to study in-situ interfaces of particles and droplets in solution.

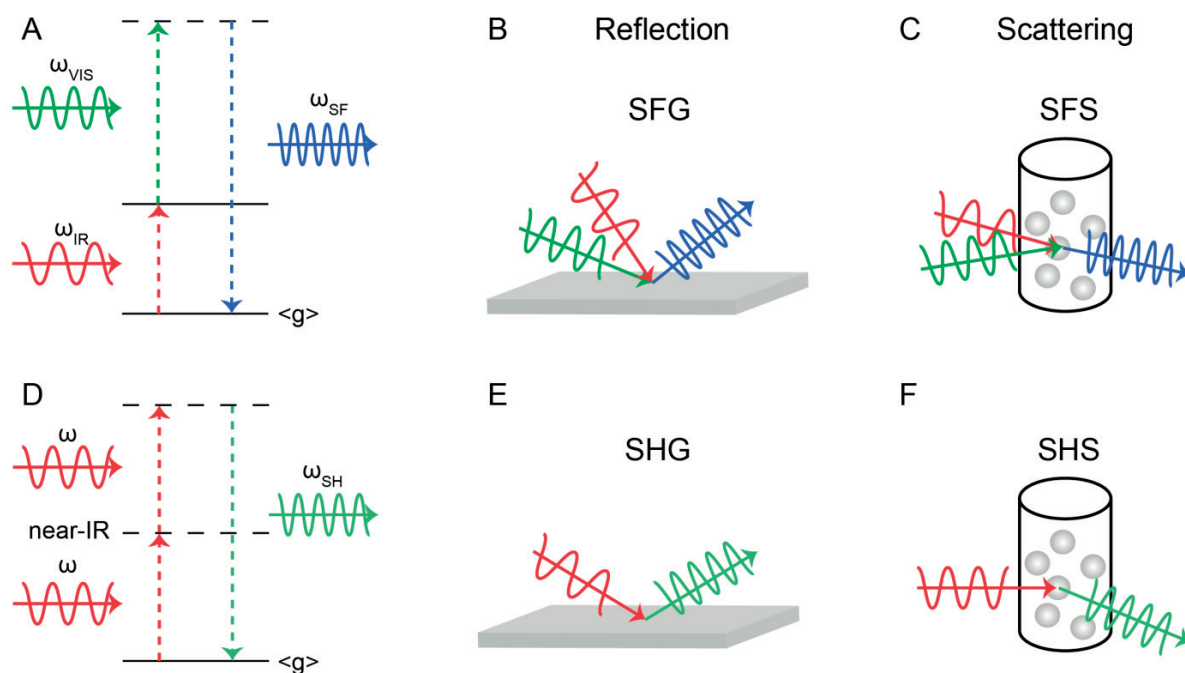


**Figure 1.4: Schematic illustration of the optical processes of SFG/SFS and SHG/SHS.** (A) Energy level transitions in SFG: The incident infrared (IR) photon is resonant with the vibrational mode, resulting in an excitation (red arrow) of the molecular vibration. This molecular vibration is upconverted to a virtual state (green arrow) by a nonresonant interaction with the incident visible (VIS) photon. Subsequently, the molecule returns to the initial ground state (blue arrow) with an emission of a photon with the sum frequency of the IR and VIS photons. (B) Sum frequency planar reflection geometry (C) Sum frequency scattering geometry (D) Energy level transition in SHG: Two incident photons with the same frequency excite a molecule from the ground state to a virtual state (red arrows). Subsequently, the molecule returns (green arrow) to the ground state with an emission of a photon with the double frequency. (E) Collinear second harmonic planar reflection geometry (F) Collinear second harmonic scattering geometry

This problem was solved by Roke *et al.* in 2003,<sup>104</sup> who combined SFG with a scattering configuration (Fig. 1.4C), resulting in the technique known as sum frequency scattering (SFS). Since then, SFS has been successfully used to study the surface structure of colloidal particles,<sup>105-107</sup> nanoscopic oil nanodroplets,<sup>10,29,45,108</sup> and vesicles and liposomes.<sup>32,109,110</sup> In SFS, the SF photons are generated at the surface of the particles in solution and are scattered. The interference of the response of all the particles is measured in the far field, and the induced SF polarization is given by



$$P_i^{(2)}(\theta, \omega_{SF}) \propto \Gamma_{ijk}^{(2)}(\theta, \omega_{SF}) E_j(\omega_{VIS}) E_k(\omega_{IR}) \quad (1.5)$$

Here  $\theta$  is the scattering angle with respect to the phase matching direction, and  $\Gamma_{ijk}^{(2)}$  is the effective particle susceptibility.<sup>111, 112</sup>  $\Gamma_{ijk}^{(2)}$  contains all the information about the scatterer and the scattering geometry, and depends, among others, on the  $\chi^{(2)}$  values at the scatterer interface. Employing the appropriate nonlinear light scattering theory, the molecular structure of the interface of the scatterer can be revealed.<sup>111-114</sup> More details are given in Ch. 2.

### 1.2.3 Second Harmonic Scattering (SHS)

In the case of second harmonic generation (SHG), two incident photons with the same frequency ( $\omega$ ) lead to the emission of a third photon at the double frequency, i.e. the second harmonic frequency ( $\omega_{SH}$ ). Figure 1.4D shows the energy diagram for a nonresonant SHS process, like the one employed in this thesis: The two incoming photons with frequency  $\omega$  excite the molecule from the ground state  $\langle g \rangle$  to a virtual state, and the molecule returns to the ground state with the emission of a photon with frequency  $\omega_{SH} = 2\omega$ . Equation 1.4 can be used for SHG as well. However, in the case that there is only one (degenerate) incoming beam, providing both photons of frequency  $\omega$ ,  $j \equiv k$ .

SHG was first discovered in 1961<sup>115</sup> and the formulation and development of the theory of surface SHG started in 1962.<sup>98</sup> The first surface experiment was conducted in 1969.<sup>116</sup> Since then, it has been extensively used for the study of numerous planar interfaces,<sup>117,118</sup> including liquid/liquid interfaces.<sup>119</sup> The collinear SH planar reflection geometry is shown in Fig. 1.4E. Similar to the case of SFG, with a reflection configuration of SHG it is not possible to study in-situ interfaces of particles and droplets in solution. Wang *et al.*<sup>120</sup> provided a solution with the first resonant second harmonic scattering (SHS) experiment on colloidal particles, employing SHG in a scattering configuration (Fig. 1.4F), probing dye molecules adsorbed on a particle surface. Yan *et al.* applied nonresonant SHS for the first time in 1998<sup>121</sup> to probe interfacial water molecules of a colloidal dispersion and since then it has been extensively used.<sup>108,122</sup> Similar to SFS, SH photons are generated at the surface of the particles in solution and scattered, while the SH polarization in the far field can be described by Eq. 1.5 for  $j \equiv k$ . Nonresonant SHS is a technique that lacks inherent chemical specificity, since none of the frequencies of the incoming or generated photons coincides with a molecular transition. However, the SHS signal is dominated by the response of interfacial water molecules for particles in aqueous solutions.<sup>123,124</sup> This is due to two reasons: First, only non-centrosymmetric molecules, like water, can generate SH photons.

Most importantly, though, SH intensity scales quadratically with the density of molecules, and water greatly outnumbers all other molecules at the interface.

## 1.3 This thesis

The remainder of this thesis is organized as follows:

In Chapter 2, we first describe the methods of sum frequency scattering (SFS) and second harmonic scattering (SHS) that were employed in this study. Dynamic light scattering and  $\zeta$ -potential measurements are also discussed. Then we provide experimental details of SFS and SHS setups, as well as some details for the respective data analysis.

In Chapter 3, we elucidate the stabilization mechanism of oil nanodroplets in water stabilized with anionic, cationic and neutral surfactants. We discuss the effect of interfacial charge on the stabilization mechanism, and propose a stabilization model that differs from the extended planar interfaces.

In Chapter 4, we study the effect of the inversion of the two phases (oil-in-water and water-in-oil) on the stability of nanometer- and micrometer-sized emulsions. We correlate the structure of surfactants with droplets stability both for a surfactant mostly soluble in the water phase, and for a surfactant mostly soluble in the oil phase, with a comparison between the two different sized systems.

In Chapter 5, we compare the adsorption of anions with different molecular structure at the interface of oil nanodroplets in water stabilized with a positive surfactant. The anions chosen are known to exhibit different adsorption propensities in planar systems. The effect of anions on the interfacial structure, along with their interactions with the interfacial charges, the bare hydrophobic interfacial patches and the interfacial water molecules are discussed.

In Chapter 6, we continue from Chapter 5 and study in further detail the speciation of the anion that exhibited the most complex adsorption pattern (namely  $\text{SCN}^-$ ), in combination with *ab-initio* molecular dynamics simulations.

In Chapter 7, we provide a summary of the results obtained in this study, as well as an outlook for future studies.

## 1.4 References

1. Hunter, R. J. *Foundations of colloid science* (Oxford University Press, New York, 2001).
2. McClements, J. D. Critical review of techniques and methodologies for characterization of emulsion stability. *Crit. Rev. Food Sci. Nutr.* **47**, 611-649 (2007).
3. Mason, T. G., Wilking, J. N., Meleson, K., Chang, C. B. & Graves, S. M. Nanoemulsions: Formation, structure, and physical properties. *J. Phys.: Condens. Matter* **18**, R635-R666 (2006).
4. Theberge, A. B., Courtois, F., Schaerli, Y., Fischlechner, M., Abell, C., Hollfelder, F. & Huck Wilhelm, T. S. Microdroplets in microfluidics: An evolving platform for discoveries in chemistry and biology. *Angew. Chem. Int. Ed.* **49** (34), 5846-5868 (2010).
5. Shembekar, N., Chaipan, C., Utharala, R. & Merten, C. A. Droplet-based microfluidics in drug discovery, transcriptomics and high-throughput molecular genetics. *Lab Chip* **16** (8), 1314-1331 (2016).
6. Atkins, P. & De Paula, J. *Atkins' physical chemistry* (Oxford University Press, Oxford, 2010).
7. Hardy, W. B. & Harvey, H. W. Note on the surface electric charges of living cells. *Proc. Royal Soc. Lond. B* **84**, 217-226 (1911).
8. Harkins, W. D., Davies, E. C. H. & Clark, G. L. The orientation of molecules in the surfaces of liquids, the energy relations at surfaces, solubility, adsorption, emulsification, molecular association, and the effect of acids and bases on interfacial tension. *J. Am. Chem. Soc.* **39**, 354-364 (1917).
9. Langmuir, I. The constitution and fundamental properties of solids and liquids. II Liquids. *J. Am. Chem. Soc.* **39**, 1848-1906 (1917).
10. De Aguiar, H. B., Samson, J. S. & Roke, S. Probing nanoscopic droplet interfaces in aqueous solution with vibrational sum-frequency scattering: A study of the effects of path length, droplet density and pulse energy. *Chem. Phys. Lett.* **512**, 76-80 (2011).
11. Fischer, E. K. & Harkins, W. D. Monomolecular films, the liquid-liquid interface and the stability of emulsions. *J. Phys. Chem.* **36**, 98-110 (1932).
12. Israelachvili, J. N. *Intermolecular and surface forces* (Academic Press, San Diego, 2011).
13. Lyklema, J. *Fundamentals of interface and colloid science: Soft colloids* (Elsevier Science, Amsterdam, 2005).
14. Adamson, A. W. & Gast, A. P. *Physical chemistry of surfaces* (Wiley, New York, 1997).

15. Berge, B., Konovalov, O., Lajzerowicz, J., Renault, A., Rieu, J. P., Vallade, M., Als-Nielsen, J., Grubel, G. & Legrand, J. F. Melting of short 1-alcohol monolayers on water: Thermodynamics and X-ray scattering studies. *Phys. Rev. Lett.* **73** (12), 1652-1655 (1994).
16. Als-Nielsen, J. & Mcmorrow, D. *Elements of modern X-ray physics* (Wiley, Hoboken, 2011).
17. Lu, J. R., Marrocco, A., Su, T. J., Thomas, R. K. & Penfold, J. Adsorption of dodecyl sulfate surfactants with monovalent metal counterions at the air-water interface studied by neutron reflection and surface tension. *J. Colloid Interface Sci.* **158** (2), 303-316 (1993).
18. Sloutskin, E., Sapir, Z., Bain, C. D., Lei, Q., Wilkinson, K. M., Tamam, L., Deutsch, M. & Ocko, B. M. Wetting, mixing, and phase transitions in Langmuir-Gibbs films. *Phys. Rev. Lett.* **99**, 136102-136104 (2007).
19. Guyot-Sionnest, P., Hunt, J. H. & Shen, Y. R. Sum-frequency vibrational spectroscopy of a Langmuir film: Study of molecular-orientation of a two dimensional system. *Phys. Rev. Lett.* **59** (14), 1597-1600 (1987).
20. Harris, A. L., Chidsey, C. E. D., Levinos, N. J. & Loiacono, D. N. Monolayer vibrational spectroscopy by infrared-visible sum generation at metal and semiconductor surfaces. *Chem. Phys. Lett.* **141**, 350-356 (1987).
21. Conboy, J. C., Messmer, M. C. & Richmond, G. L. Dependence of alkyl chain conformation of simple ionic surfactants on head group functionality as studied by vibrational sum-frequency spectroscopy. *J. Phys. Chem. B* **101** (34), 6724-6733 (1997).
22. Knock, M. M., Bell, G. R., Hill, E. K., Turner, H. J. & Bain, C. D. Sum-frequency spectroscopy of surfactant monolayers at the oil-water interface. *J. Phys. Chem. B* **107**, 10801-10814 (2003).
23. Messmer, M. C., Conboy, J. C. & Richmond, G. L. Observation of molecular ordering at the liquid-liquid interface by resonant sum-frequency generation. *J. Am. Chem. Soc.* **117**, 8039-8040 (1995).
24. Richmond, G. L. Structure and bonding of molecules at aqueous surfaces. *Annu. Rev. Phys. Chem.* **52**, 357-389 (2001).
25. Pratt, L. R. & Pohorille, A. Hydrophobic effects and modeling of biophysical aqueous solution interfaces. *Chem. Rev.* **102** (8), 2671-2691 (2002).
26. Kuna, J. J., Voitchovsky, K., Singh, C., Jiang, H., Mwenifumbo, S., Ghorai, P. K., Stevens, M. M., Glotzer, S. C. & Stellacci, F. The effect of nanometre-scale structure on interfacial energy. *Nat. Mater.* **8**, 837 (2009).

27. Acharya, H., Vembanur, S., Jamadagni, S. N. & Garde, S. Mapping hydrophobicity at the nanoscale: Applications to heterogeneous surfaces and proteins. *Faraday Discuss.* **146** (0), 353-365 (2010).
28. Jackson, A. M., Myerson, J. W. & Stellacci, F. Spontaneous assembly of subnanometre-ordered domains in the ligand shell of monolayer-protected nanoparticles. *Nat. Mater.* **3** (5), 330-336 (2004).
29. De Aguiar, H. B., De Beer, A. G. F., Strader, M. L. & Roke, S. The interfacial tension of nanoscopic oil droplets in water is hardly affected by SDS surfactant. *J. Am. Chem. Soc.* **132**, 2122-2123 (2010).
30. Kurylowicz, M., Paulin, H., Mogyoros, J., Giuliani, M. & Dutcher, J. R. The effect of nanoscale surface curvature on the oligomerization of surface-bound proteins. *J. R. Soc., Interface* **11** (94), (2014).
31. Long, J. A., Rankin, B. M. & Ben-Amotz, D. Micelle structure and hydrophobic hydration. *J. Am. Chem. Soc.* **137** (33), 10809-10815 (2015).
32. Smolentsev, N., Lütgebaucks, C., Okur, H. I., De Beer, A. G. F. & Roke, S. Intermolecular headgroup interaction and hydration as driving forces for lipid transmembrane asymmetry. *J. Am. Chem. Soc.* **138** (12), 4053-4060 (2016).
33. Smolentsev, N., Smit, W. J., Bakker, H. J. & Roke, S. The interfacial structure of water droplets in a hydrophobic liquid. *Nat. Commun.* **8**, 15548 (2017).
34. Rehfeld, S. J. Adsorption of sodium dodecyl sulfate at various hydrocarbon-water interfaces. *J. Phys. Chem.* **71** (3), 738-745 (1967).
35. Conboy, J. C., Messmer, M. C. & Richmond, G. L. Investigation of surfactant conformation and order at the liquid-liquid interface by total internal reflection sum-frequency vibrational spectroscopy. *J. Phys. Chem.* **100**, 7617-7622 (1996).
36. Conboy, J. C., Messmer, M. C. & Richmond, G. L. Effect of alkyl chain length on the conformation and order of simple ionic surfactants adsorbed at the D<sub>2</sub>O/CCl<sub>4</sub> interface as studied by sum-frequency vibrational spectroscopy. *Langmuir* **14**, 6722-6727 (1998).
37. McClements, D. J. Nanoemulsions versus microemulsions: Terminology, differences, and similarities. *Soft Matter* **8** (6), 1719 (2012).
38. De Aguiar, H. B., Strader, M. L., De Beer, A. G. F. & Roke, S. Surface structure of sodium dodecyl sulfate surfactant and oil at the oil-in-water droplet liquid/liquid interface: A manifestation of a non-equilibrium surface state. *J. Phys. Chem. B* **115**, 2970-2978 (2011).
39. Company, A. P. *Atlas surface active agents* (Industrial Chemicals Department, Atlas Powder Company, 1948).

40. Velev, O. D., Danov, K. D. & Ivanov, I. B. Stability of emulsions under static and dynamic conditions. *J. Dispersion Sci. Technol.* **18** (6-7), 625-645 (1997).
41. Sjoblom, J. *Emulsions and emulsion stability: Surfactant science series/61* (CRC Press, Boca Raton, 2006).
42. McClements, J. & McClements, D. J. Standardization of nanoparticle characterization: Methods for testing properties, stability, and functionality of edible nanoparticles. *Crit. Rev. Food Sci. Nutr.* **56** (8), 1334-1362 (2016).
43. McClements, D. J. *Food emulsions: Principles, practices, and techniques* (CRC Press, Florida, 2004).
44. Zdrali, E., Chen, Y., Okur, H. I., Wilkins, D. M. & Roke, S. The molecular mechanism of nanodroplet stability. *ACS Nano* **11** (12), 12111-12120 (2017).
45. Oshima, H. *Theory of colloid and interfacial phenomena* (Academic Press, 2006).
46. Chaffey, N., Alberts, B., Johnson, A., Lewis, J., Raff, M., Roberts, K. & Walter, P. Molecular biology of the cell. 4th edn. *Ann. Bot.* **91** (3), 401-401 (2003).
47. Jena, K. C., Scheu, R. & Roke, S. Surface impurities are not responsible for the charge on the oil/water interface: A comment. *Angew. Chem. Int. Ed.* **51** (52), 12938-12940 (2012).
48. Salis, A. & Ninham, B. W. Models and mechanisms of Hofmeister effects in electrolyte solutions, and colloid and protein systems revisited. *Chem. Soc. Rev.* **43** (21), 7358-7377 (2014).
49. Jungwirth, P. & Tobias, D. J. Specific ion effects at the air/water interface. *Chem. Rev.* **106** (4), 1259-1281 (2006).
50. Hofmeister, F. Zur lehre von der wirkung der salze. *Archiv für experimentelle Pathologie und Pharmakologie* **24** (4), 247-260 (1888).
51. Pluharova, E., Baer, M. D., Schenter, G. K., Jungwirth, P. & Mundy, C. J. Dependence of the rate of lif ion-pairing on the description of molecular interaction. *J. Phys. Chem. B* **120** (8), 1749-1758 (2016).
52. Bruneval, F., Donadio, D. & Parrinello, M. Molecular dynamics study of the solvation of calcium carbonate in water. *J. Phys. Chem. B* **111** (42), 12219-12227 (2007).
53. Pluharova, E., Marsalek, O., Schmidt, B. & Jungwirth, P. Ab initio molecular dynamics approach to a quantitative description of ion pairing in water. *J. Phys. Chem. Lett.* **4** (23), 4177-4181 (2013).
54. Buchner, R., Hefter, G. T. & May, P. M. Dielectric relaxation of aqueous NaCl solutions. *J. Phys. Chem. A* **103** (1), 1-9 (1999).
55. Chen, D., Zhang, Y., He, T. & Liu, F. Raman and UV–visible absorption spectra of ion-paired aggregates of copper porphyrins. *Spectrochim. Acta A* **58** (10), 2291-2297 (2002).



56. Van Der Post, S. T., Scheidelaar, S. & Bakker, H. J. Water dynamics in aqueous solutions of tetra-n-alkylammonium salts: Hydrophobic and Coulomb interactions disentangled. *J. Phys. Chem. B* **117** (48), 15101-15110 (2013).
57. Kuroda, D. G. & Hochstrasser, R. M. Dynamic structures of aqueous oxalate and the effects of counterions seen by 2D IR. *Phys. Chem. Chem. Phys.* **14** (18), 6219-6224 (2012).
58. Shih, O., England, A. H., Dallinger, G. C., Smith, J. W., Duffey, K. C., Cohen, R. C., Prendergast, D. & Saykally, R. J. Cation-cation contact pairing in water: Guanidinium. *J. Chem. Phys.* **139** (3), (2013).
59. Heyda, J., Okur, H. I., Hladílková, J., Rembert, K. B., Hunn, W., Yang, T., Dzubiella, J., Jungwirth, P. & Cremer, P. S. Guanidinium can both cause and prevent the hydrophobic collapse of biomacromolecules. *J. Am. Chem. Soc.* **139**, 863-870 (2017).
60. Lo Nostro, P. & Ninham, B. W. Hofmeister phenomena: An update on ion specificity in biology. *Chem. Rev.* **112** (4), 2286-2322 (2012).
61. Garrett, B. C. Ions at the air/water interface. *Science* **303** (5661), 1146-1147 (2004).
62. Bian, H., Feng, R., Xu, Y., Guo, Y. & Wang, H. Increased interfacial thickness of the NaF, NaCl and NaBr salt aqueous solutions probed with non-resonant surface second harmonic generation (shg). *Phys. Chem. Chem. Phys.* **10** (32), 4920-4931 (2008).
63. Bian, H., Chen, H., Zhang, Q., Li, J., Wen, X., Zhuang, W. & Zheng, J. Cation effects on rotational dynamics of anions and water molecules in alkali ( $\text{Li}^+$ ,  $\text{Na}^+$ ,  $\text{K}^+$ ,  $\text{Cs}^+$ ) thiocyanate ( $\text{SCN}^-$ ) aqueous solutions. *J. Phys. Chem. B* **117** (26), 7972-7984 (2013).
64. Vrbka, L., Mucha, M., Minofar, B., Jungwirth, P., Brown, E. C. & Tobias, D. J. Propensity of soft ions for the air/water interface. *Curr. Opin. Colloid Interface Sci.* **9** (1), 67-73 (2004).
65. Okur, H. I., Hladílková, J., Rembert, K. B., Cho, Y., Heyda, J., Dzubiella, J., Cremer, P. S. & Jungwirth, P. Beyond the Hofmeister series: Ion-specific effects on proteins and their biological functions. *J. Phys. Chem. B* **121** (9), 1997-2014 (2017).
66. Hess, B. & Van Der Vegt, N. F. A. Cation specific binding with protein surface charges. *Proc. Natl. Acad. Sci. U.S.A.* **106** (32), 13296-13300 (2009).
67. Vlachy, N., Jagoda-Cwiklik, B., Vácha, R., Touraud, D., Jungwirth, P. & Kunz, W. Hofmeister series and specific interactions of charged headgroups with aqueous ions. *Adv. Colloid Interface Sci.* **146** (1-2), 42-47 (2009).
68. Jungwirth, P. & Winter, B. Ions at aqueous interfaces: From water surface to hydrated proteins. *Annu. Rev. Phys. Chem.* **59** (1), 343-366 (2008).

69. Lund, M., Vácha, R. & Jungwirth, P. Specific ion binding to macromolecules: Effects of hydrophobicity and ion pairing. *Langmuir* **24** (7), 3387-3391 (2008).
70. Zhang, Y. J. & Cremer, P. S. Chemistry of Hofmeister anions and osmolytes. *Annu. Rev. Phys. Chem.* **61**, 63-83 (2010).
71. Boström, M., Deniz, V. & Ninham, B. W. Ion specific surface forces between membrane surfaces. *J. Phys. Chem. B* **110** (19), 9645-9649 (2006).
72. Casillas-Ituarte, N., Chen, X., Castada, H. & Allen, H. C. Na<sup>+</sup> and Ca<sup>2+</sup> effect on the hydration and orientation of the phosphate group of DPPC at air-water and air-hydrated silica interfaces. *J. Phys. Chem. B* **114** (29), 9485-9495 (2010).
73. P, V., Aroti, A., Motschmann, H. & Leontidis, E. Vibrational sum frequency generation spectroscopic investigation of the interaction of thiocyanate ions with zwitterionic phospholipid monolayers at the air-water interface. *J. Phys. Chem. B* **113** (44), 14816-14823 (2009).
74. Dreier, L. B., Nagata, Y., Lutz, H., Gonella, G., Hunger, J., Backus, E. H. G. & Bonn, M. Saturation of charge-induced water alignment at model membrane surfaces. *Sci. Adv.* **4** (3), (2018).
75. Dengler, S., Klaus, A., Tiddy, G. J. T. & Kunz, W. How specific are ion specificities? A pilot NMR study. *Faraday Discuss.* **160** (0), 121-133 (2013).
76. Franks, G. V., Djerdjev, A. M. & Beattie, J. K. Absence of specific cation or anion effects at low salt concentrations on the charge at the oil/water interface. *Langmuir* **21** (19), 8670-8674 (2005).
77. Chen, X., Yang, T., Kataoka, S. & Cremer, P. S. Specific ion effects on interfacial water structure near macromolecules. *J. Am. Chem. Soc.* **129**, 12272-12279 (2007).
78. Flores, S. C., Kherb, J., Konelick, N., Chen, X. & Cremer, P. S. The effects of Hofmeister cations at negatively charged hydrophilic surfaces. *J. Phys. Chem. C* **116** (9), 5730-5734 (2012).
79. Murgia, S., Monduzzi, M. & Ninham, B. W. Hofmeister effects in cationic microemulsions. *Curr. Opin. Colloid Interface Sci.* **9** (1), 102-106 (2004).
80. Evans, A. W. The effect of uni-univalent electrolytes upon the interfacial tension between normal-hexane and water. *Trans. Faraday Soc.* **33** (0), 794-800 (1937).
81. Lima, E. R. A., Melo, B. M. D., Baptista, L. T. & Paredes, M. L. L. Specific ion effects on the interfacial tension of water/hydrocarbon systems. *Braz. J. Chem. Eng.* **30**, 55-62 (2013).
82. Ikeda, N., Aratono, M. & Motomura, K. Thermodynamic study on the adsorption of sodium chloride at the water/hexane interface. *J. Colloid Interface Sci.* **149** (1), 208-215 (1992).



83. Aveyard, R. & Saleem, S. M. Interfacial tensions at alkane-aqueous electrolyte interfaces. *J. Chem. Soc. Faraday Trans. 1* **72** (0), 1609-1617 (1976).
84. Schwierz, N., Horinek, D. & Netz, R. R. Anionic and cationic Hofmeister effects on hydrophobic and hydrophilic surfaces. *Langmuir* **29** (8), 2602-2614 (2013).
85. Kunz, W. Specific ion effects in colloidal and biological systems. *Curr. Opin. Colloid Interface Sci.* **15** (1–2), 34-39 (2010).
86. Beattie, J. K., Djerdjev, A. M., Franks, G. & Warr, G. Dipolar anions are not preferentially attracted to the oil/water interface. *J. Phys. Chem. B* **109** (33), 15675-15676 (2005).
87. Wojciechowski, K., Bitner, A., Warszyński, P. & Żubrowska, M. The Hofmeister effect in zeta potentials of CTAB-stabilised toluene-in-water emulsions. *Colloids Surf. A* **376** (1), 122-126 (2011).
88. Luo, G., Malkova, S., Yoon, J., Schultz, D. G., Lin, B., Meron, M., Benjamin, I., Vanýsek, P. & Schlossman, M. L. Ion distributions near a liquid-liquid interface. *Science* **311** (5758), 216-218 (2006).
89. Slavchov, R. I. & Peshkova, T. V. Adsorption of ions at the interface oil/aqueous electrolyte and at interfaces with adsorbed alcohol. *J. Colloid Interface Sci.* **428**, 257-266 (2014).
90. Onorato, R. M., Otten, D. E. & Saykally, R. J. Adsorption of thiocyanate ions to the dodecanol/water interface characterized by UV second harmonic generation. *Proc. Natl. Acad. Sci. U.S.A.* **106** (36), 15176-15180 (2009).
91. Gurau, M. C., Lim, S. M., Castellana, E. T., Albertorio, F., Kataoka, S. & Cremer, P. S. On the mechanism of the Hofmeister effect. *J. Am. Chem. Soc.* **126**, 10522-10523 (2004).
92. Marcus, Y. Effect of ions on the structure of water: Structure making and breaking. *Chem. Rev.* **109** (3), 1346-1370 (2009).
93. Scheu, R., Chen, Y. X., De Aguiar, H. B., Rankin, B. M., Ben-Amotz, D. & Roke, S. Specific ion effects in amphiphile hydration and interface stabilization. *J. Am. Chem. Soc.* **136** (5), 2040-2047 (2014).
94. Coulson, C. A., Maccoll, A. & Sutton, L. E. The polarizability of molecules in strong electric fields. *Transactions of the Faraday Society* **48**, 106-113 (1952).
95. Cyvin, S. J., Rauch, J. E. & Decius, J. C. Theory of hyper-Raman effects (nonlinear inelastic light scattering): Selection rules and depolarization ratios for the second-order polarizability. *J. Chem. Phys.* **43**, 4083-4083 (1965).
96. Lambert, A. G., Davies, P. B. & Neivandt, D. J. Implementing the theory of sum frequency generation vibrational spectroscopy: A tutorial review. *Appl. Spectrosc. Rev.* **40**, 103-144 (2005).

97. Bloembergen, N. & Pershan, P. S. Light waves at the boundary of nonlinear media. *Phys. Rev.* **128** (2), 606-622 (1962).
98. Hunt, J. H., Guyot-Sionnest, P. & Shen, Y. R. Observation of C-H stretch vibrations of monolayers of molecules optical sum-frequency generation. *Chem. Phys. Lett.* **133** (3), 189-192 (1987).
99. Harris, A. L., Chidsey, C. E. D., Levinos, N. J. & Loiacono, D. N. Monolayer vibrational spectroscopy by infrared-visible sum generation at metal and semiconductor surfaces. *Chem. Phys. Lett.* **141** (4), 350-356 (1987).
100. Nihonyanagi, S., Mondal, J. A., Yamaguchi, S. & Tahara, T. Structure and dynamics of interfacial water studied by heterodyne-detected vibrational sum-frequency generation. *Annu. Rev. Phys. Chem.* **64**, 579-603 (2013).
101. Shen, Y. R. & Ostroverkhov, V. Sum-frequency vibrational spectroscopy on water interfaces: Polar orientation of water molecules at interfaces. *Chem. Rev.* **106** (4), 1140-1154 (2006).
102. Tian, C. S. & Shen, Y. R. Recent progress on sum-frequency spectroscopy. *Surf. Sci. Rep.* **69** (2), 105-131 (2014).
103. Roke, S., Roeterdink, W. G., Wijnhoven, J. E. G. J., Petukhov, A. V., Kleyn, A. W. & Bonn, M. Vibrational sum frequency scattering from a submicron suspension. *Phys. Rev. Lett.* **91** (25), 258302 (2003).
104. Roke, S., Berg, O., Buitenhuis, J., Van Blaaderen, A. & Bonn, M. Surface molecular view of colloidal gelation. *Proc. Nat. Acad. Sci.* **103** (36), 13310-13314 (2006).
105. Johnson, C. M., Sugiharto, A. B. & Roke, S. Surface and bulk structure of poly(lactic acid) films studied by vibrational sum frequency spectroscopy. *Chem. Phys. Lett.* **449**, 191-195 (2007).
106. De Beer, A. G. F., De Aguiar, H. B., Nijsen, J. W. F. & Roke, S. Detection of buried microstructures with nonlinear light scattering spectroscopy. *Phys. Rev. Lett.* **102**, 95502-95504 (2009).
107. Roke, S. & Gonella, G. Nonlinear light scattering and spectroscopy of particles and droplets in liquids. *Annu. Rev. Phys. Chem.* **63**, 353-378 (2012).
108. Gomopoulos, N., Lutgebaucks, C., Sun, Q. C., Macias-Romero, C. & Roke, S. Label-free second harmonic and hyper rayleigh scattering with high efficiency. *Opt. Express* **21** (1), 815-821 (2013).
109. Okur, H. I., Chen, Y., Smolentsev, N., Zdrali, E. & Roke, S. Interfacial structure and hydration of 3d lipid monolayers in aqueous solution. *J. Phys. Chem. B* **121** (13), 2808-2813 (2017).
110. Roke, S., Bonn, M. & Petukhov, A. V. Nonlinear optical scattering: The concept of the effective susceptibility. *Phys. Rev. B* **70**, 115106-115110 (2004).

111. De Beer, A. G. F. & Roke, S. Obtaining molecular orientation from second harmonic and sum frequency scattering experiments in water: Angular distribution and polarization dependence. *J. Chem. Phys.* **132** (23), 234702 (2010).
112. De Beer, A. G. F. & Roke, S. Nonlinear mie theory for second-harmonic and sum-frequency scattering. *Phys. Rev. B* **79**, 155420-155429 (2009).
113. De Beer, A. G. F., Roke, S. & Dadap, J. I. Theory of optical second-harmonic and sum-frequency scattering from arbitrarily shaped particles. *J. Opt. Soc. Am. B* **28** (6), 1374-1384 (2011).
114. Franken, P. A., Hill, A. E., Peters, C. W. & Weinreich, G. Generation of optical harmonics. *Phys. Rev. Lett.* **7** (4), 118-119 (1961).
115. Brown, F. & Matsuoka, M. Effect of adsorbed surface layers on second-harmonic light from silver. *Phys. Rev.* **185** (3), 985-987 (1969).
116. Richmond, G. L., Robinson, J. M. & Shannon, V. L. Second harmonic generation studies of interfacial structure and dynamics. *Prog. Surf. Sci.* **28** (1), 1-70 (1988).
117. Shen, Y. R. Surface properties probed by second-harmonic and sum-frequency generation. *Nature* **337**, 519-519 (1989).
118. Eienthal, K. B. Liquid interfaces probed by second-harmonic and sum-frequency spectroscopy. *Chem. Rev.* **96** (4), 1343-1360 (1996).
119. Wang, H., Yan, E. C. Y., Borguet, E. & Eienthal, K. B. Second harmonic generation from the surface of centrosymmetric particles in bulk solution. *Chem. Phys. Lett.* **259** (1-2), 15-20 (1996).
120. Yan, E. C. Y., Liu, Y. & Eienthal, K. B. New method for determination of surface potential of microscopic particles by second harmonic generation. *J. Phys. Chem. B.* **102**, 6331-6336 (1998).
121. Gonella, G. & Dai, H.-L. Second harmonic light scattering from the surface of colloidal objects: Theory and applications. *Langmuir* **30** (10), 2588-2599 (2014).
122. Gonella, G., Lütgebaucks, C., De Beer, A. G. F. & Roke, S. Second harmonic and sum-frequency generation from aqueous interfaces is modulated by interference. *J. Phys. Chem. C* **120** (17), 9165-9173 (2016).
123. Schürer, B., Wunderlich, S., Sauerbeck, C., Peschel, U. & Peukert, W. Probing colloidal interfaces by angle-resolved second harmonic light scattering. *Phys. Rev. B* **82** (24), 241404-241404 (2010).



## Chapter 2: Experimental Details and Methodology

*In this chapter is presented the theoretical background of the nonlinear spectroscopic techniques used in this thesis, namely sum frequency scattering (SFS) and second harmonic scattering (SHS), along with the respective experimental setups. Dynamic light scattering (DLS) and electrokinetic mobility ( $\zeta$ -potential) measurements are also briefly presented.*

## 2.1 Introduction

Here, initially we present the theoretical basis of sum frequency scattering (SFS) and second harmonic scattering (SHS) that were employed to access the buried liquid hydrophobic aqueous interface. Dynamic light scattering (DLS) and electrokinetic mobility measurements, used to characterize the nanodroplets and their stability, are briefly introduced as well. Last, the experimental setups of SFS and SHS are presented.

## 2.2 Theoretical background

### 2.2.1 Vibrational Sum Frequency Scattering

#### Geometry of SFS experiment

Vibrational SFS gives the possibility to retrieve the orientational distribution of interfacial molecular groups from polarization dependent measurements of SFS intensity ( $I_{SF}$ ).<sup>1</sup> Mathematically, this can be achieved through successive transformations of coordinate systems, from the molecular to the macroscopic level (explained below), along with the introduction of the second-order effective susceptibility,  $\Gamma^{(2)}$ .<sup>2</sup>  $\Gamma^{(2)}$  contains all information about the scatterer and the scattering geometry, and allows the connection of the scattered SF intensity measured in the lab to the molecular structure at the interface. Specifically,  $I_{SF}$  is converted to  $\Gamma^{(2)}$ , then  $\Gamma^{(2)}$  to the second-order surface susceptibility  $\chi^{(2)}$  of the interface, and finally  $\chi^{(2)}$  to the molecular hyperpolarizability  $\beta^{(2)}$ . The derivation of the respective theory was initially conducted by Roke<sup>2,3</sup> *et al.*, while a detailed presentation can be found in Ref.<sup>4</sup> by de Beer and Roke. Figure 2.1 presents the geometry of the sum frequency scattering experiment. A nanodroplet with radius  $R$  lies at the  $(0, 0, 0)$  point of the lab frame, named as the  $(x, y, z)$  coordinate system. For simplicity, different coordinate systems are used to describe each of the nonlinear quantities: For  $\beta^{(2)}$  the molecular frame  $(a, b, c)$  is used, for  $\chi^{(2)}$  the interfacial frame  $(r', \theta', \varphi')$ , for  $\Gamma^{(2)}$  the rotated lab frame  $(q_x, q_y, q_z)$ , and for the measured  $I_{SH}$  the lab frame  $(x, y, z)$ . In the following we describe the definition of those frames, as well as the transformations between them.

A VIS beam, with wavevector  $\mathbf{k}_1$ , and an IR beam, with wavevector  $\mathbf{k}_2$ , illuminate the nanodroplet. Both of these incoming beams lie in the  $(xz)$  plane, which is the scattering plane, while the  $z$ -axis is aligned with the sum of the wavevectors of the two incoming beams  $\mathbf{k}_1 + \mathbf{k}_2$ .

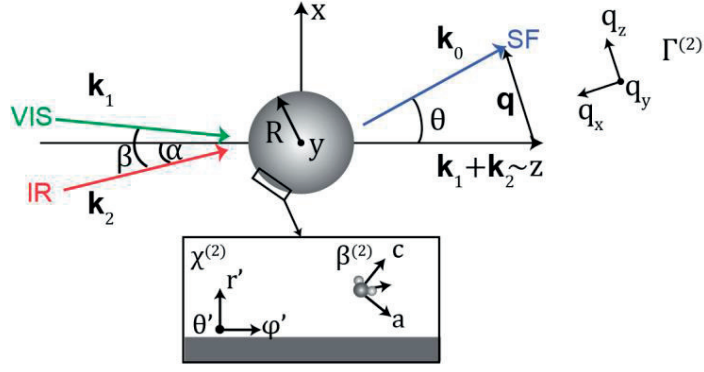


**Figure 2.1: Top view of the SFS geometry (sketch).** A VIS beam, with wavevector  $\mathbf{k}_1$ , and an IR beam, with wavevector  $\mathbf{k}_2$ , illuminate the nanodroplet. Both beams lie in the  $xz$  (scattering) plane. The  $z$ -axis is aligned with the sum of the wavevectors of the two incoming beams  $\mathbf{k}_1 + \mathbf{k}_2$  and the scattering vector  $\mathbf{q}$  is defined as  $\mathbf{k}_0 - (\mathbf{k}_1 + \mathbf{k}_2)$ . The effective susceptibility  $\Gamma^{(2)}$  is defined in the rotated lab frame  $(q_x, q_y, q_z)$ . The surface susceptibility  $\chi_s^{(2)}(\mathbf{r}') = \chi^{(2)}(\mathbf{r}')\delta(|\mathbf{r}'| - R)$  is defined in the surface coordinates  $(r', \theta', \varphi')$ , while the hyperpolarizability  $\beta^{(2)}$  is defined in the molecular coordinate system.

The wavevector of the scattered SF light is denoted with  $\mathbf{k}_0$ . The angle between the IR beam and the  $z$ -axis is labeled by  $\alpha$ , between the IR and the VIS beams by  $\beta$ , and between  $\mathbf{k}_1 + \mathbf{k}_2$  and  $\mathbf{k}_0$  by  $\theta$ . The latter angle,  $\theta$ , is called scattering angle. The scattering vector  $\mathbf{q}$  is defined as  $\mathbf{q} = \mathbf{k}_0 - (\mathbf{k}_1 + \mathbf{k}_2)$  with  $q \equiv |\mathbf{q}| = 2k_0 \sin(\theta/2)$ . For in-plane scattering the  $\mathbf{k}$  vectors can be expressed as

$$\begin{pmatrix} \mathbf{k}_0 \\ \mathbf{k}_1 \\ \mathbf{k}_2 \end{pmatrix} = \begin{pmatrix} k_0 \sin \theta & 0 & k_0 \cos \theta \\ -k_0 \sin(\beta - \alpha) & 0 & k_0 \cos(\beta - \alpha) \\ k_0 \sin \alpha & 0 & k_0 \cos \alpha \end{pmatrix} \begin{pmatrix} \hat{x} \\ \hat{y} \\ \hat{z} \end{pmatrix} \quad (2.1)$$

and

$$\mathbf{k}_1 + \mathbf{k}_2 = |\mathbf{k}_1 + \mathbf{k}_2| \hat{z} \quad (2.2)$$

where  $\hat{x}$ ,  $\hat{y}$  and  $\hat{z}$  are the unit vectors along the  $x, y$  and  $z$  axes respectively.

The rotated lab frame  $(q_x, q_y, q_z)$  can be calculated from the lab frame  $(x, y, z)$  as

$$\begin{pmatrix} \mathbf{q}_x \\ \mathbf{q}_y \\ \mathbf{q}_z \end{pmatrix} = \begin{pmatrix} -\sin(\theta/2) & 0 & -\cos(\theta/2) \\ 0 & 1 & 0 \\ \cos(\theta/2) & 0 & -\sin(\theta/2) \end{pmatrix} \begin{pmatrix} \hat{x} \\ \hat{y} \\ \hat{z} \end{pmatrix} \quad (2.3)$$

where  $\mathbf{q}_x, \mathbf{q}_y$  and  $\mathbf{q}_z$  are the unit vectors along the  $q_x, q_y$  and  $q_z$  axes respectively.

For the description of the susceptibility at the interface of the spherical nanodroplet, the spherical coordinate system  $(r', \theta', \varphi')$  is used, with its polar axis along the  $q_z$  axis of the

rotated lab frame, while axis  $r'$  is perpendicular to the interface and with its positive side towards the surrounding medium of the nanodroplet. The unit vectors  $\mathbf{e}_{r'}$ ,  $\mathbf{e}_{\theta'}$  and  $\mathbf{e}_{\varphi'}$  of the  $(r', \theta', \varphi')$  lab frame can be calculated from the unit vectors of the rotated lab frame as

$$\begin{pmatrix} \mathbf{e}_{r'} \\ \mathbf{e}_{\theta'} \\ \mathbf{e}_{\varphi'} \end{pmatrix} = \begin{pmatrix} \sin \theta' \cos \varphi' & \sin \theta' \sin \varphi' & \cos \theta' \\ \cos \theta' \cos \varphi' & \cos \theta' \sin \varphi' & -\sin \theta' \\ -\sin \varphi' & \cos \varphi' & 0 \end{pmatrix} \begin{pmatrix} \mathbf{q}_x \\ \mathbf{q}_y \\ \mathbf{q}_z \end{pmatrix} \quad (2.4)$$

Last, the unit vectors  $\hat{\mathbf{a}}$ ,  $\hat{\mathbf{b}}$  and  $\hat{\mathbf{c}}$  of the molecular lab frame  $(a, b, c)$  can be calculated from the unit vectors of the interfacial spherical frame as

$$\begin{pmatrix} \hat{\mathbf{a}} \\ \hat{\mathbf{b}} \\ \hat{\mathbf{c}} \end{pmatrix} = \begin{pmatrix} -\sin \psi_v \sin \varphi_v + \cos \theta_v \cos \varphi_v \cos \psi_v & \sin \psi_v \cos \varphi_v + \cos \theta_v \sin \varphi_v \cos \psi_v & -\cos \psi_v \sin \theta_v \\ -\cos \psi_v \sin \varphi_v - \cos \theta_v \cos \varphi_v \sin \psi_v & \cos \psi_v \cos \varphi_v - \cos \theta_v \sin \varphi_v \sin \psi_v & \sin \psi_v \sin \theta_v \\ \sin \theta_v \cos \varphi_v & \sin \theta_v \sin \varphi_v & \cos \theta_v \end{pmatrix} \begin{pmatrix} \mathbf{e}_{r'} \\ \mathbf{e}_{\theta'} \\ \mathbf{e}_{\varphi'} \end{pmatrix} \quad (2.5)$$

where  $\varphi_v$ ,  $\theta_v$  and  $\psi_v$  are the three Euler angles that describe the orientation of the molecular frame with respect to the interfacial frame. Specifically, the molecular frame results after three consecutive rotations around the axes of the interfacial frame: first by an angle  $\varphi_v$  counterclockwise around the original axis  $\varphi'$ , then by an angle  $\theta_v$  counterclockwise around the once-rotated axis  $\theta'$ , and last by an angle  $\psi_v$  counterclockwise around the twice-rotated axis  $\varphi'$ .<sup>5</sup>

## SFS from nanoscale interfaces

The measured SF intensity in the far field is  $I_{SF} \propto |\mathbf{E}_{SF}|^2$ , where  $E_{SF}$  the amplitude of the electric SF field.  $\mathbf{E}_{SF}$  can be expressed as a function of the effective susceptibility  $\Gamma^{(2)}$ :

$$\mathbf{E}_0(\omega_{SF}) \propto \mathbf{E}_1(\omega_{VIS}) \mathbf{E}_2(\omega_{IR}) \sum_{\alpha_0 \alpha_1 \alpha_2} \Gamma_{\alpha_0 \alpha_1 \alpha_2}^{(2)}(\omega_{SF}) \prod_{i=0}^2 (\mathbf{q}_{a_i} \cdot \mathbf{u}_{i,l}) \quad (2.6)$$

with

$$\Gamma_{\alpha_0 \alpha_1 \alpha_2}^{(2)}(\omega_{SF}) = \sum_{c_0 c_1 c_2} \int d\mathbf{r}'^3 \left\{ \chi_{c_0 c_1 c_2}^{(2)}(\omega_{SF}) \delta(|\mathbf{r}'| - R) e^{-i\mathbf{q} \cdot \mathbf{r}'} \prod_{i=0}^2 (\mathbf{e}_{c_i} \cdot \mathbf{q}_{a_i}) \right\} \quad (2.7)$$



Equations 2.6 and 2.7 are both in SI units.  $i = 0, 1, 2$  and corresponds to the SF, VIS, IR beams respectively (increasing number for decreasing frequency).  $a_i$  can take the values  $(x, y, z)$ , so that  $\mathbf{q}_{a_i}$  are the unit vectors of the rotated lab frame. The index  $l$  corresponds to the polarization of the corresponding beam, which is either parallel (P) or perpendicular (S) to the scattering plane  $xz$ , thus  $l$  takes the value P or S and unit polarization vectors can be defined for all three beams as

$$\begin{pmatrix} \mathbf{u}_{0,p} \\ \mathbf{u}_{1,p} \\ \mathbf{u}_{2,p} \end{pmatrix} = \begin{pmatrix} \cos \theta & 0 & -\sin \theta \\ \cos(\beta - \alpha) & 0 & \sin(\beta - \alpha) \\ \cos \alpha & 0 & -\sin \alpha \end{pmatrix} \begin{pmatrix} \hat{x} \\ \hat{y} \\ \hat{z} \end{pmatrix} \quad (2.8)$$

and

$$\begin{pmatrix} \mathbf{u}_{0,s} \\ \mathbf{u}_{1,s} \\ \mathbf{u}_{2,s} \end{pmatrix} = \begin{pmatrix} 0 & 1 & 0 \\ 0 & 1 & 0 \\ 0 & 1 & 0 \end{pmatrix} \begin{pmatrix} \hat{x} \\ \hat{y} \\ \hat{z} \end{pmatrix} = \begin{pmatrix} \hat{y} \\ \hat{y} \\ \hat{y} \end{pmatrix} \quad (2.9)$$

Here,  $c_i$  are the coordinates with respect to the spherical interfacial frame  $(r', \theta', \phi')$  for which  $d\mathbf{r}'^3 = r'^2 dr' \sin \theta' d\theta' d\phi'$ ; For a spherical scatterer,  $\Gamma^{(2)}$  equals to the integral of the surface second order susceptibility,  $\chi_s^{(2)}(\mathbf{r}') = \chi^{(2)}(\mathbf{r}')\delta(|\mathbf{r}'| - R)$ , over the whole spherical interface, so the spherical coordinates take the values  $r' = [0, R]$ ,  $\theta' = [0, \pi]$ ,  $\phi' = [0, 2\pi]$  and  $d\mathbf{r}'^3 = r'^2 dr' \sin \theta' d\theta' d\phi'$ ; Applying the transformations described in Eq. 2.1 – 2.5 and 2.8 – 2.9, Eq. 2.6 and 2.7 can be calculated analytically.

For achiral droplet interfaces between isotropic liquid media there are only four polarization combinations, namely PPP, SSP, SPS and PSS, that are non-zero.<sup>3</sup> The amplitude of the SFS electric field corresponding to these four polarization combinations can be given by<sup>4</sup>

$$\begin{aligned} E_{ppp} &\propto \cos\left(\frac{\theta}{2}\right) \cos\left(\frac{\theta}{2} - \alpha\right) \cos\left(\frac{\theta}{2} - \alpha + \beta\right) \Gamma_1^{(2)} + \cos(\theta - \alpha + \beta) \cos\left(\frac{\theta}{2} - \alpha\right) \Gamma_2^{(2)} + \\ &\quad + \cos(\theta - \alpha) \cos\left(\frac{\theta}{2} - \alpha + \beta\right) \Gamma_3^{(2)} + \cos(\beta) \cos\left(\frac{\theta}{2}\right) \Gamma_4^{(2)} \\ E_{ssp} &\propto \cos\left(\frac{\theta}{2} - \alpha\right) \Gamma_2^{(2)} \\ E_{sps} &\propto \cos\left(\frac{\theta}{2} - \alpha + \beta\right) \Gamma_3^{(2)} \\ E_{pss} &\propto \cos\left(\frac{\theta}{2}\right) \Gamma_4^{(2)} \end{aligned} \quad (2.10)$$

where  $\Gamma_1^{(2)} = \Gamma_{\perp\perp\perp}^{(2)} - \Gamma_{\parallel\parallel\perp}^{(2)} - \Gamma_{\parallel\perp\parallel}^{(2)} - \Gamma_{\perp\parallel\parallel}^{(2)}$ ,  $\Gamma_2^{(2)} = \Gamma_{\parallel\parallel\perp}^{(2)}$ ,  $\Gamma_3^{(2)} = \Gamma_{\parallel\perp\parallel}^{(2)}$ , and  $\Gamma_4^{(2)} = \Gamma_{\perp\parallel\parallel}^{(2)}$ . The indices  $\parallel$  and  $\perp$  denote the directions parallel and perpendicular to the plane for which the scattering vector  $\mathbf{q}$  is the normal vector, so  $\perp$  is parallel to  $q_z$  and  $\parallel$  perpendicular to it.

For achiral interfacial molecules, Eq. 2.7 becomes

$$\begin{pmatrix} \Gamma_1^{(2)} \\ \Gamma_2^{(2)} \\ \Gamma_3^{(2)} \\ \Gamma_4^{(2)} \end{pmatrix} = \begin{pmatrix} 2F_1 - 5F_2 & 0 & 0 & 0 \\ F_2 & 2F_1 & 0 & 0 \\ F_2 & 0 & 2F_1 & 0 \\ F_2 & 0 & 0 & 2F_1 \end{pmatrix} \begin{pmatrix} \chi_1^{(2)} \\ \chi_2^{(2)} \\ \chi_3^{(2)} \\ \chi_4^{(2)} \end{pmatrix} \quad (2.11)$$

where  $\chi_1^{(2)} = \chi_{\perp\perp\perp}^{(2)} - \chi_{\parallel\parallel\perp}^{(2)} - \chi_{\parallel\perp\parallel}^{(2)} - \chi_{\perp\parallel\parallel}^{(2)}$ ,  $\chi_2^{(2)} = \chi_{\parallel\parallel\perp}^{(2)}$ ,  $\chi_3^{(2)} = \chi_{\parallel\perp\parallel}^{(2)}$ , and  $\chi_4^{(2)} = \chi_{\perp\parallel\parallel}^{(2)}$ . Here the indices  $\parallel$  and  $\perp$  denote parallel and perpendicular directions with respect to the relevant surface coordinate system. In this case of scattering from a spherical particle,  $\perp$  represents the direction parallel to  $\mathbf{r}'$  and  $\parallel$  is orthogonal to that (parallel to  $\theta'$  and  $\phi'$ ).  $F_1$  and  $F_2$  are the two scattering form function. For second-order scattering from spherical nanodroplets, and under the Rayleigh-Gans-Debye (RGD) approximation, they are equal to<sup>4,6</sup>

$$F_1(qR) = 2\pi R^2 i \left( \frac{\sin(qR)}{(qR)^2} - \frac{\cos(qR)}{qR} \right) \quad (2.12)$$

$$F_2(qR) = 4\pi R^2 i \left( 3 \frac{\sin(qR)}{(qR)^4} - 3 \frac{\cos(qR)}{(qR)^3} - \frac{\sin(qR)}{(qR)^2} \right)$$

where  $q$  is the magnitude of the scattering vector and  $R$  is the radius of the spherical particle. For scattering from a spherical particle, the RGD approximation holds when  $qR(1 - m) \ll 1$ , with  $m$  the relative refractive index of the scatterer with respect to the solvent.<sup>7</sup> For the samples studied here, namely hexadecane nanodroplets dispersed in water, this condition holds.<sup>6</sup>

The surface susceptibility  $\chi^{(2)}$  is an orientation-weighted sum of the molecular hyperpolarizability tensor  $\beta^{(2)}$  of the surface molecules. Provided that the interface is azimuthally isotropic,  $\chi^{(2)}$  can be calculated as:

$$\begin{pmatrix} \chi_1^{(2)} \\ \chi_2^{(2)} \\ \chi_3^{(2)} \\ \chi_4^{(2)} \end{pmatrix} = \frac{N_s \langle \cos \phi \rangle}{2} \begin{pmatrix} 5D - 3 & 0 & 0 & 0 \\ 1 - D & 2 & 0 & 0 \\ 1 - D & 0 & 2 & 0 \\ 1 - D & 0 & 0 & 2 \end{pmatrix} \begin{pmatrix} \beta_1^{(2)} \\ \beta_2^{(2)} \\ \beta_3^{(2)} \\ \beta_4^{(2)} \end{pmatrix} \quad (2.13)$$

where  $\beta_1^{(2)} = \beta_{ccc}^{(2)} - \beta_2^{(2)} - \beta_3^{(2)} - \beta_4^{(2)}$ ,  $\beta_2^{(2)} = (\beta_{aac}^{(2)} + \beta_{bbc}^{(2)})/2$ ,  $\beta_3^{(2)} = (\beta_{aca}^{(2)} + \beta_{bcb}^{(2)})/2$ ,  $\beta_4^{(2)} = (\beta_{caa}^{(2)} + \beta_{cbb}^{(2)})/2$  and  $(a, b, c)$  is the local coordinate system of the molecule to be probed (calculated in Eq. 2.5).  $N_s$  is the surface number density of the probed chemical groups.  $\phi$  is the tilt angle between the axis of the chemical group and the normal to the interface (parallel to axis  $r'$ ), and  $\langle \cos \phi \rangle$  is the average cosine of the molecular tilt angle  $\phi$ . The parameter  $D$  is called orientation parameter and equals to  $D = \langle \cos^3 \phi \rangle / \langle \cos \phi \rangle$ .

Thus, through Eq. 2.1-2.13 it can be seen how the molecular structure (tilt angle,  $\phi$ , and surface density,  $N_s$ ) of the probed molecular group ( $\beta^{(2)}$ ) at the interface determines the measured SF intensity,  $I_{SF}$ . The tensor elements  $\beta_{n,ijk}^{(2)}$  that describe the second-order response of the molecule when the  $n$ -th molecular vibration is probed depend on the IR and Raman properties of the vibration:<sup>8</sup>

$$\beta_{n,ijk}^{(2)} \propto \frac{\partial \alpha_{ij}}{\partial Q_n} \frac{\partial \mu_k}{\partial Q_n} \quad (2.14)$$

Here  $i, j$  and  $k$  are the coordinates with respect to the molecular coordinate system,  $\alpha_{ij}$  is the  $ij$ -th component of the Raman polarizability tensor,  $\mu_k$  is the  $k$ -th component of the IR transition dipole tensor, and  $Q_n$  the normal coordinate probed molecular vibration.  $\frac{\partial \alpha_{ij}}{\partial Q_n}$  and  $\frac{\partial \mu_k}{\partial Q_n}$  are their partial derivatives. From Eq. 2.14 it can be seen that, in order for a vibrational mode to have a non-zero SF response, it should be both IR and Raman active, or else, the centrosymmetry should be broken on a molecular level as well, apart from the interfacial level.

As can be seen from Eq. (2.10), the SFS amplitude depends on the scattering angle. The angle of maximum scattering differs for droplets of different radii as the particle size decreases the maximum scattering shifts to higher angles. A detailed discussion can be found in Ref. <sup>4</sup>. Indicatively, the maximum scattering angle for a particle of a radius of 50 nm is at  $\sim 75^\circ$ , whereas for a radius of 200 nm at  $\sim 45^\circ$  and for 1  $\mu\text{m}$  at  $\sim 10^\circ$ .

## 2.2.2 Second Harmonic Scattering

The geometry for a collinear second harmonic scattering (SHS) experiment is the same as for SFS, only with one incident beam instead of two. Figure 2.2 displays the SHS geometry, with an incoming near-IR beam with wavevector  $\mathbf{k}_1$ , and the scattered SH light with wavevector  $\mathbf{k}_0$ . The scattered beam lies in the  $(xz)$  plane, while the scattering vector  $\mathbf{q}$  is defined as  $\mathbf{q} \equiv \mathbf{k}_0 - 2\mathbf{k}_1$ . Employing Eq. 2.10 for angles  $\alpha$  and  $\beta$  equal to zero, and given that the polarization of the incoming fields is identical, the two remaining independent components of the SH field are:

$$E_{ppp} \propto \cos^3\left(\frac{\theta}{2}\right) \Gamma_1^{(2)} + \cos(\theta) \cos\left(\frac{\theta}{2}\right) \Gamma_2^{(2)} + \cos(\theta) \cos\left(\frac{\theta}{2}\right) \Gamma_3^{(2)} + \cos\left(\frac{\theta}{2}\right) \Gamma_4^{(2)} \quad (2.15)$$

$$E_{pss} \propto \cos\left(\frac{\theta}{2}\right) \Gamma_4^{(2)}$$

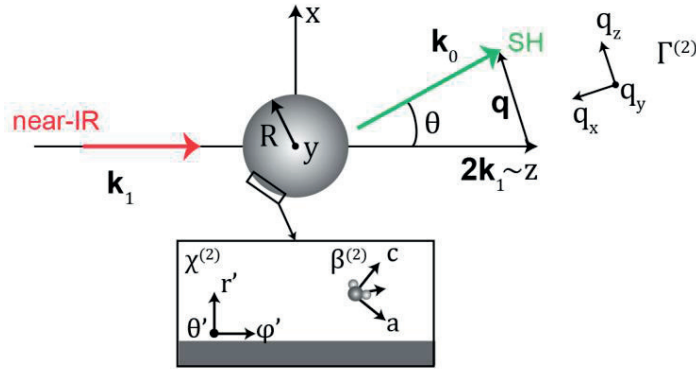


**Figure 2.2: Top view of the collinear SFS geometry (sketch).** A near-IR beam, with wavevector  $\mathbf{k}_1$  illuminates the nanodroplet. The SH beam beams lie in the  $xz$  (scattering) plane and the  $z$ -axis is aligned with the sum of the wavevectors of the two incoming beams  $\mathbf{k}_1$ . Similar to SFS, the scattering vector  $\mathbf{q}$  is defined as  $\mathbf{k}_0 - 2\mathbf{k}_1$  and the effective susceptibility  $\Gamma^{(2)}$  is defined in the rotated lab frame  $(q_x, q_y, q_z)$ . The surface susceptibility  $\chi_s^{(2)}(\mathbf{r}') = \chi^{(2)}(\mathbf{r}')\delta(|\mathbf{r}'| - R)$  is defined in the surface coordinates  $(r', \theta', \varphi')$ , while the hyperpolarizability  $\beta^{(2)}$  is defined in the molecular coordinate system.

For SHS the maximum scattering angles are smaller than for SFS. As such, for a particle of a radius of 50 nm the maximum scattering occurs at  $\sim 60^\circ$ , whereas for a radius of 200 nm at  $\sim 25^\circ$  and for  $1 \mu\text{m}$  at  $\sim 5^\circ$ .

### 2.2.3 Dynamic Light Scattering (DLS) measurements

DLS measurements, also known as photon correlation spectroscopy, are used to characterize the size distribution of nanodroplets studied in this thesis. DLS measures the linear light scattering (Rayleigh scattering) intensity from small particles in suspension as a function of time. The sample is illuminated with a red HeNe laser (632 nm) and the scattered light is detected at the back-scattering geometry (175°) with a fast photodiode. The measured light intensity,  $I$ , fluctuates due to the Brownian (random) motion of the particles in solution, and an intensity autocorrelation function,  $G(\tau)$ , is obtained directly from the measurement:

$$G(\tau) = \langle I(t) \times I(t + \tau) \rangle \quad (2.16)$$

where  $\tau$  is the time difference of the correlator. Assuming that the particles follow a Brownian motion,  $G(\tau)$  is connected to the electric field autocorrelation function,  $g(\tau)$ , as

$$G(\tau) = A[1 + Bg(\tau)^2] \quad (2.17)$$

where  $A$  is the baseline of function  $G$ , and  $B$  the intercept of function  $g$ . For a monodisperse solution,  $g(\tau)$  is an exponential decay:

$$g(\tau) = e^{-Dq^2\tau} \quad (2.18)$$

where  $D$  is called translational diffusion coefficient, and  $q$  is the wavevector of the linear scattering that depends on the scattering angle  $\theta$ , the wavelength  $\lambda$  and the refractive index of the medium:  $q = (4\pi/\lambda) \sin(\theta/2)$ . The diffusion coefficient  $D$  is related to the hydrodynamic radius  $R$  of the particle by the Stokes-Einstein relation for spherical particles<sup>9</sup>

$$R = \frac{k_B T}{6\pi\eta D} \quad (2.19)$$

where  $\eta$  is the solvent dynamic viscosity,  $k_B$  is Boltzmann's constant and  $T$  is the absolute temperature.

DLS measurements also provide the polydispersity index ( $PDI$ ), an important index for the evaluation of the stability of the samples used in this thesis. Specifically, Eq. 2.17 is fitted with a cumulant fit, which uses a single exponential to obtain the mean radius,  $R$ , and

the standard deviation,  $\sigma(R)$ , of the sized distribution. The polydispersity index is then defined as

$$PDI \equiv \left( \frac{\sigma(R)}{R} \right)^2 \quad (2.20)$$

If not otherwise indicated, a nanoemulsion is considered stable as long as the size distribution remains monomodal, and the PDI is smaller than 0.3.<sup>10</sup> Figure 2.3 displays two indicative size distributions measured by DLS for a stable (red) and an unstable (black) nanoemulsion.

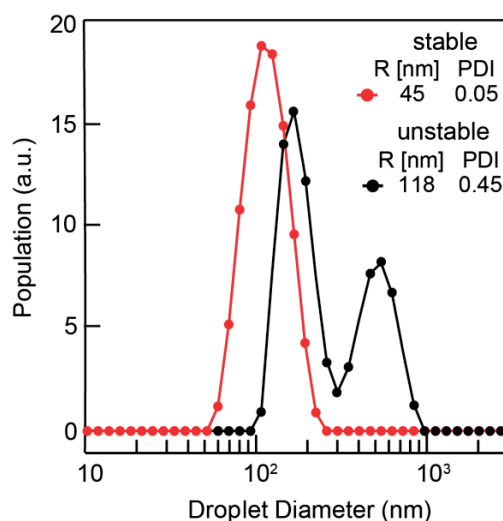


**Figure 2.3: Particle size distribution measured by DLS.** Size distribution of the nanodroplets of a stable (red) and an unstable (black) nanoemulsion of 2 vol. % hexadecane in D<sub>2</sub>O stabilized with 10 mM sodium dodecyl sulfate.

## 2.2.4 Electrophoretic measurements and $\zeta$ -potential

A colloidal particle in aqueous solution accumulates charges around it. This charge distribution is crucial for the stability of the dispersion, as the repulsion between particles with surface charges of the same polarity hinders destabilization processes.<sup>9,11</sup> Hence the  $\zeta$ -potential (defined below) is an appropriate parameter for the characterization of emulsion stability, as it describes the ion atmosphere around a particle. Figure 2.4 describes the ion distribution around a charged particle in an aqueous solution. The particle here is negatively charged, but the same rules apply for positively charged ones. Specifically, counterions are attracted to the particle surface while coions are repulsed from it. Close to the interface, there is a region where the density of counterions is particularly high, known as Stern layer. Further into the bulk, the counterion distribution follows an exponential decay. When an

external field is applied in the solution, the charged particle will move, together with the ions of its ionic atmosphere that are tightly bound to it (closer to its surface). Moreover, the direction and velocity of this movement depends on the sign and magnitude of the surface charges. Above some distance from the particle surface, the friction with the liquid will overcome the electrostatic interaction between the ions and the particle, and the ions will not follow the movement of the particle. This is the distance where the (fictitious) slipping plane is found, and  $\zeta$ -potential is the potential measured at the slipping plane with respect to the bulk value.

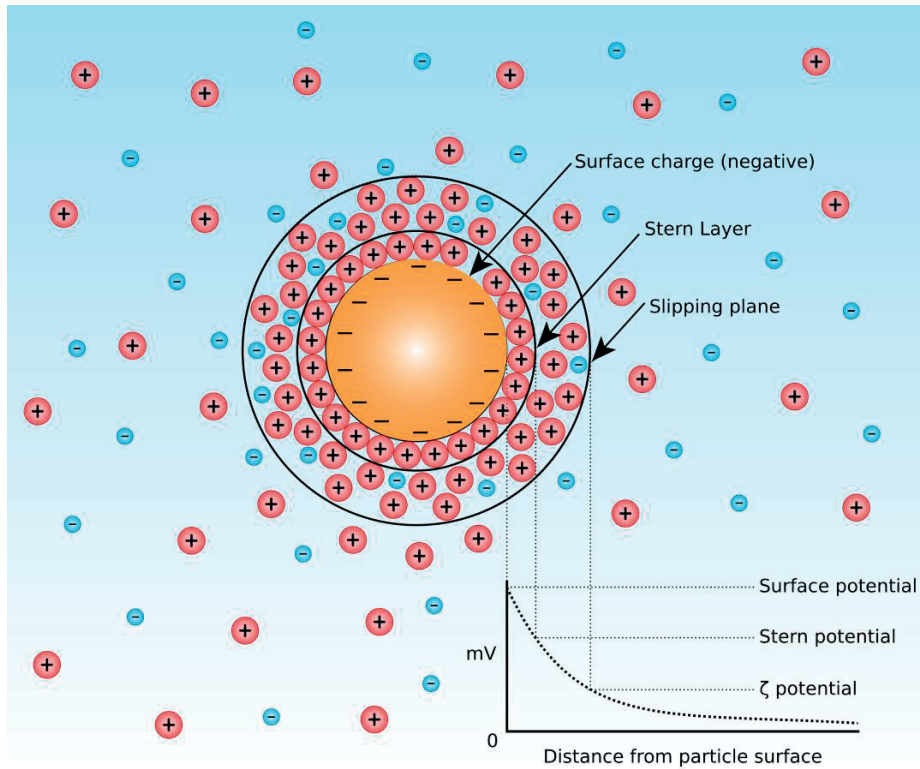


**Figure 2.4: Ion distribution around a particle.** Sketch of the ionic distribution around a negatively charged particle in an aqueous solution. The same applies for a positively charged particle, with the inversion of the sign of all charges shown in the figure. This figure was modified and adapted from the image: [https://commons.wikimedia.org/wiki/File:Diagram\\_of\\_zeta\\_potential\\_and\\_slipping\\_planeV2.svg](https://commons.wikimedia.org/wiki/File:Diagram_of_zeta_potential_and_slipping_planeV2.svg) by Mjones1984 and Larryisgood.

The  $\zeta$ -potential of small particles in solution can be measured with electrokinetic mobility measurements. In detail, an external field is applied on the particle dispersion, and the velocity  $v_e$  of the particle is measured with Laser Doppler velocimetry. Subsequently, the electrophoretic mobility is calculate as

$$\mu_e = \frac{v_e}{E_{ext}} \quad (2.21)$$

where  $E_{ext}$  is the applied external electric field. The  $\zeta$ -potential can be finally calculated employing the Henry equation

$$\mu_e = \frac{2\varepsilon\zeta f(\kappa R)}{3\eta} \quad (2.22)$$

where  $\varepsilon$  is the dielectric constant of the medium,  $\zeta$  is the  $\zeta$ -potential around the particle,  $f$  is Henry's function,  $\kappa$  is the Debye parameter,  $R$  is the radius of the particle and  $\eta$  is the viscosity of the medium.  $\kappa$  equals to <sup>12</sup>

$$\kappa = \sqrt{\frac{2000e^2 N_{Av} z^2 c}{\varepsilon_0 \varepsilon_r k_B T}} \quad (2.23)$$

In Eq. (2.23) all units are in the SI system, except for the concentration  $c$  that is expressed in mol/l. For  $R \gg 1/\kappa$ , the Smoluchowski approximation can be applied that results in  $f(\kappa R)=1.5$ . This approximation is suitable for nanoparticles with radius  $\sim 100$  nm and ionic concentrations  $> \sim 100$   $\mu$ M, as is the case for the samples studied in this thesis.

## 2.3 Experimental Details

In this part, the experimental setup and of acquisition of SFS measurements is presented, followed by the analysis method of the SFS spectra. Then, we present the experimental setup for SHS measurements. Both setups were previously built by PhD and post-doc students in the Laboratory for Fundamental Biophotonics under her supervision of Prof. Roke. Last we present a brief description of the setup for Raman hydration shell spectroscopy, where measurements presented in Chapter 3 were conducted by Dr. B. M. Ranking, under the supervision of Prof. D. Ben-Amotz in Purdue University.

### 2.3.1 Experimental setup and measurements of SFS

The experimental setup used for SFS measurements is shown in detail in Fig. 2.5. Laser pulses of 3 nJ, 800 nm, 50 fs and 18 nm spectral FWHM are generated by a fs oscillator (Integral 50, Femtolasers) at a repetition rate of 85 MHz and used as a seed to a commercial chirped pulse Ti:Sapphire amplifier (Spitfire, Spectra-Physics). The amplification occurs at a repetition rate of 1 kHz, and the pulses are amplified in two stages, a regenerative amplifier (RGA) and a double pass amplifier (DPA), pumped by Nd:YLF lasers (527 nm, 150 ns, 1 kHz, 20 mJ). The energy of the output pulses is  $\sim 6$  mJ, their duration  $\sim 100$  fs, at a repetition rate of 1 kHz, and centred at 800 nm. At this step the beam is split in two: 90% of the power is used for the generation of IR pulses through a commercial optical parametric amplifier



(HE-Topas, Light conversion). The wavelength of the generated IR pulses can be tuned between 2.5 and 15  $\mu\text{m}$ . The rest 10% of the power (termed as the VIS pulse) passes through a home-built pulse shaper where it is dispersed horizontally (blazed diffraction grating for 800 nm: PC 1800 50×50×10 NIR, Spectrogon), and then passes through a vertical slit that cuts out some frequency components, before being reflected back to the grating, so that the spectral width of the output pulses is reduced down below 15  $\text{cm}^{-1}$ . The pulse energy after the pulse shaper can reach 30  $\mu\text{J}$ .

The broadband IR pulses ( $\sim 120 - 210 \text{ cm}^{-1}$ , depending on the frequency) and narrowband VIS pulses ( $< 15 \text{ cm}^{-1}$ ) are subsequently temporally and spatially overlapped on a sample cuvette with a path length of 200  $\mu\text{m}$ . The time delay of the VIS pulses relative to the generated IR pulses is adjusted by a retroreflecting mirror on a motorized translation stage that increases/decreases the VIS path length (after the pulse shaper). The IR pulses that propagate towards the sample pass through two  $\text{BaF}_2$  wire grid polarizers (WP25HB, Thorlabs) that control their energy and polarization, as well as a germanium longpass IR filter (704024001, 50% at 2.4  $\mu\text{m}$ , Laser Components GmbH), and are focused on the sample by a 90° off-axis parabolic bare gold mirror with an effective focal length of 101.6 mm (84-625, Edmund optics). The polarization of the VIS beam is controlled by a polarizing beam splitter cube (PBS-800-050, CVI) and a half-wave plate (460-4215, EKSMA) and focused on the sample by a plano-convex lens with a focal length of 125 mm (LA1986-B, Thorlabs). The focus of the IR beam is  $\sim 70 \mu\text{m}$  in diameter, and of the VIS beam  $\sim 150 \mu\text{m}$ , and they are overlapped under an angle of 15° (measured in air) in the sample. The angle between the IR beam and the normal direction of the incident window of the sample cuvette is 45°. The sample cuvette consists of a 1.3 mm thick  $\text{CaF}_2$  window (CeNing optics) facing the incident IR and VIS beam, and a Quartz cell with a 0.2 mm depth (106-QS, Hellma analytics). The cuvette is mounted in such a way that the outgoing window is perpendicular to the direction at which the maximum SF intensity is emitted.

The scattered SF light from the sample is collected at a scattering angle of  $\sim 55^\circ$  (measured in air), where the maximum for the SF scattering pattern is expected for scatterers with a diameter of  $\sim 100 - 200 \text{ nm}$ .<sup>4</sup> Especially for the measurements of SF light from micrometer-sized droplets, like the ones presented in Section 4.4, the detection path is moved to a scattering angle of  $\sim 10^\circ$ , where the maximum SFS intensity is expected for droplets of radii between 5  $\mu\text{m}$  and 20  $\mu\text{m}$ . In any case, the SF light is collimated by a plano-convex lens with a focal length of 15 mm (LA1540-B, Thorlabs) and an acceptance angle of 30°. After passing through two shortpass filters (3RD770SP, 3rd Millennium) and a Glan-Taylor polarizer (GT15-B, Thorlabs), the SF beam is focused into a spectrometer (SpectraPro 2300i, Acton) by a plano-convex lens with a focal length of 50 mm (LA1131-B,

Thorlabs). The spectrum of the SF beam is recorded with an I-CCD camera (PI-Max3, Princeton instruments).

## **Spectral recording**

SFS spectra are recorded in the four polarization combinations of nonzero coherent SFS signal, namely PPP, SSP, SPS, and PSS. The gate width of the I-CCD is set to 10 ns and the I-CCD is synchronized with the Spitfire amplification unit so that the detections takes place only during the arrival of the incoming pulses and, hence, the generation of SF light. The acquisition time for a single spectrum is between 150 and 300 s, averaging between 3 and 5 spectra for an acquisition time of 60 s each. All SFS spectra shown are normalized by the spectrum of the incident IR pulses. The latter is obtained by measuring the SF spectrum in reflection geometry from a z-cut quartz crystal (for measurements presented in Chapter 3) or the SF spectrum in scattering geometry from a dispersion of potassium niobate (KNbO<sub>3</sub>) nanoparticles (Sigma-Aldrich) in D<sub>2</sub>O (for measurements presented in Chapters 4 - 6). The spectrum of the incident VIS pulses is measured directly in the reflection geometry, removing the two shortpass filters of the detection path. The background noise is recorded while spoiling the temporal overlap of the incident IR and VIS pulses. The SFS spectrum of a reference sample (a nanoemulsion with 2 vol % d<sub>34</sub>-hexadecane, radius ~100 nm, in D<sub>2</sub>O with 10 mM sodium dodecyl sulfate (SDS)) is measured between every other measurement to detect and correct for possible fluctuations during the course of the experiment.

## **Spectral characteristics of the IR pulses**

The IR pulses are tuned to the frequency of vibrational mode of interest. For the measurement of the CH stretch vibrational modes of alkyl chains, the IR pulses are centred at 2900 cm<sup>-1</sup> (FWHM = 120 cm<sup>-1</sup>); for the SO symmetric stretch vibrational mode of the -SO<sub>3</sub> headgroup of SDS, at 1080 cm<sup>-1</sup> (FWHM = 180 cm<sup>-1</sup>); for the SO symmetric stretch vibrational mode of the -SO<sub>3</sub> headgroup of d<sub>25</sub>-SDS, at 1040 cm<sup>-1</sup> (FWHM = 180 cm<sup>-1</sup>); for the SO symmetric stretch vibrational mode of SO<sub>4</sub><sup>2-</sup> anions, at 990 cm<sup>-1</sup> (FWHM = 210 cm<sup>-1</sup>); for the NO symmetric stretch vibrational mode of NO<sub>3</sub><sup>-</sup> anions, at 1050 cm<sup>-1</sup> (FWHM = 200 cm<sup>-1</sup>); and for the CN stretch vibrational mode of SCN<sup>-</sup> anions, at 2050 cm<sup>-1</sup> (FWHM = 150 cm<sup>-1</sup>).

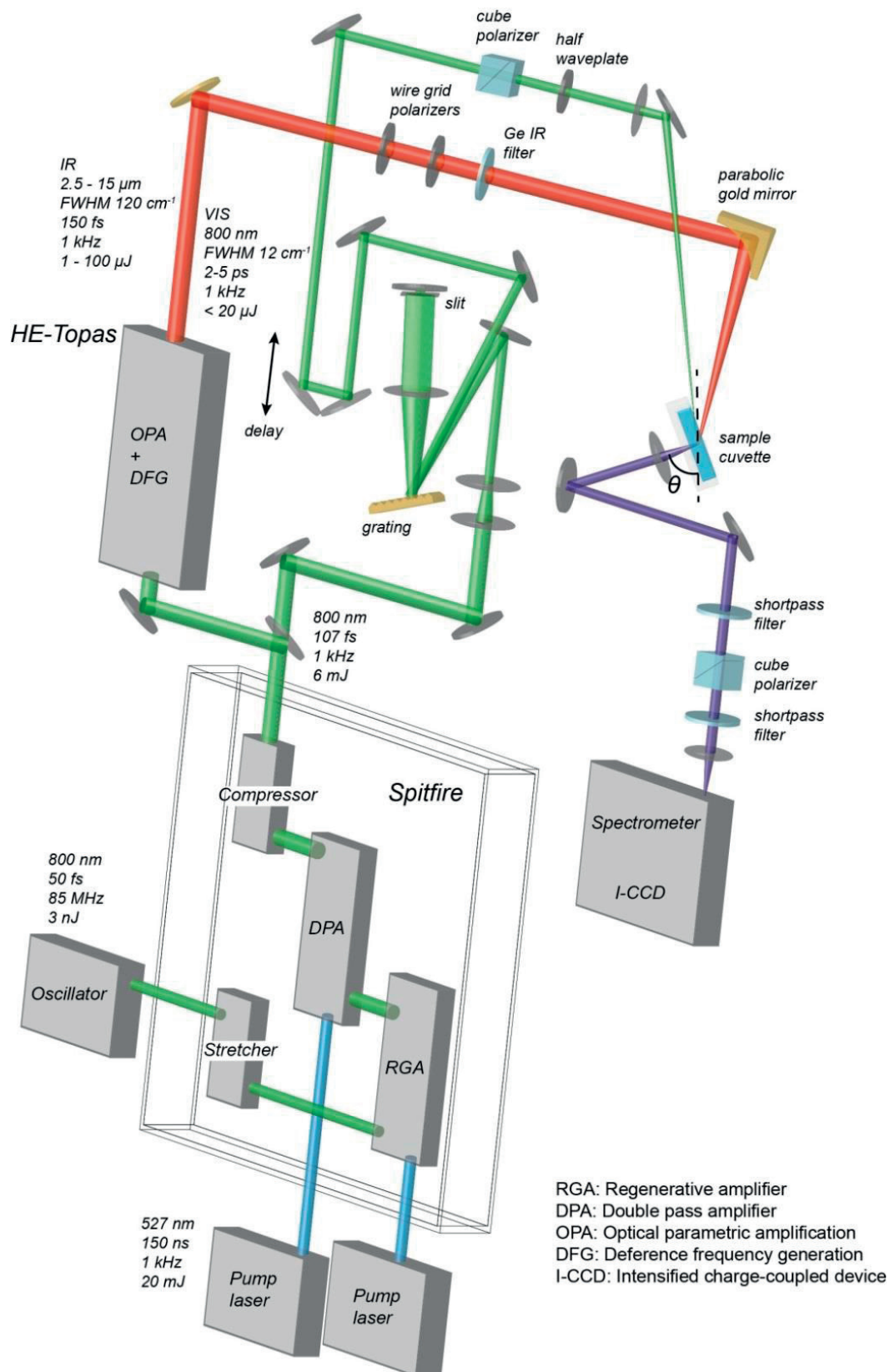


**Figure 2.5: Illustration of the SFS experimental setup.** The SFS experimental setup consists of a laser system providing a VIS and a tuneable IR beam, an SFS stage, and a detection unit. The image is a courtesy of Dr. Yixing Chen.

### 2.3.2 SFS Spectral Analysis

The measured SFS spectra are processed with IGOR PRO 6 (WaveMetrics) in order to retrieve the molecular configuration at the interface. Specifically, first the narrow spectrum of the VIS pulses is fitted with a Gaussian function, and subsequently the SF sample data are rescaled using the central frequency of the VIS pulse, so that the frequency of the sample spectra corresponds to the frequency of the probed molecular vibrational modes. Then the background noise spectra are subtracted. After that, the sample spectra are normalized by the profile of the IR spectrum, the acquisition time, and the incident IR and VIS pulse energies. The processed spectra are fitted with a global fitting procedure<sup>13</sup> employing Levenberg – Marquardt iterations<sup>14, 15</sup> with a superposition of  $n$  Lorentzian shaped vibrational modes:

$$I_{SFS}(\omega) = \left| \left( A_{NR} e^{-i\varphi_{NR}} + \sum_n \frac{A_n \gamma_n e^{-i\varphi_n}}{\omega - \omega_n - i\gamma_n} \right) \right|^2 \quad (2.24)$$

For every vibrational mode  $n$  the amplitude  $A_n$ , phase  $\varphi_n$ , resonance frequency  $\omega_n$  and linewidth  $\gamma_n$  can be retrieved. A non-resonant ( $NR$ ) background with amplitude  $A_{NR}$  and phase  $\varphi_{NR}$  can also be present.

### 2.3.3 Experimental setup and measurements of SHS

The experimental setup for SHS measurements is shown in Fig. 2.6. The setup has been described in detail in Ref.<sup>16</sup>, and has been extensively characterized in Ref.<sup>17,18</sup>. As fundamental beam we use a laser beam with pulses at  $1030 \pm 5$  nm,  $<200$  fs, at a repetition rate of 200 kHz (PHAROS-SP, Light conversion). Its polarization is controlled by a Glan-Taylor polarizer (GT10-B, Thorlabs) and a zero-order half wave plate (WPH05M-1030). The beam is filtered (with a FEL0750 filter, Thorlabs) and focused by a plano-convex lens ( $f = 7.5$  cm) into a cylindrical glass cuvette (LS instruments) with an inner diameter of 4.2mm. The energy of the polarized input pulses is between 0.2 and 0.3  $\mu$ J, for incident laser power between 40 and 60 mW respectively. The focused beam has a waist diameter of  $\sim 35$   $\mu$ m and a Rayleigh length of 0.94 mm. The scattered SH beam is collected and collimated with a plano-convex lens ( $f = 5$  cm), with an angle of acceptance controlled by an iris behind the collimating lens. Then, the collimated SH beam is analysed (GT10-A, Thorlabs), filtered with a notch filter (ET525/50, Chroma), and finally focused by a plano-convex lens ( $f = 1.5$  cm) into a gated PMT (H7421-40, Hamamatsu). The signal from the PMT is amplified by a GHz

wide band amplifier (HFAC-26dB, Becker & Hickl) and is then read out by a two channel gated photon counter (SR400, Stanford research systems).

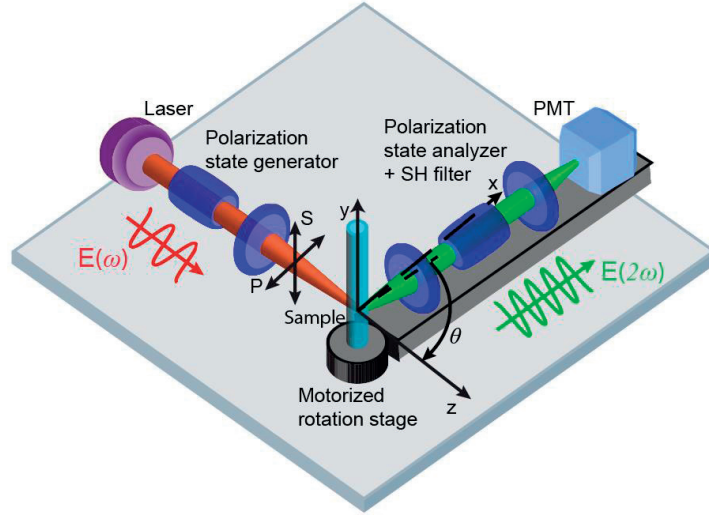


**Figure 2.6: Illustration of the SHS experimental setup.** A single incoming beam is focused in the sample cuvette and the SH response can be recorded at a scattering angle between  $-90^\circ$  and  $90^\circ$ . The reproducibility of the SHS measurements is 1-2 % for aqueous solutions.

The SHS intensity can be measured at different scattering angles between  $-90^\circ$  and  $90^\circ$ , and different polarization combinations, namely PPP, SSS, PSS, SPP. In this thesis, the SH measurements were conducted in the PPP polarization combination. At single angle measurements for nanodroplets the SH intensity from the dispersion of nanodroplets,  $I_{SH,emulsion,PPP}(\theta)$ , is measured at a fixed scattering angle ( $\theta$ ) of maximum SH intensity. For nanodroplets with radius  $\sim 100$  nm the value of  $\theta$  is  $\sim 45^\circ$ . The measurement is corrected by subtracting the SH response of the corresponding aqueous solution (same as our sample but without the dispersed nanodroplets),  $I_{HRS,solution,PPP}(\theta)$ , measured at the same scattering angle. The latter signal is called hyper Rayleigh scattering (HRS), and is the response of the bulk water phase in the SH frequency, originating from isotropically distributed non-centrosymmetric water molecules.<sup>19</sup> By subtracting this background signal, we isolate the SH response originating from the water molecules at the droplet surface that we are actually interested in. Finally, the SH signal is corrected for possible fluctuations of the laser intensity during the experiment, or between different days by dividing with the response of pure water  $I_{HRS,water,PPP}(\theta)$ :

$$\frac{I_{SH,emulsion,PPP}(\theta) - I_{HRS,solution,PPP}(\theta)}{I_{HRS,water,PPP}(\theta)} \quad (2.25)$$

All measurements are performed in a temperature- and humidity-control room ( $T = 24\text{ }^{\circ}\text{C}$ , relative humidity, 26.0%).

For the measurements presented in this work the input pulse energy at the sample was set to  $0.25\text{ }\mu\text{J}$  (incident laser power of  $50\text{ mW}$ ) and the acceptance angle was set to  $11.4^{\circ}$ . The detection angle was set to  $45^{\circ}$ , for the detection of maximum SH intensity. All data points were acquired with gate width of  $10\text{ ns}$ , synchronized with the laser system so that the detections takes place only during the arrival of the incoming pulses and, hence, the generation of SH light. Each data point of SH intensity presented in Chapter 3 was recorded for  $50\text{ s}$ , and is the average of 50 acquisitions with an acquisition time of  $1\text{ s}$  each. For SH intensity data presented in Chapters 5 – 6, each data point was recorded for  $150\text{ s}$ , and is the average of 30 acquisitions with an acquisition time of  $5\text{ s}$  each. The reason for this discrepancy is the larger fluctuations in the SHS signal of nanoemulsions with electrolytes, studied in Chapters 5 and 6 (compared to samples studied in Chapter 3), that require longer integration time per acquisition for a satisfactory signal to noise ratio of the SH signal.

### 2.3.4 Raman hydration shell spectroscopy

For the acquisition of Raman hydration shell spectra, conducted by the Prof. Ben-Amotz's research group in Purdue University, the experimental setup and the measurement analysis have been analytically presented before (see SI of Ref. <sup>20</sup> and the references therein). Briefly, an argon-ion laser centered at  $514.5\text{ nm}$  was used as the excitation source, with approximately  $15\text{ mW}$  of power at the sample. Duplicate spectra were collected with an integration time of  $5\text{ min}$ . The backscattered Raman photons were collected and delivered at the entrance slit of a  $300\text{ gr/mm}$ -grating using a fiber bundle consisting of seven  $100\text{ }\mu\text{m}$  core diameter fibers (arranged in a close packed circular array at the collection end and a linear stack at the entrance slit). The spectral resolution of the Raman system is estimated  $\sim 1\text{ nm}$  ( $\sim 25\text{ cm}^{-1}$  or  $\sim 4\text{ CCD pixels}$ ). All Raman spectra are unpolarized, including both S and P polarized scattering. The Raman-MCR decomposition of measured spectra into SC and pure water components was performed using self-modeling curve resolution (SMCR) by keeping the  $\text{Br}^{-}$  concentration the same in both solvent (as  $\text{Na}^{+}\text{Br}^{-}$ ) and  $\text{OTA}^{+}$  surfactant solutions (as  $\text{OTA}^{+}\text{Br}^{-}$ )<sup>21, 22</sup>. Since the O-H stretch signature of water molecules around  $\text{Na}^{+}$  ions is virtually indistinguishable from that of pure water,<sup>23</sup> and thus,  $\text{Na}^{+}$  ions have essentially no influence on the above SC spectra, or those obtained from  $\text{OS}^{-}\text{Na}^{+}$  surfactant solutions (with salt-free water as the solvent).



## 2.4 Sample preparation

In this part are presented the chemicals employed in the present work as well as the sample preparation processes for the production of nanometer- and micrometer-sized droplets.

### 2.4.1 Chemicals

Throughout this work we used n-hexadecane ( $C_{16}H_{34}$ , Sigma Aldrich, analytical standard) and deuterated ( $d_{34}$ )-hexadecane ( $C_{16}D_{34}$ , Cambridge Isotope Laboratories, 98% deuteration). The latter was used when the CH vibrational modes of a third molecule were targeted, in order to shift the CH vibrational response of hexadecane outside the measuring window. Aqueous solutions of amphiphiles and salts were prepared using ultra-pure water ( $H_2O$ , Milli-Q UF plus, Millipore, Inc., electrical resistance of 18.2 M $\Omega$  cm,  $D_2O$ , 99.8%, Armar, > 2 M $\Omega$  cm) or  $D_2O$  (99.8%, Armar, > 2 M $\Omega$  cm). The amphiphiles/surfactants and salts used in each chapter are as follows. In Chapter 3 we used h-sodium dodecylsulfate (SDS) (99%, Biomol), deuterated ( $d_{25}$ -) SDS (99% d, Cambridge Isotope), h-dodecyltrimethylammonium bromide (DTAB) (99%, Sigma-Aldrich), d-DTAB (99% d, Cambridge Isotope), 1-hexanol ( $CH_3(CH_2)_5OH$ , 99.5%, Sigma-Aldrich), 1-hexan- $d_{13}$ -ol ( $CD_3(CD_2)_5OH$ , 98% d, Sigma-Aldrich), 1,2-dipalmitoyl-*sn*-glycero-3-phosphocholine (DPPC, 99%, Avanti), sodium chloride (NaCl, 99.999%, Acros Organics), sodium bromide (NaBr, 98.52%, J.T. Baker), trimethyloctylammonium bromide ( $OTA^+$ ,  $\geq 98.0\%$ , Sigma-Aldrich) and sodium octylsulfate (SOS,  $\sim 95\%$  Sigma-Aldrich). In Chapter 4 we used SDS (ReagentPlus®,  $\geq 98.5\%$ , GC quality), deuterated ( $d_{25}$ -) SDS (Cambridge Isotope Laboratories, 98% deuteration) and Span80 (Sigma Aldrich, GC quality). In Chapters 5 and 6 we used h-dodecyltrimethylammonium bromide (DTAB) (99%, Sigma-Aldrich), d-DTAB (99% d, Cambridge Isotope), sodium chloride (NaCl, 99.999%, Acros Organics), sodium thiocyanate ( $NaSCN$ ,  $\geq 99.99\%$ , Sigma-Aldrich), sodium nitrate ( $NaNO_3$ , 99.999%, Fluka) and sodium sulfate ( $Na_2SO_4$ ,  $\geq 99.99\%$ , Sigma-Aldrich). All chemicals we used as received.

### 2.4.2 Production of nanometer-sized droplets

Throughout this work we mostly studied dispersions of nanometer-sized oil nanodroplets in water stabilized with different surfactants. In some cases additional electrolytes were added in the bulk water phase. In order to achieve the demanded concentrations of oil, surfactant and salt, stock dispersions of oil nanodroplets in water were prepared with 1, 1.5 or 2 vol % of hexadecane or  $d_{34}$ -hexadecane in  $D_2O$  (for SFS) or  $H_2O$  (for SHS). Subsequently, they were diluted with solutions of appropriate concentrations of surfactant and salt in  $D_2O$  or  $H_2O$  accordingly. In this way the size distribution of nanodroplets was kept constant between

samples stabilized with the same surfactant.<sup>29</sup> The stock dispersions were mixed for 2 minutes with a hand-held homogenizer (TH, OMNI International) with angular velocity of 300 rpm and then placed in an ultrasonic bath (35 kHz, 400 W, Bandelin). The size (hydrodynamic radius) distribution of the droplets was measured with dynamic light scattering (DLS, Malvern ZS nanosizer) and was monitored every few minutes during the sonication process, until a monodisperse sample was formed. For stable samples, the size distribution was consistently found to have a mean radius in the range of 45-125 nm with a polydispersity index (PDI) of less than 0.3. The process typically lasts for less than 10 minutes for a generic sample preparation. The hydrodynamic radii were calculated from the intensity autocorrelation function, using the optical properties of the liquids (hexadecane,  $d_{34}$ -hexadecane,  $H_2O$  and  $D_2O$ ). The samples resulting from the process described above were used for SFS measurements and were diluted with pure water for SHS measurements. For measurements presented in Chapter 3 the dilution resulted in 0.1 vol % of hexadecane while in Chapters 5 and 6 in 0.5 vol % of hexadecane. The reason for this discrepancy is the larger fluctuations in the SHS signal of nanoemulsions with electrolytes studied in Chapters 5 and 6 (Compared to samples studied in Chapter 3) that require larger number density of nanodroplets for the extraction of the SH signal. Still, controls were made while measuring for excluding multiple scattering.

All samples were stored and measured in sealed (glass) cuvettes and all measurements were performed at 24 °C. Especially for the case of DPPC (Chapter 3), the solutions were mixed at a temperature of 45 °C (above the transition temperature of 41 °C for DPPC) with 1 mM of DPPC powder using the above mentioned homogenizer for 4 minutes and ultrasonic bath for the same duration.

For the preparation of the nanometer-sized water droplets in oil studied in Chapter 4 the same preparation process was followed by exchanging the water and the oil phases. Please note that when the oil soluble surfactant Span80 was used, it was added to the oil phase before the mixing of the two phases, while the water soluble SDS in the water phase.

### **Exclusion of SDS hydrolysis at the oil/water nanointerface**

Experiments on SDS at the air/water interface have shown progressive hydrolysis of SDS that results in the production of dodecanol, which has been measured with SFG as a densely packed monolayer on the water surface<sup>24</sup>. This unwanted hydrolysis reaction was experimentally shown to be excluded for the case of the oil/water nanointerface studied here<sup>13</sup>. Specifically, SFS spectra for the C-H region and S-O region of SDS on the surface of oil droplets in water exhibit the same intensity changes as a function of surfactant density<sup>13</sup>. In addition, the SFS spectrum of dodecanol has been measured in the C-H region<sup>25</sup>, and is



similar to that of a liquid film of dodecanol on the air/water interface. Thus, if the hydrolysis reaction occurred at the oil/water interface, we would have observed changes in the C-H stretch modes as a function of time, which would also result in a dramatic increase of the sum frequency intensity (but only in the C-H stretch region, and not in the S-O stretch region). This is, in fact, not what we observe for the SDS stabilized nanodroplet emulsion samples. In contrast, we observe the same spectral features and spectral intensities within the time frame of our experiments. As such, we are confident that SDS hydrolysis does not occur up to detectable concentrations for the systems reported here. The SFS spectra for SDS at a given surface coverage, normalized for the change in radius (see section S2 of the SI of Ref. <sup>26</sup>) are stable in time, over periods of months or even years.

### **Contamination minimization: Cleaning process and chemicals**

Extra care was taken to minimize any possible contamination during the preparation of nanometer-sized oil droplets in water and water droplets in oil, according to a specific protocol. As a first step, all glassware used to prepare and store solutions and samples was cleaned prior to use according to the following process. Glassware was soaked in a freshly prepared piranha solution (3:1 H<sub>2</sub>SO<sub>4</sub> (95-98%, Sigma-Aldrich) and H<sub>2</sub>O<sub>2</sub> (30%, Macron Fine Chemicals)) for a minimum of 30 minutes and subsequently rinsed with copious amounts of ultrapure water prior to use. The above cleaning process was compared with two other processes and they were all found to give rise to identical emulsion samples (size, PDI, zeta-potential, SHS, and SFS). Specifically, the first process includes soaking of glassware in a freshly prepared NoChromix®:H<sub>2</sub>SO<sub>4</sub> (Sigma Aldrich) mixture that is mixed based on the provided instructions, followed by thoroughly washing and rinsing with MilliQ water to remove acidic components from the glass surface; the second included glassware being cleaned with a Deconex® (Sigma-Aldrich) solution prepared by 1:20 dilution with MilliQ water, then sonicated for an hour, and subsequently washed and rinsed at least 10 times with MilliQ water. Apart from the cleaning process, the choice of employed chemicals is another possible way to minimize impurities. Hence, the chemicals with highest commercially available purity were always used. The purity of alkanes was verified with a Zisman test<sup>27, 28</sup>. We also tested if further purification of the hexadecane phase had any effect on emulsion quality. For these tests hexadecane was purified by running it through an activated alumina (Sigma-Aldrich) column, which is preprocessed by heating to 500°C for 2 hours. Such processed hexadecane gives rise to identical emulsion samples with the samples using the commercially available pure hexadecane.

### 2.4.3 Production of micrometer-sized droplets

Emulsion droplets with radius between 5 and 20  $\mu\text{m}$  studied in Chapter 4 were produced with microfluidic devices. These devices were made of polydimethylsiloxane (PDMS) using soft lithography.<sup>29</sup> To produce oil-in-water emulsions the channel walls were made hydrophilic by exposing them for 30 min to an aqueous solution containing 2 wt% poly(diallyldimethylammonium chloride) and 1M NaCl. To produce water-in-oil emulsions the channel walls were made hydrophobic by exposing them for 10 min to a dodecane-based solution (Abcr) containing 2 vol% of Trichlorodecylsilane (Sigma-Aldrich). Fluids were injected into the microfluidic device using volume-controlled syringe pumps (Cronus Sigma 1000, Labhut, UK). Oil in water emulsion droplets were produced by injecting the outer phase at rates between 600 and 800  $\mu\text{L/h}$  and the inner phase at 10-60  $\mu\text{L/h}$ . Water in oil emulsion droplets were made by injecting the outer phase at rates between 100-200  $\mu\text{L/h}$  and the inner phase at rates between 80-400  $\mu\text{L/h}$ .

#### Stability control

The droplet formation was recorded using a high-speed camera operated at 506 frames per second (Mikrotron EoSens CL, Germany) and attached to an inverted microscope (Nikon, Eclipse TS100, Japan). Alternatively, we also prepared micrometer-sized droplets by vortexing a solution composed of 10% of the oil phase and 90% of the water phase, each one containing the appropriate surfactant. This rapid preparation is to visually test the stability of micrometer-sized droplets by observing the resulting droplets over a period of 8 hours.

## 2.5 References

1. Wang, H. F., Gan, W., Lu, R., Rao, Y. & Wu, B. H. Quantitative spectral and orientational analysis in surface sum frequency generation vibrational spectroscopy (SFG-VS). *Int. Rev. Phys. Chem.* **24**, 191-256 (2005).
2. Roke, S., Bonn, M. & Petukhov, A. V. Nonlinear optical scattering: The concept of the effective susceptibility. *Phys. Rev. B* **70**, 115106-115110 (2004).
3. Roke, S., Roeterdink, W. G., Wijnhoven, J. E. G. J., Petukhov, A. V., Kleyn, A. W. & Bonn, M. Vibrational sum frequency scattering from a submicron suspension. *Phys. Rev. Lett.* **91** (25), 258302 (2003).
4. De Beer, A. G. F. & Roke, S. Obtaining molecular orientation from second harmonic and sum frequency scattering experiments in water: Angular distribution and polarization dependence. *J. Chem. Phys.* **132** (23), 234702 (2010).
5. Goldstein, H., Poole, C. P. & Safko, J. L. *Classical mechanics* (Addison Wesley, Bungay 2002).
6. De Beer, A. G. F., Campen, R. K. & Roke, S. Separating surface structure and surface charge with second-harmonic and sum-frequency scattering. *Phys. Rev. B* **82**, 235431-235431 (2010).
7. Bohren, C. & Huffman, D. *Absorption and scattering of light by small particles* (Wiley-Interscience, New York, 2007).
8. Moad, A. J. & Simpson, G. J. A unified treatment of selection rules and symmetry relations for sum-frequency and second harmonic spectroscopies. *J. Phys. Chem. B* **108** (11), 3548-3562 (2004).
9. Hunter, R. J. *Foundations of colloid science* (Oxford University Press, New York, 2001).
10. McClements, J. D. Critical review of techniques and methodologies for characterization of emulsion stability. *Crit. Rev. Food Sci. Nutr.* **47**, 611-649 (2007).
11. Israelachvili, J. N. *Intermolecular and surface forces* (Academic Press, San Diego, 2011).
12. Oshima, H. *Theory of colloid and interfacial phenomena* (Academic Press, 2006).
13. De Aguiar, H. B., Strader, M. L., De Beer, A. G. F. & Roke, S. Surface structure of sodium dodecyl sulfate surfactant and oil at the oil-in-water droplet liquid/liquid interface: A manifestation of a non-equilibrium surface state. *J. Phys. Chem. B* **115**, 2970-2978 (2011).
14. Levenberg, K. A method for the solution of certain non-linear problems in least squares. *Quart. Appl. Math.* **2** (2), 164-168 (1944).

15. Marquardt, D. W. An algorithm for least-squares estimation of nonlinear parameters. *SIAM J. Appl. Math.* **11** (2), 431-441 (1963).
16. Gomopoulos, N., Lütgebaucks, C., Sun, Q. C., Macias-Romero, C. & Roke, S. Label-free second harmonic and hyper rayleigh scattering with high efficiency. *Opt. Express* **21** (1), 815-821 (2013).
17. Lütgebaucks, C. U. Lipid membrane characterization with second harmonic scatteringsurface potentials, ionization, membrane asymmetry and hydration. EPFL, 2017.
18. Chen, Y. Molecular insights in aqueous systemsfrom electrolyte solutions to aqueous nanoscale interfaces. EPFL, 2017.
19. Roke, S. & Gonella, G. Nonlinear light scattering and spectroscopy of particles and droplets in liquids. *Annu. Rev. Phys. Chem.* **63**, 353-378 (2012).
20. Davis, J. G., Gierszal, K. P., Wang, P. & Ben-Amotz, D. Water structural transformation at molecular hydrophobic interfaces. *Nature* **491** (7425), 582-585 (2012).
21. Davis, J. G., Rankin, B. M., Gierszal, K. P. & Ben-Amotz, D. On the cooperative formation of non-hydrogen-bonded water at molecular hydrophobic interfaces. *Nat. Chem.* **5** (9), 796-802 (2013).
22. Rankin, B. M. & Ben-Amotz, D. Expulsion of ions from hydrophobic hydration shells. *J. Am. Chem. Soc.* **135** (24), 8818-8821 (2013).
23. Perera, P. N., Browder, B. & Ben-Amotz, D. Perturbations of water by alkali halide ions measured using multivariate Raman curve resolution. *J. Phys. Chem. B* **113** (7), 1805-1809 (2009).
24. Casson, B. D., Braun, R. & Bain, C. D. Phase transitions in monolayers of medium-chain alcohols on water studied by sum-frequency spectroscopy and ellipsometry. *Faraday Discuss.* **104**, 209-229 (1996).
25. Chen, Y. X., Jena, K. C. & Roke, S. From hydrophobic to hydrophilic: The structure and density of the hexadecane droplet/alkanol/water interface. *J. Phys. Chem. C* **119** (31), 17725-17734 (2015).
26. Smolentsev, N., Lütgebaucks, C., Okur, H. I., De Beer, A. G. F. & Roke, S. Intermolecular headgroup interaction and hydration as driving forces for lipid transmembrane asymmetry. *J. Am. Chem. Soc.* **138** (12), 4053-4060 (2016).
27. Bigelow, W. C., Pickett, D. L. & Zisman, W. A. Oleophobic monolayers: I. Films adsorbed from solution in non-polar liquids. *J. Colloid Sci* **1** (6), 513-538 (1946).
28. Day, J. P. R. & Bain, C. D. Ellipsometric study of depletion at oil-water interfaces. *Phys. Rev. E* **76**, 41601-41610 (2007).

29. Xia, Y. & Whitesides, G. M. Soft lithography. *Angew. Chem. Int. Ed.* **37** (5), 550-575 (1998).



## Chapter 3: The Molecular Mechanism of Nanodroplet Stability

*Mixtures of nano- and microscopic oil droplets in water have recently been rediscovered as miniature reaction vessels in microfluidic environments and are important constituents of many environmental systems, food, personal care and medical products. The oil nanodroplet/water interface stabilized by surfactants determines the physicochemical properties of the droplets. Surfactants are thought to stabilize nanodroplets by forming densely packed monolayers that shield the oil phase from the water. This idea has been inferred from droplet stability measurements in combination with molecular structural data obtained from extended planar interfaces. Here, we present a molecular level investigation of the surface structure and stability of nanodroplets, and show that the surface structure of nanodroplets is significantly different from this of extended planar interfaces. Charged surfactants form monolayers that are more than one order of magnitude more dilute than geometrically packed ones, and there is no experimental correlation between stability and surfactant surface density. Moreover, dilute negatively charged surfactant monolayers produce more stable nanodroplets than dilute positively charged and dense geometrically packed neutral surfactant monolayers. Droplet stability is found to depend on the relative cooperativity between charge-charge, charge-dipole and hydrogen bonding interactions. The difference between extended planar interfaces and nanoscale interfaces stems from a difference in the thermally averaged total charge – charge interactions in the two systems. Low dielectric oil droplets with a size smaller than the Debye length in oil permit repulsive interactions between like charges from opposing interfaces in small droplets. This behaviour is generic and extends up to the micron length scale.*

*This chapter is based on the paper by Evangelia Zdrali, Yixing Chen, Halil I. Okur, David M. Wilkins and Sylvie Roke “The molecular mechanism of nanodroplet stability” published in ACS Nano 11(12), 12111-12120 (2017).*

### 3.1 Introduction

Mixtures of nano- and microscopic oil droplets in water or water droplets in oil are known as emulsions.<sup>1-3</sup> Emulsions are widely applied in technological applications, featuring as food products, agrochemical compounds, drugs, and paints, among other things. Recently, droplets in microfluidic systems have found new applications, like minuscule reaction vessels<sup>4-9</sup> useful for drug screening,<sup>10</sup> analysis of biomolecules,<sup>11</sup> and cell screening.<sup>12,13</sup> In these emulsions the droplets are kinetically stable, which means that eventually the system will phase-separate into an oil and a water phase, driven by processes such as flocculation, coalescence, and Ostwald ripening.<sup>1,2</sup> The stability of droplets can be increased by surfactants that alter the interfacial structure, and thereby create an interface with a minimal free energy. In order to achieve better control over droplet systems and their applications it is important to understand the molecular mechanism behind droplet stability. To do so, molecular interfacial structural information needs to be correlated with droplet stability data. This is typically done<sup>14-17</sup> by correlating surface structural data from extended planar interfaces, such as that gathered from X-ray,<sup>18-20</sup> neutron scattering/reflection,<sup>21,22</sup> and sum frequency generation (SFG)<sup>23-28</sup> studies, to stability data of droplets made of the same chemicals as the planar systems. These studies show that surfactants lower the interfacial energy of macroscopic planar interfaces by forming a densely packed (geometric) monolayer. However, recent reports<sup>29-33</sup> shows that the curved interfaces of droplets do not display the same molecular structure as planar extended interfaces. Simple geometrical packing<sup>14</sup> is insufficient to explain interfacial amphiphile structure. For example, sodium dodecyl sulphate was found to form very dilute monolayers on nanodroplets that differ in density from the corresponding planar interfaces by at least an order of magnitude,<sup>29</sup> the water molecules at the surface of water droplets in a hydrophobic liquid are much more ordered than water molecules at identical planar/water interfaces,<sup>30</sup> and liposomes exhibit transmembrane asymmetry in their hydrating water rather than in their lipid distribution.<sup>34</sup> These findings were made employing vibrational sum frequency scattering (SFS),<sup>35,36</sup> and angle resolved<sup>37</sup> second harmonic scattering (SHS)<sup>36,38</sup> techniques that probe the molecular structure of the oil, the water and the surfactant on nanodroplet/particle surfaces in aqueous solution.<sup>39</sup> Vibrational SFS is a coherent surface spectroscopy that provides information of chemical composition, molecular order and orientation of interfacial molecules present on droplets or particles.<sup>29,40,41</sup> Non-resonant angle resolved SHS is a probe of the orientational order of interfacial water molecules: It reports on the difference in orientational directionality between interfacial water molecules and bulk water molecules.<sup>42,43</sup>

Here we provide a systematic investigation of the macroscopic stability, the molecular structure, and the relevant interactions for oil droplets in aqueous solutions. In



order to produce smooth, defect-free interfaces, we use  $\sim 100$  nm in radius hexadecane oil droplets stabilized with neutral (alkanols and zwitterionic lipids), positively charged (dodecyltrimethylammonium bromide, DTAB) and negatively charged (sodium dodecylsulfate, SDS) amphiphiles. These chemicals are chosen such that they represent different charges with and without hydrogen bonding in contact with a water/dielectric nanoparticle interface. We present stabilizing performance, charging, hydration and surface density data of the amphiphilic molecules as well as structural information of the interfacial oil and interfacial water molecules. Finally, the combined data is broken down in terms of relevant interactions and a mechanism relevant for surface structure and stability is proposed, which differs from the framework used for planar interfaces. We observe that high droplet stability does not necessarily require a high surface charge density but rather a sufficient amount of surface charge, and cooperativity between hydrogen bonding and charge-dipole interactions. The nano/sub-micron size of the droplets, in combination with a lack of conducting species in the oil phase, results in non-zero repulsive interactions between the surface charges on opposite sides of the droplet. This interaction is absent for neutral/zwitterionic droplet surfaces and limits the surface charge density to one that is lower compared to equivalent planar interfaces. This proposed mechanism is supported by a simple electrostatic model that captures the essence of the relevant physics, as well as surface charge density measurements as a function of ionic strength.

## 3.2 Results and Discussion

### 3.2.1 Stability

To quantify droplet stability, nanodroplets were prepared with  $150\text{ }\mu\text{M}$  of either SDS (critical micelle concentration, cmc, of  $8.25\text{ mM}$  at  $T = 293\text{ K}$ ),<sup>44</sup> DTAB (cmc of  $15.9\text{ mM}$  at  $T = 293\text{ K}$ ),<sup>44</sup> or hexanol (solubility of  $65\text{ mM}$  at  $T = 293\text{ K}$ ).<sup>45</sup> The preparation procedure can be found in the Paragraph 2.4. With the chosen low concentration of surfactants the destabilization process occurs within a time frame of several days. The stability was determined by a standard protocol<sup>2</sup> of visual inspection, and size distribution measurements. The droplet size distribution was measured over 10 days with dynamic light scattering (DLS). The droplet size distribution of freshly prepared samples consists of a single peak centred at a radius  $R$  in the range  $45 < R < 125\text{ nm}$  (see Fig. 3.1a, red and black, for two size distributions representative of the range of samples that have been prepared) with a polydispersity index (PDI) of  $0.05 < \text{PDI} < 0.25$ . These values are typical for nanoemulsions.<sup>3</sup> The nanodroplets were considered unstable<sup>2</sup> if (i) there was a phase separation, (ii) new peaks appeared in the size distribution (see Fig. 3.1a for an example in grey), and/or (iii) the PDI became larger than 0.3

or (iv) the droplet size increased by more than 15% over a time span of 10 days. Each measurement was performed three times on each sample. Figure 3.1b displays the percentage of samples that remained stable over time, measured up to 10 days after their preparation. Here it can be seen that the dodecylsulfate ion ( $\text{DS}^-$ ) is the best stabilizer, as all samples remained stable for at least ten days. The dodecyltrimethylammonium ( $\text{DTA}^+$ ) ion follows, with 30 % of the samples becoming unstable after five days. All hexanol nanodroplets were destabilized after 7 days, making hexanol the least effective stabilizer of the three representative surface active compounds studied here. Further data are summarized in Table 3.1.

### 3.2.2 Surface density

The surface density of amphiphiles can be derived from SFS spectral amplitudes, recorded from nanodroplets that contain the same droplet size distribution but a different total surfactant concentration.<sup>29</sup> With an identical size distribution, and an average surfactant orientation that is not changing over the probed concentration range, a change in the SFS amplitude is proportional to a change in surface density.<sup>29,46</sup> Figure 3.1c shows the relative amplitude change for the interfacial S-O symmetric stretch mode of  $\text{DS}^-$  anions, and the C-H stretch modes of  $\text{DTA}^+$  cations and hexanol molecules. It can be seen that, over the same concentration range, the relative increase of the surface density of hexanol is much larger ( $\times 13$ ) than those of the two ionic surfactants ( $\times 2$  for  $\text{DTA}^+$  and  $\times 3$  for  $\text{DS}^-$ ). The maximum surface density (or minimum projected surface area) of each amphiphile can be retrieved by assuming that, as an upper limit, for the lowest total concentration (e.g. 55  $\mu\text{M}$  for SDS or 100  $\mu\text{M}$  for DTAB) all surfactant molecules are adsorbed at the interface. Without this assumption the retrieved surface density values will be even lower. In addition, it is possible to use a modified Langmuir adsorption model to estimate the surface density of amphiphiles.<sup>47</sup> Using these procedures we found lower limits for the projected surface density of hexanol ( $27 \pm 7 \text{ \AA}^2 / \text{hexanol}$ ),<sup>46</sup>  $\text{DS}^-$  ( $> 425 \text{ \AA}^2$ ),<sup>48</sup> and  $\text{DTA}^+$  ( $> 500 \text{ \AA}^2$ ). The surface density of hexanol is at least an order of magnitude higher than those of the two ionic surfactants. Dodecanol was shown to have a surface density very similar to that of hexanol,<sup>46</sup> with  $29 \pm 5 \text{ \AA}^2$  per molecule. These experimental findings suggest that the adsorption behaviour of amphiphiles, as well as the resulting droplet stability, is related to their charge, rather than their molecular packing. This notion is supported by the fact that the observations are done for a distribution of different sizes and PDIs, and that curvature related packing differences are most commonly found in systems smaller than  $\sim 50 \text{ nm}$ .<sup>49</sup>

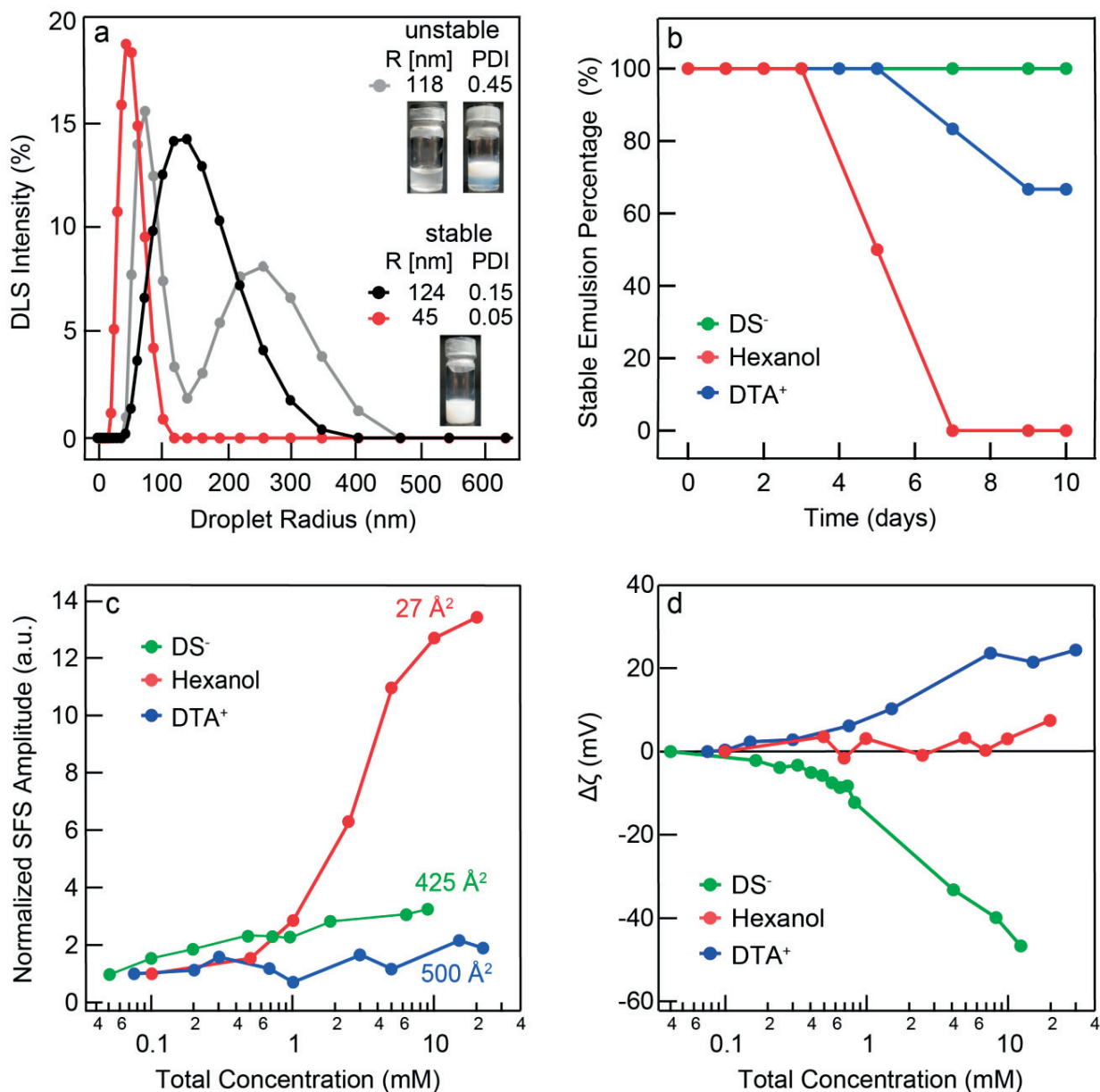


**Figure 3.1: Stability and surface group density.** (a) Three typical droplet size distributions of stable (red and black) and unstable (grey) droplets as determined by DLS. The inset displays photographs of stable and unstable samples. Note that the X-axis has a linear scale. (b) Percentage of droplets that remains stable as a function of time. Each sample consists of 1 vol. % hexadecane (99.8 % pure) nanodroplets in ultrapure water with 150  $\mu\text{M}$  of SDS, DTAB or hexanol. (c) SFS amplitude, which is proportional to the surfactant surface density, as a function of total surfactant concentration in the sample. The calculated minimum area per molecule for the maximum concentration (in  $\text{\AA}^2$ ) is given for each surfactant. The SFS spectra were collected with the infrared (visible, sum frequency) beam polarized parallel (perpendicular) to the scattering plane (SSP), and recorded for the S-O symmetric stretch mode ( $\sim 1080\text{ cm}^{-1}$ ) for  $\text{DS}^-$ , and for the C-H stretch modes ( $\sim 2900\text{ cm}^{-1}$ ) for  $\text{DTA}^+$  and hexanol. SFS measurements are normalized with the DLS size distribution according to the protocol in Ref. <sup>34</sup>. (d) Change in the droplets  $\zeta$ -potential as a function of total surfactant concentration.

### 3.2.3 Electrokinetic mobility

A commonly used indicator for droplet stability is the electrokinetic mobility of particles in aqueous solutions,<sup>2</sup> that is reflected in the  $\zeta$ -potential.<sup>50</sup> Higher stability is generally achieved with a higher  $\zeta$ -potential amplitude, which results in efficient droplet repulsion, thereby preventing coalescence that leads to instability.<sup>1</sup> Figure 3.1d shows the change in the  $\zeta$ -potential of hexadecane nanodroplets in water with increasing concentrations of SDS, DTAB and hexanol. The  $\zeta$ -potential changes with different magnitudes as the  $\text{DS}^-$  and  $\text{DTA}^+$  concentrations increase in the solutions. Increasing the surfactant concentration from  $\sim 75 \mu\text{M}$  to  $\sim 10 \text{ mM}$ , results in a change of  $-40 \text{ mV}$  for SDS, while only  $\sim 20 \text{ mV}$  is added to the initially positive  $\zeta$ -potential of droplets in DTAB solutions. Hexanol stabilized droplets do not have a different  $\zeta$ -potential than pure oil droplets in water. Comparing the  $\text{DTA}^+$  and  $\text{DS}^-$  stabilized droplets, we find that the more stable nanodroplets have a higher surface density, and a bigger relative change in the  $\zeta$ -potential. The surface density ratio of  $\text{DS}^-$  and  $\text{DTA}^+$  ions ( $\times 1.3$  at  $10 \text{ mM}$ ) correlates well with the  $\Delta\zeta$ -potential ratio of  $\text{DS}^-$  and  $\text{DTA}^+$  ( $\times 1.8$  at  $10 \text{ mM}$ ). Nanodroplet stability is thus clearly correlated with the amount of surface charge, which is in agreement with expectations.<sup>1</sup> The increase of surface charge can explain the stability achieved by the addition of ionic surfactants; however, it does not explain the case of hexanol or the low surface densities that are found for the charged surfactants. For further understanding of the relationship between surface stability and surface molecular structure we revisit derived structural changes of the oil and water molecules, as well as the bulk hydration characteristics for the three systems.

### 3.2.4 Molecular interfacial structure and bulk hydration

The structural changes imposed by the amphiphiles on the interfacial oil molecules are reflected in the SFS spectra of the C-H stretch modes of hexadecane droplets dispersed in  $\text{D}_2\text{O}$  (Fig. 3.2a), in which the bulk concentrations of deuterated ( $\text{d}_{25}$ )-SDS ( $0.98 \times \text{cmc}$ ),  $\text{d}_{34}$ -DTAB ( $0.93 \times \text{cmc}$ ) or  $\text{d}_{13}$ -hexanol were different.<sup>51</sup> Using selective deuteration, the vibrational modes of the surfactant are removed from the SFS spectral window, allowing independent probing of the structural changes of the oil surface. Compared to pure hexadecane droplets in water, it can be seen that  $\text{DS}^-$  ions do not significantly alter the conformation of oil molecules, as they leave the vibrational spectrum unchanged. The same behaviour is observed for oil droplets made of dodecane and hexane.<sup>48</sup> In contrast,  $\text{DTA}^+$  and hexanol cause a significant change in the interfacial vibrational spectrum, and, hence, are concluded to perturb the interfacial oil structure.<sup>51</sup> Analysis of these spectral changes resulted in a structural interpretation that has the  $\text{DTA}^+$  and the hexanol molecules

penetrating into the oil phase, while the  $\text{DS}^-$  molecules lie flat on the oil surface without much interaction.<sup>48,51,52</sup> Figure 3.2b displays the change in the SHS intensity of 100 nm (radius) hexadecane droplets in water as a function of the surfactant concentration (published previously in Refs<sup>29,46</sup>). This data shows that the orientational order of interfacial water is altered when the amount of surfactant is increased. The change is also different for each surfactant:  $\text{DS}^-$  increases the water order, while  $\text{DTA}^+$  decreases the water order, and hexanol induces a smaller loss in water order than  $\text{DTA}^+$ . This behaviour differs significantly from what is expected for geometrical packing, and can be explained by the interplay of the different interactions:<sup>53</sup> For negatively charged interfacial  $\text{DS}^-$  ions, both hydrogen bonding and charge-water dipole interaction require water molecules to be oriented predominantly with their hydrogen atoms towards the interface. However, for a positively charged  $\text{DTA}^+$  covered interface, there is little hydrogen bonding, and a charge-dipole interaction that is oppositely oriented. Hexanol, on the other hand, induces a decrease in the directionality of water along the surface normal, which is caused by the formation of hydrogen bonds between the OH group of hexanol and the interfacial water molecules. This decrease in the directionality of water matches with the increasing surface density of hexanol as the concentration of hexanol in the solution is increased (see also Ref.<sup>46</sup>). Figure 3.2c shows the Raman hydration shell spectra of the O-H stretch region of 0.1 M solutions of octylsulfate ( $\text{OS}^-$ ) anions, octyltrimethylammonium ( $\text{OTA}^+$ ) cations<sup>29</sup> and hexanol molecules.<sup>54</sup> The hydration shell spectra represent the spectral difference in Raman intensity between a solute/solvent mixture and the pure solvent. The spectral content is explained as the differential vibrational response of the hydration shell and bulk water. Thus, it reports on solvent-solute interactions that are different from those in bulk water.<sup>55</sup> For these measurements octyl alkyl chains were chosen instead of dodecyl so as to exploit the higher cmc concentrations of  $>100 \text{ mM}$ <sup>44</sup> for sodium octylsulfate (SOS), and octyl trimethylammonium bromide (OTAB) (enabling spectral recordings with a better signal to noise ratio). The influence of counter-ions was eliminated.<sup>51</sup> Compared to bulk water, the three hydration shell spectra are different, with hexanol and  $\text{OTA}^+$  cations having a similar, more red shifted, spectrum, and the  $\text{OS}^-$  anions having a more intense, and blue shifted spectrum. The red shift can be interpreted as a sign of enhanced tetrahedral ordering of water molecules around the  $\text{OTA}^+$  ions, and hexanol molecules.<sup>46, 51</sup> The hydration shell spectrum of  $\text{OS}^-$  anions was interpreted to have more, but weaker, hydrogen bonds between water molecules around  $\text{OS}^-$  than in an identical volume of pure water.<sup>51</sup> This difference in hydration matches well with the different interfacial water ordering of Fig. 3.2b. The rearrangement of interfacial water molecules around  $\text{DTA}^+$  and hexanol, due to electrostatic and hydrogen bonding interactions respectively, disrupts the already existing water ordering, resulting in a decrease in the SH intensity. In the case of  $\text{DS}^-$ , the large increase observed in

the SH intensity is due to hydrogen bonding and electrostatic field interactions, that both result in more orientational order of water along the surface normal. The subsequent decrease ( $> 1$  mM) arises from the screening of the surface electrostatic field by the counter-ions, resulting in less ordered water molecules.

Figures 3.2d-f are indicative illustrations of the interfacial structure of the three systems studied here, allowing a structural comparison. The surface density of the interfacial ions ( $\text{DS}^-$  in Fig. 3.2d,  $\text{DTA}^+$  in Fig. 3.2e), or hexanol molecules, (in Fig. 3.2f) as well as the respective orientation of the interfacial water molecules, are displayed in the top panels. The bottom panels show the interaction of the amphiphiles with the interfacial oil layer and interfacial water molecules in more detail. In the following we discuss the correlation between the interfacial structure of these three exemplary systems and the observed droplet stability.

### 3.2.5 Stability and structure

For a geometrical interfacial packing, with all structure-determining interactions being nonspecific, no difference in the emulsion stability between  $\text{DS}^-$ ,  $\text{DTA}^+$ , and hexanol would be expected. Similar saturated surface densities, and similar changes to the respective interfacial oil and water structures for all three surfactants, would be expected. On nanoscale systems, an increasing curvature ( $R \downarrow$ ) is typically interpreted as leading to an increase in available molecular surface volume, and thus an increase in surface density. This behaviour very strongly depends on the actual curvature and becomes important on metal (high dielectric) particles, or when surfactants are paired with counter ions.<sup>49,56</sup>

Combining all stability and structural findings in Table 3.1, we find a very different picture than the one suggested by geometrical packing. Instead, a distinct trend in stability dependent on surface chemistry, a very low surface density for the charged surfactants, and specific changes in the oil/water structure per surfactant are observed. In addition, in contrast to expectations for geometrical packing, we observe the same behaviour for a rather large variety of sizes ( $45 \text{ nm} < R < 125 \text{ nm}$ ) and distributions  $0.05 < \text{PDI} < 0.25$  for the 25 different samples that were prepared and probed here.

Based on these many differences, it seems necessary to abandon the classical effect of curvature and instead consider that a balance of interactions is responsible for the stability of the nanodroplets. For hexanol, nanoemulsions are stable only for several days. The repulsion between the droplets is therefore probably weak (in the absence of any interfacial ionic species), but the oriented interfacial water molecules (see Fig. 3.2f) present an oriented layer of dipoles which does provide dipolar electrostatic repulsion. Moving upward in stability with  $\text{DTA}^+$ , there is a dilute layer of charges at the interface (Fig. 3.2e), which results in positively charged droplets that repel each other. The positive charges are screened by the



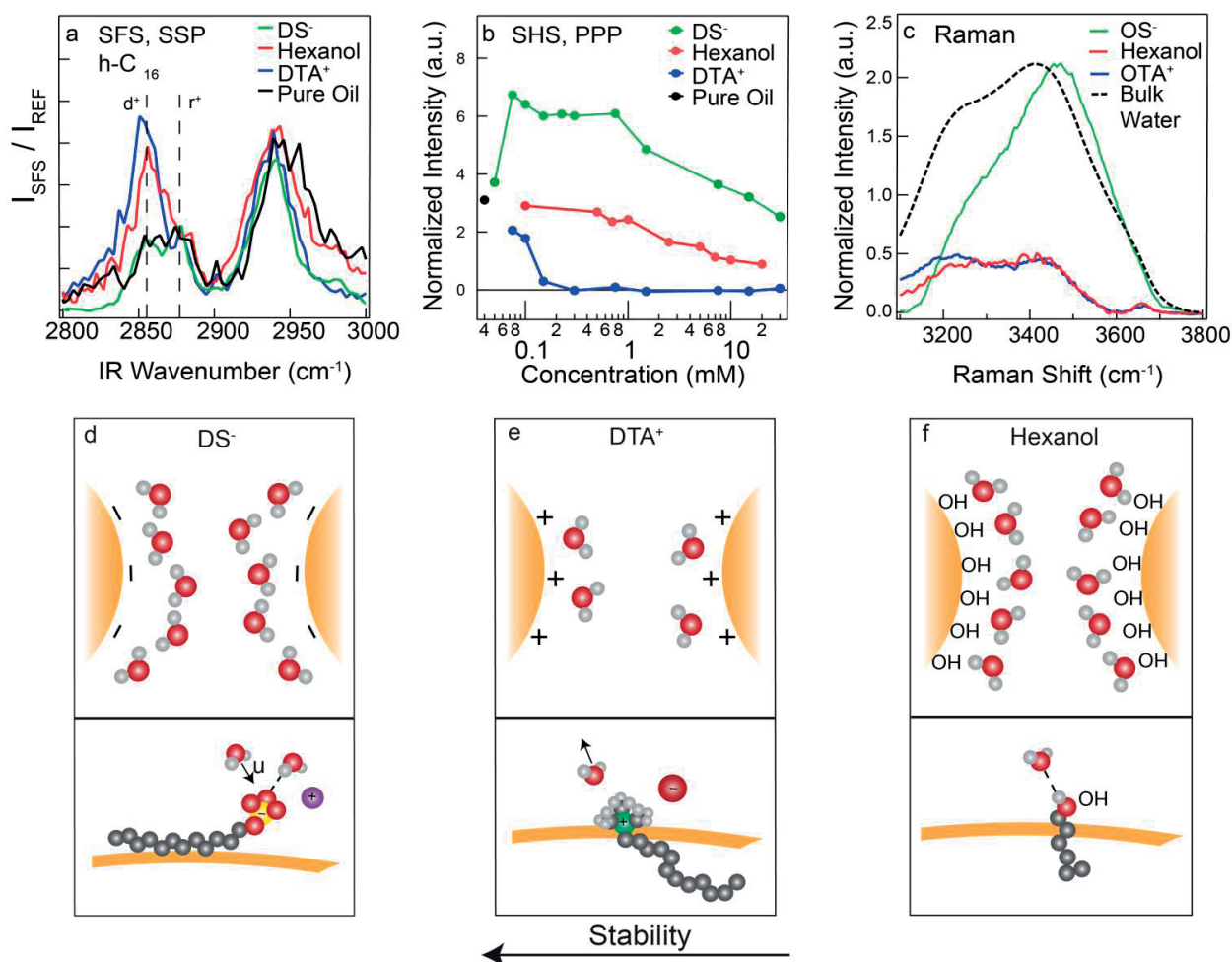


**Figure 3.2: Interfacial structure and bulk hydration.** (a) Normalized SFS spectra of the C-H stretch modes of hexadecane droplet interfaces stabilized with d<sub>25</sub>-DS<sup>-</sup> (8 mM, green), d<sub>34</sub>-DTA<sup>+</sup> (12 mM, blue) or d<sub>13</sub>-Hexanol (5 mM, red). The SFS spectrum of pure oil nanodroplets in water is also shown (black). The SFS spectra were collected in the SSP polarization combination. (b) SHS intensity, recorded with all beams polarized in the horizontal plane, at a scattering angle of 45°, of a 0.1 vol% d<sub>34</sub>-hexadecane/water nanoemulsion stabilized with hexanol, SDS or DTAB as a function of the amphiphile concentration. The intensity of the SFS and SHS measurements is normalized using an effective droplet radius retrieved from the DLS size distribution according to the protocol in Ref. <sup>34</sup> Intensities are therefore independent of droplet radius and size distribution. (c) Raman hydration shell spectra of 100 mM aqueous solutions of octylsulfate anions (OS<sup>-</sup>), octyltrimethylammonium cations (OTA<sup>+</sup>) and hexanol molecules. The spectra display the O-H stretch vibrational response of the water surrounding the surfactant ions. The O-H Raman spectrum of pure water is also presented and scaled to the same height as the OS<sup>-</sup> hydration-shell O-H band (black). (d-f) Schematic diagrams of the influence of the surfactants surface structure of the systems measured in Fig. 3.2a and 3.2b. The dashed lines represent hydrogen bonds, and the arrows represent dipole moments. The bottom panels display the primary interaction(s) of a surfactant molecule with the interfacial water molecules. (d) A DS<sup>-</sup> ion influences the water orientation with respect to the interface through both hydrogen bonding and electrostatic interactions. (e) A DTA<sup>+</sup> ion influences the water orientation with respect to the interface through electrostatic interactions only. (f) A hexanol molecule influences the water orientation with respect to the interface through hydrogen bonding only. The top panels illustrate the relationship between the molecular interactions and the interactions that take place when droplets approach each other, which relates to droplet stability.

counterions, and by oriented water dipoles, but there are no hydrogen bonds between  $\text{DTA}^+$  and the interfacial water molecules. For  $\text{DS}^-$ , in addition to charge-charge repulsion, and screening by counterions and water dipoles, there is a population of oriented water molecules that form hydrogen bonds with the sulphate head groups (Fig. 3.2d). The charge of the  $\text{DS}^-$  ions thus experiences a more thorough screening than that of the  $\text{DTA}^+$  ions, which is reflected in the lower surface density and lower  $\zeta$ -potential change of  $\text{DTA}^+$  compared to  $\text{DS}^-$  (Fig. 3.1c, 3.1d).

**Table 3.1: Stability and interfacial structure of amphiphiles.** Summary of the characteristics of the studied hexadecane-in-water nanodroplets.

Component	Stability (days)	Min. surface area/molecule ( $\text{nm}^2$ )	Interfacial water alignment	Interfacial oil structural changes
$\text{DS}^-$	> 10	> 4.25	increases	not detectable
$\text{DS}^- + 30 \text{ mM NaCl}$	> 10	> 2.13	increases	not detectable
$\text{DTA}^+$	< 5	> 5.00	vanishes	more chain disorder
hexanol	< 3	0.27	decreases	more chain disorder
dodecanol	< 3	0.27	decreases	more chain disorder
DPPC	< 3	0.48	decreases	more chain disorder

That the surface density of  $\text{DS}^-$  and  $\text{DTA}^+$  is much lower than what is expected based on planar surface experiments<sup>25, 57</sup> can then be explained by considering interactions rather than excluded volume. The interaction between charged molecules in a solution is determined by a balance of Coulombic interactions between ions, and their thermal motion. The Debye screening length ( $1/\kappa$ ) provides an indication for the distance over which ions are separated in a liquid.<sup>16</sup> The electrostatic potential has decayed to  $\sim 2\%$  of its value after a distance  $4/\kappa$ . The Debye length in water is on the order of 3–30 nm for the ionic strength range 10–0.1 mM. The solubility of single ions in oil (or any other low dielectric medium) is  $\sim 10^{-9}$  M, and thus the Debye length in the oil phase is typically  $\sim 1.5 \mu\text{m}$ . On a planar surface the total charge-charge repulsion/attraction is reduced by half compared to an aqueous bulk solution, since only the water phase contains a significant amount of charge (Fig. 3.3a), and the oil phase is essentially infinite. Thus, charges at a planar interface experience Coulombic repulsion from other co-ions situated in a hemisphere with a radius  $\sim 4/\kappa$  adjacent to the interface. Experimental data<sup>26,58,59</sup> shows that high charge densities can be obtained for surfactants adsorbed at planar oil/water interfaces. For nanodroplets and nanoparticles that are smaller than  $4/\kappa \sim 6 \mu\text{m}$ , it can be expected that the electrostatic field from the surface charges will not be screened by the oil (as illustrated in Fig. 3.3b). Every interfacial charge



will thus experience the electrostatic repulsion from all other interfacial charges on opposing surfaces through the oil phase, and from all the charges in the bulk that are separated by a few Debye lengths in the aqueous phase. As such, the surface charge density will likely be similar to the charge spacing in the aqueous phase.

In order to understand whether the physical picture described above contains the right essentials, we consider a system in which space is modified into three areas with different dielectric constants and Debye lengths ( $\epsilon_1$ ,  $\kappa_1$  for the water phases on the outer side, and  $\epsilon_2$ ,  $\kappa_2$  for the oil phase with a thickness  $R$  between the water phases, Fig 3.3c), and insert two parallel sheets  $S$  with surface charge density  $\sigma$  in the water phase, at a distance of  $3 \text{ \AA}$  (the size of a water molecule) away from the oil/water interface, in order to mimic two opposing layers of adsorbate. We calculate the electric potential  $V(z)$  by solving the linearized Poisson-Boltzmann equation (where  $z$  is the distance perpendicular to the oil/water interfaces). Knowing  $V(z)$  we calculate the energy required to create the two charged sheets as a function of  $\sigma$  and the thickness of the oil phase. Setting this energy equal to the thermal energy  $k_B T$ , we then obtain an expression for  $\sigma$  in terms of  $R$ . Figure 3.3d shows the relative change  $(\sigma - \sigma_0)/\sigma_\infty$  as a function of  $\kappa_2 2R$ , where  $\sigma_0$  is the surface charge density at  $R=0$  and  $\sigma_\infty$  the limiting values for large radius ( $R \rightarrow \infty$ ). The Debye parameters and dielectric constants used are those discussed in the previous paragraph for water ( $\epsilon_1 = 78$ ,  $\kappa_1 = 0.33 \text{ nm}^{-1}$  and  $1/\kappa_1 = 3 \text{ nm}$ ) and hexadecane ( $\epsilon_2 = 2$ ,  $\kappa_2 = 0.67 \text{ }\mu\text{m}^{-1}$  and  $1/\kappa_2 = 1.49 \text{ }\mu\text{m}$ ). The experimentally accessed values are  $0.06 < \kappa_2 2R < 0.17$  (using the average intensity weighted radii; with larger radii that are also present in the distribution the limiting value would be 0.5). It can be seen that, as the interfaces approach each other, the surface charge density on each sheet reduces, as a consequence of the increasing repulsive interaction between the charges on both sheets. The same trend is observed when changing the interfacial thickness, or else, the distance of the sheets  $S$  from the interface at a constant  $R$ : the surface charge density on each sheet decreases as the interfacial thickness decreases. Although this simplistic model does not resemble a droplet interface, it shows that the expected mechanism for the interaction of charges adsorbed to opposing interfaces indeed occurs. This picture implies that in absence of any interactions stronger than the electrostatic repulsion considered here, the spacing of charges for small enough droplets (*i.e.* with  $R < 3 \text{ }\mu\text{m}$ ) should be comparable to the distance of charges in solution. To further test our hypothesis, we compare the Debye length in solution to the interfacial charge spacing, and measure changes therein, as a function of ionic strength.

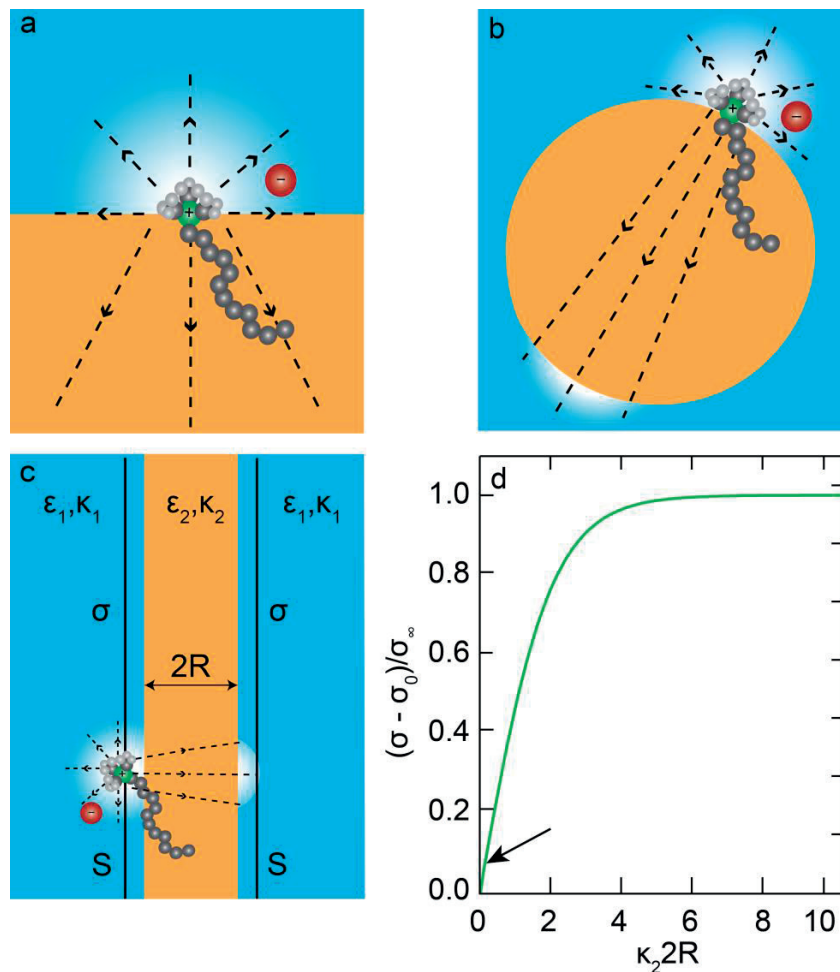


**Figure 3.3: Sketch of interfacial ion-induced electric field.** Sketch of the electrostatic field lines of the field created by a  $\text{DTA}^+$  cation on (a) a single planar interface (b) on a droplet and (c) on two opposing planar interfaces. The two regions of water, with dielectric constant  $\epsilon_1$  and Debye screening parameter  $\kappa_1$ , are separated by an intervening region of oil, with dielectric constant  $\epsilon_2$ , Debye screening parameter  $\kappa_2$ , depth  $2R$ , and surface charge density  $\sigma$ . (d) Relative surface charge density  $\sigma$  of the opposing surfaces shown in (c) as a function of  $R$ , normalized to the value with  $R \rightarrow \infty$ .  $\sigma_0$  is the charge density value for  $R = 0$  (at the absence of the intervening dielectric) and is used as a reference value. The values used are  $\epsilon_1 = 78$ ,  $\kappa_1 = 0.33 \text{ nm}^{-1}$  ( $1/\kappa_1 = 3 \text{ nm}$ ),  $\epsilon_2 = 2$  and  $\kappa_2 = 0.67 \text{ } \mu\text{m}^{-1}$  ( $1/\kappa_2 = 1.49 \text{ } \mu\text{m}$ ). The arrow indicates the region of  $\kappa_2 2R$  values corresponding to the droplets under study, with radius  $R$  in the range  $45 \text{ nm} < R < 125 \text{ nm}$ . See the SI for further information about the calculation.

### 3.2.6 Electrostatic interactions in charged systems

To do so, we prepared 1 vol% suspensions of  $\sim 100 \text{ nm}$  in radius  $\text{d}_{34}$ -hexadecane droplets in  $\text{D}_2\text{O}$ , with a constant droplet size and distribution with different amounts of SDS added to the solution (similar with that in Fig. 3.1c, Ref. <sup>29</sup> SI). Figure 3.4a displays the SFS amplitude of the S-O stretch vibration as a function of the total  $\text{DS}^-$  concentration in solution without (green) and with (black) the addition of 30 mM NaCl. All values are normalized to the SFS amplitude obtained from the solution with the smallest amount of  $\text{DS}^-$  ions ( $100 \text{ } \mu\text{M}$ ). Without NaCl, Fig. 3.1c shows that the surface density of  $\text{DS}^-$  anions increases by a factor of  $\sim 2$

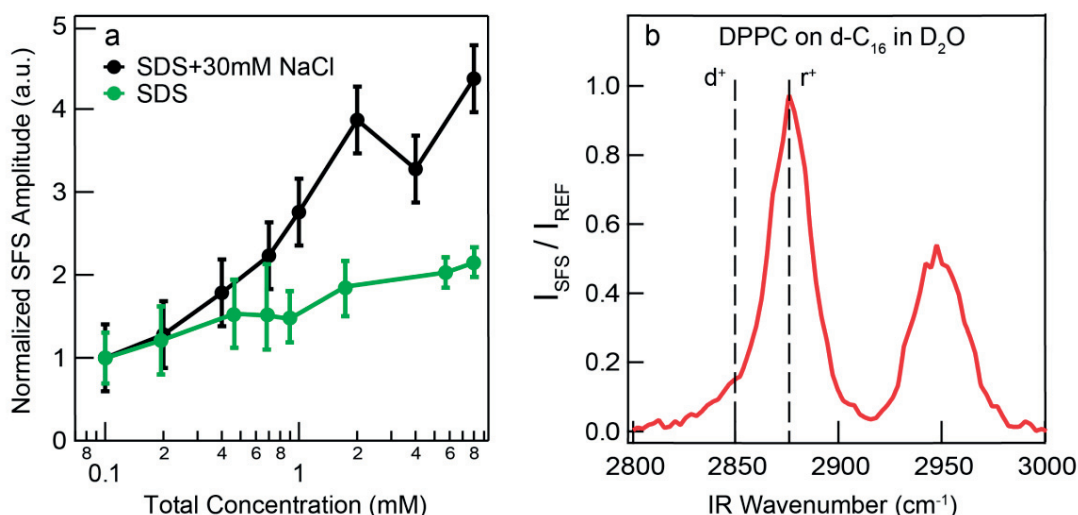


**Figure 3.4: Electrostatic interactions.** (a) SFS amplitudes of the S-O symmetric stretch mode of DS<sup>-</sup> ions at the interface of d<sub>34</sub>-hexadecane nanodroplets in D<sub>2</sub>O for different SDS concentrations with (black) and without (green) 30 mM NaCl. The SFS spectra were recorded in the frequency range of 1000 – 1150 cm<sup>-1</sup>. (b) SFS spectra of DPPC monolayers on 2 vol % d<sub>34</sub>-hexadecane nanodroplets in D<sub>2</sub>O taken for 1 mM of DPPC bulk concentration in the C-H stretch region. The symmetric methylene (d<sup>+</sup> at ~2850 cm<sup>-1</sup>) and the symmetric methyl (r<sup>+</sup> at ~2876 cm<sup>-1</sup>) stretch vibrational modes are indicated by the vertical lines. All SFS spectra for (a) and (b) were collected with the IR (VIS, SF) beam polarized parallel (perpendicular) to the scattering plane (SSP) and normalized with the DLS size distribution according to the protocol in Ref. <sup>34</sup>.

when the DS<sup>-</sup> concentration is varied from 100  $\mu$ M to 8 mM. Thus, a minimum projected surface area of 4.25 nm<sup>2</sup> is reached (at 8 mM), corresponding to an interfacial DS<sup>-</sup> spacing of >2.1 nm. Additionally, the Debye length in the bulk solution is ~3 nm. The similarity of the two values is striking and, in absence of ion pairing,<sup>43</sup> in agreement with the prediction presented above, namely that the surface charge separation, should be similar to the spacing of surfactant molecules in the aqueous phase. With 30 mM NaCl and 8 mM SDS ( $1/\kappa=1.57$  nm), Fig. 3.4a shows that the SFS amplitude increases to a higher value, corresponding to an increased surface density by ~2.2 times at 8 mM, equivalent to a projected surface area of >2.1 nm<sup>2</sup> per DS<sup>-</sup> ion. This area corresponds to a surface spacing of >1.5 nm, again close to the Debye length in solution. Thus, increasing the electrostatic screening in the bulk solution, results in an interfacial layer that is more densely packed. Note that higher NaCl concentrations will not lead to even more densely packed films, as this will instead result in more efficient micellization (the cmc for SDS is 3 mM with 30 mM NaCl added to the solution<sup>44</sup>). In addition, the resemblance between the ion spacing at the interface and the Debye length in solution suggests that, indeed, the small droplets do not screen the electrostatic field from interfacial surfactant molecules. Thus, the surfactants experience the same electrostatic field on the droplet surface as in the bulk, and this is expected for all aqueous solutions of nanoparticles that have a low dielectric constant and negligible amount

of charged species in their bulk phase. On the contrary, on extended planar interfaces a surfactant molecule close to the interface does not experience any electrostatic field through the oil phase (Fig. 3.3a), while a surfactant molecule in the bulk water experiences the electrostatic field from all surfactant molecules in solution at a distance up to  $4/\kappa$ . This difference from the nanodroplets is reflected on the ion spacing at the flat interface, which is  $\sim 0.7$  nm,<sup>57</sup> clearly smaller than the Debye length of  $\sim 3$  nm. This tight packing is also facilitated by counter ion condensation, which is also different for different surface geometries<sup>60</sup> and further reduces the electrostatic repulsion between like charges.

To confirm the importance of counterions, we compare the surface density of  $DS^-$ ,  $DTA^+$  and hexanol to that of a zwitterionic lipid 1,2-dipalmitoyl-*sn*-glycero-3-phosphocholine (DPPC). Figure 3.4b shows the SFS spectrum of the C-H stretch mode region of DPPC lipids adsorbed at the  $d_{34}$ -hexadecane/ $D_2O$  nanodroplet interface. Comparing the SFS spectra of droplets coated with different amounts of DPPC, and comparing the data to SFG spectra from a DPPC monolayer at the air/water interface with a known surface density, it was found that DPPC can self-assemble to form a dense monolayer with a projected molecular area of  $0.48$  nm.<sup>57</sup> This confirms that, for the case of charged surfactants that are adsorbed as dissociated charges, there is a net repulsion between the surface ions, which ensures droplet stability, but also reduces the surface density. However, as determined from the above discussion, a high surface density of surfactants (above a certain barrier) is apparently not needed for droplet stability. Indeed, adding NaCl to the emulsion with SDS does not result in a difference in the stability of the nanodroplets, while it does lead to an increase in the surface density of  $DS^-$ .

### 3.3 Conclusions

We have investigated the stability and molecular structure of oil nanodroplets in water that were stabilized with negatively charged, positively charged, neutral, and zwitterionic molecules. We used a combination of methods that report on macroscopic properties, and molecular interfacial structures. We find that ionic surfactants are better stabilizers than neutral and zwitterionic ones. Contrary to the general expectation based on geometrical packing, that a good stability is accompanied by a high surface density, the neutral/zwitterionic surfactants have a  $>15$  times higher surface density than the charged surfactants, but the droplets are also less stable. Head group hydration influences the orientational ordering of water, which is affected by both charge-dipole interactions as well as hydrogen bonding. Specifically, hexanol forms hydrogen bonds with water and, as a consequence, there is a polarized layer of weakly oriented water dipoles that provides some stability to the droplets.  $DTA^+$  ions repel each other, and form a dilute interfacial layer, with

the somewhat hydrophobic cations situated inside the oil. Additionally, there is no hydrogen bonding between  $\text{DTA}^+$  and water in this system, but the interfacial water network is disrupted because of charge-dipole interactions.  $\text{DS}^-$  ions also repel each other, but they form a denser layer than  $\text{DTA}^+$ , as the water molecules screen the charges more effectively (by combined ion-dipole and hydrogen bonding interactions). The effect of electrostatic screening on the interfacial structure has been further investigated for  $\text{DS}^-$  ions by adding NaCl to the solution, which results in more densely packed surfactant layers. The surface spacing of surfactant ions is still comparable to the Debye length in solution. In contrast, charge neutralized zwitterionic layers do not display this behaviour and instead form densely packed monolayers. The latter demonstrates again the important difference between charged and charge neutral surfactants.

The differences between nanoscale interfaces and extended planar interfaces are caused by a difference in charge – charge screening interactions on the sub-micron length scale. For small droplet systems there is less screening in the oil phase, resulting in a lower surface density of free charges. This behaviour is generic, extends up to the micron-scale and is thus expected to occur for any type of dielectric particle in water. It is also expected to occur for the inverse system of water droplets in oil.

## 3.4 Appendix

### 3.4.1 Calculation of Interfacial Charge Density

We consider a system with the geometry presented in Fig. 3.5a. It comprises a region (1), with dielectric constant  $\epsilon_1$ , and Debye parameter  $\kappa_1$ , separated by an intervening region (2), with dielectric constant  $\epsilon_2$ , Debye parameter  $\kappa_2$ , and depth  $2R$ . Two infinite sheets of charge (S, in xy plane), with surface charge density  $\sigma$ , are placed in region 1, symmetrically on both sides of region 2, at distance  $\delta r$  from the two interfaces. Here we derive an analytical expression for the surface charge density  $\sigma$  as a function of  $\delta r$  and  $2R$ .

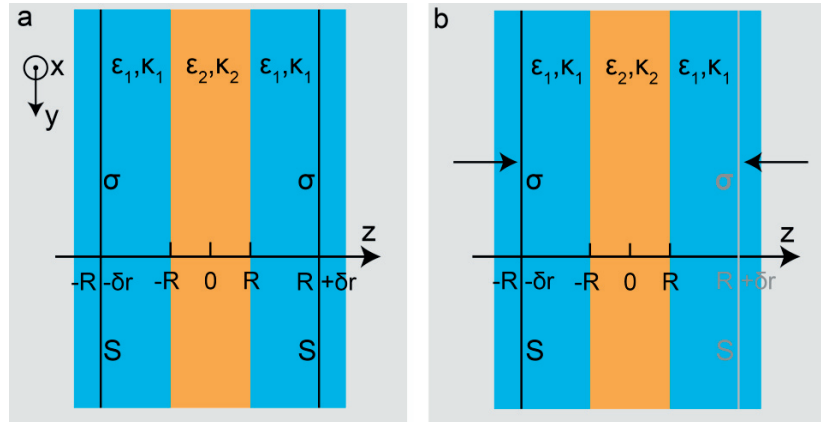


**Figure 3.5: Geometry of Interest.** (a) Two infinite sheets (S) each with charge density  $\sigma$ , normal to the  $z$ -axis, reside in a medium with dielectric constant  $\epsilon_1$ , and Debye screening parameter  $\kappa_1$ . Equidistant from these two sheets is a slab of material with a dielectric constant  $\epsilon_2$ , and Debye screening parameter  $\kappa_2$ . The width of the slab is  $2R$ , and the distance of each sheet from the nearest dielectric boundary is  $\delta r$ . (b) Same as (a), only that the sheet on the right side has been removed. The grey line indicates the previous position of S with charge surface density  $\sigma$ .

We begin by deriving an expression for the energy required to create the two charged sheets. For a charge density  $\sigma$ , the energy required to create a sheet of area  $A$  is proportional to the energy needed to bring a single ion to one of the surfaces, from a position infinitely far away from this surface. This process requires the ion to do work because of the electric field due to (1) the charged sheet on the same side of the dielectric boundary, and (2) the sheet on the opposite side of the boundary. The superposition principle can be used to simplify this problem: the energy cost is the same as that required to bring one ion from  $z = -\infty$  to  $z = -R - \delta r$ , and to bring another ion from  $z = +\infty$  to  $z = +R + \delta r$ , in the presence of a single charged plate at  $z = -R - \delta r$  (see Fig. 3.5b). This problem can now be

divided into four regions. For each of these we can write and solve a linearized Poisson-Boltzmann equation (LPBE) for the electrostatic potential  $V(z)$ :

$$z \leq -R - \delta r \quad \Rightarrow V_1''(z) = \kappa_1^2 V_1(z) \quad \Rightarrow V_1(z) = a_1 e^{\kappa_1 z} \quad (3.1)$$

$$-R - \delta r < z \leq -R \quad \Rightarrow V_2''(z) = \kappa_1^2 V_2(z) \quad \Rightarrow V_2(z) = a_2 e^{\kappa_1 z} + b_2 e^{-\kappa_1 z} \quad (3.2)$$

$$-R < z \leq R \quad \Rightarrow V_3''(z) = \kappa_2^2 V_3(z) \quad \Rightarrow V_3(z) = a_3 e^{\kappa_2 z} + b_3 e^{-\kappa_2 z} \quad (3.3)$$

$$R < z \quad \Rightarrow V_4''(z) = \kappa_1^2 V_4(z) \quad \Rightarrow V_4(z) = a_4 e^{-\kappa_1 z} \quad (3.4)$$

The coefficients  $b_1$  and  $a_4$  are zero because the potential must vanish as  $z \rightarrow \pm\infty$ . This means that there are six unknowns, for whom we have six boundary conditions: the potential must be continuous along the three boundaries, and the difference in the dielectric displacement  $D(z) = \epsilon(z)E(z)$ , when crossing a boundary, is equal to the charge density on that boundary. These equations can be solved to give the potential for all values of  $z$ , from which we find that the potential for one ion at the surface of a sheet in the two-sheet system of Fig. 3.5a is:

$$V_{sheet} = V_1(-R - \delta r) + V_4(+R + \delta r).$$

If we take a portion of these sheets with area  $A$ , then the energy of this portion is  $U_{sheet} = \frac{1}{2} A \sigma V_{sheet}$ . For the sake of a concrete example, we set  $U_{sheet} = N k_B T$ , where  $N = \sigma A / Z e$  is the total number of charges on this sheet ( $Z$  is the charge of the ions in the units of electron charge  $e$ ): that is, the energy of each ion is equal to the thermal energy. This gives us an equation for  $\sigma$ , which can be solved to find

$$\sigma = \frac{\epsilon_1 \kappa_1 k_B T}{e} \frac{4}{Z} \left[ 1 + e^{-2\kappa_1 \delta r} \left( 1 - \frac{2\kappa_2}{\kappa_2 + (\epsilon_1/\epsilon_2) \coth(\kappa_2 R)} \right) \right]^{-1}. \quad (3.5)$$

From Eq. (S1) we see that, if  $\kappa_2 = 0$  (if there are not any ions in region 2), Eq. (S1) is reduced to  $\sigma = \frac{\epsilon_1 \kappa_1 k_B T}{e} \frac{4}{Z} [1 + e^{-2\kappa_1 \delta r}]^{-1}$ . This means that, if the intervening dielectric does not give rise to Debye screening, then the entire system behaves as though this dielectric was absent. In this case the electric field in region 2 will be constant, and will simply undergo a 'jump' when going from  $\epsilon_1$  to  $\epsilon_2$  (due to dielectric difference): when it goes back from  $\epsilon_2$  to  $\epsilon_1$ , on the other side, it will jump back to its value before entering region 2, and will continue as though the region was not there.

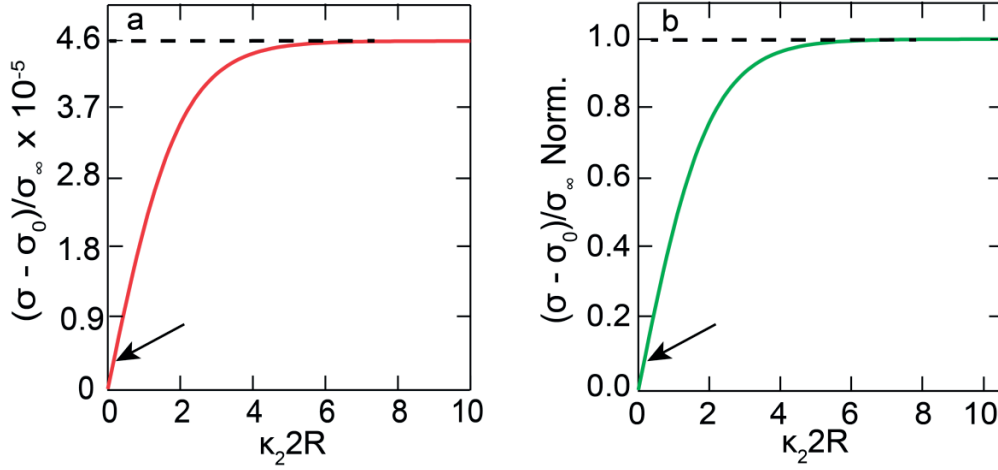


**Figure 3.6: Surface Charge Densities on Sheet S.** (a) Normalized relative surface charge density  $\sigma$  of a system comprising two charged sheets S (as shown in Fig. 3.5a), as a function of the depth  $2R$  of the intervening dielectric with constant  $\epsilon_2$ .  $\sigma_0$  is the charge density value for  $R = 0$  (absence of intervening dielectric) and is used as a reference value. The dashed line indicates the limiting surface charge density at large  $R$ . (b) Same as (a), but normalized to the maximal value. The values used in Eq. S1 for the plots are the respective ones of hexadecane nanodroplets ( $\epsilon_2 = 2$ ) in water ( $\epsilon_1 = 78$ ) stabilized with monovalent ions ( $Z=1$ ). The ionic strength in water is  $\sim 10$  mM with  $\kappa_1 = 0.33 \text{ nm}^{-1}$  ( $1/\kappa_1 = 3 \text{ nm}$ ), the ionic strength in the oil phase is  $\sim 1$  nM with  $\kappa_2 = 0.67 \text{ } \mu\text{m}^{-1}$  ( $1/\kappa_2 = 1.49 \text{ } \mu\text{m}$ ) and  $\delta r = 3 \text{ } \text{\AA}$ . The arrows indicate the region of  $\kappa_2 2R$  values corresponding to the droplets under study, with radius  $R$  in the range  $45 \text{ nm} < R < 125 \text{ nm}$ .

If  $\kappa_2 > 0$ , then the depth  $2R$  of the intervening region will affect the surface charge density, as shown in Fig. 3.6. Here  $(\sigma - \sigma_0)/\sigma_\infty$  is plotted over  $\kappa_2 2R$ , where  $\sigma_0$  is the surface charge density for  $R = 0$ , or else, when the dielectric region with  $\epsilon_2$  and  $\kappa_2$  is absent and  $\sigma_\infty$  is the surface charge density for  $R \rightarrow \infty$ , or else, when the dielectric region with  $\epsilon_1$  and  $\kappa_1$  is absent. It shows that, for larger  $R$  the energy of a charge at the position of the sheet will decrease for the same surface density, because the field due to the sheet on the opposite side is screened. So  $\sigma$  will increase to give the same energy  $Nk_B T$ .

### 3.4.2 DLVO theory predictions

In this section we discuss the predictions of the well-established DLVO theory of colloidal stability for the emulsion systems studied in Chapter. 3. Briefly, the DLVO theory describes the interaction between charged surfaces through a liquid medium by taking into account both the effect of the van der Waals attraction and the electrostatic repulsion due to the double layer of counterions formed at each surface. Due to relevance, here we focused on the case of two identical oil spheres interacting through water. However, Ref. <sup>14</sup> provides a quite nice exploration of various geometrical considerations. As described there, the double-layer



interaction depends strongly on the ionic strength in solution. However, the van der Waals interaction/pair potential is largely insensitive to variations in electrolyte concentration and pH, and so may be considered fixed in a first approximation.

The pair potential (interaction energy) of two identical spheres of radius  $R$  at distance  $D$  in an aqueous electrolyte solution with Debye length  $1/\kappa$  is given by

$$W(D) = \frac{1}{2} RZ e^{-\kappa D} - \frac{AR}{12D} . \quad (3.6)$$

The first term describes the double-layer interaction and  $Z$  is the interaction constant equal to

$$Z = 64\pi\epsilon_0\epsilon(kT/e)^2 \tanh^2(e\psi_0/4kT) \quad (3.7)$$

where  $\psi_0$  is the surface potential of the spheres. For an aqueous solution at 24 °C, i.e. the temperature at which all experiments of SFS and SHS, as well as the electrophoretic mobility measurements took place, Eq. (3.7) takes the value

$$Z = 9.22 \times 10^{-11} \tanh^2(\psi_0/103) \text{ J/m}^{-1} \quad (3.8)$$

with  $\psi_0$  expressed in mV. The second term of Eq. (3.6) describes the attractive van der Waals forces through the Hamaker constant  $A$ . For an oil (hexadecane)/water emulsion, like the ones studied in Chapter 3, the Hamaker constant can be calculated as follows (Eq. 13.16 in Ref. <sup>14</sup>)

$$A = \frac{3}{4} kT \left( \frac{\epsilon_{oil} - \epsilon_{water}}{\epsilon_{oil} + \epsilon_{water}} \right)^2 + \frac{3h\nu_e}{16\sqrt{2}} \frac{(n_{oil}^2 - n_{water}^2)^2}{(n_{oil}^2 + n_{water}^2)^{3/2}} \quad (3.9)$$

with  $\epsilon_{oil} = \epsilon_{hexadecane} = 2.09$ ,  $\epsilon_{water} = 78$ ,  $n_{oil} = n_{hexadecane} = 1.43$ ,  $n_{water} = 1.33$  and  $\nu_e$  is the main electronic absorption frequency, typically in the UV around  $3 \times 10^{15} \text{ s}^{-1}$ . In this way a Hamaker constant of  $0.55 \times 10^{-20} \text{ J}$  is calculated.

A qualitative comparison is possible between the DLVO theory calculations and our experimental results by employing Eq. (3.6) and (3.8) for our experimental values. Experimentally, though, we can only measure the  $\zeta$ -potential instead of surface potential ( $\psi_0$ ) values and hydrodynamic radius instead of the radius of the oil phase of the nanodroplets. As such, the DLVO calculations conducted here refer to the system shown in Fig. (3.7) and  $D$  is the distance between the two slipping planes of the oil nanodroplets in water. (Hydrodynamic radius and  $\zeta$ -potential measurements were discussed in detail in Sections 2.3.3. and 2.3.4 of this work respectively.) This discrepancy is not a fundamental problem as

the experimental values used reflect better what actually happens in reality. Specifically, each nanodroplet moves in the aqueous solution with an ionic atmosphere around it delimited by the slipping plane, and each other nanodroplet ‘sees’ this moving volume as a larger droplet with hydrodynamic radius and  $\zeta$ -potential when trying to approach closer.

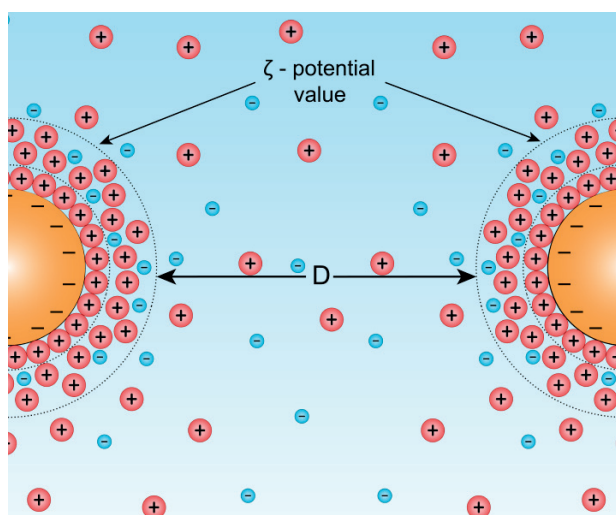


**Figure 3.7: Ion distribution around two approaching particles in solution.** Sketch of the ionic distribution around two approaching negatively charged droplets in an aqueous ionic solution. The same applies for positively charged droplets with the inversion of the signs of all charges shown in the figure. The  $\zeta$ -potential value is measured at the slipping plane of the droplets and  $D$  is the distance between two slipping planes. Graphic adopted from [https://commons.wikimedia.org/wiki/File:Diagram\\_of\\_zeta\\_potential\\_and\\_slipping\\_planeV2.svg](https://commons.wikimedia.org/wiki/File:Diagram_of_zeta_potential_and_slipping_planeV2.svg) by Mjones1984 and Larryisgood.

In this section, for the calculations presented in Fig. 3.8, we assumed a constant hydrodynamic radius of 100 nm for all nanodroplets and a constant a value of Hamaker constant of  $0.55 \times 10^{-20}$  J. Although the exact value of the Hamaker constant is not known, the calculated value is in the correct order of magnitude based on values reported in Section 14.22 of Ref. <sup>14</sup>.

**Table 3.2: Fitting parameters for DLVO pair potentials for nanodroplets stabilized with differently charged surfactants.** The values are used for the calculations presented in Fig. 3.8a and 3.8b.

Component(s)	Ionic strength (mM)	Debye Length $1/\kappa$ (nm)	$\zeta$ -potential (mV)
8 mM DS <sup>-</sup>	8	3.4	$-116 \pm 7$
8 mM DS <sup>-</sup> + 30 mM NaCl	38	1.56	$-64.1 \pm 7$
15 mM DTA <sup>+</sup>	15	2.48	$71.6 \pm 7$
20 mM hexanol	20	2.15	$-54 \pm 7$

Table 3.2 presents the value of ionic strength, Debye length and  $\zeta$ -potential used for the calculation of the pair potentials presented in Fig. 3.8 for each of the system stabilized with a different surfactant in the presence and absence of salt.

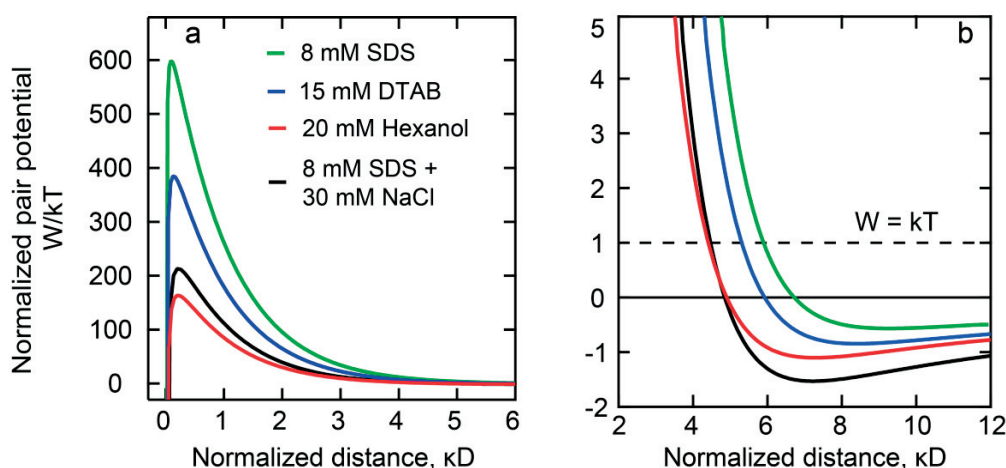


**Figure 3.8: DLVO pair potentials of surfactant stabilized hexadecane nanodroplets in water.** Normalized (by the thermal energy) pair potential over normalized distance between their slipping planes (by the Debye length) for hexadecane nanodroplets in water stabilized with 8 mM SDS without extra electrolyte (green) or with the addition of 30 mM NaCl (black), 15 mM DTAB (blue) or 20 mM hexanol (red). a) Overall trend of the pair potential between 0 and 9 Debye lengths. b) Pair potential between 2 and 12 Debye lengths, over which range it becomes equal to  $kT$  and a local minimum appears. Equations 3.6 and 3.8 were employed with the values presented in Table 3.2 and values of radius  $R = 100$  nm and Hamaker constant  $A = 0.55 \times 10^{-20}$  J for all systems.

The theoretically calculated pair potentials are presented in Fig. 3.8. Specifically, Fig. 3.8 displays the pair potential of two hexadecane nanodroplets in an aqueous solution stabilized with different surfactants normalized by the thermal energy ( $W/kT$ ) over the distance between their slipping planes expressed in Debye lengths ( $\kappa D$ ). Figure 3.8a displays normalized pair potentials for distances  $D$  between 0 and 6 Debye lengths for a comparison of the overall trend. Fig. 3.8b shows the pair potentials for distances between 2 and 12 Debye lengths, where a secondary minimum appears and pair potentials become comparable to the thermal energy  $kT$ . Starting from Fig. 3.8a, the maximum value for each line is called the *energy barrier*, for particles to approach one another. When the emulsion destabilizes, the pair potential of the droplets becomes attractive enough to overcome the energy barrier. In this case, the system results in its primary minimum at  $D \approx 0$  after droplet aggregation/coagulation and thermodynamic stability is achieved. As a result, the higher the energy barrier the more stable an emulsion is expected to be. In Fig. 3.8a, it can be seen that for 8 mM SDS (without NaCl, green) stabilized emulsions the energy barrier is higher than for the 15 mM DTAB stabilized emulsions (blue), followed by the 20 mM hexanol

stabilized emulsions (hexanol). This DLVO predicted suggested trend is indeed verified by our experimental results, as discussed in detail in Chapter 3. However, when 30 mM NaCl is added in the SDS stabilized system (black) the pair potential significantly drops and becomes comparable to the hexanol stabilized droplets (red line). As such, DLVO theory predicts that the stability of SDS stabilized emulsions in an aqueous solution of 30 mM NaCl will be comparable to hexanol stabilized emulsions. However, based on our experience with the sample preparation and the observation of their size distribution with DLS measurements over long periods of time, SDS stabilized emulsions did not considerably differ in the absence or presence of NaCl and, in any case, was considerably better than the hexanol stabilized ones. It is, thus, suggested that the mean field theory and continuum model adopted in the DLVO theory cannot capture molecular level information of the interfacial structure of nanoemulsions that have shown to be crucial for the nanodroplet stability. This is clearly demonstrated in Section 5.4.1, where DLVO prediction are compared with experimental results for positively charged nanodroplets in the presence of different electrolytes. In Fig. 3.8b it can be seen that for all tested systems a secondary minimum appears between 5 and 8 Debye lengths. For a system that is kinetically stable (like the nanodroplets studied in the present work), the nanodroplets will sit either in the secondary minimum or will remain totally dispersed in the solution for as long as kinetic stability is maintained. In 2% v/v oil in water emulsions with nanodroplets of radius of  $\sim 100$  nm, and assuming homogeneously distributed spherical droplets in the whole sample volume, the average distance of the centre of two droplets in solution is estimated to be 350 nm, corresponding to a distance  $D$  of 150 nm. Such a value corresponds to 50 – 100 Debye lengths (50 -100  $\kappa D$ ).

### 3.5 References

1. Taly, V., Kelly, B. T. & Griffiths, A. D. Droplets as microreactors for high-throughput biology. *ChemBioChem* **8** (3), 263-272 (2007).
2. Teh, S., Lin, R., Hung, L. & Lee, A. P. Droplet microfluidics. *Lab Chip* **8** (2), 198-220 (2008).
3. Ralf, S., Martin, B., Thomas, P. & Stephan, H. Droplet based microfluidics. *Rep. Prog. Phys.* **75** (1), 016601 (2012).
4. Guo, M. T., Rotem, A., Heyman, J. A. & Weitz, D. A. Droplet microfluidics for high-throughput biological assays. *Lab Chip* **12** (12), 2146-2155 (2012).
5. Amstad, E., Gopinadhan, M., Holtze, C., Osuji, C. O., Brenner, M. P., Spaepen, F. & Weitz, D. A. Production of amorphous nanoparticles by supersonic spray-drying with a microfluidic nebulator. *Science* **349** (6251), 956-960 (2015).
6. Grzybowski, B. A. & Huck, W. T. S. The nanotechnology of life-inspired systems. *Nat. Nanotechnol.* **11** (7), 585-592 (2016).
7. Miller, O. J., Harrak, A. E., Mangeat, T., Baret, J.-C., Frenz, L., Debs, B. E., Mayot, E., Samuels, M. L., Rooney, E. K., Dieu, P., Galvan, M., Link, D. R. & Griffiths, A. D. High-resolution dose-response screening using droplet-based microfluidics. *Proc. Natl. Acad. Sci. U. S. A.* **109** (2), 378-383 (2012).
8. Pekin, D., Skhiri, Y., Baret, J.-C., Le Corre, D., Mazutis, L., Ben Salem, C., Millot, F., El Harrak, A., Hutchison, J. B., Larson, J. W., Link, D. R., Laurent-Puig, P., Griffiths, A. D. & Taly, V. Quantitative and sensitive detection of rare mutations using droplet-based microfluidics. *Lab Chip* **11** (13), 2156-2166 (2011).
9. Debs, B. E., Utharala, R., Balyasnikova, I. V., Griffiths, A. D. & Merten, C. A. Functional single-cell hybridoma screening using droplet-based microfluidics. *Proc. Natl. Acad. Sci. U. S. A.* **109** (29), 11570-11575 (2012).
10. Sjostrom, S. L., Bai, Y., Huang, M., Liu, Z., Nielsen, J., Joensson, H. N. & Andersson Svahn, H. High-throughput screening for industrial enzyme production hosts by droplet microfluidics. *Lab Chip* **14** (4), 806-813 (2014).
11. McClements, J. D. Critical review of techniques and methodologies for characterization of emulsion stability. *Crit. Rev. Food Sci. Nutr.* **47**, 611-649 (2007).
12. Hunter, R. J. *Foundations of colloid science* (Oxford University Press, New York, 2001).
13. Fischer, E. K. & Harkins, W. D. Monomolecular films, the liquid-liquid interface and the stability of emulsions. *J. Phys. Chem.* **36**, 98-110 (1932).
14. Israelachvili, J. N. *Intermolecular and surface forces* (Academic Press, San Diego, 2011).
15. Atkins, P. & De Paula, J. *Atkins' physical chemistry* (Oxford University Press, Oxford, 2010).
16. Lyklema, J. *Fundamentals of interface and colloid science: Soft colloids* (Elsevier Science, Amsterdam, 2005).
17. Adamson, A. W. & Gast, A. P. *Physical chemistry of surfaces* (Wiley, New York, 1997).
18. Als-Nielsen, J. & McMorrow, D. *Elements of modern X-ray physics* (Wiley, Hoboken, 2011).

19. Berge, B., Konovalov, O., Lajzerowicz, J., Renault, A., Rieu, J. P., Vallade, M., Als-Nielsen, J., Grubel, G. & Legrand, J. F. Melting of short 1-alcohol monolayers on water: Thermodynamics and X-ray scattering studies. *Phys. Rev. Lett.* **73** (12), 1652-1655 (1994).
20. Lu, J. R., Marrocco, A., Su, T. J., Thomas, R. K. & Penfold, J. Adsorption of dodecyl sulfate surfactants with monovalent metal counterions at the air-water interface studied by neutron reflection and surface tension. *J. Colloid Interface Sci.* **158** (2), 303-316 (1993).
21. Sloutskin, E., Sapir, Z., Bain, C. D., Lei, Q., Wilkinson, K. M., Tamam, L., Deutsch, M. & Ocko, B. M. Wetting, mixing, and phase transitions in Langmuir-Gibbs films. *Phys. Rev. Lett.* **99**, 136102-136104 (2007).
22. Mason, T. G., Wilking, J. N., Meleson, K., Chang, C. B. & Graves, S. M. Nanoemulsions: Formation, structure, and physical properties. *J. Phys.: Condens. Matter* **18**, R635-R666 (2006).
23. Guyot-Sionnest, P., Hunt, J. H. & Shen, Y. R. Sum-frequency vibrational spectroscopy of a Langmuir film: Study of molecular-orientation of a two dimensional system. *Phys. Rev. Lett.* **59** (14), 1597-1600 (1987).
24. Harris, A. L., Chidsey, C. E. D., Levinos, N. J. & Loiacono, D. N. Monolayer vibrational spectroscopy by infrared-visible sum generation at metal and semiconductor surfaces. *Chem. Phys. Lett.* **141**, 350-356 (1987).
25. Conboy, J. C., Messmer, M. C. & Richmond, G. L. Dependence of alkyl chain conformation of simple ionic surfactants on head group functionality as studied by vibrational sum-frequency spectroscopy. *J. Phys. Chem. B* **101** (34), 6724-6733 (1997).
26. Knock, M. M., Bell, G. R., Hill, E. K., Turner, H. J. & Bain, C. D. Sum-frequency spectroscopy of surfactant monolayers at the oil-water interface. *J. Phys. Chem. B* **107**, 10801-10814 (2003).
27. Messmer, M. C., Conboy, J. C. & Richmond, G. L. Observation of molecular ordering at the liquid-liquid interface by resonant sum-frequency generation. *J. Am. Chem. Soc.* **117**, 8039-8040 (1995).
28. Richmond, G. L. Structure and bonding of molecules at aqueous surfaces. *Annu. Rev. Phys. Chem.* **52**, 357-389 (2001).
29. De Aguiar, H. B., De Beer, A. G. F., Strader, M. L. & Roke, S. The interfacial tension of nanoscopic oil droplets in water is hardly affected by SDS surfactant. *J. Am. Chem. Soc.* **132**, 2122-2123 (2010).
30. Smolentsev, N., Smit, W. J., Bakker, H. J. & Roke, S. The interfacial structure of water droplets in a hydrophobic liquid. *Nat. Commun.* **8**, 15548 (2017).
31. Kurylowicz, M., Paulin, H., Mogyoros, J., Giuliani, M. & Dutcher, J. R. The effect of nanoscale surface curvature on the oligomerization of surface-bound proteins. *J. Royal Soc. Interface* **11** (94), (2014).
32. Jackson, A. M., Myerson, J. W. & Stellacci, F. Spontaneous assembly of subnanometre-ordered domains in the ligand shell of monolayer-protected nanoparticles. *Nat. Mater.* **3** (5), 330-336 (2004).

33. Long, J. A., Rankin, B. M. & Ben-Amotz, D. Micelle structure and hydrophobic hydration. *J. Am. Chem. Soc.* **137** (33), 10809-10815 (2015).
34. Smolentsev, N., Lütgebaucks, C., Okur, H. I., De Beer, A. G. F. & Roke, S. Intermolecular headgroup interaction and hydration as driving forces for lipid transmembrane asymmetry. *J. Am. Chem. Soc.* **138** (12), 4053-4060 (2016).
35. Roke, S., Roeterdink, W. G., Wijnhoven, J. E. G. J., Petukhov, A. V., Kleyn, A. W. & Bonn, M. Vibrational sum frequency scattering from a submicron suspension. *Phys. Rev. Lett.* **91** (25), 258302 (2003).
36. Roke, S. & Gonella, G. Nonlinear light scattering and spectroscopy of particles and droplets in liquids. *Annu. Rev. Phys. Chem.* **63**, 353-378 (2012).
37. Schürer, B., Wunderlich, S., Sauerbeck, C., Peschel, U. & Peukert, W. Probing colloidal interfaces by angle-resolved second harmonic light scattering. *Phys. Rev. B* **82** (24), 241404-241404 (2010).
38. Wang, H., Yan, E. C. Y., Borguet, E. & Eisenthal, K. B. Second harmonic generation from the surface of centrosymmetric particles in bulk solution. *Chem. Phys. Lett.* **259** (1-2), 15-20 (1996).
39. De Aguiar, H. B., Samson, J. S. & Roke, S. Probing nanoscopic droplet interfaces in aqueous solution with vibrational sum-frequency scattering: A study of the effects of path length, droplet density and pulse energy. *Chem. Phys. Lett.* **512**, 76-80 (2011).
40. De Beer, A. G. F. & Roke, S. Obtaining molecular orientation from second harmonic and sum frequency scattering experiments in water: Angular distribution and polarization dependence. *J. Chem. Phys.* **132** (23), 234702 (2010).
41. Johansson, P. K. & Koelsch, P. Vibrational sum-frequency scattering for detailed studies of collagen fibers in aqueous environments. *J. Am. Chem. Soc.* **136** (39), 13598-13601 (2014).
42. Petersen, P. B. & Saykally, R. J. Probing the interfacial structure of aqueous electrolytes with femtosecond second harmonic generation spectroscopy. *J. Phys. Chem. B* **110** (29), 14060-14073 (2006).
43. Scheu, R., Chen, Y. X., Subinya, M. & Roke, S. Stern layer formation induced by hydrophobic interactions: A molecular level study. *J. Am. Chem. Soc.* **135** (51), 19330-19335 (2013).
44. Mukerjee, P. M. K. J. Critical micelle concentrations of aqueous surfactant systems *Natl. Stand. Ref. Data Ser. (U. S., Natl. Bur. Stand.)* **36**, 1-222 (1971).
45. Stephenson, R., Stuart, J. & Tabak, M. Mutual solubility of water and aliphatic alcohols. *J. Chem. Eng. Data* **29** (3), 287-290 (1984).
46. Chen, Y. X., Jena, K. C. & Roke, S. From hydrophobic to hydrophilic: The structure and density of the hexadecane droplet/alkanol/water interface. *J. Phys. Chem. C* **119** (31), 17725-17734 (2015).
47. Wang, H. F., Yan, E. C. Y., Liu, Y. & Eisenthal, K. B. Energetics and population of molecules at microscopic liquid and solid surfaces. *J. Phys. Chem. B* **102**, 4446-4450 (1998).



48. De Aguiar, H. B., Strader, M. L., De Beer, A. G. F. & Roke, S. Surface structure of sodium dodecyl sulfate surfactant and oil at the oil-in-water droplet liquid/liquid interface: A manifestation of a non-equilibrium surface state. *J. Phys. Chem. B* **115**, 2970-2978 (2011).
49. Cederquist, K. B. & Keating, C. D. Curvature effects in DNA: Au nanoparticle conjugates. *ACS Nano* **3** (2), 256-260 (2009).
50. Hunter, R. J. *Zeta potential in colloid science : Principles and applications* (Academic Press, London; New York, 1981).
51. Scheu, R., Chen, Y. X., De Aguiar, H. B., Rankin, B. M., Ben-Amotz, D. & Roke, S. Specific ion effects in amphiphile hydration and interface stabilization. *J. Am. Chem. Soc.* **136** (5), 2040-2047 (2014).
52. Vacha, R. & Roke, S. Sodium dodecyl sulfate at water-hydrophobic interfaces: A simulation study. *J. Phys. Chem. B* **116** (39), 11936-11942 (2012).
53. Scheu, R., Rankin, B. M., Chen, Y. X., Jena, K. C., Ben-Amotz, D. & Roke, S. Charge asymmetry at aqueous hydrophobic interfaces and hydration shells. *Angew. Chem., Int. Ed.* **53** (36), 9560-9563 (2014).
54. Davis, J. G., Gierszal, K. P., Wang, P. & Ben-Amotz, D. Water structural transformation at molecular hydrophobic interfaces. *Nature* **491** (7425), 582-585 (2012).
55. Fega, K. R., Wilcox, D. S. & Ben-Amotz, D. Application of Raman multivariate curve resolution to solvation-shell spectroscopy. *Appl. Spectrosc.* **66** (3), 282-288 (2012).
56. Fayer, M. D. & Levinger, N. E. Analysis of water in confined geometries and at interfaces. *Annu. Rev. Anal. Chem.* **3** (1), 89-107 (2010).
57. Rehfeld, S. J. Adsorption of sodium dodecyl sulfate at various hydrocarbon-water interfaces. *J. Phys. Chem.* **71**, 738-745 (1967).
58. Möhwald, H. Surfactant layers at water surfaces. *Rep. Prog. Phys.* **56** (5), 653 (1993).
59. Schlossman, M. L. & Tikhonov, A. M. Molecular ordering and phase behavior of surfactants at water-oil interfaces as probed by x-ray surface scattering. *Annu. Rev. Phys. Chem.* **59**, 153-177 (2008).
60. Manning, G. S. Counterion condensation on charged spheres, cylinders, and planes. *J. Phys. Chem. B* **111** (29), 8554-8559 (2007).



## Chapter 4: The interfacial structure of nanometer- and micrometer-sized oil and water droplets stabilized with SDS and Span80

*In this work we provide a direct link between the stability of micrometer-sized and nanometer-sized droplets and their interfacial structure by employing a multi-instrumental approach comprised of the surface-sensitive technique of sum frequency scattering as well as dynamic light scattering and microscopy. We monitor the stability of oil-in-water and water-in-oil emulsions, and the structure of surfactants at the oil/water nano-interface, when stabilized with an oil-soluble neutral surfactant (Span80), a water-soluble anionic surfactant (sodium dodecyl sulfate, SDS), or with a combination of the two. Micron-sized droplets are found to be stabilized only when a surfactant soluble in the continuous phase is present in the system, in agreement with what is traditionally observed empirically. Surprisingly, the nanodroplets behave differently. Both oil and water nanodroplets can be stabilized by the same (neutral Span80) surfactant, but with different surface structures. A combination of SDS and Span80 also suffices, but for the case of water droplets, the strongly amphiphilic SDS molecules are not detected at the interface. For the case of oil droplets, both surfactants are at the interface but do not structurally affect one another. Thus, it appears that empirical rules such as the Bancroft rule, the HLB scale and the Surfactant Affinity Difference work best when emulsion droplets exceed a certain size, probably due to a different balance of interactions on different length scales.*

*For the work presented in this chapter, Evangelia Zdrali performed SFS measurements on nanometer-sized and micrometer-sized oil droplets in water, and related data analysis. Nikolay Smolentsev performed SFS measurements on nanometer-sized water droplets in oil and related data analysis.*

*Gianluca Etienne and Prof. Esther Amstad (from the Soft Materials Laboratory at EPFL) performed the preparation of the micrometer-sized droplets and the characterization of their stability with microscopy.*

## 4.1 Introduction

Emulsions are extensively used in a variety of industrial products, including food, cosmetic, and pharmaceutical goods. In addition, they are employed as miniature reaction vessels, for example to conduct biochemical reactions or to perform high throughput screening assays<sup>1</sup>.<sup>2</sup> A basic requirement for their efficient use is the preparation of stable emulsions. There are two different views on emulsion stability within the material science research field: For the physical chemistry community, the identity of the two liquid phases, and their interface, including the mechanism by which surfactants impart stability to emulsion drops, are of highest importance. Therefore, special attention is given to the interfacial properties of droplets. In contrast, the community studying colloids considers emulsion droplets as one homogeneous entity and attributes a crucial role to their arrangement and interactions.

Emulsion droplets are often stabilized with surfactants to prevent their coalescence by increasing the repulsive barrier between the droplets<sup>3</sup>. To impart good stability to emulsion drops, appropriate surfactants are selected according to empirical criteria; this choice depends on the composition of the fluids, if oil-in-water or water-in-oil emulsions are needed, the ratio of water-to-oil,<sup>4</sup> and the temperature and pressure<sup>3,5-11</sup>. The choice of the appropriate surfactant is often based on empirical rules such as the Bancroft rule<sup>5</sup> or the surfactant affinity difference (SAD), the difference in surfactant chemical potentials between oil and water phase. The Bancroft rule states that surfactants should be dispersed in the continuous phase, in agreement with the Hydrophile – Lipophile – Balance (HLB) scale<sup>12</sup>. The SAD depends on a number of experimental observables as well as structural information, such as the interfacial tension, the computed surfactant curvature, the cloud points of the surfactant in solution, the electrolyte concentration, the amount of carbon in the surfactant, the temperature<sup>13</sup>. Accordingly, water-soluble, hydrophilic surfactants are expected to stabilize oil-in-water emulsions, while oil-soluble, hydrophobic surfactants stabilize water-in-oil emulsions. The basic idea behind these three empirical classifications is that when two emulsion droplets come in close proximity, a thin film of the continuous phase forms between them that prevents merging of the droplets<sup>11</sup>. Extensive studies have shown that such films are more stable if they comprise surfactants, which is the case if surfactants are dissolved in the continuous phase<sup>3</sup>. Indeed, stability data dating back to 1940s<sup>14, 15</sup> demonstrate the incapability of water-soluble or charged surfactants to stabilize water droplets in oil.

Even though emulsion stability is recognized to critically depend on the structural properties of the interfacial region and the interfacial interactions, the underlying mechanisms are still elusive on the molecular level. Emulsion stability is typically characterized by phase

inversion studies, phase separation, gravitational / centrifugal sedimentation, size distribution, nuclear magnetic resonance, ultrasound, optical microscopy and similar techniques.<sup>3, 16-18</sup> These techniques provide information on a macroscopic level, for example, they allow determining the number of phases present in the system, or the partitioning of surfactants in each phase. The necessary knowledge about the interfacial regions is inferred from studies on extended planar interfaces<sup>19-23</sup> or molecular dynamics simulations. However, if studies on planar systems could be used to characterize the interface of both water-in-oil and oil-in-water systems, then the empirical rules regarding emulsion stability should not hold. Indeed, recent studies employing advanced experimental spectroscopic techniques<sup>24</sup> reveal previously unexpected discrepancies between planar and droplet interfaces<sup>25, 26</sup>, demonstrating the need to link stability to droplet interfacial structure.

Here, we systematically study the effect of reversing the dispersed phase with the continuous phase on the stability of emulsions. In particular, we focus on the structure of surfactants adsorbed on droplet surfaces. We study oil-in-water and water-in-oil emulsions with droplets whose radius is on the order of several micrometers (~5-20  $\mu\text{m}$ ) and ten – hundred nanometers (~65-100 nm). These droplets are stabilized with either a neutral oil-soluble surfactant (Span80), a negatively charged water-soluble surfactant (sodium dodecyl sulfate, SDS), or a combination of the two. We characterize the surfactants at the liquid-liquid interface using a multi-instrumental approach that combines macroscopic data, from microscope images, with molecular level information, obtained with vibrational Sum Frequency Scattering (SFS)<sup>24, 27</sup>. SFS is a coherent surface spectroscopy that directly probes the structure of the surfactants present at the interface of the droplets. We find that the micrometer-sized droplets can be stabilized only with a surfactant that is dissolved in the continuous phase, in agreement with expectations based on empirical rules. For nanometer-sized droplets, the situation is different. Neutral surfactants stabilize the interface of all nanodroplet samples, irrespective of whether the surfactant is dissolved in the continuous or dispersed phase. The surface structures are different, however. If two surfactants coexist, the tendency of one to approach the interface is not altered by the presence of the other.

## 4.2 Results and discussion

To investigate the structure of surfactants at the surface of dispersed droplets, we employ oil droplets in water and water droplets in oil. Droplets are stabilized with 8 mM of the anionic water-soluble surfactant sodium dodecyl sulfate (SDS, cmc, of 8.25 mM at  $T = 293\text{ K}$ <sup>36</sup>), with 5 mM of the neutral oil-soluble surfactant Span80 (HLB value of 4.3), or with a combination of the two with the same concentrations. We compare the stability of nanometer-sized

droplets with that of micrometer-sized ones. During the preparation of the nanodroplet emulsions, SDS is dissolved in the water phase and Span80 in the hexadecane oil phase. Nanoemulsions contain ~ 1 vol. % of the dispersed phase that is constituted of droplets with radii of ~ 65 - 100 nm. To evaluate their stability, the droplet size distribution of nanoemulsions is measured with Dynamic Light Scattering (DLS). A sample is considered stable when the size distribution consists of a single peak with a polydispersity index (PDI) below 0.3.<sup>37</sup> Stable nanoemulsions were investigated with SFS. Emulsions with micrometer-sized droplets contain ~ 9 vol. % of dispersed phase that is composed of droplets with radii of ~ 5 - 20  $\mu\text{m}$ . The stability of these emulsions is characterized by comparing microscopy images of the microemulsions immediately after formation in a flow focusing microfluidic device with images taken within 0.2 ms after the droplets are getting in contact with each other. If droplets coalesce within such a short amount of time, we consider them to be unstable. The stability of micrometer-sized droplets was also tested by mixing the two phases containing the appropriate surfactant(s) by vortexing them for 30 s. If we observe a macroscopic phase separation within 8 h of storage, we consider the emulsions with micrometer-sized droplets as unstable.<sup>3</sup> If neither coalescence is microscopically detected nor phase separation is macroscopically observed, the emulsions are considered stable.

#### 4.2.1 Nanometer-sized oil-in-water emulsions

We performed SFS measurements on stable hexadecane nanometer-sized droplets in water to study the interfacial structure of surfactants adsorbed on the surface of nanodroplets. To determine if surfactants are present at the interface and to obtain information about their conformation, we make use of deuterated  $\text{d}_{34}$ -hexadecane as oil and monitor the vibrational modes of the surfactants only. Fig. 4.1 shows SFS spectra for a range of samples and vibrational modes. For Span80 molecules and/or hydrogenated (h-)  $\text{DS}^-$  anions, Fig. 4.1B-D and Fig. 4.1F demonstrate SFS spectra of the methyl ( $\text{CH}_3$ ) and methylene ( $\text{CH}_2$ ) stretch modes of the alkyl chains. Figure 4.1E reports the S-O symmetric stretch mode ( $\sim 1045 \text{ cm}^{-1}$ ) of the deuterated ( $\text{d}_{25}$ -)  $\text{DS}^-$  anions sulfate head group. The significant SFS intensity for Span80 in Fig. 4.1B shows that the neutral oil-soluble Span80 molecules populate the nanometer-sized droplet interface and stabilize the emulsion despite being dissolved in the aqueous dispersed phase. To test whether charged surfactants are also located at the oil droplet interface, we prepare nanoemulsions with SDS (8 mM) and measure the SFS intensity, as shown in Fig. 4.1C. The CH modes of the alkyl chains of the hydrogenated interfacial  $\text{DS}^-$  anions are clearly observed, indicating that SDS indeed adsorbs at the droplet interface. To test if one of the surfactants preferentially adsorbs at the interface, we stabilize

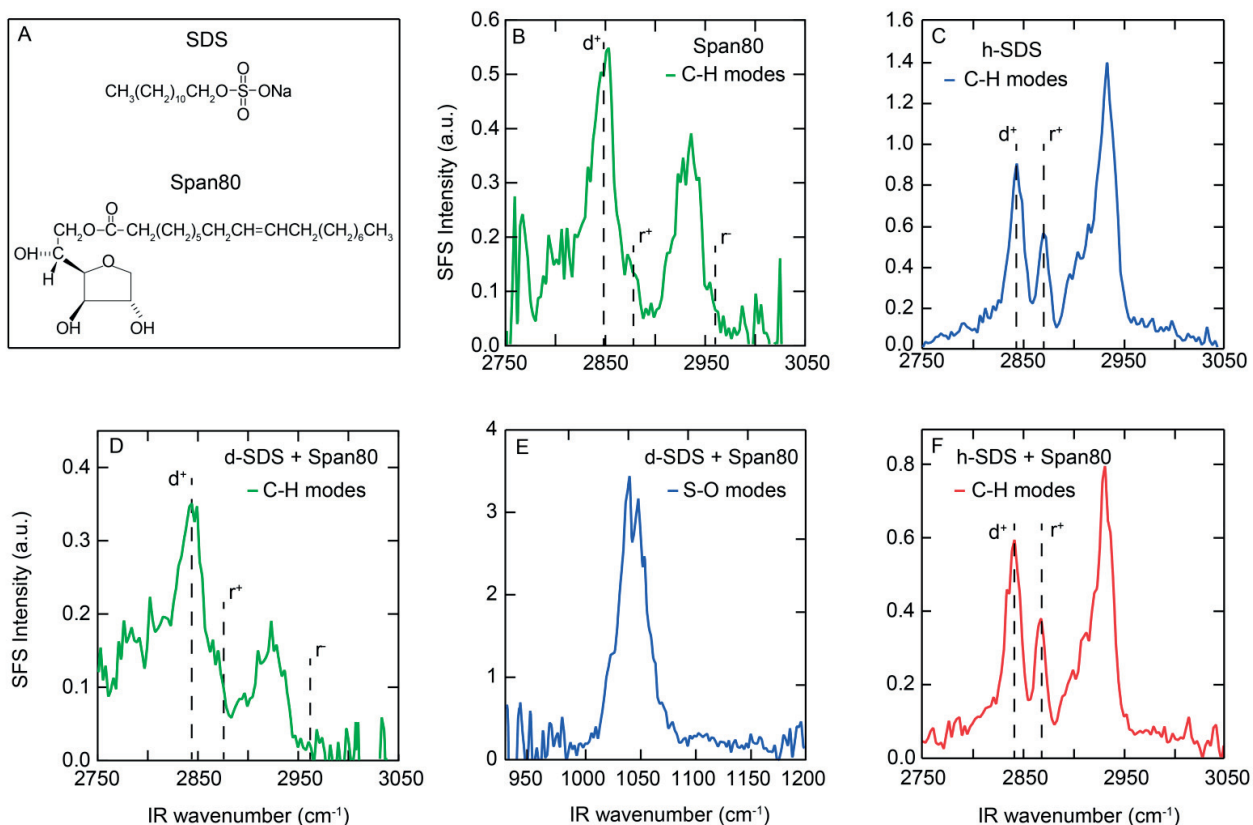


**Figure 4.1: Surface structure of surfactants stabilizing nanometer-sized oil droplets in water.** (A) Molecular structure of SDS (top) and Span80 (bottom). (B-F) Normalized SFS intensity spectra of the vibrational modes of surfactant molecules adsorbed at nanometer-sized droplets of  $\text{d}_{34}$ -hexadecane (1 vol. %) in  $\text{D}_2\text{O}$ . The surfactant(s) used to stabilize the system are shown at the top right corner of each panel and also indicate whether hydrogenated (h-) or deuterated (d-) SDS was employed. (B-D, F) CH stretch modes ( $\sim 2845 - 2965 \text{ cm}^{-1}$ ) of the methyl and methylene groups of the alkyl chains of the interfacial (B) Span80 molecules on droplets stabilized with 5 mM Span80, (C)  $\text{DS}^-$  anions on droplets stabilized with 8 mM SDS, (D) Span80 molecules on droplets stabilized with a combination of 5 mM Span80 and 8 mM  $\text{d}_{25}$ -SDS and (F) both Span80 and  $\text{DS}^-$  anions on droplets stabilized with a combination of 5 mM Span80 and 8 mM SDS. (E) Symmetric S-O stretch mode of the sulphate head group of interfacial  $\text{d}_{25}$ - $\text{DS}^-$  ( $\sim 1045 \text{ cm}^{-1}$ ) molecules on droplets stabilized with a combination of 5 mM Span80 and 8 mM SDS. Deuterated ( $\text{d}_{25}$ -) instead of hydrogenated (h-) SDS is used for (D) and (E) to isolate the CH modes of Span80 when combined with SDS. All SFS spectra were collected with the IR (VIS, SF) beam polarized parallel (perpendicular) to the scattering plane (SSP). The radius of the nanoemulsion and its PDI are (B) 100 nm and 0.27, (C) 65 nm and 0.15, (D, E) 70 nm and 0.14 and (F) 70 nm and 0.15.

$\text{d}_{34}$ -hexadecane nanometer-sized droplets with a combination of 8 mM  $\text{d}_{25}$ -SDS and 5 mM Span80, and use the S-O stretch mode and C-H stretch modes to track each surfactant separately. Figures 1D and 1E show the presence of CH stretch vibrational modes and S-O symmetric stretch modes, respectively, indicating the presence of both interfacial Span80 and SDS molecules. To obtain more information about the interfacial structure, we measure the SFS intensity of the CH modes from both  $\text{d}_{34}$ -hexadecane droplets that are stabilized

with Span80 molecules and h-DS<sup>-</sup> anions. The resulting SFS spectrum (Fig. 4.1F) shows a striking similarity to the spectrum in Fig. 4.1C. This similarity suggests that the SFS response is dominated by the alkyl chains of the interfacial DS<sup>-</sup> anions, with Span80 molecules contributing considerably less. To test if Span80 influences the SDS structure we measured of the S-O stretch mode with SSP and PPP polarizations, in the presence and absence of Span80. Figure 4.5 in the Appendix shows different SSP/PPP ratios, indicating that the configuration of the sulfate headgroup of the DS<sup>-</sup> anions is affected by the presence of Span80 at the interface. (See section 4.4.1 and Fig. 4.5 for more information). For the CH spectra, the positions of the symmetric CH<sub>2</sub> (d<sup>+</sup>, ~ 2850 cm<sup>-1</sup>), the symmetric CH<sub>3</sub> (r<sup>+</sup>, ~ 2875 cm<sup>-1</sup>), and the antisymmetric CH<sub>3</sub> (r<sup>-</sup>, ~ 2965 cm<sup>-1</sup>) stretch modes are indicated with dashed lines. The value of the amplitude ratio d<sup>+</sup>/r<sup>+</sup> is a common empirical indicator for the conformation of alkyl chains. When d<sup>+</sup>/r<sup>+</sup> ~ 0 the alkyl chains adopt an all-trans conformation, while a value of d<sup>+</sup>/r<sup>+</sup> >1 is an indicator of the presence of gauche defects.<sup>38</sup> We also note that for all observed SFS spectra obtained in the CH stretch mode region a value of d<sup>+</sup>/r<sup>+</sup> >1 is observed, indicating that in all cases the surfactant alkyl tails exhibit a conformation dominated by the presence of gauche defects.

## 4.2.2 Micrometer-sized oil-in-water emulsions

To test whether the droplet size influences the adsorption of surfactants, therefore droplet stability, we study hexadecane-in-water microemulsions stabilized with the same combinations of surfactants. Droplets of radii (R) ranging from 5 μm to 20 μm are prepared in a microfluidic flow focusing device (See Paragraph 2.4). To characterize the stability of microemulsions, we visualize droplets immediately after they entered the analysis chamber and 0.2 ms thereafter, when they have come in contact with each other, as shown in Fig. 4.2. Unstable droplets coalesce when they come in contact with each other; this results in changes in their number and size. Microscopy images suggest that droplets stabilized with SDS (Fig. 4.2A) or a combination of SDS and Span80 (Fig. 4.2C) are stable. By contrast, droplets stabilized with Span80 coalesce, as shown in Fig 2B. To test this finding further, we vortex a solution composed of 10% of the oil phase and 90% of the water phase, each one containing the appropriate surfactant and observe the resulting emulsion over 8 h. The microemulsions are considered to be stable when the lighter oil droplets gather at the top of the cuvette, forming a horizontal layer of droplets which covers the meniscus and scatters light, leaving the heavier water phase at the bottom, as was seen for emulsions stabilized with SDS or a combination of SDS and Span80. (Respective movies available if requested).

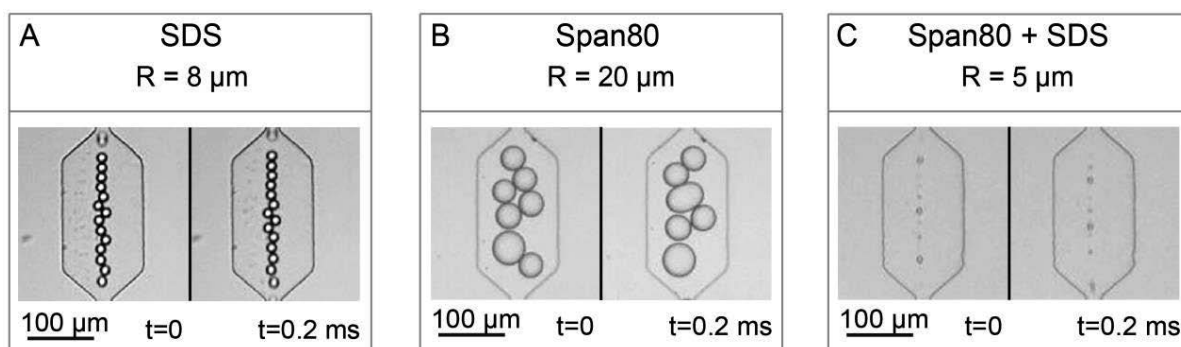


**Figure 4.2: Stability of micrometer-sized oil droplets in water.** Microscopy images of hexadecane micrometer-sized droplets in water (radius  $R = 5\text{--}20\ \mu\text{m}$ ) at  $t = 0$  (left panels) and  $t = 0.2\ \text{ms}$  (right panel), after the injection of droplets into the analysis chamber. Within the analysis chamber that is incorporated into the main channel downstream the flow focusing junction, droplets are slowed down and forced to contact each other. The systems are stabilized with (A) 10 mM SDS, (B) 5mM Span80, or (C) a combination of 10 mM SDS and 5 mM Span80.

By contrast, when emulsions are unstable, the two fluids phase separate and a clear meniscus forms between the two phases, as was observed for emulsions stabilized with Span80. (Respective movies available if requested.) These results are in good agreement with our molecular-level observation and confirm that micrometer-sized droplets stabilized with SDS (Fig. 2A) or a combination of SDS and Span80 (Fig. 2C) are stable, whereas microdroplets stabilized only with Span80 (Fig. 2B) are unstable. The presence of both surfactants at the micro-interface is verified with SFS measurements, as discussed in section 4.4.2 in the Appendix.

The results shown in Fig. 4.2 indicate that the stabilization of micrometer-sized droplets requires the presence of a surfactant soluble in the continuous phase, in agreement with expectations from empirical rules. However, in all cases, micrometer-sized droplets are more difficult to stabilize than nanometer-sized droplets.<sup>39</sup> Moreover, the microfluidic formation of emulsion droplets depends on the presence of the surfactants that affect the interfacial tension. As a result, the size of the micrometer-sized droplets produced in microfluidic devices strongly depends on the type of surfactant employed. Thus, the interaction of the surfactants with the hexadecane/water interface does not seem to be a simple matter of adding the effects of both surfactants, which is different from the results obtained from the nanometer-sized droplets.

### 4.2.3 Nanometer-sized water-in-oil emulsions

If surface curvature influences emulsion properties, we expect the interfacial surfactant structure of nanometer-sized water-in-oil emulsions to be different from that of oil-in-water



emulsions. To test this expectation, we measured the adsorption of surfactants at the interface of nanometer-sized water droplets dispersed in hexadecane with SFS. The results are shown in Fig. 4.3. Droplets are stabilized with 5 mM Span80 (Fig. 4.3A), or with a combination of 8 mM SDS and 5 mM Span80 (Fig. 4.3B). As expected, it was impossible to stabilize water droplets in oil by using only SDS. In contrast, water droplets in oil were stabilized when Span80 was added to the oil phase. Indeed, in this case, the observation of CH stretch surface vibrational modes ( $\sim 2850 - 2970 \text{ cm}^{-1}$ ) in Fig. 4.3A shows that Span80 is adsorbed at the droplet interface. The value of the amplitude ratio  $r^-/r^+$  can be used to calculate the average tilt angle of the  $\text{CH}_3$  group with respect to the droplet surface, as discussed in Ref.<sup>26</sup>. A ratio of  $r^-/r^+ \sim 0.27$  indicates that the  $\text{CH}_3$  groups of the interfacial Span80 molecules are approximately parallel to the surface normal, as detailed in Ref.<sup>26</sup>. By contrast, if nanometer-sized water droplets are formed with SDS only, they immediately coalesce. Interestingly, when droplets are stabilized with a combination of surfactants, SFS spectra of the S-O symmetric stretch mode displayed in Figure 3B show a complete absence of SDS molecules at the interface. The response of the S-O symmetric stretch mode of the sulfate head group of  $\text{d}_{25}\text{-DS}^-$  when both SDS and Span80 are used to stabilize nanometer-sized oil droplets is repeated in Fig. 4.3B for comparison.

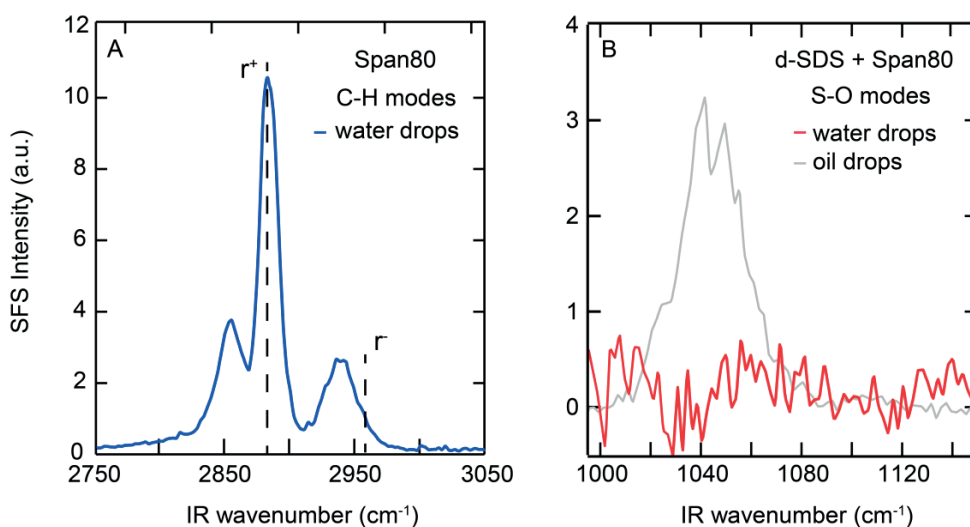


**Figure 4.3: Surface structure of surfactant stabilizing nanometer-sized water droplets in oil.** Normalized SFS intensity spectra of interfacial surfactant molecules adsorbed at nanometer-sized droplets of  $\text{D}_2\text{O}$  (1 vol. %) in (A)  $\text{d}_{34}$ -hexadecane stabilized with 5 mM Span80 or (B)  $\text{h}_{34}$ -hexadecane stabilized with a combination of 8 mM  $\text{d}_{25}\text{-SDS}$  and 5 mM Span80. (A) CH stretch modes of the methyl and methylene groups of the interfacial Span80 molecules. Symmetric and antisymmetric stretches of the  $\text{CH}_3$  groups are indicated with dashed lines at  $2845 \text{ cm}^{-1}$  ( $r^+$ ) and  $2965 \text{ cm}^{-1}$  ( $r^-$ ). (B) Spectra of the symmetric S-O stretch mode of the sulfate head group (with a resonance frequency of  $1045 \text{ cm}^{-1}$ ) of interfacial  $\text{d}_{25}\text{-DS}^-$  molecules. All SFS spectra were collected with the IR (VIS, SF) beam polarized parallel (perpendicular) to the scattering plane (SSP). The radius of the nanoemulsion and its PDI are (A) 75 nm and 0.16 and (B) 100 nm and 0.2.



## 4.2.4 Micrometer-sized water-in-oil emulsions

To test the stability of micrometer-sized water droplets in oil, we prepare water droplets in oil with Span80, SDS, or a combination of the two surfactants using our microfluidic device. Micrometer-sized droplets of radii between  $\sim 7 - 15 \mu\text{m}$  are prepared. The results are shown in Fig. 4.4. Droplets stabilized with SDS coalesce, as can be seen by the increase in the size of droplets after they have been in the analysis chamber for 0.2 ms as shown in Fig. 4.4A.

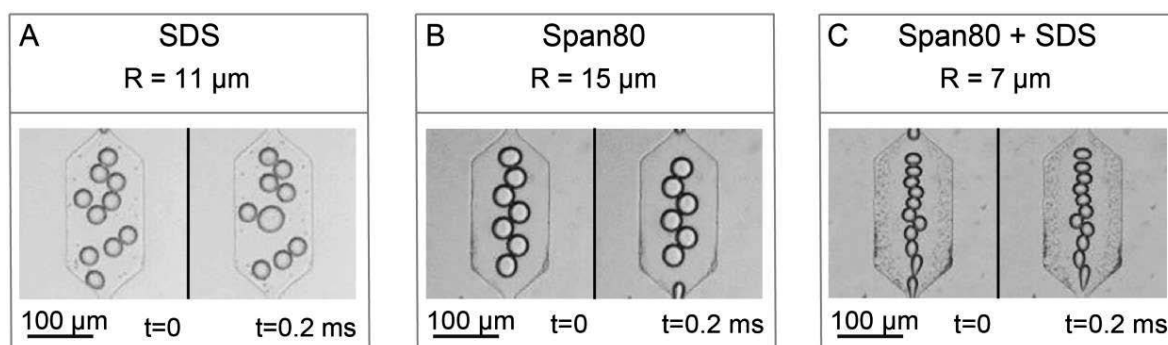


**Figure 4.4: Stability of micrometer-sized water droplets in oil.** Microscopy images of micrometer-sized water droplets in oil (radius  $\sim 7\text{--}15 \mu\text{m}$ ) when they entered the analysis chamber at  $t = 0$  (left panels) and  $t = 0.2 \text{ ms}$  thereafter (right panel). The systems are stabilized with (A) 8 mM SDS, (B) 5mM Span80, or (C) a combination of 8 mM SDS and 5 mM Span80.

In contrast, Figs. 4B and 4C show that droplets stabilized with Span80 or a combination of SDS and Span80 are stable, as can be found by comparing the size of droplets immediately after they entered the analysis chamber and those that have been there for 0.2 ms. To confirm these results, we vortexed a solution containing 10 % of the water phase is with 90% of the oil phase, each containing the surfactant required, for  $\sim 30 \text{ s}$  and observe the resulting emulsion over 8 h. Macroscopic phase separation cannot be observed within 8h if microemulsions are stabilized with Span80 or a combination of SDS and Span80, indicating that these microemulsions are stable. (Respective movies available if requested.) In contrast, emulsions stabilized only with SDS phase separate within 30 s, indicating that these emulsions are unstable. (Respective movies available if requested.) These macroscopic data support the microscopic observation that water micrometer-sized droplets stabilized with Span80 or a combination of SDS and Span80 are stable, in contrast to micrometer-sized droplets stabilized with SDS only.

**Table 4.1: Summary of findings regarding stability and droplet interfacial structure for nanometer-sized and micrometer-sized droplets.**

	Surfactant(s) used to stabilize the system		
	SDS	Span80	SDS + Span80
Formation of stable nanometer-sized			
- Oil droplets	Yes	Yes	Yes
- Water droplets	No	Yes	Yes
Surfactants at the interface of the nanometer-sized			
- Oil droplets	Yes	Yes	Yes + Yes
- Water droplets	No*	Yes	No + Yes
Formation of stable micrometer-sized			
- Oil droplets	Yes	No	Yes
- Water droplets	No	Yes	Yes

\* The absence of surfactant from the nanointerface is postulated from the instability of the respective system. Here, SFS measurements could not be conducted as they require stable droplets.

## 4.2.5 Discussion

Empirical rules that govern emulsion stability, such as the Bancroft rule, the HLB scale, and SAD predict that (kinetically stable) emulsions are stable if surfactants are mainly present in the continuous phase. However, such rules are based on macroscopic observations and the molecular mechanisms behind them are still not understood. From a geometric point of view, surface of emulsion droplets with radii that exceed the size of the adsorbing species by at least 2-3 orders of magnitudes can be considered as flat. This suggests that, the adsorption of surfactants whose size is on the order of 1-2 nm on the surface of droplets with radius of order of 100 nm or more should be similar to a flat interface. Hence, surfactants encapsulated in droplets in the size range studied here would be expected to adsorb at the liquid-liquid interface in a similar way as surfactants added to the continuous phase. If this were the case, the same surfactant should stabilize both water-in-oil and oil-in-water emulsions. Instead, Table 4.1 shows that this simple picture does not hold.

In terms of stability, we find that nanodroplets of both oil and water can be stabilized with the neutral hydrophobic surfactant such as Span80. For nanodroplets there are a few other notable findings that are unexpected, based on the empirical Bancroft rule, the HLB scale, or the SAD. Figure 4.1 shows that hexadecane-in-water nanoemulsions can be stabilized by both SDS, and Span80, as well as by a combination of the two surfactants. The water-soluble DS<sup>-</sup> anions populate the interface (Fig. 4.1C, E, F) and stabilize it by forming a

dilute layer of charges<sup>25</sup> with surfactant areas of  $> 4.25 \text{ nm}^2$ <sup>25</sup>. Since the density of SDS at the interface of these small droplets is considerably lower than that measured for macroscopic interfaces,<sup>40</sup> there is enough room for Span80 molecules to co-adsorb. Furthermore, the very different SFS intensity spectra measured for oil (Fig. 4.1B) and water (Fig. 4.3A) nanometer-sized droplets indicate that Span80 attains a very different interfacial configuration in the two systems (oil-in-water or water-in-oil). The SFS intensity, which differs by a factor of 20 between the two systems (max. of  $\sim 0.55$  in Fig. 4.1B versus  $\sim 11$  in Fig. 4.3A), indicates that the density of Span80 at the surface of oil nanodroplets in water is much lower than at the surface of water nanodroplets in oil, even when their sizes are similar. Another interesting feature is that there is no signature of SDS on the water nanodroplet surface, even when it is present in the aqueous phase, as displayed in Fig. 4.3B. This suggests that SDS stays in the dispersed water phase, while Span80 adsorbs at the liquid-liquid interface and imparts stability to the system. Given that SDS is an amphiphilic molecule and that the water / hexadecane interface is a water / oil interface, this may be considered surprising from a surface chemistry point of view.

In contrast, micrometer-sized droplet behaviour is in agreement with empirical expectations. Stability arises only when a surfactant is added that is soluble in the main phase. The difference between both behaviours may have something to do with the size of the droplets compared to the length scale over which interactions occur. For nanometer-sized droplets, the droplet size is on the order of, or below, the electrostatic interaction length scale<sup>40</sup>, which impacts the interfacial structure. If this is also true for other types of interactions remains an open question, although recent measurements of the hydrogen bond network structure on the surface of a water droplet suggest that hydrogen bonds rearrange differently over different length scales<sup>26</sup>.

## 4.3 Conclusions

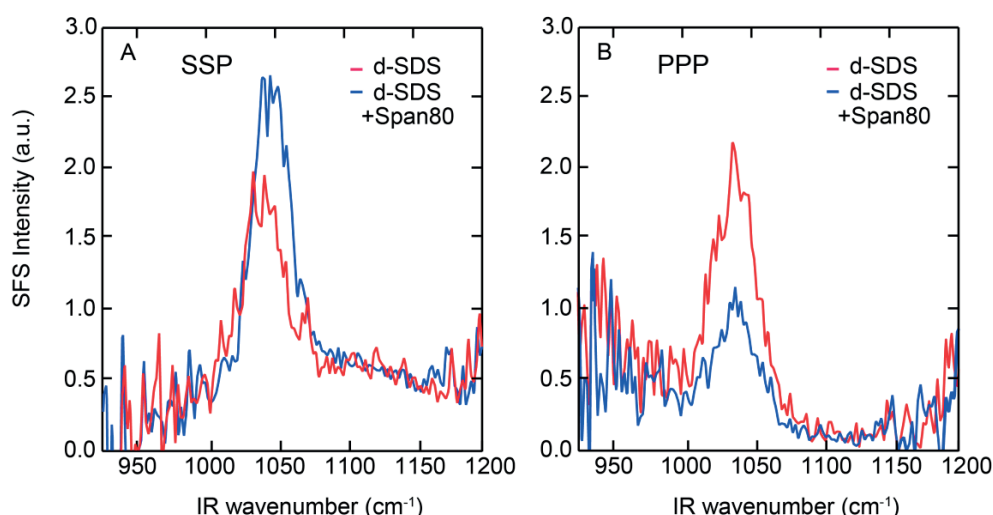
In this work we provided a direct link between the stability of micrometer-sized and nanometer-sized droplets and their interfacial structure by employing a multi-instrumental approach comprised of the surface-sensitive technique of sum frequency scattering as well as dynamic light scattering and microscopy. We monitored the stability of oil-in-water and water-in-oil emulsions, and the presence of surfactants at the oil/water nano-interface, when stabilized with an oil-soluble neutral surfactant (Span80), a water-soluble anionic surfactant (sodium dodecyl sulfate, SDS), or with a combination of the two. Micrometer-sized droplets are found to be stabilized only when a surfactant soluble in the continuous phase is present in the system, in agreement with what is traditionally observed empirically. Surprisingly, the

nanodroplets behave differently. Both oil and water nanodroplets can be stabilized by the same neutral Span80 surfactant, but with different surface structures. A combination of SDS and Span80 also suffices, but for the case of water droplets, the strongly amphiphilic SDS molecules are not detected at the interface. For the case of oil droplets, both surfactants are at the interface but do not structurally affect one another. Thus, it appears that empirical rules such as the Bancroft rule, the HLB scale and the SAD Difference work best when emulsion droplets exceed a certain size, probably due to a different balance of interactions on different length scales. This outcome is of great interest to a wide array of researchers working in chemistry, soft matter science, and biological sciences.

## 4.4 Appendix

### 4.4.1 Surface structure of SDS with and without the addition of Span80 in a system of nanometer-sized oil droplets in water.

Figure 4.5 presents the SFS intensity spectra of the SO symmetric stretch mode of the sulfate headgroup ( $\sim 1045\text{ cm}^{-1}$ ) of the interfacial dodecyl sulfate ( $\text{DS}^-$ ) anions on nanometer-sized droplets of  $\text{d}_{34}$ -hexadecane (1 vol %) in  $\text{D}_2\text{O}$ . The nanoemulsions are stabilized with 10 mM  $\text{d}_{25}$ -SDS alone (red) or with a combination of 5 mM Span80 and 10 mM  $\text{d}_{25}$ -SDS (blue). The stability of the samples was verified by DLS measurements of droplet size distribution and the size and PDI values for each nanoemulsion studied are mentioned in the caption of Fig. 4.5. Figure 4.5A shows the SFS intensity spectra measured with the infrared (IR) beam polarized parallel to the scattering plane while the visible (VIS) and sum-frequency (SF) beams are polarized perpendicular to the scattering plane (SSP). Figure 4.5B shows the SFS intensity spectra of exactly the same systems as Fig. 4.2A, but with all three beams (IR, VIS, SF) polarized parallel to the scattering plane (PPP). It can be seen that for SSP polarization combination (Fig. 4.5A) the SFS intensity is larger in the



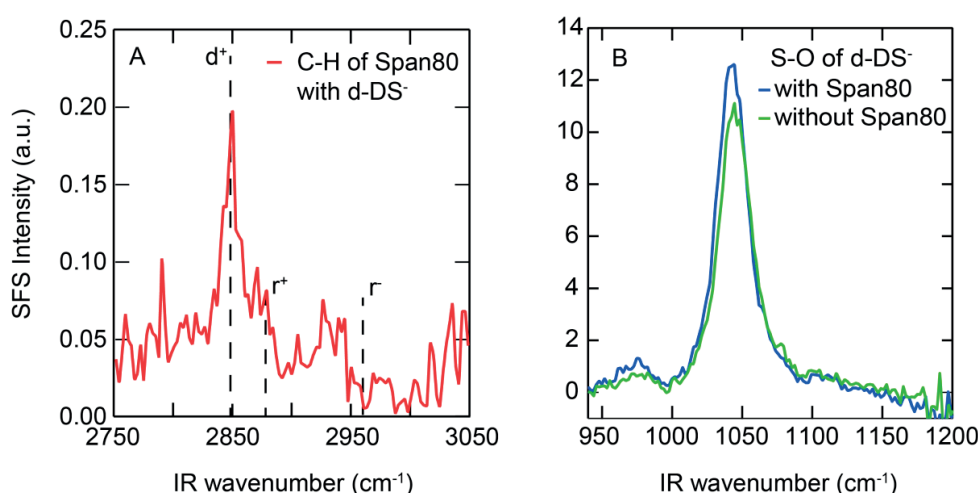
**Figure 4.5: Interfacial structure of SDS with and without Span80 on nanometer-sized oil droplets.** Normalized SFS intensity of the SO stretch mode ( $\sim 1045\text{ cm}^{-1}$ ) of the sulphate head group of  $\text{DS}^-$  anions at the interface of nanometer-sized droplets of  $\text{d}_{34}$ -hexadecane (1 vol %) in  $\text{D}_2\text{O}$  stabilized with 10 mM  $\text{d}_{25}$ -SDS alone (red) or with a combination of 5 mM Span80 and 10 mM  $\text{d}_{25}$ -SDS (blue). (A) SFS spectra collected with the IR (VIS, SF) beam polarized parallel (perpendicular) to the scattering plane (SSP). (B) SFS spectra collected with all three beams (IR, VIS, SF) polarized parallel to the scattering plane (PPP). The radius of the nanometer-sized droplets and the PDI are (red) 72 nm and 0.17, and (blue) 100 nm and 0.27 respectively.

Figure 4.5B shows the SFS intensity spectra of exactly the same systems as Fig. 4.2A, but with all three beams (IR, VIS, SF) polarized parallel to the scattering plane (PPP). It can be seen that for SSP polarization combination (Fig. 4.5A) the SFS intensity is larger in the

presence of  $d_{25}$ -SDS. However, for PPP (Fig. 4.5B) the SFS intensity is smaller in the presence of  $d_{25}$ -SDS. This change in the relative amplitudes of the SFS response indicates that the configuration of the headgroups of the interfacial  $DS^-$  anions is altered by the presence of Span80 molecules.

#### 4.4.2 Surface structure of SDS and Span80 in a system of micrometer-sized oil droplets in water.

Figure 4.6 presents the SFS intensity spectra of the vibrational modes of Span80 and SDS molecules at the interface of micrometer-sized hexadecane droplets in  $D_2O$ . Figure 4.6A shows the stretch modes ( $\sim 2845 - 2965 \text{ cm}^{-1}$ ) of the methyl and methylene groups of the alkyl chains of the interfacial Span80 molecules in a system stabilized with 5 mM Span80 and 10 mM deuterated ( $d$ -)SDS. Figure 4.6B shows the spectra of the symmetric SO stretch mode of the sulphate head group of interfacial  $d_{25}$ - $DS^-$  ( $\sim 1045 \text{ cm}^{-1}$ ) molecules in a system stabilized only with 10 mM SDS (green), or with a combination of 5 mM Span80 and 10 mM SDS.



**Figure 4.6: Interfacial structure of SDS and Span80 on micrometer-sized oil droplets.** Normalized SFS intensity of (A) the CH stretch modes ( $\sim 2845 - 2965 \text{ cm}^{-1}$ ) of the methyl and methylene groups of the alkyl chains of the Span80 molecules and (B) the SO stretch mode ( $\sim 1045 \text{ cm}^{-1}$ ) of the sulphate head group of  $DS^-$  anions at the interface of micrometer-sized droplets of  $d_{34}$ -hexadecane (9 vol %) in  $D_2O$  stabilized with 10 mM  $d_{25}$ -SDS alone (green) or with a combination of 5 mM Span80 and 10 mM  $d_{25}$ -SDS (red, blue). All SFS spectra were collected with the IR (VIS, SF) beam polarized parallel (perpendicular) to the scattering plane (SSP).

All spectra were measured with the infrared (IR) beam polarized parallel to the scattering plane while the visible (VIS) and sum-frequency (SF) beams polarized perpendicular to the scattering plane (SSP). It can be seen that, in correspondence to the nanometer-sized oil-in-water emulsions, both SDS and Span80 populate the micro-interface, contributing to the stability of the system.

## 4.5 References

1. Theberge, A. B., Courtois, F., Schaerli, Y., Fischlechner, M., Abell, C., Hollfelder, F. & S, H. W. T. Microdroplets in microfluidics: An evolving platform for discoveries in chemistry and biology. *Angew. Chem. Int. Ed.* **49** (34), 5846-5868 (2010).
2. Shembekar, N., Chaipan, C., Utharala, R. & Merten, C. A. Droplet-based microfluidics in drug discovery, transcriptomics and high-throughput molecular genetics. *Lab on a Chip* **16** (8), 1314-1331 (2016).
3. Sjblom, J. *Emulsions and emulsion stability: Surfactant science series/61* (CRC Press, Boca Raton, 2006).
4. Ostwald, W. Beiträge zur kenntnis der emulsionen. *Zeitschrift für Chemie und Industrie der Kolloide* **6** (2), 103-109 (1910).
5. Bancroft, W. D. The theory of emulsification, v. *J. Phys. Chem.* **17**, 501-519 (1913).
6. Bancroft, W. D. The theory of emulsification, vi. *J. Phys. Chem.* **19**, 275-309 (1915).
7. Langmuir, I. The constitution and fundamental properties of solids and liquids. li. Liquids.1. *J. Am. Chem. Soc.* **39** (9), 1848-1906 (1917).
8. Davies, J. T. & Rideal, E. R. *Interfacial phenomena* (Academic Press, 1963).
9. Ivanov, I. B. & Kralchevsky, P. A. Stability of emulsions under equilibrium and dynamic conditions. *Colloids and Surfaces A: Physicochemical and Engineering Aspects* **128** (1), 155-175 (1997).
10. Kabalnov, A. & Wennerström, H. Macroemulsion stability: The oriented wedge theory revisited. *Langmuir* **12** (2), 276-292 (1996).
11. Velev, O. D., Danov, K. D. & Ivanov, I. B. Stability of emulsions under static and dynamic conditions. *J. Dispersion Sci. Technol.* **18** (6-7), 625-645 (1997).
12. Company, A. P. *Atlas surface active agents* (Industrial Chemicals Department, Atlas Powder Company, 1948).
13. Salager, J. L., Forgari, A. & Ballon, J. (CRC Press, London, 2014).
14. Griffin, W. C. Classification of surface-active agents by "hlb". *J. Soc. Cos. Chemists* **1** (5), 311-326 (1949).
15. Ho, O. B. Electrokinetic studies on emulsions stabilized by ionic surfactants: The electroacoustophoretic behavior and estimation of davies' hlb increments. *J. Colloid Interface Sci.* **198** (2), 249-260 (1998).
16. Gianluca, E., Michael, K. & Esther, A. Influence of fluorinated surfactant composition on the stability of emulsion drops. *Macromol. Chem. Phys.* **218** (2), 1600365 (2017).
17. McClements, J. & McClements, D. J. Standardization of nanoparticle characterization: Methods for testing properties, stability, and functionality of edible nanoparticles. *Crit. Rev. Food Sci. Nutr.* **56** (8), 1334-1362 (2016).

18. McClements, D. J. *Food emulsions: Principles, practices, and techniques* (CRC Press, Florida, 2004).
19. Adamson, A. W. & Gast, A. P. *Physical chemistry of surfaces* (Wiley-interscience, Sidney, 1997).
20. Lu, J. R., Marrocco, A., Su, T. J., Thomas, R. K. & Penfold, J. Adsorption of dodecyl sulfate surfactants with monovalent metal counterions at the air-water interface studied by neutron reflection and surface tension. *J. Colloid Interface Sci.* **158** (2), 303-316 (1993).
21. Sloutskin, E., Sapir, Z., Bain, C. D., Lei, Q., Wilkinson, K. M., Tamam, L., Deutsch, M. & Ocko, B. M. Wetting, mixing, and phase transitions in Langmuir-Gibbs films. *Phys. Rev. Lett.* **99**, 136102-136104 (2007).
22. Conboy, J. C., Messmer, M. C. & Richmond, G. L. Investigation of surfactant conformation and order at the liquid-liquid interface by total internal reflection sum-frequency vibrational spectroscopy. *J. Phys. Chem.* **100**, 7617-7622 (1996).
23. Knock, M. M., Bell, G. R., Hill, E. K., Turner, H. J. & Bain, C. D. Sum-frequency spectroscopy of surfactant monolayers at the oil-water interface. *J. Phys. Chem. B* **107**, 10801-10814 (2003).
24. Roke, S., Roeterdink, W. G., Wijnhoven, J. E. G. J., Petukhov, A. V., Kleyn, A. W. & Bonn, M. Vibrational sum frequency scattering from a submicron suspension. *Phys. Rev. Lett.* **91** (25), 258302 (2003).
25. De Aguiar, H. B., De Beer, A. G. F., Strader, M. L. & Roke, S. The interfacial tension of nanoscopic oil droplets in water is hardly affected by SDS surfactant. *J. Am. Chem. Soc.* **132**, 2122-2123 (2010).
26. Smolentsev, N., Smit, W. J., Bakker, H. J. & Roke, S. The interfacial structure of water droplets in a hydrophobic liquid. **8**, 15548 (2017).
27. Roke, S. & Gonella, G. Nonlinear light scattering and spectroscopy of particles and droplets in liquids. *Annu. Rev. Phys. Chem.* **63**, 353-378 (2012).
28. Casson, B. D., Braun, R. & Bain, C. D. Phase transitions in monolayers of medium-chain alcohols on water studied by sum-frequency spectroscopy and ellipsometry. *Faraday Discuss.* **104** (0), 209-229 (1996).
29. De Aguiar, H. B., Strader, M. L., De Beer, A. G. F. & Roke, S. Surface structure of sodium dodecyl sulfate surfactant and oil at the oil-in-water droplet liquid/liquid interface: A manifestation of a non-equilibrium surface state. *J. Phys. Chem. B* **115**, 2970-2978 (2011).
30. Chen, Y., Jena, K. C. & Roke, S. From hydrophobic to hydrophilic: The structure and density of the hexadecane droplet/alkanol/water interface. *J. Phys. Chem. C* **119** (31), 17725-17734 (2015).



31. Smolentsev, N., Lütgebaucks, C., Okur, H. I., De Beer, A. G. F. & Roke, S. Intermolecular headgroup interaction and hydration as driving forces for lipid transmembrane asymmetry. *J. Am. Chem. Soc.* **138** (12), 4053-4060 (2016).
32. Bigelow, W. C., Pickett, D. L. & Zisman, W. A. Oleophobic monolayers: I. Films adsorbed from solution in non-polar liquids. *J. Colloid Sci* **1** (6), 513-538 (1946).
33. Day, J. P. R. & Bain, C. D. Ellipsometric study of depletion at oil-water interfaces. *Physical Review E* **76** (4), 041601 (2007).
34. Xia, Y. & Whitesides, G. M. Soft lithography. *Angew. Chem. Int. Ed.* **37** (5), 550-575 (1998).
35. De Aguiar, H. B., Scheu, R., Jena, K. C., De Beer, A. G. F. & Roke, S. Comparison of scattering and reflection SFG: A question of phase-matching. *Phys. Chem. Chem. Phys.* **14**, 6826-6832 (2012).
36. Mukerjee, P. M. K. J. Critical micelle concentrations of aqueous surfactant systems *Nat. Stand. Ref. Data Ser., Nat. Bur. Stand* **36**, 1-222 (1971).
37. McClements, J. D. Critical review of techniques and methodologies for characterization of emulsion stability. *Crit. Rev. Food Sci. Nutr.* **47**, 611-649 (2007).
38. Chen, Y. X., Jena, K. C. & Roke, S. From hydrophobic to hydrophilic: The structure and density of the hexadecane droplet/alkanol/water interface. *J. Phys. Chem. C* **119** (31), 17725-17734 (2015).
39. McClements, D. J. Nanoemulsions versus microemulsions: Terminology, differences, and similarities. *Soft Matter* **8** (6), 1719-1729 (2012).
40. Zdrali, E., Chen, Y., Okur, H. I., Wilkins, D. M. & Roke, S. The molecular mechanism of nanodroplet stability. *ACS Nano* **11** (12), 12111-12120 (2017).



## Chapter 5: Specific ion effects at the interface of nanometer-sized oil droplets in water

*The interaction of ions with biological interfaces controls innumerable processes that are vital for life, such as signalling through a cell membrane. Important differences (known as specific ion effects) are observed for ions with different molecular structure in their interaction with such interfaces. The latter are often composed of nanoscale structures of hydrophobic and hydrophilic groups adjacent to one another. Despite its importance, ionic specificity is still not fully understood on a molecular level. To study the complex mechanisms involved in ionic specificity directly at the nanoscale, here we use a hexadecane nanodroplet system, stabilized with a dilute monolayer of positively charged (DTA<sup>+</sup>) groups, in contact with aqueous electrolyte solutions (NaSCN, NaNO<sub>3</sub>, NaCl and Na<sub>2</sub>SO<sub>4</sub>). Using vibrational sum frequency scattering, second harmonic scattering and  $\zeta$ -potential measurements we find a unique adsorption pattern for each anion that changes with increasing bulk salt concentration, involving reorientation of the anions, and adsorption to different patches of the interface. Interestingly, not only the weakly-hydrated SCN<sup>-</sup> and NO<sub>3</sub><sup>-</sup>, but also the well-hydrated SO<sub>4</sub><sup>2-</sup> approaches the nanointerface, inducing strong interfacial water ordering.*

## 5.1. Introduction

The interaction of ions with aqueous nanoscale interfaces, and specific ion effects (also known as Hofmeister effects) thereat are crucial for life and omnipresent in biology, physics and chemistry.<sup>1-3</sup> The term refers to effects for which differences are observed when the composition/structure of ions, ionic groups, or the charge of ionic species varies. Both experiments and simulations indicate that ions of different size, structure and charge partition differently at aqueous interfaces.<sup>4, 5</sup> Since the first observation of ionic specificity,<sup>6</sup> extensive studies have been conducted for the discovery of general rankings of ions at different systems and interfaces. However, over the years it has become clear that ionic ordering is not unique, as there are cases of inversion of the 'direct' Hofmeister series, it depends on the counterions present, and ionic specificity is generally more pronounced for anions than cations.<sup>7</sup>

Despite the extensive studies for more than 130 years, the origin of ionic specificity on a molecular level, and the interactions at the nanoscale are still not fully understood. Today it is generally accepted that the different polarization and hydration shell of every ion, the molecular structure of the interface that they adsorb at, as well as the detailed molecular structure and hydrogen bonding of the water network (or other solute if present), are crucial and should be taken into account for the comprehension of specific ion effects.<sup>3, 8</sup> Molecular level experimental studies, as well as computational methods and simulations, are mostly conducted for planar interfaces, like the air/water,<sup>2,9-12</sup> and membrane(lipid)/water<sup>9-13</sup> interface, thus molecular level information directly at the nanoscale is missing. Experimental results have shown that system downscaling to nanometer sizes leads to substantial differences in the molecular structure of the oil/water nanointerface compared to its planar counterpart,<sup>14-16</sup> and one could expect that the specific ion interactions are also different at the nanointerface.

Here we employ a multi-instrumental approach, that ensures direct access to the molecular level structure of the nanointerface, and probe specific ion effects directly at the nanoscale. Specifically, we study an already well characterized system,<sup>17</sup> namely hexadecane nanodroplets (radius  $\sim 100$  nm) in water stabilized with dodecyl trimethylammonium cations (DTA<sup>+</sup>). The interaction of the four different anions SCN<sup>-</sup>, NO<sub>3</sub><sup>-</sup>, Cl<sup>-</sup> and SO<sub>4</sub><sup>2-</sup> with the positively charged oil/water nanointerface is compared for increasing sodium salt (NaSCN, NaNO<sub>3</sub>, NaCl and Na<sub>2</sub>SO<sub>4</sub>) concentration in the bulk water phase (up to 600 mM). The anions chosen are typical for the Hofmeister series, and known to interact with the air/water and protein/water interface with the order SCN<sup>-</sup> > NO<sub>3</sub><sup>-</sup> > Cl<sup>-</sup> > SO<sub>4</sub><sup>2-</sup>, with SCN<sup>-</sup> being the most and SO<sub>4</sub><sup>2-</sup> the least surface active.<sup>18</sup> In the above system we can

measure the  $\zeta$ -potential (with electrokinetic mobility measurements) and determine the water orientation (with second harmonic scattering<sup>19, 20</sup>) and the structure of the polyatomic anions of interest, by probing their vibrational modes (with sum frequency scattering<sup>19, 21</sup>). We find a unique adsorption pattern for each anion:  $\text{Cl}^-$  anions populate the electric double layer around the positively charged nanodroplets and this adsorption is accompanied by a slight increase in interfacial water ordering for high ( $> 100$  mM) salt concentrations. For the polyatomic anions, a complex multi-regime-behaviour is observed over increasing bulk ionic concentration. The different trends in SFS and SHS intensity point towards reorientation of the adsorbed ions, accompanied by disruption of the interfacial hydrogen-bond network. Interestingly, not only the weakly-hydrated  $\text{SCN}^-$  and  $\text{NO}_3^-$  but also the well-hydrated  $\text{SO}_4^{2-}$  approaches the nanointerface probably with a disrupted hydration shell, inducing strong interfacial water ordering.

## 5.2. Results and discussion

In the following sections we describe the influence of the addition of NaSCN,  $\text{NaNO}_3$ , NaCl and  $\text{Na}_2\text{SO}_4$  on the interfacial structure of hexadecane nanodroplets stabilized with a dilute layer of  $\text{DTA}^+$  ions. The interfacial structure is characterized with electrokinetic mobility, SHS and SFS measurements. In order to compare the effect of the different anions, the cation is kept constant ( $\text{Na}^+$ ). According to the typical order of the anionic Hofmeister series,  $\text{SCN}^-$  is expected to be the most surface active anion of all.  $\text{NaNO}_3$  has also a propensity to approach the interface, however less than  $\text{SCN}^-$ .  $\text{SO}_4^{2-}$ , on the other hand, is well hydrated and preferably remains dissolved in the bulk aqueous solution, while Cl is usually considered the dividing line between these two types of behaviour.<sup>18</sup>

### 5.2.1. Electrokinetic mobility

Figure 5.1A presents the  $\zeta$ -potential<sup>22</sup> around DTAB stabilized nanodroplets (radius  $\sim 100$  nm, oil concentration 0.5 vol. %) for increasing bulk NaSCN,  $\text{NaNO}_3$ , NaCl and  $\text{Na}_2\text{SO}_4$  salt concentrations, ranging from 0 to 600 mM. For  $\text{Na}_2\text{SO}_4$ , the maximum concentration is 300 mM due to destabilization of the samples for higher values. It can be seen that in the absence of salt the  $\zeta$ -potential value is  $\sim 80 \pm 7$  mV and, as a general trend, it drops when any of the sodium salts is added in the bulk aqueous phase, already at concentrations as low as 5 mM.

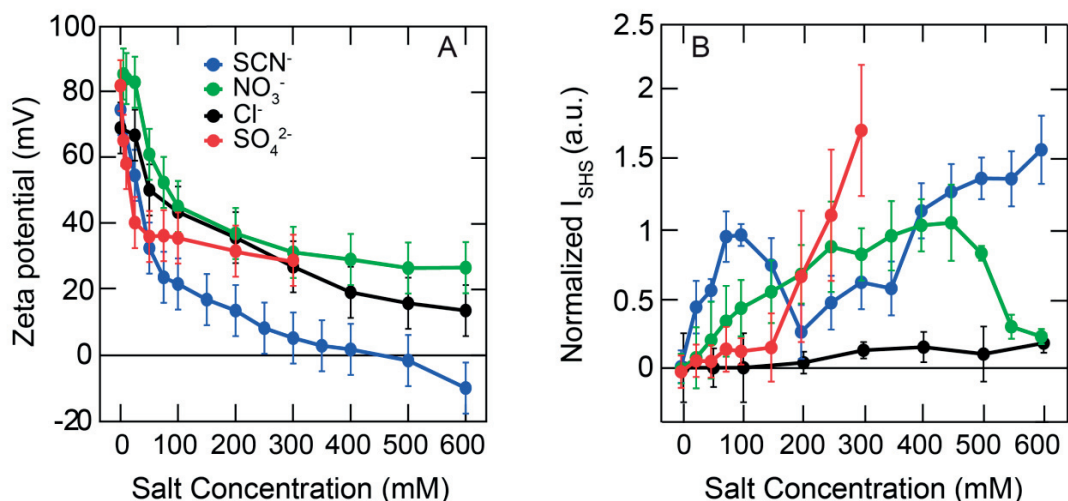


**Figure 5.1: Electrokinetic potential and interfacial water ordering.** (A)  $\zeta$ -Potential of 0.5 vol % n-hexadecane nanodroplets in H<sub>2</sub>O stabilized with 15 mM DTAB over increasing bulk concentrations of NaSCN (blue), NaNO<sub>3</sub> (green), NaCl (black) and Na<sub>2</sub>SO<sub>4</sub> (blue). (B) SHS intensity of the same droplet samples. Both the fundamental and the second harmonic frequency beams were polarized parallel to the scattering plane (i.e. P-polarized). SHS intensities were measured at a scattering angle of maximum intensity of 45° with respect to the incoming beam and normalized by the pure water signal at the same angle and polarization combination (see Paragraph 2.3.3 for more details).

Comparing the four salts, it can be seen in Fig. 5.1A that at low concentrations the decrease is steep, while for higher concentrations it becomes more gradual. For the three monovalent anions (SCN<sup>-</sup>, Cl<sup>-</sup> and NO<sub>3</sub><sup>-</sup>) this change is observed at ~100 mM bulk salt concentration, while for SO<sub>4</sub><sup>2-</sup> it occurs at ~50 mM. Looking more closely at the data, it can be seen that for Na<sub>2</sub>SO<sub>4</sub> the average  $\zeta$ -potential decrease rate changes from -1.5 mV/mM to -0.04 mV/mM; for NaCl from -0.23 mV/mM to -0.05 mV/mM; for NaNO<sub>3</sub> from -0.38 mV/mM to -0.03 mV/mM; and for NaSCN from -0.48 mV/mM to -0.06 mV/mM. Clearly the addition of NaSCN induces the overall largest drop in the  $\zeta$ -potential values than any other salt. Moreover, for NaCl, NaNO<sub>3</sub> and Na<sub>2</sub>SO<sub>4</sub> the  $\zeta$ -potential remains positive over the whole concentration range, while for NaSCN it crosses the isoelectric point<sup>22</sup> at ~ 400 mM, reaching a negative minimum value of  $-11.2 \pm 7$  mV at 600 mM. Interestingly, the droplets remain stable over the whole concentration range tested here, even in the region where their overall charge is neutral.

The monotonic decrease of the  $\zeta$ -potential presented in Fig. 5.1A points towards a continuously increasing concentration of the four anions inside the electric double layer. However, the discrepancies between the four salts suggest a stronger interfacial activity of SCN<sup>-</sup> compared to the NO<sub>3</sub><sup>-</sup>, Cl<sup>-</sup> and SO<sub>4</sub><sup>2-</sup>. A concentration of anions close to the interface is expected to induce changes in the interfacial water ordering, which was tested by the SHS measurements presented in the following section.

### 5.2.2. Interfacial water ordering

SHS intensity ( $I_{\text{SHS}}$ ) reports on the interfacial water ordering along the surface normal, which is crucially affected by both the surface density and structure of the molecular components of the oil-nanodroplet/water interface<sup>23</sup>. As shown before, the  $I_{\text{SHS}}$  measured for nanodroplets stabilized with 15 mM of DTAB, without the addition of salt, is zero. Thus, the presence of such droplets does not induce any extra interfacial water ordering along the surface normal, as compared to hyper-Rayleigh scattering of bulk water.<sup>24</sup> Figure 5.1B presents the SHS intensity<sup>25</sup> when NaSCN, NaNO<sub>3</sub>, NaCl or Na<sub>2</sub>SO<sub>4</sub> is added in the above system for bulk salt concentrations up to 600 mM for the monovalent anions, and 300 mM for the divalent one. It can be seen that for addition of NaCl only a slight increase in  $I_{\text{SHS}}$  is observed, and only for concentrations >100 mM, with the value levelling off at 0.18 above 200 mM. This result can be rationalized by noting that a slightly increased concentration of Cl<sup>-</sup> ions in the electric double layer (as observed in Fig. 5.1A), induces a small amount of additional water ordering along the interfacial normal due to ion–water dipole interaction. In the case of NaNO<sub>3</sub>, a monotonic increase is observed reaching a maximum of ~1 at 450 mM salt, followed by a monotonic decrease. For the case of NaSCN, a strikingly different behaviour from Cl<sup>-</sup> and NaNO<sub>3</sub><sup>-</sup> is observed, despite the same charge of the three anions: For low salt concentrations (<100 mM) a steep monotonic increase in SHS intensity appears, reaching a maximum of ~1. At middle concentrations (between 100 mM and 400 mM) a drop is observed, with a minimum at 200 mM, while at high concentrations (>400 mM) a monotonic increase is again observed, as if continuing the increase observed at low concentrations. Last, when Na<sub>2</sub>SO<sub>4</sub> is added in the system, a slight increase is observed until 150 mM, followed by a very steep monotonic increase between 150 mM and 300 mM.

Overall, interesting observations can be made from the comparison of the effect of the four salts on the interfacial water ordering (Fig. 5.1B), in view of their continuously increasing adsorption at the oil/water interface, as suggested already by the decreasing  $\zeta$ -potential values (Fig. 5.1A): First, the maximum (change in the) value of  $I_{\text{SHS}}$  measured for the three polyatomic ions (SCN<sup>-</sup>, NO<sub>3</sub><sup>-</sup> and SO<sub>4</sub><sup>2-</sup>) is of an order of magnitude larger (~ 1-2) compared to Cl<sup>-</sup> (~ 0.1-0.2), reflecting a considerably larger number of oriented interfacial water molecules for these salt systems. However, the similar  $\zeta$ -potential values for Cl<sup>-</sup> and NO<sub>3</sub><sup>-</sup> suggest a similar population/number density of Cl<sup>-</sup> and NO<sub>3</sub><sup>-</sup> anions inside the electric double layer of the nanodroplets. Such a difference suggests what was already observed before,<sup>24</sup> namely that the orientation of the interfacial water extends far beyond the ion-charge – water-dipole interaction, and that is affected by the development of H-bonds between the adsorbing ion and the water network. Secondly, both SCN<sup>-</sup> and NO<sub>3</sub><sup>-</sup> are known

to be more surface active compared to  $\text{Cl}^-$ .<sup>26</sup> However, the observed two-distinct-regimes behaviour for  $\text{NO}_3^-$  (<450 mM and >450 mM) and three-distinct-regimes behaviour for  $\text{SCN}^-$  (<100 mM, between 100 and 400 mM, >400 mM) are rather surprising and point towards a complex adsorption pattern for these two anions, possibly involving their re-orientation. In detail, as mentioned above, the orientation of interfacial water is partly due to the adsorbed ion-water dipole interaction electrostatic interaction, partly due to the development of H-bonds between the ion and the water molecules, and partly due to the re-arrangement of the water network itself (i.e. H-bonding between water molecules) around a well- / weakly-hydrated adsorbent. As such, a change in adsorption orientation of the ions could result in breaking already existing H-bonds or making new H-bonds, which would in turn be reflected in the orientation of the local water molecules. Thirdly, the effect of  $\text{SO}_4^{2-}$  on the interfacial water ordering (Fig. 5.1B) is small (comparable to the effect of  $\text{Cl}^-$ ) up to the addition of 150 mM salt, while above this concentration it becomes an order of magnitude stronger, surpassing both  $\text{NO}_3^-$  and  $\text{SCN}^-$ . This unexpected behaviour could probably result from the difference in hydration between the three anions<sup>18, 27</sup>: While  $\text{NO}_3^-$  and  $\text{SCN}^-$  are weakly hydrated, thus expected to reside in close proximity/on the interface,  $\text{SO}_4^{2-}$  has a very large and strong hydration shell<sup>28</sup> which, while preserved, could keep the anion further away from the surface, leaving the already existing/absent interfacial water ordering unchanged. While the surface concentration of  $\text{SO}_4^{2-}$  reaches a critical point (in Fig. 5.2B seems to be ~ 150 mM) a shedding/disruption of the hydration shells could start, which is reflected in the interfacial water orientation. Although the above explanations seem possible, they are still speculative and further information for the interfacial structure are required. In the following section SFS measurements are presented that were conducted to investigate the chemical speciation of the anions in more detail.

### 5.2.3. Surface density and structure of $\text{SCN}^-$ , $\text{NO}_3^-$ and $\text{SO}_4^{2-}$

SFS measurements, due to the molecular specificity can report directly on the ion of interest.<sup>29, 30</sup> The technique is based on probing a vibrational mode of the ion by an incoming infrared beam tuned at the central frequency of the mode targeted. Notably, the mode should be both infrared and Raman active.<sup>31</sup> A second incoming beam, tuned at a different frequency, upconverts the infrared photons, resulting in the emission of photons in the sum frequency of the two incoming beams. As a consequence, SFS is applicable to the polyatomic ions that possess appropriate vibrational modes but not to spherical atomic ions, such as  $\text{Cl}^-$ . Figure 5.2 displays the SFS spectra of the vibrational modes of the three anions at the interface of DTAB stabilized  $d_{34}$ -hexadecane nanodroplets in  $\text{D}_2\text{O}$  for 100 mM bulk salt



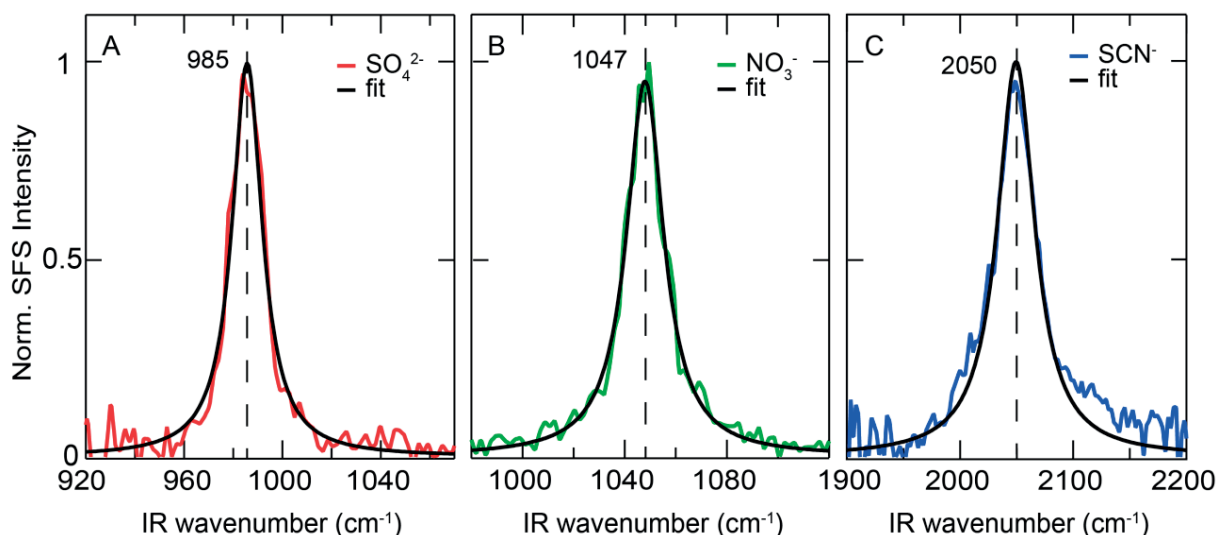


**Figure 5.2: Normalized vibrational SFS spectra of  $\text{SO}_4^{2-}$ ,  $\text{NO}_3^-$  and  $\text{SCN}^-$ .** SFS measurements on hexadecane nanodroplets ( $R \sim 100$  nm, 1 vol % concentration) stabilized with 15 mM DTAB in 100 mM (A)  $\text{Na}_2\text{SO}_4$ , (B)  $\text{NaNO}_3$ , or (C)  $\text{NaSCN}$  solution in  $\text{D}_2\text{O}$ . Vibrational spectra of (A) the symmetric stretch SO mode at  $\sim 985$   $\text{cm}^{-1}$  of interfacial  $\text{SO}_4^{2-}$  anions, (B) the symmetric stretch NO mode at  $1047$   $\text{cm}^{-1}$  of interfacial  $\text{NO}_3^-$  anions and (C) the CN stretch mode of interfacial  $\text{SCN}^-$  anions normalized to the peak SFS intensity. The black lines are Lorentzian fits according to Eq. (2.24). The spectra were recorded in the SSP polarization combination, which indicates that the sum frequency and visible beams were polarized perpendicular with respect to the scattering plane, while the infrared beam was polarized parallel to it.

concentrations normalized to the maximum SFS intensity. Figure 5.2A shows the symmetric SO stretch mode of  $\text{SO}_4^{2-}$  centred at  $\sim 985$   $\text{cm}^{-1}$ ,<sup>32</sup> Fig. 5.2B the symmetric NO stretch mode of  $\text{NO}_3^-$  centred at  $\sim 1047$   $\text{cm}^{-1}$ ,<sup>33</sup> and Fig. 5.3C the CN stretch mode of  $\text{SCN}^-$  centred at  $\sim 2050$   $\text{cm}^{-1}$ .<sup>34</sup> The fact that the symmetric stretch modes of  $\text{SO}_4^{2-}$  and  $\text{NO}_3^-$  are SFS active reflects lowering of symmetry of the two anions at the interface. Specifically, when  $\text{SO}_4^{2-}$  is fully solvated, it possesses  $T_d$  symmetry and little or no SFS activity is expected, as the symmetric stretch SO of  $\text{SO}_4^{2-}$  is IR inactive.<sup>31</sup> The same applies for the free  $\text{NO}_3^-$  that possesses  $D_{3h}$  symmetry under full solvation. Symmetry lowering reflects perturbation of the anionic environment that can originate from neighbouring cations (possibly ion-pairing) and/or water molecules that change the hydration of the anions.<sup>35, 36, 37</sup> An interpretation for the SO and NO modes observed here is suggested in the Discussion part. The vibrational modes in Fig. 5.2 were fitted with a single Lorentzian resonance using Eq. (2.24) presented by the black lines in each panel of Fig. 5.2. Similar spectra were measured for different salt concentrations between 0 mM and 300 mM for  $\text{Na}_2\text{SO}_4$ , and between 0 mM and 600 mM for  $\text{NaNO}_3$  and  $\text{NaSCN}$ . Figure 5.3 presents the integrated intensity of the SFS spectra normalized to the maximum value over increasing salt concentration. The spectral window for integration corresponding to each salt is  $930$   $\text{cm}^{-1} - 1040$   $\text{cm}^{-1}$  for  $\text{SO}_4^{2-}$ ,  $1000$   $\text{cm}^{-1} - 1090$

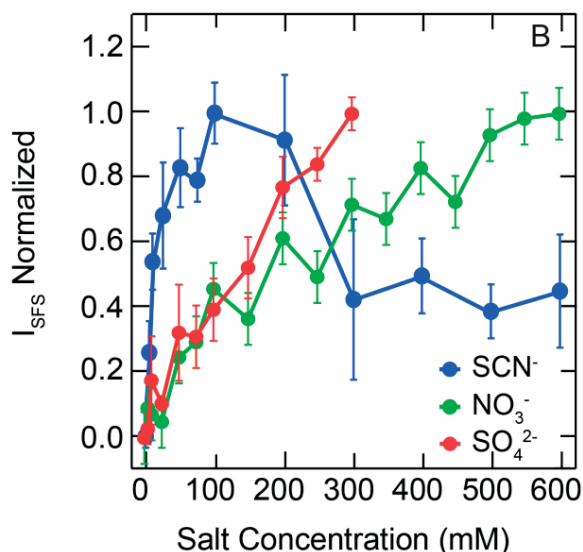


**Figure 5.3: Integrated SFS intensity for  $\text{SO}_4^{2-}$ ,  $\text{NO}_3^-$  and  $\text{SCN}^-$ .** SFS measurements on hexadecane nanodroplets ( $R \sim 100$  nm, 1 vol % concentration) stabilized with 15 mM DTAB in solution of  $\text{Na}_2\text{SO}_4$  (red),  $\text{NaNO}_3$  (green) or  $\text{NaSCN}$  (blue) in  $\text{D}_2\text{O}$ . Integrated SFS intensity calculated by integration of the area of the vibrational spectra in the range  $930\text{ cm}^{-1} - 1040\text{ cm}^{-1}$  for  $\text{SO}_4^{2-}$  (red),  $1000\text{ cm}^{-1} - 1090\text{ cm}^{-1}$  for  $\text{NaNO}_3^-$  (green), and  $1950\text{ cm}^{-1} - 2150\text{ cm}^{-1}$  for  $\text{SCN}^-$  (blue) over increasing bulk concentration of the respective sodium salt. For each salt concentration, the value of integrated intensity at 0 mM salt was subtracted, followed by a normalization to the maximum value of integrated SFS intensity over all concentrations for the respective salt. The SFS spectra used for the integration were recorded in the SSP polarization combination, which indicates that the sum frequency and visible beams were polarized perpendicular with respect to the scattering plane, while the infrared beam was polarized parallel to it.

$\text{cm}^{-1}$  for  $\text{NO}_3^-$ , and  $1950\text{ cm}^{-1} - 2150\text{ cm}^{-1}$  for  $\text{SCN}^-$ . It can be seen that, within error, for  $\text{SO}_4^{2-}$  and  $\text{NO}_3^-$  ions a monotonic increase in  $I_{\text{SFS}}$  is observed for increasing bulk concentration over the whole concentration range. However, in the case of  $\text{SCN}^-$  a distinctively different behaviour is observed: There are three concentration ranges over which the  $I_{\text{SFS}}$  of the CN mode follows different trends: At low bulk  $\text{NaSCN}$  concentrations ( $<100$  mM) an increase is observed, followed by a decrease at middle concentrations (between 100 mM and 300 mM), while for large concentrations ( $>300$  mM) the intensity fluctuates about a constant value. Changes in the SFS intensity reflect changes in the surface density and/or orientational distribution of the probed chemical group.<sup>31</sup> Specifically,  $I_{\text{SFS}}$  is proportional to the net polar orientation of the fluctuating molecular group (here S-O, N-O and C-N) and no sum frequency emission arises from isotropically distributed molecules. Accordingly, large sum frequency emission arises from dipolar molecules that adopt a parallel orientation. Thus, the increase in  $I_{\text{SFS}}$  points towards an increasing surface density of the chemical group with a parallel orientation, or towards a re-orientation in parallel of already adsorbed species. In contrast, decrease in  $I_{\text{SFS}}$  points towards a decreasing surface density of the chemical group, or towards a change in the orientational distribution of the molecules. The most

straightforward explanation for a constant value would be a saturation of the surface density at a constant average configuration of the group under study. Interestingly, though, change in  $I_{\text{SFS}}$  would neither be observed when the surface density of the studied chemical group increases (decreases) with pairs of chemical groups with anti-parallel orientation arriving at (leaving) the interface. Thus, the trend of the SFS isotherm presented in Fig. 5.3, combined with  $\zeta$ -potential and SHS measurements (Fig. 5.1) reflects a different adsorption pattern for each anion.

#### 5.2.4. Discussion

Combining  $\zeta$ -potential, SFS and SHS measurements, different adsorption behaviours for the different anions at the DTAB-stabilized hexadecane/water nanointerface are inferred.

When the hexadecane/water nanointerface is stabilized by 15 mM DTAB (Fig. 5.4A) without any other salt present in the system except the counterions, the orientation of the interfacial water molecules along the normal to the interface is indistinct from bulk water, as shown before.<sup>24</sup> The absence of any SH intensity from DTA<sup>+</sup> stabilized hexadecane nanodroplets is a result of two competing mechanisms: The presence of the bare negatively charged<sup>38</sup> oil/water nanointerface induces on average an ordering of interfacial water molecules with their H atoms towards the interface. This ‘H down’ directionality competes with an ‘H up’ directionality induced by the DTA<sup>+</sup> ions. Charge-dipole interactions between interfacial DTA<sup>+</sup> cations and water favour an opposite water orientation.

When NaCl is added to the bulk water phase (Fig. 5.4B) of the DTAB-stabilized nanoemulsion, Cl<sup>-</sup> anions populate the electric double layer around the positively charged nanodroplets, as evidenced by the monotonically decreasing  $\zeta$ -potential values as a function of increasing salt concentration (Fig. 5.1A). This change in the electric double layer structure is accompanied by the slight increase in  $I_{\text{SHS}}$  observed above 100 mM (Fig. 5.1B) due to ion-water dipole interaction.

SCN<sup>-</sup> is expected to be the most surface active anion of all and, indeed, the most complexed behaviour is observed when NaSCN is added in the system: Inversion of the surface charge for large concentrations (Fig. 5.1A), and three-distinct-regimes behaviour for interfacial water ordering (Fig. 5.1B) and SCN<sup>-</sup> surface adsorption (Fig. 5.3). The interaction of SCN<sup>-</sup> with the DTAB stabilized nanointerface has been studied in more detail using *ab initio* molecular dynamics simulations. The results are presented in detail in Chapter 6. To aid the discussion of the other salts we mention here the most important findings (Fig. 5.4C): Already at 5 mM SCN<sup>-</sup> ion-pairs with the interfacial DTA<sup>+</sup> cations via the S-atom, and this interaction remains undisturbed for the whole concentration range of 0 – 600 mM (configuration ‘1’ in Fig. 5.4C). At the same time there is an increasing population of SCN<sup>-</sup>

anions adsorbing to the bare  $\text{DTA}^+$  free patches of the hydrophobic nanointerface, again with the S-atom facing the interface (configuration '2' in Fig. 5.4C). This behaviour is reflected in the increase in the SHS and SFS until  $\sim 100$  mM. When the dipole-dipole repulsion between the CN dipoles becomes too strong,  $\text{SCN}^-$  keep adsorbing to the bare patches, but now with an opposite CN dipole orientation (with the N-atom towards the interface, configuration '3' in Fig. 5.4C). This change is reflected in the drop in SHS and SFS intensity between 100 mM and 400 mM. Above 400 mM a balance between interactions seems to have been achieved, with  $\text{SCN}^-$  adsorbing to the interface with both orientations, keeping the SFS intensity constant but resulting in an increasing SHS intensity.

$\text{NO}_3^-$ , which is also weakly hydrated but less so than  $\text{SCN}^-$ ,<sup>3</sup> also displays a two-district-regime behaviour, both in the SFS and SHS experiments (Figs. 5.1B and 5.3 respectively). The similarity with  $\text{SCN}^-$  suggests some similarity with the adsorption behaviour of  $\text{SCN}^-$ . In analogy, the decreasing  $\zeta$ -potential values (Fig. 5.1A) suggest an increasing population of  $\text{NO}_3^-$  anions in the electric double layer (or at the interface) with increasing bulk  $\text{NaNO}_3$  concentrations. At the same time, the increase in SFS intensity until 400-450 mM (Fig. 5.3) points towards an increasing population of adsorbed  $\text{NO}_3^-$  at the interface. The central frequency of the N-O symmetric stretch vibrational mode of  $\sim 1047\text{ cm}^{-1}$  measured here has been reported before for ion-paired  $\text{NO}_3^-$  with  $\text{Mg}^{+2}$  at the air/water interface.<sup>33</sup> This frequency is red-shifted by  $16\text{ cm}^{-1}$  compared to the frequency for free  $\text{NO}_3^-$  at the air/water interface,<sup>33</sup> reflecting the donation of electron density to the  $\text{Mg}^{+2}$  cations. It is likely that a similar phenomenon takes place here: Upon adsorption to the interface,  $\text{NO}_3^-$  ion-pairs with the  $\text{DTA}^+$  interfacial cations, probably with their most electronegative part towards the cations (configuration '1' in Fig. 5.4D). The possibility of already existing  $\text{Na}^+ - \text{NO}_3^-$  ion pairs adsorbing to the interface is in conflict with the steep  $\zeta$ -potential drop observed (Fig. 5.1) up to 100 mM  $\text{NaNO}_3$ . Additionally,  $\text{Na}^+ - \text{NO}_3^-$  ion pairs in bulk  $\text{D}_2\text{O}$  have been observed for concentrations of several molar,<sup>39</sup> while the reported peak here appears already at 10 mM  $\text{NaNO}_3$ . Moreover,  $\text{DTA}^+ - \text{NO}_3^-$  ion pairing is expected to be highly favourable,<sup>3</sup> and in accordance with the law of matching water affinities, which predicts ion pairing between two soft weakly-hydrated ions. When  $\text{NO}_3^-$  adsorbs at the interfacial  $\text{DTA}^+$ , H-bonds can be formed between the adsorbed  $\text{NO}_3^-$  anions and the interfacial water molecules<sup>39</sup>, leading to the observed increase in the ordering of interfacial water (Fig. 5.1B). Above  $\sim 450$  mM the SFS intensity saturates while the SHS intensity displays a steep decrease. These two findings combined, it's possible that the  $\text{NO}_3^-$  ions keep adsorbing at the interface at a different place and with a different orientation, namely with their vibrating N-O bonds more parallel towards the interface (configuration '2' in Fig. 5.4D), so that they do not generate a detectable SFS response. In this way the H-bond network at the interface (around the  $\text{NO}_3^-$ ) would get disrupted due to H-bond directionality between  $\text{N-O}\cdots\text{H-OH}$ ,

thus resulting in a decrease in SHS intensity. Although the above explanation is in agreement with the experimental data, atomistic simulations would allow for a more definitive assignment of the involved molecular speciation.

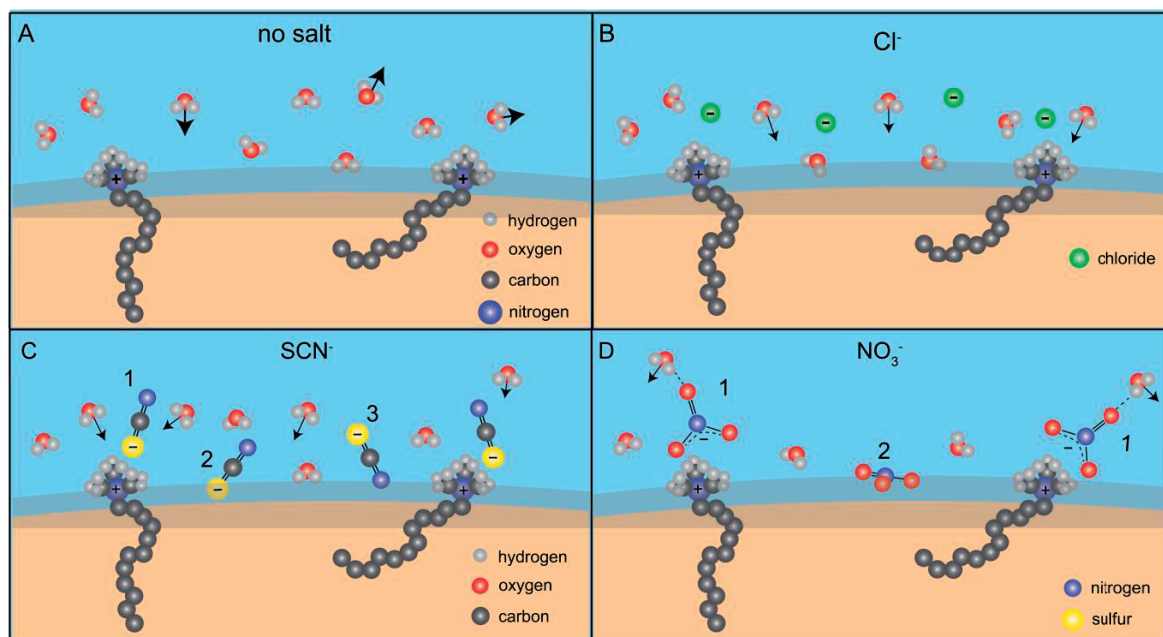


**Figure 5.4: Interfacial structure of DTAB stabilized nanodroplets without added salt and with NaCl, NaSCN and NaNO<sub>3</sub> added.** Schematic illustration of the interfacial structure of the DTAB - stabilized nanodroplet oil/water interface (A) without extra salt added and with (B) NaCl, (C) NaSCN and (D) NaNO<sub>3</sub> added to the bulk aqueous phase. The arrows represent the dipole moment of water molecules. For simplicity, the Br<sup>-</sup> and Na<sup>+</sup> ions are excluded, while the dipole moment of water is drawn only for some water molecules. (A) In the presence of DTA<sup>+</sup> cations only, the orientational ordering of the interfacial water molecules is indistinguishable from bulk water. (B) Some Cl<sup>-</sup> anions approach the positively charged interface inducing additional interfacial water orientation/ordering compared to bulk water. (C) SCN<sup>-</sup> anions adsorb to the interfacial DTA<sup>+</sup> cations with their sulphur atom (configuration '1'), while they can adsorb to the hydrophobic patches either with their sulphur (configuration '2') or with their nitrogen (configuration '3') atom. SCN<sup>-</sup> anions with configuration 1 or 2 increase the ordering of interfacial water compared to bulk water, whereas with configuration 3 disrupt it. (D) NO<sub>3</sub><sup>-</sup> anions adsorb to the interfacial DTA<sup>+</sup> cations with their most electronegative part (configuration '1') while they adsorb to the hydrophobic patches with a configuration more parallel to the interface (configuration '2'). NO<sub>3</sub><sup>-</sup> anions with configuration 1 increase the ordering of interfacial water compared to bulk water, whereas with configuration 2 disrupt it.

From the group of very well hydrated anions, we have tested Na<sub>2</sub>SO<sub>4</sub> and our experimental data suggest that it acts differently than Cl<sup>-</sup>, SCN<sup>-</sup> and NO<sub>3</sub><sup>-</sup>. The steep monotonic increase in SFS intensity over the whole concentration range of Na<sub>2</sub>SO<sub>4</sub> (Fig. 5.3), points towards a continuous adsorption of the detected interfacial SO<sub>4</sub><sup>2-</sup> species with a constructive (parallel) orientation. The enhanced surface concentration of SO<sub>4</sub><sup>2-</sup> is also reflected in the monotonic drop in ζ-potential (Fig. 5.1A) for increasing bulk Na<sub>2</sub>SO<sub>4</sub>

concentrations (Fig. 5.1A), especially for concentrations < 50 mM. The vibrational mode detected with SFS at  $\sim 985\text{ cm}^{-1}$  (Fig. 5.2A) resembles to the symmetric SO stretch mode when  $\text{SO}^{2-}$  directly binds to a  $\text{CaF}_2$  interface detected at  $\sim 990\text{ cm}^{-1}$ .<sup>32</sup> The appearance of this peak requires a lowering of the  $T_d$  symmetry of the fully solvated  $\text{SO}_4^{2-}$ ,<sup>31</sup> thus a disruption of the hydration shell of the anions. As such, the interfacial  $\text{SO}_4^{2-}$  anions detected should have different hydration shell than in the bulk.  $\text{SO}_4^{2-}$  is known to not approach hydrophobic interfaces<sup>18</sup>, thus we postulate that the adsorbed  $\text{SO}_4^{2-}$  species remain close to the interfacial  $\text{DTA}^+$  cations, with the presence of weakly hydrated  $\text{DTA}^+$  disrupting the hydration shell of  $\text{SO}_4^{2-}$ . As far as interfacial water ordering is concerned, the SHS intensity (Fig. 5.1B) reflects a slight orientation of the interfacial water by the adsorbing  $\text{SO}_4^{2-}$  for concentrations < 150 mM that changes to a strong interfacial water alignment for concentrations > 150 mM. Altogether, the adsorption behaviour of  $\text{SO}_4^{2-}$  seems to be more complex than  $\text{NO}_3^-$ , no further conclusions can be drawn by the present evidence and MD simulations are necessary for a more detailed molecular picture.

### 5.3 Conclusions

We investigated the influence of anionic Hofmeister ions on the interfacial and electric double layer structure of hydrophobic nanodroplets (radius  $\sim 100\text{ nm}$ ) dispersed in aqueous solution and stabilized with a dilute positively charged monolayer of  $\text{DTA}^+$  cations. The adsorption behaviour of the weakly-hydrated  $\text{SCN}^-$  and  $\text{NO}_3^-$ , the well-hydrated  $\text{SO}_4^{2-}$ , and  $\text{Cl}^-$  that lies in between, were compared. Na was always used as the cation in the respective salts added in the bulk aqueous phase. For this study a multi-instrumental approach was implemented, including SFS, SHS and electrokinetic potential measurements. Our results show that all four anions populate the electric double layer of the positively charged interface, neutralizing part of its surface charge, with  $\text{SCN}^-$  having the strongest effect, resulting in inversion of the surface charge. Moreover, the adsorption of  $\text{Cl}^-$  at the nanointerface is accompanied by a slight increase in interfacial water ordering for high concentrations (>100 mM). Interestingly, a complex-multi-regime adsorption pattern is observed for the polyatomic ions for increasing bulk salt concentrations that can be explained as follows:  $\text{SCN}^-$  ion-pairs with/adsorb to interfacial  $\text{DTA}^+$  cations, while it also adsorbs to the bare hydrophobic interface, first (< 100 mM) with its S-atom, then (100 mM – 400 mM) with its N-atom and last (>400 mM) with both orientations;  $\text{NO}_3^-$  first (< 450 mM) adsorbs to/ion-pairs with the interfacial  $\text{DTA}^+$  cations with its most electronegative part (the two oxygens with single N-O bonds), while for larger concentrations (> 400 mM) keeps adsorbing with a configuration more parallel to the interface, possibly at the bare hydrophobic patches; in both cases the water ordering follows,



with a three-regime behaviour of increase-decrease-increase for  $\text{SCN}^-$ , and two-regime behaviour of increase-decrease for,  $\text{NO}_3^-$ . Moreover, indication of ion-pairing/strong interaction of  $\text{SCN}^-$  and  $\text{NO}_3^-$  with the interfacial  $\text{DTA}^+$  cations is observed at concentrations as low as 5 mM. The case of  $\text{SO}_4^{2-}$  seems to be more complex, and only a disruption of its hydration shell upon adsorption can be deduced. Still, the fact that  $\text{SO}_4^{2-}$  is also detected at the nano-interface and affects the orientation of interfacial water, overall even stronger than  $\text{SCN}^-$  and  $\text{NO}_3^-$ .

While the above scenario is not definitive, and simulations are required to further support the picture of the molecular structure of the interface for every anion, our results show the following: The turning point(s) in the multi-regime-behaviour (reflected to the SHS and SFS intensities) signal the bulk salt concentrations at which the balance of intermolecular interactions at the interface changes, allowing for a new adsorption patterns of the newly-coming anions. The above results can be useful for the prediction of the adsorption behaviour of anions on mixed hydrophobic nanointerfaces of charged and bare hydrophobic domains, which are abundant in membranes and proteins.

## 5.4 Appendix

### 5.4.1 DLVO theory predictions

In this section we discuss the predictions of the DLVO theory of colloidal stability for the emulsion systems studied Chapter. 5, following the exact same approach described in detail in Chapter 3.4.2. For convenience we repeat that the DLVO pair potential (interaction energy) of two identical spheres of radius  $R$  at distance  $D$  in an aqueous electrolyte solution with Debye length  $1/\kappa$  is given by

$$W(D) = \frac{1}{2} RZ e^{-\kappa D} - \frac{AR}{12D} \quad (5.1)$$

with the first term describing the double-layer interaction.  $Z$  is the interaction constant and for a temperature of 24 °C (experimental temperature) equals to

$$Z = 9.22 \times 10^{-11} \tanh^2(\psi_0/103) J/m^{-1} \quad (5.2)$$

where  $\psi_0$  is the surface potential of the spheres expressed in mV. The second term of Eq. (5.1) describes the attractive van der Waals forces through the Hamaker constant  $A$ . For the hexadecane/water nanoemulsions studied here (in Chapters 5 and 6) is assumed to have a constant value of  $0.55 \times 10^{-20}$  J (as calculate in detail in Paragraph 3.4.2). For a qualitative comparison of our experimental results with the DLVO theoretical predictions, we assume a constant hydrodynamic radius  $R = 100$  nm and again employ the measured  $\zeta$ -potential values.

In the following, we compare the DLVO pair potentials calculated theoretically when different amounts of the electrolytes NaSCN, NaNO<sub>3</sub>, NaCl and Na<sub>2</sub>SO<sub>4</sub> is added to DTAB stabilized nanodroplets, in correspondence to the systems studied in Chapter 5 and 6. Specifically, Fig. 5.5 displays the theoretically calculated pair potential of two hexadecane nanodroplets in an aqueous solution stabilized with 15 mM DTAB normalized by the thermal energy ( $W/kT$ ) over the distance between their slipping planes expressed in Debye lengths ( $\kappa D$ ) for the addition of different sodium electrolytes in different amounts. The values of the ionic strength, Debye length and  $\zeta$ -potentials used for each panel are presented in Tables 5.1 (for panels a and b), 5.2 (for panel c) and 5.3 (for panel d).



**Table 5.1: Fitting parameters for DLVO pair potentials for DTAB stabilized nanodroplets with the addition of 100 mM of different sodium electrolytes.** The values are used for the calculations presented in Fig. 5.5a and 5.5b.

Component(s)	Ionic strength (mM)	Debye length $1/\kappa$ (nm)	$\zeta$ -potential (mV)
15 mM DTA <sup>+</sup>	15	2.48	71.6 $\pm$ 7
15 mM DTA <sup>+</sup> + 100 mM NaSCN	115	0.9	17.3 $\pm$ 7
15 mM DTA <sup>+</sup> + 100 mM NaNO <sub>3</sub>	115	0.9	37 $\pm$ 7
15 mM DTA <sup>+</sup> + 100 mM NaCl	115	0.9	38.5 $\pm$ 7
15 mM DTA <sup>+</sup> + 100 mM Na <sub>2</sub> SO <sub>4</sub>	315	0.54	29.9 $\pm$ 7

**Table 5.2: Fitting parameters for DLVO pair potentials for DTAB stabilized nanodroplets with the addition of the critical coagulation concentration of different sodium electrolytes.** The values are used for the calculations presented in Fig. 5.5c.

Component(s)	Ionic strength (mM)	Debye length $1/\kappa$ (nm)	$\zeta$ -potential (mV)
15 mM DTA <sup>+</sup>	15	2.48	71.6 $\pm$ 7
15 mM DTA <sup>+</sup> + 100 mM NaSCN	115	0.9	17.3 $\pm$ 7
15 mM DTA <sup>+</sup> + 400 mM NaNO <sub>3</sub>	415	0.47	24 $\pm$ 7
15 mM DTA <sup>+</sup> + 300 mM NaCl	315	0.54	22 $\pm$ 7
15 mM DTA <sup>+</sup> + 200 mM Na <sub>2</sub> SO <sub>4</sub>	615	0.39	26.3 $\pm$ 7

**Table 5.3: Fitting parameters for DLVO pair potentials for DTAB stabilized nanodroplets with the addition of different concentrations of NaSCN.** The values are used for the calculations presented in Fig. 5.5d.

Component(s)	Ionic strength (mM)	Debye length $1/\kappa$ (nm)	$\zeta$ -potential (mV)
15 mM DTA <sup>+</sup> +			
25 mM NaSCN	40	1.52	47 $\pm$ 7
100 mM NaSCN	115	0.9	17.3 $\pm$ 7
350 mM NaSCN	365	0.5	0.4 $\pm$ 7
600 mM NaSCN	615	0.39	-11.2 $\pm$ 7

In a DLVO pair potential plot the peak of the plot is the *energy barrier* that the pair potential of two droplets has to overcome in order to reach the *primary minimum*, i.e. the minimum value that corresponds to thermodynamic stability and is situated close to  $\kappa D = 0$ . The latter reflects the coagulation of the droplets and, as expected, for thermodynamic stability phase separation is required and the emulsions can remain only kinetically stable for some time. It follows that the higher the energy barrier the better the stability of an emulsion is expected to

be. However, sometimes a *secondary minimum* appears in the DLVO pair potential plot, where the droplets can sit while being kinetically stable. Below some certain charge or potential, or above some electrolyte concentration known as the *critical coagulation concentration*, the energy barrier falls below the axis  $W = 0$  and the particles coagulate rapidly, with the emulsion being unstable.

In Fig. 5.5 we first (panels a and b) compare the pair potentials for DTAB stabilized nanodroplets without and with the addition of 100 mM of each salt, a salt concentration for which the  $\zeta$ -potential of the nanodroplets is still clearly positive (Fig. 5.1a). It can be seen that the addition of any salt results in a drop of the energy barrier, resulting in a less stable emulsion. Especially the addition of  $\text{NaNO}_3$  and  $\text{NaCl}$  has apparently similar effect on the value of the energy barrier. This is followed by a smaller energy barrier for  $\text{Na}_2\text{SO}_4$  and  $\text{NaSCN}$ . While with the addition of 100 mM  $\text{NaNO}_3$ ,  $\text{NaCl}$  and  $\text{Na}_2\text{SO}_4$  the emulsion seems to still remain stable, the 100 mM seems to be the critical coagulation concentration for  $\text{NaSCN}$ , rendering the emulsion unstable. Note that the ion specificity in these DLVO plots is not coming from the mean field model employed for the calculations, but from the experimental  $\zeta$ -potential data that we have measured.

A step further, we checked for each salt which of the concentration measured experimentally is closer to the critical coagulation concentration and the results are presented in Fig. 5.5c. It can be seen that the energy barrier is  $\sim 0$  for 100 mM  $\text{NaSCN}$ , 400 mM  $\text{NaNO}_3$ , 300 mM  $\text{NaCl}$  and 200 mM  $\text{Na}_2\text{SO}_4$ . As such, emulsions with the addition of each salt at concentrations higher than the ones presented in Fig. 5.5c are expected to be unstable. This was indeed found to be the case for  $\text{Na}_2\text{SO}_4$ . However, for the rest of the salts the nanoemulsions remained stable over the whole range between 0 and 600 mM. The discrepancy between DLVO theory predictions and our experimental results is the most striking in the case of  $\text{NaSCN}$  as shown in Fig. 5.5d. Here the pair potential is calculated for 25 mM, 100 mM, 350 mM and 600 mM  $\text{NaSCN}$ . As can be seen from Table 5.3, at this concentration values the  $\zeta$ -potential starts from very positive (+ 47 mV), continues to less positive (+ 17.3 mV), then becomes about zero (+ 0.4 mV) and then slightly negative (- 11.2 mV). From Fig. 5.5d it would be expected that all DTAB stabilized emulsions with added  $\text{NaSCN}$  in concentrations equal or higher than 100 mM should be unstable. However, this is clearly not the case as shown with our experimental studies in this Chapter, and as well with the results of Chapter 6.

Overall, it can be seen that the DLVO theory, which is based on the mean field approximation and continuum models, cannot capture the stability of systems with complex interfacial structure like the nanodroplets studied in this work. As discussed in detail in Chapter 3, 5 and 6, a complex interfacial pattern with hydrophobic and hydrophilic parts/patches that affects the interfacial water structure accordingly can ensure kinetic

stability of nanoemulsions even when the overall electrostatic repulsion between nanodroplets seems to be too low. As such, molecular level information is necessary for a thorough study and comprehension of the stability mechanisms of nanoemulsions.

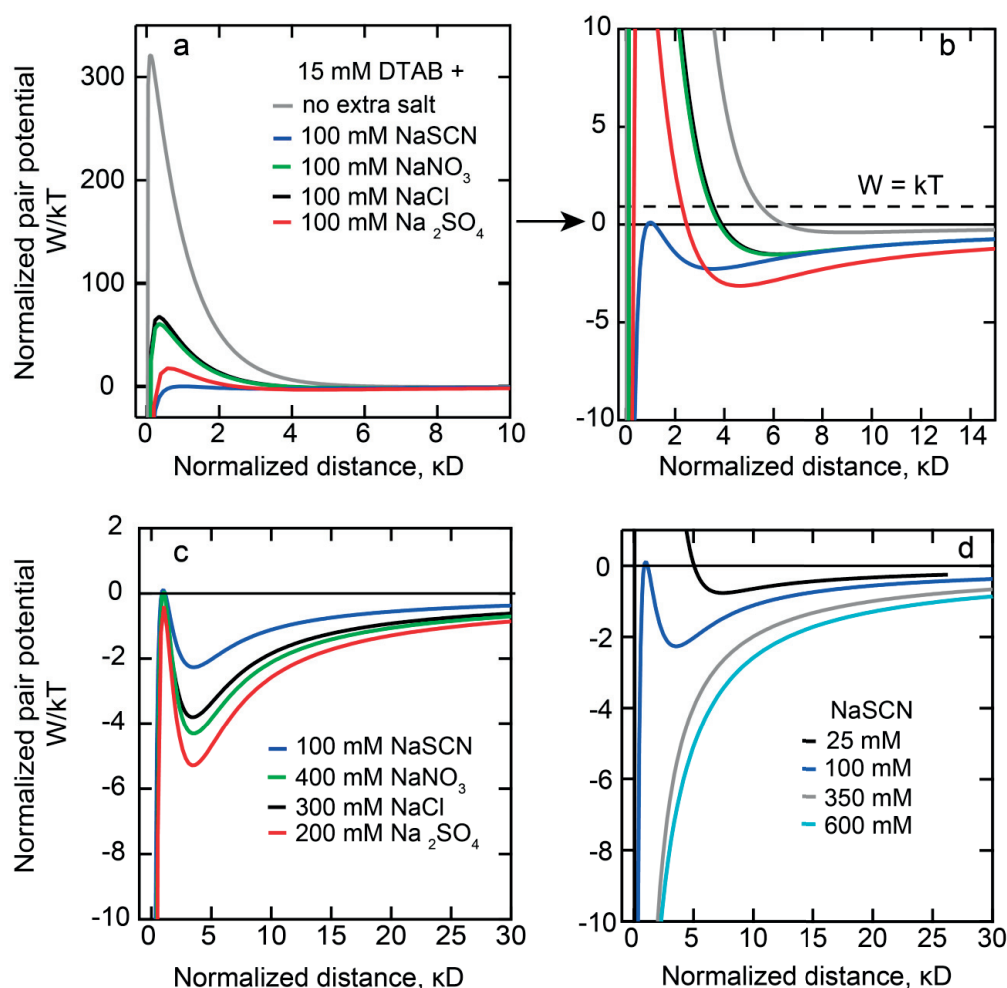


**Figure 5.5: DLVO pair potentials of DTAB stabilized hexadecane nanodroplets in water for the addition of different electrolytes.** Pair potential of hexadecane nanodroplets in water stabilized with 15 mM DTAB (expressed in  $kT$ ) over distance between their slipping planes (expressed in Debye lengths) for the addition of different types and amounts of sodium electrolytes. In panels a, b and c the cases of addition of no extra salt (grey), NaSCN (blue), NaNO<sub>3</sub> (green), NaCl (black) and Na<sub>2</sub>SO<sub>4</sub> (red) are compared. In panel d results are shown only for the addition of different concentrations of NaSCN, from 25 mM (black), 100 mM (blue), 350 mM (grey) and 600 mM (light blue). Equations 5.1 and 5.2 were employed for radius  $R = 100$  nm and Hamaker constant  $A = 0.55 \times 10^{-20}$  J for all systems. The values of  $\zeta$ -potential and Debye lengths are presented in Table 5.1 for panels a and b, 5.2 for panel c and 5.3 for panel d.

## 5.5 References

1. Salis, A. & Ninham, B. W. Models and mechanisms of Hofmeister effects in electrolyte solutions, and colloid and protein systems revisited. *Chem. Soc. Rev.* **43** (21), 7358-7377 (2014).
2. Jungwirth, P. & Tobias, D. J. Specific ion effects at the air/water interface. *Chem. Rev.* **106** (4), 1259-1281 (2006).
3. Kunz, W. Specific ion effects in colloidal and biological systems. *Curr. Opin. Colloid Interface Sci.* **15** (1), 34-39 (2010).
4. Scheu, R., Rankin, B. M., Chen, Y. X., Jena, K. C., Ben-Amotz, D. & Roke, S. Charge asymmetry at aqueous hydrophobic interfaces and hydration shells. *Angew. Chem., Int. Ed.* **53** (36), 9560-9563 (2014).
5. Tobias, D. J. & Hemminger, J. C. Getting specific about specific ion effects. *Science* **319** (5867), 1197-1198 (2008).
6. Hofmeister, F. Zur lehre von der wirkung der salze. *Arch. Exp. Pathol. Pharmacol.* **24**, 247-260 (1888).
7. Flores, S. C., Kherb, J., Konelick, N., Chen, X. & Cremer, P. S. The effects of Hofmeister cations at negatively charged hydrophilic surfaces. *J. Phys. Chem. C* **116** (9), 5730-5734 (2012).
8. Luo, G., Malkova, S., Yoon, J., Schultz, D. G., Lin, B., Meron, M., Benjamin, I., Vanýsek, P. & Schlossman, M. L. Ion distributions near a liquid-liquid interface. *Science* **311** (5758), 216-218 (2006).
9. Boström, M., Deniz, V. & Ninham, B. W. Ion specific surface forces between membrane surfaces. *J. Phys. Chem. B* **110** (19), 9645-9649 (2006).
10. Casillas-Ituarte, N., Chen, X., Castada, H. & Allen, H. C. Na<sup>+</sup> and Ca<sup>2+</sup> effect on the hydration and orientation of the phosphate group of DPPC at air-water and air-hydrated silica interfaces. *J. Phys. Chem. B* **114** (29), 9485-9495 (2010).
11. P, V., Aroti, A., Motschmann, H. & Leontidis, E. Vibrational sum frequency generation spectroscopic investigation of the interaction of thiocyanate ions with zwitterionic phospholipid monolayers at the air-water interface. *J. Phys. Chem. B* **113** (44), 14816-14823 (2009).
12. Dreier, L. B., Nagata, Y., Lutz, H., Gonella, G., Hunger, J., Backus, E. H. G. & Bonn, M. Saturation of charge-induced water alignment at model membrane surfaces. *Science Advances* **4** (3), (2018).
13. Dengler, S., Klaus, A., Tiddy, G. J. T. & Kunz, W. How specific are ion specificities? A pilot NMR study. *Faraday Discussions* **160** (0), 121-133 (2013).

14. De Aguiar, H. B., De Beer, A. G. F., Strader, M. L. & Roke, S. The interfacial tension of nanoscopic oil droplets in water is hardly affected by SDS surfactant. *J. Am. Chem. Soc.* **132**, 2122-2123 (2010).
15. De Aguiar, H. B., Strader, M. L., De Beer, A. G. F. & Roke, S. Surface structure of sodium dodecyl sulfate surfactant and oil at the oil-in-water droplet liquid/liquid interface: A manifestation of a non-equilibrium surface state. *J. Phys. Chem. B* **115**, 2970-2978 (2011).
16. Smolentsev, N., Smit, W. J., Bakker, H. J. & Roke, S. The interfacial structure of water droplets in a hydrophobic liquid. *Nat. Commun.* **8**, 15548 (2017).
17. Zdrali, E., Chen, Y., Okur, H. I., Wilkins, D. M. & Roke, S. The molecular mechanism of nanodroplet stability. *ACS Nano* **11** (12), 12111-12120 (2017).
18. Zhang, Y. & Cremer, P. S. Chemistry of Hofmeister anions and osmolytes. *Annu. Rev. Phys. Chem.* **61** (1), 63-83 (2010).
19. Roke, S. & Gonella, G. Nonlinear light scattering and spectroscopy of particles and droplets in liquids. *Annu. Rev. Phys. Chem.* **63**, 353-378 (2012).
20. Wang, H., Yan, E. C. Y., Borguet, E. & Eisenthal, K. B. Second harmonic generation from the surface of centrosymmetric particles in bulk solution. *Chem. Phys. Lett.* **259** (1-2), 15-20 (1996).
21. Roke, S., Roeterdink, W. G., Wijnhoven, J. E. G. J., Petukhov, A. V., Kleyn, A. W. & Bonn, M. Vibrational sum frequency scattering from a submicron suspension. *Phys. Rev. Lett.* **91** (25), 258302 (2003).
22. Hunter, R. J. *Zeta potential in colloid science: Principles and applications* (Academic Press, London, 1981).
23. Scheu, R., Chen, Y. X., Subinya, M. & Roke, S. Stern layer formation induced by hydrophobic interactions: A molecular level study. *J. Am. Chem. Soc.* **135** (51), 19330-19335 (2013).
24. Scheu, R., Chen, Y. X., De Aguiar, H. B., Rankin, B. M., Ben-Amotz, D. & Roke, S. Specific ion effects in amphiphile hydration and interface stabilization. *J. Am. Chem. Soc.* **136** (5), 2040-2047 (2014).
25. Schürer, B., Wunderlich, S., Sauerbeck, C., Peschel, U. & Peukert, W. Probing colloidal interfaces by angle-resolved second harmonic light scattering. *Phys. Rev. B* **82** (24), 241404-241404 (2010).
26. Okur, H. I., Hladílková, J., Rembert, K. B., Cho, Y., Heyda, J., Dzubiella, J., Cremer, P. S. & Jungwirth, P. Beyond the Hofmeister series: Ion-specific effects on proteins and their biological functions. *J. Phys. Chem. B* **121** (9), 1997-2014 (2017).

27. Robinson, J. B., Strottmann, J. M. & Stellwagen, E. Prediction of neutral salt elution profiles for affinity chromatography. *Proc. Natl. Acad. Sci. U. S. A.* **78** (4), 2287-2291 (1981).
28. Wang, X.-B., Yang, X., Nicholas, J. B. & Wang, L.-S. Bulk-like features in the photoemission spectra of hydrated doubly charged anion clusters. *Science* **294** (5545), 1322-1325 (2001).
29. Van Der Vegt, N. F. A., Haldrup, K., Roke, S., Zheng, J., Lund, M. & Bakker, H. J. Water-mediated ion pairing: Occurrence and relevance. *Chem. Rev.* **116** (13), 7626-7641 (2016).
30. Johnson, C. M. & Baldelli, S. Vibrational sum frequency spectroscopy studies of the influence of solutes and phospholipids at vapor/water interfaces relevant to biological and environmental systems. *Chem. Rev.* **114** (17), 8416-8446 (2014).
31. Lambert, A. G., Davies, P. B. & Neivandt, D. J. Implementing the theory of sum frequency generation vibrational spectroscopy: A tutorial review. *Appl. Spectr. Rev.* **40**, 103-144 (2005).
32. Jubb, A. M. & Allen, H. C. Sulfate adsorption at the buried fluorite–solution interface revealed by vibrational sum frequency generation spectroscopy. *J. Phys. Chem. C* **116** (16), 9085-9091 (2012).
33. Xu, M., Tang, C. Y., Jubb, A. M., Chen, X. & Allen, H. C. Nitrate anions and ion pairing at the air–aqueous interface. *J. Phys. Chem. C* **113** (6), 2082-2087 (2009).
34. Kinell, P. O. & Strandberg, B. Infrared and Raman spectra of some systems contraining thiocyanate groups. *Acta Chem. Scand.* **13** (8), 1607-1622 (1959).
35. Hester, R. E. & Plane, R. A. Vibrational spectroscopic study of contact ion pairing between  $\text{zn}^{++}$  and  $\text{no}_3^-$  in water. *J. Chem. Phys.* **45** (12), 4588-4593 (1966).
36. Irish, D. E. & Walrafen, G. E. Raman and infrared spectral studies of aqueous calcium nitrate solutions. *J. Chem. Phys.* **46** (1), 378-384 (1967).
37. Wahab, A., Mahiuddin, S., Hefter, G., Kunz, W., Minofar, B. & Jungwirth, P. Ultrasonic velocities, densities, viscosities, electrical conductivities, Raman spectra, and molecular dynamics simulations of aqueous solutions of  $\text{mg}(\text{oac})_2$  and  $\text{mg}(\text{no}_3)_2$ : Hofmeister effects and ion pair formation. *J. Phys. Chem. B* **109** (50), 24108-24120 (2005).
38. Marinova, K. G., Alargova, R. G., Denkov, N. D., Velev, O. D., Petsev, D. N., Ivanov, I. B. & Borwankar, R. P. Charging of oil–water interfaces due to spontaneous adsorption of hydroxyl ions. *Langmuir* **12** (8), 2045-2051 (1996).
39. Riddell, J. D., Lockwood, D. J. & Irish, D. E. Ion pair formation in  $\text{nano}_3/\text{D}_2\text{O}$  solutions: Raman and infrared spectra, partial molal volumes, conductance, and viscosity. *Can. J. Chem.* **50** (18), 2951-2962 (1972).

## Chapter 6: The diverse nature of ion speciation at the nanoscale hydrophobic/water interface

*Many biological systems are composed of nanoscale structures having hydrophobic and hydrophilic groups adjacent to one another and in contact with aqueous electrolyte solution. The interaction of ions with such structures is of fundamental importance. Although many studies have focused on characterizing planar extended (often air/water) interfaces, little is known about ion speciation at complex nanoscale biological systems. To start understanding the complex mechanisms involved, we use a hexadecane nanodroplet system, stabilized with a dilute monolayer of positively charged (DTA<sup>+</sup>) groups in contact with an electrolyte solution (NaSCN). Using vibrational sum frequency scattering, second harmonic scattering,  $\zeta$ -potential measurements and quantum density functional theory we find DTA<sup>+</sup>-SCN<sup>-</sup> ion pairing at concentrations as low as 5 millimolar. A variety of ion species emerge at different ionic strengths, with differently oriented SCN<sup>-</sup> groups adsorbed on hydrophilic or hydrophobic parts of the surface. This diverse and heterogeneous chemical environment is surprisingly different from the behaviour at extended liquid planar interfaces, where ion pairing is typically detected at molar concentrations and nanoscale system stability is no requirement.*

*For the work presented in this chapter, Evangelia Zdrali performed SFS and SHS measurements and related data analysis.*

*Dr. Marcel D. Baer and Prof. Christopher Mundy (from the Pacific Northwest National Laboratory) performed the ab-initio molecular dynamics simulations and the related data analysis.*



## 6.1 Introduction

Biological change occurs at the interfaces of cell membranes, organelles, and on the complex interfaces of proteins and other macromolecules<sup>1</sup>. What all of these systems have in common is a mixed hydrophobic / hydrophilic heterogeneous environment confined to a sub-micron length scale or divided in the micron-sized non-uniform structures<sup>2</sup>. The interaction with electrolytes in the adjacent cytoplasm or extracellular matrix is particularly important as it drives a myriad of biological processes in the cells. Nevertheless, the rules that govern these interactions are not fully understood, and are generally inferred from experiments and computations performed on more simple systems: Ion-ion and ion-solute interactions in bulk solutions have been extensively studied with a quantum mechanical description of the molecular interaction in conjunction with molecular dynamics (MD) simulations<sup>3-10</sup>, as well as with numerous experimental techniques. More specifically, conductometry and solubility measurements along with a variety of spectroscopic methods, such as dielectric relaxation<sup>11</sup>, UV-VIS<sup>12</sup>, fs mid-IR<sup>13</sup>, fs 2D IR<sup>14</sup>, X-ray absorption<sup>15</sup> and X-ray scattering<sup>16</sup> have been employed. Ion-ion and ion-water interactions have been studied as well on air/water interfaces<sup>17-20</sup> with optical reflection schemes employing surface-specific experimental techniques<sup>21</sup>, such as sum frequency generation<sup>22-24</sup>, second harmonic generation<sup>10,25</sup> and surface-enhanced Raman spectroscopy<sup>26</sup>.

Due to the complexity of real biological systems, the molecular level details of the interactions of ions with ionic, hydrophilic and hydrophobic groups at nanoscale and sub-micron-sized-domain liquid interfaces have remained unexplored. It is becoming increasingly clear, however, that system downscaling towards nanometers leads to significant differences in the balance of interactions, molecular structure, and function. This is exemplified by the fact that the interfacial structure of water on nanoscale interfaces is much more ordered than on the equivalent macroscopic interface<sup>27</sup>. In addition, the stability and structure of charged nanoscale objects is different, not only because of curvature<sup>28</sup>, but also because of a different balance in electrostatic and hydrogen bonding interactions<sup>29</sup>. Such effects are observed in nanoscale membrane systems<sup>30</sup>.

Given the complexity, ideally one combines a well understood nanoscale interfacial model system, with interfacial charges as well as hydrophobic and hydrophilic groups, with the appropriate experimental techniques. These groups, as well as the water and the ions in the electrolyte solution are ideally experimentally verifiable with unique observables which should then be able to be connected to molecular structures via a waterproof interpretation. In line with this approach, here, we use a combination of sum frequency scattering (SFS)<sup>31,32</sup>, angle resolved<sup>33</sup> second harmonic scattering (AR-SHS)<sup>32,34</sup>, electrokinetic mobility measurements and ab-initio MD simulations, which are essential for the interpretation of the



experimental data. With SFS the vibrational mode(s) of the ion(s) of interest can be probed, which directly report(s) on ion speciation<sup>21</sup>: Changes in the amplitude, peak position, full width at half maximum and the appearance of a new vibrational band<sup>23,24</sup> can be considered strong evidence of a reconfiguration of the interfacial structure, such as the formation of ion pairs. Additionally, non-resonant AR-SHS is a probe for the orientational order of interfacial water molecules, detailing the differences in orientational directionality along the surface normal between interfacial water molecules and bulk water molecules<sup>25,35</sup>. This multi-instrumental approach is employed on an appropriate system for which we can measure the  $\zeta$ -potential and determine the water orientation and the structure of ionic species: We have chosen to study hexadecane oil nanodroplets stabilized with dodecyltrimethylammonium cations (DTA<sup>+</sup>) in aqueous solution, a system for which the surface charge density, as well as the molecular structure of all participating molecules are known<sup>29</sup>. As electrolyte, NaSCN has been especially added in the aqueous solution because thiocyanate (SCN<sup>-</sup>) anions are ideal probes for their interaction with the nanointerface. The reason is that their CN vibrational mode is well characterized (both in solution<sup>36,37</sup> and at planar extended interfaces<sup>38</sup>) and very sensitive to the environment<sup>39</sup>. As such, it has been probed before with SFS in the vicinity of surfactants<sup>40</sup> and lipids<sup>41,42</sup> extracting valuable biologically relevant information. Moreover, in addition to having a charge they also have a sizeable dipole moment<sup>43</sup>.

With the above combination of system and methods we find that ion speciation at the nanoscale is remarkably diverse and different from solution and planar extended interfaces. Specifically, the CN vibration of SCN<sup>-</sup> in bulk solution gives rise to a peak at  $\sim 2065 \text{ cm}^{-1}$  while in the presence of the nanodroplet oil/water interface we detect frequency shifts: A red shifted vibrational peak is observed when the SCN<sup>-</sup> molecule is present at the neat oil/water interface, in contrast to a blue shifted peak when SCN<sup>-</sup> interacts with DTA<sup>+</sup> ions already present at the interface. The latter is observed already at NaSCN concentrations as low as 5 mM and constitutes strong evidence of ion pairing of the SCN<sup>-</sup> with the interfacial DTA<sup>+</sup>. Using these CN vibrational features as a signature, we distinguish three different ranges of increasing bulk NaSCN concentration over which the adsorbing SCN<sup>-</sup> anions follow different patterns: At low salt concentrations ( $\leq 100 \text{ mM}$ ) addition of NaSCN leads to an increase of the SCN<sup>-</sup> population adsorbed to the neat hydrophobic surface with a preferred orientation. For middle SCN<sup>-</sup> concentrations (between 100 mM and 400 mM) this SCN<sup>-</sup> population keeps increasing, however with an opposite molecular orientation. Finally, at high NaSCN concentrations ( $\geq 400 \text{ mM}$ ) no preference for one of the two orientations is observed for the newly arriving SCN<sup>-</sup>. This behaviour is attributed to dipole-dipole interactions between interfacial SCN<sup>-</sup> anions. At the same time, the amount of SCN<sup>-</sup> associated with DTA<sup>+</sup> remains practically constant over the whole concentration range.

## 6.2 Results and Discussion

In the following sections we describe the influence of the addition of NaSCN to hexadecane nanodroplets stabilized with a dilute layer of DTA<sup>+</sup> ions on the electrokinetic mobility, the SHS and the SFS responses. We distinguish three different concentration regimes for SCN<sup>-</sup> ion adsorption that give rise to different types of behaviour in the measured responses. We refer to them as 'low' ( $\leq 100$  mM NaSCN concentration added to the system), 'middle' (NaSCN concentrations between 100 mM and 400 mM), and 'high' (NaSCN concentrations  $\geq 400$  mM). We use these indicators consistently throughout the text. They are also highlighted with different background colours in Figs. 6.1 and 6.2B.

### 6.2.1 Electrokinetic mobility

Figure 6.1A presents the  $\zeta$ -potential<sup>44</sup> around DTAB stabilized nanodroplets (radius  $\sim 100$  nm, oil concentration 0.5 vol. %) over increasing bulk NaCl and NaSCN salt concentrations, ranging from 0 to 600 mM. The Cl<sup>-</sup> anion has been chosen as a reference for surface activity, as usually in Hofmeister series studies, whereas the SCN<sup>-</sup> ion is known for its strong surface activity towards various interfaces<sup>17</sup>. It can be seen that, in the absence of salt the  $\zeta$ -potential value is  $+66 \pm 7$  mV, and it drops when salt is added in the bulk aqueous phase, already at concentrations as low as 5 mM. Initially, at low concentrations, the decrease is steep (about -0.34 mV/mM for NaCl and -0.8 mV/mM for NaSCN), while for middle and high concentrations it becomes less steep ( $\sim -0.06$  mV/mM for both salts). Comparing the two salts, clearly the addition of NaSCN induces a larger drop of the  $\zeta$ -potential values than when NaCl is added, over the whole concentration range. Especially for concentrations  $>50$  mM, the value for NaSCN is  $\sim 20$  mV smaller than for NaCl. Moreover, for NaCl the  $\zeta$ -potential remains positive over the whole concentration range, reaching a minimum value of 10 mV at 600 mM, while for NaSCN it crosses the isoelectric point<sup>44</sup> at  $\sim 350 - 400$  mM, reaching a negative minimum value of -10 mV at 600 mM. Interestingly, the droplets are stable over the whole concentration range probed, even in the range where they are overall charge neutral.

The monotonic decrease of the  $\zeta$ -potential presented in Fig. 6.1A points towards a continuously increasing concentration of both Cl<sup>-</sup> and SCN<sup>-</sup> anions inside the electric double layer. However, the discrepancies between the two systems suggest a stronger interfacial activity of SCN<sup>-</sup> compared to Cl<sup>-</sup>. Note that the possibility of decreasing DTA<sup>+</sup> concentration at the interface, which would result in a similar observation even for constant or decreasing anionic concentration, has been excluded by control SFS measurements of the number density of interfacial DTA<sup>+</sup> cations<sup>45</sup> (see Paragraph 6.4.1 of the Appendix).

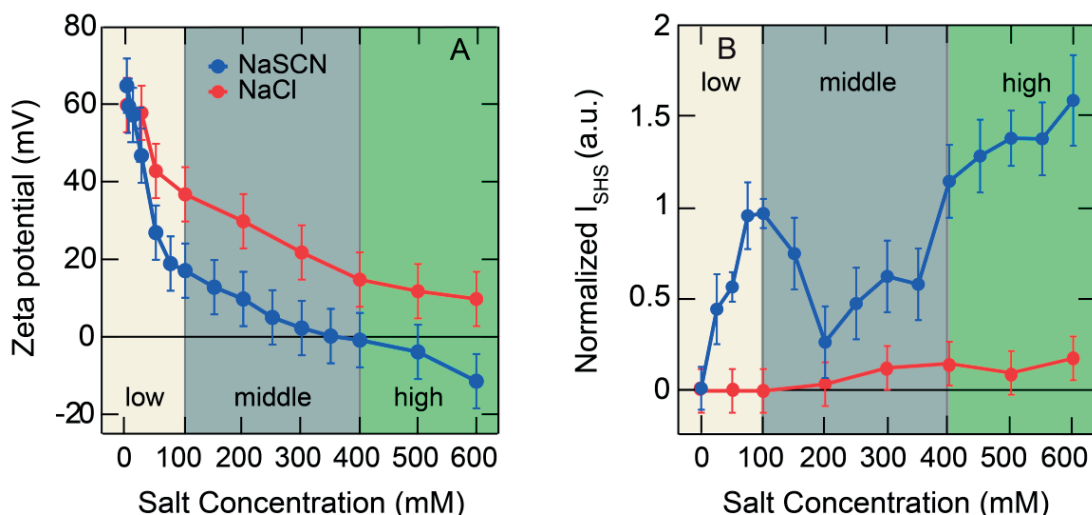


**Figure 6.1: Electrokinetic potential and interfacial water ordering.** (A)  $\zeta$ -Potential of 0.5 vol % n-hexadecane nanodroplets in  $H_2O$  stabilized with 15 mM DTAB over increasing bulk concentrations of NaCl (red) and NaSCN (blue). (B) SHS intensity of the same droplet samples. Both the fundamental and the second harmonic frequency beams were polarized parallel to the scattering plane (i.e. P-polarized). SHS intensities were measured at a scattering angle of maximum intensity of  $45^\circ$  with respect to the incoming beam and normalized by the pure water signal at the same angle and polarization combination (see Paragraph 2.3.3 for more details). The three bulk NaSCN concentration regimes over which the SHS intensity follows a different behaviour are shown in white ('low'), grey ('middle') and green ('high') background.

## 6.2.2 Interfacial water ordering

SHS intensity ( $I_{SHS}$ ) reports on the interfacial water ordering along the surface normal, which is crucially affected by both the surface density and structure of the molecular components of the oil-nanodroplet/water interface<sup>25</sup>. As shown before, the  $I_{SHS}$  measured for nanodroplets stabilized with 15 mM of DTAB, without the addition of salt, is zero<sup>46</sup>. Thus, the presence of such droplets does not induce any extra interfacial water ordering along the surface normal, as compared to bulk water. Figure 6.1B presents the SHS intensity<sup>33</sup> when NaCl and NaSCN are added in the above system for bulk salt concentrations between 0 mM and 600 mM. It can be seen that, for addition of NaCl, only a slight increase in  $I_{SHS}$  is observed, and only for concentrations  $>100$  mM, with the value levelling off at 0.18 above 200 mM. (Details about the SHS experiments and the normalization process can be found in Paragraph 2.3.3.) This result can be rationalized by noting that a slightly increased concentration of  $Cl^-$  ions in the electric double layer (as observed in Figure 6.1A), induces a small amount of additional water ordering along the interfacial normal.

In contrast, when NaSCN is added to the system, a strikingly different behaviour is observed despite the same charge of the two anions (Fig. 6.1B): For low salt concentrations

(white background) a steep monotonic increase in SHS intensity appears, reaching a maximum value of 1. At middle concentrations (grey background) a drop is observed, with a minimum at 200 mM. At high concentrations (green background) a monotonic increase is again observed, as if continuing the increase observed at low concentrations. As a result, the addition of NaSCN induces an overall maximum increase in  $I_{\text{SHS}}$  by an order of magnitude larger (1.7 at 600 mM) than  $\text{Cl}^-$  (0.17 at 600 mM).  $\text{SCN}^-$  is known to be more surface active compared to  $\text{Cl}^-$ <sup>47</sup>. Nevertheless, the three-distinct-regimes behaviour (for low, middle and high concentrations) observed for SHS intensity is rather surprising. Therefore, to investigate the chemical speciation in more detail we use SFS.

### 6.2.3 Surface density and structure of $\text{SCN}^-$

SFS measurements can report directly on the ion of interest rather than the surrounding water<sup>21,48</sup>. Figure 6.2A displays the SFS spectra of the CN stretch mode<sup>36</sup> of  $\text{SCN}^-$  anions at the DTAB stabilized  $d_{34}$ -hexadecane/ $\text{D}_2\text{O}$  nanodroplet interface, indicatively, for four bulk NaSCN aqueous concentrations between 5 mM and 600 mM. A broad peak centered at  $\sim 2045 \text{ cm}^{-1}$  with FWHM of  $\sim 50 \text{ cm}^{-1}$  is observed, with changing amplitude for different concentrations. Figure 6.2B shows the integrated intensity of the SFS spectra covering the  $2000 \text{ cm}^{-1} - 2150 \text{ cm}^{-1}$  spectral window. It can be seen that there are three concentration ranges (with different background colour) over which the SFS intensity of the CN mode follows different trends, in correspondence with the three ranges observed in SHS (Fig. 6.1B): At low bulk NaSCN concentrations an increase is observed, followed by a decrease at middle concentrations.

As discussed in previous studies performed in our laboratory<sup>46</sup>, also for SFS, such experimental spectra can be fitted with a superposition of a number of Lorentzian shaped vibrational modes. The spectra in Fig. 6.2A require three vibrational modes to obtain satisfactory fits with resonance frequencies of 2045, 2110 and  $2062 \text{ cm}^{-1}$ . (Note that the spectral fits are displayed further down in Fig. 6.4.) Figure 6.3A displays the fitted resonances together with their respective phases ( $\phi$ ), while the inset presents the amplitude of the three modes that resulted from the fitting as a function of NaSCN bulk concentration. It seems that the bands at 2045 and  $2110 \text{ cm}^{-1}$  are present over the whole NaSCN concentration range, and have the same phase ( $\phi = 0^\circ$ ), while the  $2062 \text{ cm}^{-1}$  peak appears only for concentrations  $>100 \text{ mM}$ , and has the opposite phase ( $\phi = 180^\circ$ ). Moreover, the amplitude of the mode at  $2110 \text{ cm}^{-1}$  remains practically constant between 5 mM and 600 mM, whereas the amplitude of the mode at  $2045 \text{ cm}^{-1}$  remains constant up to 100 mM, then increases up to 200 mM, and then decreases back to the value at 5 mM NaSCN. The mode

at  $2062\text{ cm}^{-1}$  is absent at first, then rises in amplitude to a maximum at 400 mM, after which it drops down. It thus follows that, since the amplitude of the mode at  $2110\text{ cm}^{-1}$  is practically constant, the peculiar shape of the SFS amplitude in Fig. 6.2B is a result of the destructive interference of the  $2045$  and  $2062\text{ cm}^{-1}$  modes. A detailed description of the fitting procedure can be found in the Appendix (paragraph 6.4.2). The phase difference observed in the fitting, as well as the need for multiple resonances, suggest that multiple surface chemical species are involved with potentially different orientations of the  $\text{SCN}^-$  ions. Such differences could also explain the fluctuations observed in the interfacial water orientation. Which species are present exactly is speculative and cannot be derived just from the vibrational resonances, without the help of simulations.

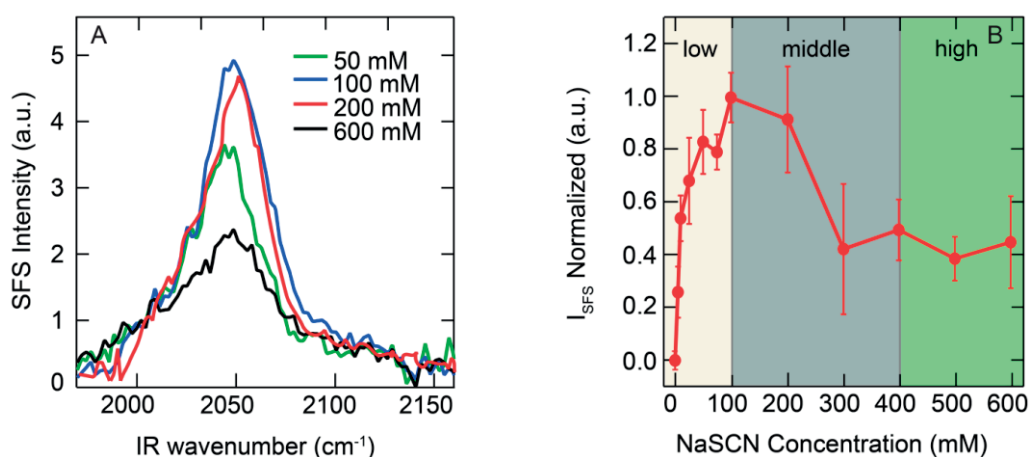


**Figure 6.2: Interfacial structure of  $\text{SCN}^-$ .** SFS measurements on hexadecane nanodroplets ( $R \sim 100\text{ nm}$ , 1 vol % concentration) stabilized with 15 mM DTAB in solution of NaSCN in  $\text{D}_2\text{O}$ . (A) Vibrational spectra of the CN bond of interfacial  $\text{SCN}^-$  anions for several bulk aqueous NaSCN concentrations between 5 mM and 600 mM. The spectra were recorded in the SSP polarization combination, which indicates that the sum frequency and visible beams were polarized perpendicular with respect to the scattering plane, while the infrared beam was polarized parallel to it. (B) Normalized integrated SFS amplitude over increasing bulk concentration of NaSCN calculated by integration of the area of the vibrational spectra between  $2000\text{ cm}^{-1}$  and  $2150\text{ cm}^{-1}$ . The value of integrated intensity at 0 mM was finally subtracted. The different backgrounds in B (white for low, grey for middle and green for high concentrations) separate the three concentration ranges over which  $I_{\text{SFS}}$  shows different trend.

## 6.2.4 MD simulation results

Therefore, we interpret the experimental results with *ab initio* Molecular Dynamics (MD) simulations of the solvation of  $\text{SCN}^-$  both at the bare hydrophobic-water interface and the hydrophobic-water interface in the vicinity of a  $\text{DTA}^+$  molecule. The results for these two limiting, experimentally relevant, cases are of fundamental importance, and allow us to provide a near quantitative interpretation of the measured data, and directly connect to the



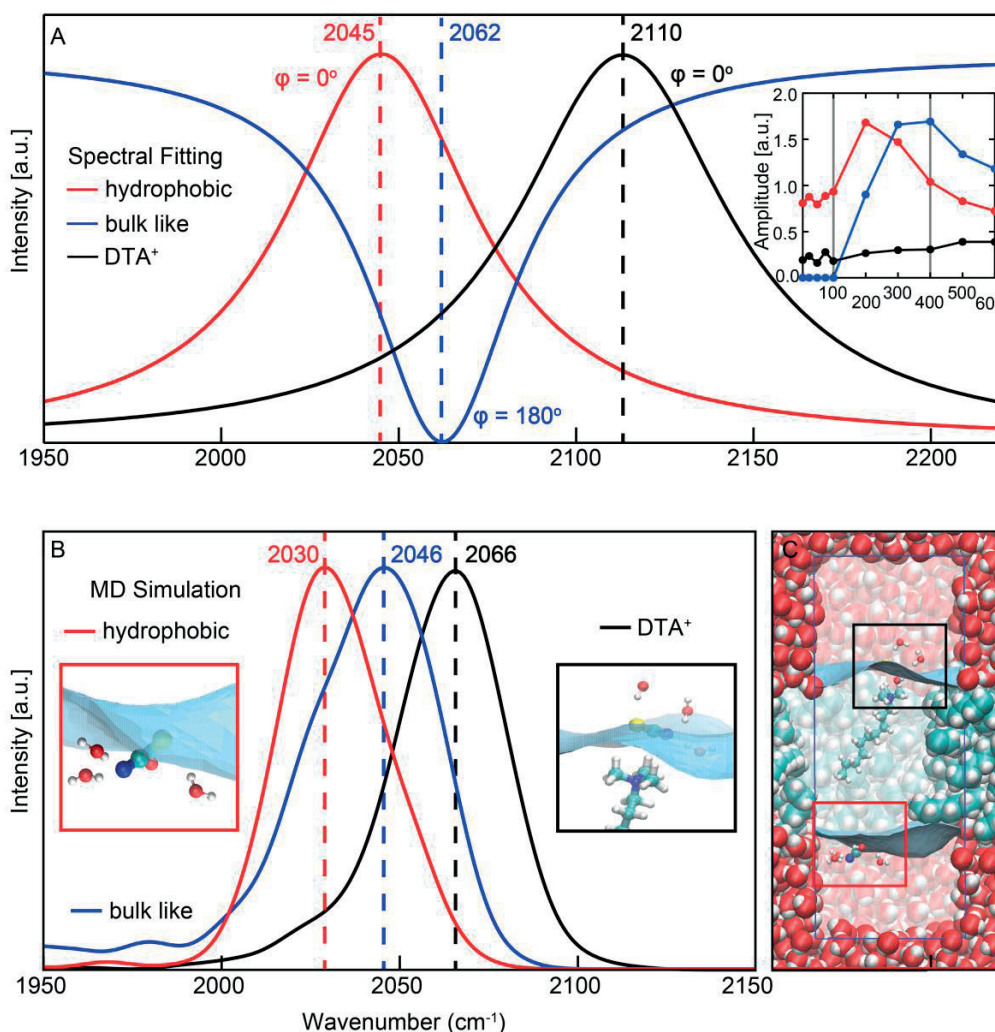


**Figure 6.3: Vibrational modes from fitting and MD simulations.** (A) The three Lorentzian shaped vibrational modes used for fitting the experimental vibrational spectra of SFS with resonance frequencies  $2045\text{ cm}^{-1}$  (red),  $2062\text{ cm}^{-1}$  (blue) and  $2110\text{ cm}^{-1}$  (black) and phases  $0^\circ$ ,  $180^\circ$  and  $0^\circ$  respectively. The amplitude of each mode for increasing NaSCN bulk concentration is plotted in the inset. (B) Averaged frequencies for the CN stretch mode from QM/MM simulations for  $\text{SCN}^-$  under bulk-like solvated conditions (blue), next to a pure hydrophobic surface (red) and associated with the  $\text{DTA}^+$  at the surface (black, see text for definition). Insets in red and black squares (corresponding to the red and black mode) show representative orientations of the  $\text{SCN}^-$  and its hydrogen bonded water molecules highlighting the instantaneous interface. (C) Graphical representation of the *ab initio* MD simulations: a dodecane/water hydrophobic interfaced stabilized with one dodecyltrimethylammonium ( $\text{DTA}^+$ ) cation with a surface density of one  $\text{DTA}^+$  molecule per  $400\text{ \AA}^2$ .

molecular structure of the interface under study. Specifically, Fig. 6.3B displays the averaged distributions of frequencies for the CN stretch mode resulting from the simulations. Figure 6.3C presents a schematic of the system simulated, namely a purely hydrophobic surface (encircled by the red square) and an additional surface containing one  $\text{DTA}^+$  (encircled by the black square). Both surfaces contain a single  $\text{SCN}^-$  anion, for a total of two  $\text{SCN}^-$  ions in the total simulation supercell. The system is neutralized by placing a proton in the water

portion of the supercell. The surface density of  $\text{DTA}^+$  is set to one molecule per  $400 \text{ \AA}^2$ , in agreement with previous results for the surface density of  $\text{DTA}^+$  on the hexadecane/water nanodroplet interface<sup>29</sup>. Two independent 35 ps simulations were performed starting from a configuration placing each  $\text{SCN}^-$  parallel to the surface normal of the oil-water interface with 1) the nitrogen next to the water-oil interface or 2) sulphur next to the water-oil interface. Earlier *ab initio* simulations depict the solvation structure of  $\text{SCN}^-$  under bulk and interfacial (air-water) condition to be almost identical, with three strong hydrogen bonds formed by water molecules to the nitrogen and two to three to the sulphur<sup>50</sup>. This structural motif is preserved in the presence of the hydrophobic/oily interface as well. Our results indicate that the  $\text{SCN}^-$  in the vicinity of the  $\text{DTA}^+$  (highlighted with the black square in Fig. 6.3B and 6.3C) produces an average structure orienting the CN-bond vector about 12 degrees with respect to the surface normal, independent of the initial orientation of the  $\text{SCN}^-$ . On the other hand, for  $\text{SCN}^-$  located at the pure hydrophobic surface (highlighted with the red square in Fig. 6.3B and 6.3C), the final structure depends on the initial orientation of the  $\text{SCN}^-$  molecule: The  $\text{SCN}^-$  oriented with the nitrogen towards the hydrophobic interface detaches from the interface and produces a solvating water layer between the nitrogen and interface. This solvating water layer is enough to produce a bulk-like solvation structure of the  $\text{SCN}^-$ . In contrast, when  $\text{SCN}^-$  is initialized with the sulphur toward the hydrophobic interfaces, the orientation of  $\text{SCN}^-$  persists, relaxing to a final orientation of 30 degrees with respect to the surface normal, consistent with an earlier finding for the air/water interface<sup>43</sup>. In the absence of statistically relevant populations of the orientation of  $\text{SCN}^-$ , we interpret our results to suggest that there is no significant driving force, e.g.  $\gg k_B T$ , that will result in a preferred orientation of  $\text{SCN}^-$  to be dominant at the neat water hydrophobic interface. More information on the orientation calculation can be found in the Appendix (Paragraph 6.4.3).

The three structural motifs described above have distinct vibrational signatures, reflected in the averaged distribution of frequencies for the CN stretch mode using QM/MM simulations (Fig. 6.3B, see paragraph 6.4.4 in the Appendix for details). First, the bulk-like solvation, resulting when nitrogen is directed towards the pure hydrophobic interface, results in a DFT frequency of  $2046 \text{ cm}^{-1}$  (blue). The latter value is red-shifted by  $19 \text{ cm}^{-1}$  compared to the respective spectrum measured for NaSCN solution in  $\text{D}_2\text{O}$ , which shows a peak at  $2065 \text{ cm}^{-1}$ . Second, the opposite orientation, with sulphur directed towards the pure hydrophobic interface surface, results in a DFT frequency of  $2030 \text{ cm}^{-1}$  (red),  $16 \text{ cm}^{-1}$  red-shifted with respect to the bulk-like frequency. Finally, when  $\text{SCN}^-$  is placed in the vicinity of the  $\text{DTA}^+$  molecule the DFT frequency is  $2066 \text{ cm}^{-1}$  (black), and a blue shift of  $20 \text{ cm}^{-1}$  is observed with respect to the bulk-like case.

## 6.2.5 Diverse ion speciation

Combining the MD simulation with the experimental SHS and SFS results and their fittings, three patterns of  $\text{SCN}^-$  adsorption to aqueous-hydrophobic interface are inferred, corresponding to three ranges of NaSCN concentration (low, middle and high). For a better understanding, Fig. 6.4 presents SFS spectra of the CN mode (A-C), schematics of the interfacial molecular structure, namely  $\text{SCN}^-$  orientation and its interaction with DTAB (D-F), and a simplified overview of the charge and dipole distribution across the interface (G-I) for low (5 – 100 mM), middle (200-300 mM) and high (400 – 600 mM) bulk NaSCN concentrations. Taken together, the simulation results (Fig. 6.3B) suggest that the three peaks shown in Fig. 6.3A are attributed to interfacial  $\text{SCN}^-$  anions interacting with the hydrophobic interface in three distinct motifs. Specifically, the peak at  $\sim 2045\text{ cm}^{-1}$  stems from the  $\text{SCN}^-$  attached to the “neat” hexadecane/water patches (devoid of  $\text{DTA}^+$ ) with their sulphur (S) atom pointing towards the interface (Fig. 6.4A and 6.4D, light green shadow). The second peak, at  $\sim 2062\text{ cm}^{-1}$ , reflects the CN vibration of anions close to the same neat interface, only with the opposite orientation (with their S-atom pointing to the bulk water phase), and with a solvating water layer between the nitrogen and the interface (mentioned as ‘bulk like’ behaviour in Fig. 6.3 and shadowed with light blue in Fig. 6.4B and 6.4E). This interpretation is consistent with the Lorentzian fittings of the SFS data. There is a destructive interference between these two modes due to the opposite orientation of  $\text{SCN}^-$  producing opposite dipoles corresponding to a phases of  $0^\circ$  and  $180^\circ$  required for the spectral fitting (and a reduction in the measured SFS intensity). The third, higher frequency peak, at  $\sim 2110\text{ cm}^{-1}$ , represents the  $\text{SCN}^-$  anions in the proximity (ion-paired) to interfacial  $\text{DTA}^+$  cations of the DTAB stabilized nanodroplets (Fig. 6.4C and 6.4F, shadowed with light red). The last have been shown by the MD simulations to always have a preferred orientation with their S-atom towards the  $\text{DTA}^+$  cations and the interface.

Within this context, the experimental SHS and SFS results are interpreted as follows: First, as  $\text{SCN}^-$  is added to the system, there is a continuous decrease in the interfacial charge and the point of zero charge is reached at  $\sim 400\text{ mM}$  (Fig. 6.1A). As discussed in the analysis of  $\zeta$ -potential measurements, this monotonic decrease implies an increasing adsorption of the  $\text{SCN}^-$  ions at the hydrophobic interface up to 600 mM NaSCN. Second, the number and orientation of the  $\text{SCN}^-$  anions that interact with the  $\text{DTA}^+$  ions do not change with increasing NaSCN, as the amplitude of the  $2110\text{ cm}^{-1}$  peak is constant. Thus, already at 5 mM of NaSCN  $\sim 10\%$  of the  $\text{DTA}^+$  ions have been charge neutralized and the  $\text{DTA}^+ - \text{SCN}^-$  ion-pairing is fully established. This means that the observed changes in the SHS and SFS signals as a function of concentration stem from changes in the hydration, configuration and



surface density of the  $\text{SCN}^-$  anions attached to the hydrophobic patches of the interface, as shown from the simplified charge and dipole distributions in Fig. 6.4G - I. For concentrations up to  $\sim 100$  mM the surface density of  $\text{SCN}^-$  increases and the increasing SFS peak intensity at  $\sim 2045\text{ cm}^{-1}$  points towards adsorption of the  $\text{SCN}^-$  ions with the nitrogen (N)-atoms pointing towards the water phase (Fig. 6.4D). The suggested configuration is in agreement with previous simulation results that show that the solvation structure of the sulphur of the thiocyanate anions is 'hydrophobic-like' while the nitrogen is 'strongly anionic' <sup>43</sup>. Concomitantly, this increasing concentration of 'strong-anionic' solvation with N-atom pointing towards the water phase results in a strong increase in the interfacial water ordering (observed in the SHS data of Fig. 6.1B). Given the large dipole moment of  $\text{SCN}^-$  in water ( $3.08\text{ D}$ ) <sup>43</sup>, there is a significant dipole - dipole interaction between these parallel aligned  $\text{SCN}^-$  molecules. At some concentration, significant  $\text{SCN}^-$  -  $\text{SCN}^-$  (dipole-dipole) repulsion is reached, which can be counteracted by introducing adsorbed  $\text{SCN}^-$  ions that have their N-atoms pointing towards the interface. The spectral signature of this bulk-like solvation is the peak at  $\sim 2062\text{ cm}^{-1}$  (Fig. 6.4E). Oppositely oriented  $\text{SCN}^-$  molecules interfere destructively in their SFS response, which will result in a decrease in SF intensity, as observed in Fig. 6.2B. At the same time, this postulated restructuring will result in a number of water molecules in the proximity of the "hydrophobic-like" sulphur atoms of the newly-arrived population of  $\text{SCN}^-$ . Therefore, a loss of order of the interfacial water dipoles and the resulting decrease in the SHS intensity is observed for concentrations 200 mM - 300 mM, as shown in Fig. 6.1B. At  $\sim 400$  mM the  $\zeta$ -potential measurements show that the interface has been practically neutralized. For higher  $\text{SCN}^-$  concentrations anions continue adsorbing at the interface and the SFS intensity remains constant. It is thus suggested that a balance between the  $\text{SCN}^-$  -  $\text{SCN}^-$  (dipole-dipole) interaction and charge repulsion has been reached. Above this concentration the newly coming  $\text{SCN}^-$  adsorb with both orientations towards the interface (Fig. 6.4F), resulting in the observed constant SFS intensity. Moreover, the negatively charged interface results in an increase in the orientation of the interfacial water, as shown from SHS measurements.

It is interesting to note that the observed behaviour is similar to that of tetrabutylammonium cations that adsorb next to dodecylsulfate ions on similar oil droplets in water<sup>25</sup>. In both cases we cannot see the formation of a typical Stern layer but rather a patchy interface with co-adsorbed cations and anions. This is probably happening to increase the stability of the droplets: When there would only be ion pairs at the interface the droplets would be completely charge neutral and the droplets would not be stable. However, by forming a heterogeneous structure, the droplet-droplet interactions can still be repulsive, even though the average surface charge (electrokinetic mobility) vanishes. Thus, the structural differences observed here, compared to the structure that one would commonly

expect to find for extended planar interfaces (namely a typical Stern layer with ion pairing at high ionic strengths), are necessary to ensure a stable droplet system.

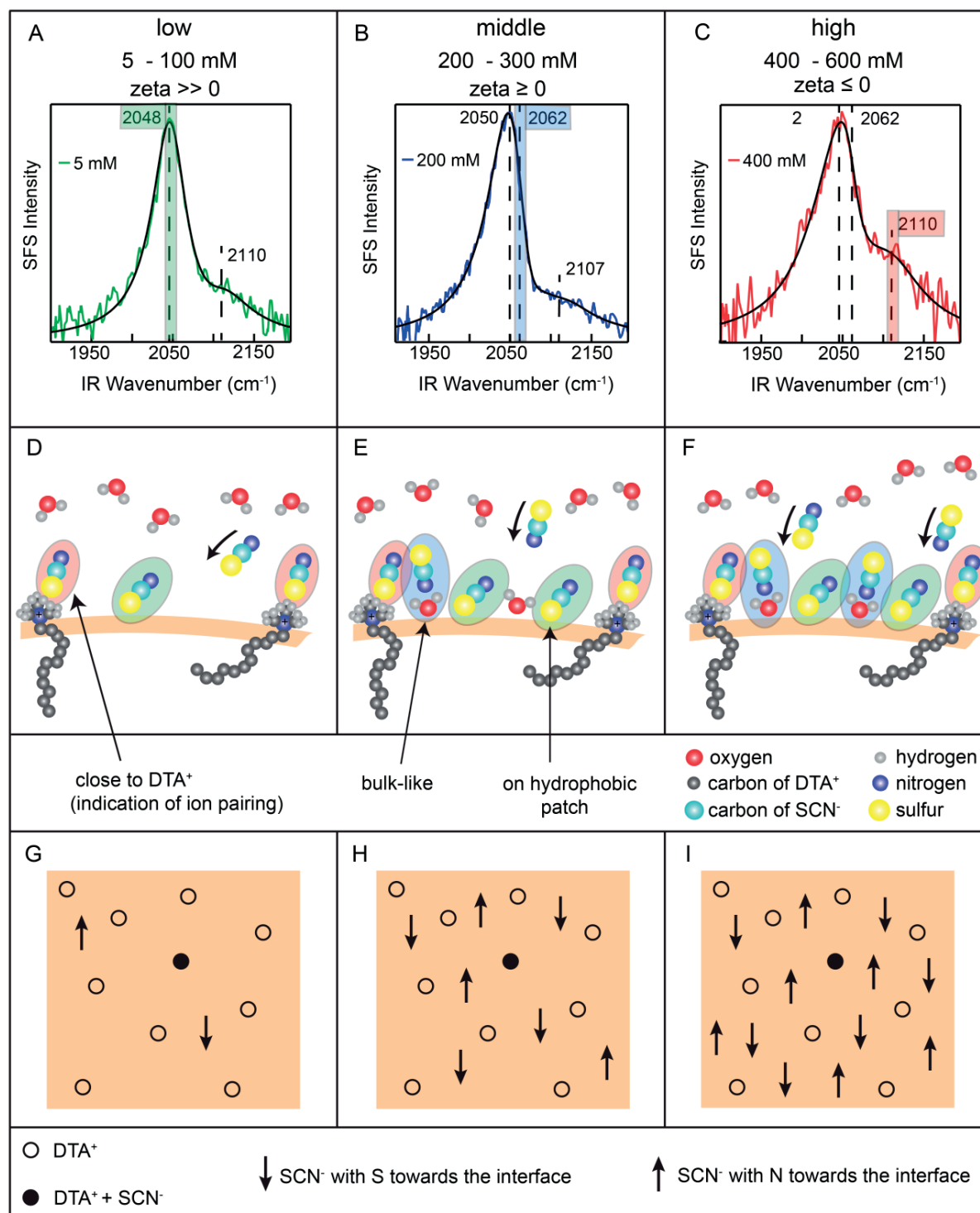


**Figure 6.4: Diverse and heterogeneous surface structures.** (A-C) Indicative vibrational SFS spectra of the CN bond of interfacial  $\text{SCN}^-$  anions with the spectral fits (black lines), (D-F) respective schematic diagrams of the interfacial structure of the nanodroplet oil/water interface and (G-I) overview of charge and dipole distribution

across the interface for bulk aqueous NaSCN concentrations of 5 – 100 mM (left), 200 – 300 mM (middle) and 400 – 600 mM (right). (A-C) The measurements were conducted on hexadecane nanodroplets ( $R \sim 100$  nm, 1 vol % concentration) in  $D_2O$  stabilized with 15 mM DTAB. The spectra were recorded in the SSP polarization combination, which indicates that the sum frequency and visible beams were polarized perpendicular with respect to the scattering plane, while the infrared beam was polarized parallel to it. Dashed lines along with the resonance frequency indicate the resonances required to fit the spectrum. (D-F) Ion pairing is observed between interfacial  $DTA^+$  and adsorbing  $SCN^-$  over the whole concentration range of 5 – 600 mM. The peak at  $\sim 2110\text{ cm}^{-1}$  is present in all spectra (A-C). (D)  $SCN^-$  anions adsorb to the bare hydrophobic patches mainly with their S-atom pointing towards the interface. Strong water ordering is observed. (E)  $SCN^-$  anions continue adsorbing at the interface, but with an opposite orientation than in (D). The  $SCN^-$  anions with their N-atom towards the interface do not attach to the interface, but remain separated from it by a layer of water, displaying bulk-like solvation characteristics. A new peak at  $\sim 2062\text{ cm}^{-1}$  with an opposite phase appears. The water ordering is disrupted. (F)  $SCN^-$  anions continue adsorbing at the interface with both orientations and the interfacial water ordering increases. Note that in (D-F) the counter-ions respectively are omitted for clarity. (G-I) Schematic overview of the distribution of interfacial charges and dipoles that agrees with the structural confirmation presented in (D-F).

## 6.3 Conclusions

We investigated the interaction of  $SCN^-$  anions with a positively charged hydrophobic nanodroplet interface for increasing bulk NaSCN concentrations. For the study conducted here a multi-instrumental approach was implemented, including SFS, SHS and electrokinetic potential measurements in addition to molecular dynamics simulations. The result is a detailed molecular picture of the interaction of  $SCN^-$  with the hydrophobic surface in the presence of  $DTA^+$ . Overall, an increasing interfacial surface density of  $SCN^-$  anions is observed upon addition of salt in the aqueous phase, up to and beyond the point of charge inversion. Interestingly, at all concentrations of NaSCN the droplets are stable, even when they are on average charge neutral. The adsorption behaviour of  $SCN^-$  is complex and we find strong evidence of ion pairing of the  $SCN^-$  with the positive interfacial charges ( $DTA^+$ ) already at concentrations as low as 5 mM. The number of ion pairs remains constant.  $SCN^-$  also adsorbs to the bare hydrophobic patches of the oil/water interface (which comprises  $\sim 90$  % of the surface area) in three different ‘phases’. Initially, for low concentrations ( $\leq 100$  mM),  $SCN^-$  adsorbs with the hydrophobic-like sulphur atom pointing to the interface (parallel to the ion paired  $SCN^-$ ). For middle concentrations ( $>100$  mM and  $< 400$  mM) the strong intermolecular dipole-dipole repulsion between parallel  $SCN^-$  ions results in a new interfacial species that has the hydrated N end pointing towards the interface. For high concentrations ( $\geq 400$  mM) the interface charge inverses and becomes negatively charged. Newly adsorbing  $SCN^-$  ions arrive with both orientations, without substantially altering the interfacial molecular structure. This complex behaviour ensures that the charge on the interface is not cancelled,

so that droplets in solution remain stable. Such a mechanism may well be relevant for interactions on nano- or sub-micron sized domains of membranes, adiposomes or proteins.

## 6.4 Appendix

### 6.4.1 SFS measurements of the interfacial DTA<sup>+</sup> cations

Figure 6.5 displays the results of the SFS measurements conducted for the determination of the surface structure of the interfacial DTA<sup>+</sup> cations of DTAB stabilized  $d_{34}$ -hexadecane nanodroplets ( $R \sim 100$  nm, 1 vol % concentration) in D<sub>2</sub>O. Figure 6.5A shows the spectra of the C-H stretch modes of the alkyl chain of the DTA<sup>+</sup> cations, indicatively, for 20 mM (green) and 400 mM (blue) bulk NaSCN concentrations. Similar spectra have been acquired for concentrations over the whole range up to 600 mM NaSCN. The black lines are fits according to Ref.<sup>49</sup>. The dashed lines indicate the central frequencies of the symmetric methylene (CH<sub>2</sub>) stretch ( $d^+$ , at  $\sim 2850$  cm<sup>-1</sup>) and the symmetric methyl (CH<sub>3</sub>) stretch ( $r^+$ , at  $\sim 2870$  cm<sup>-1</sup>) mode.

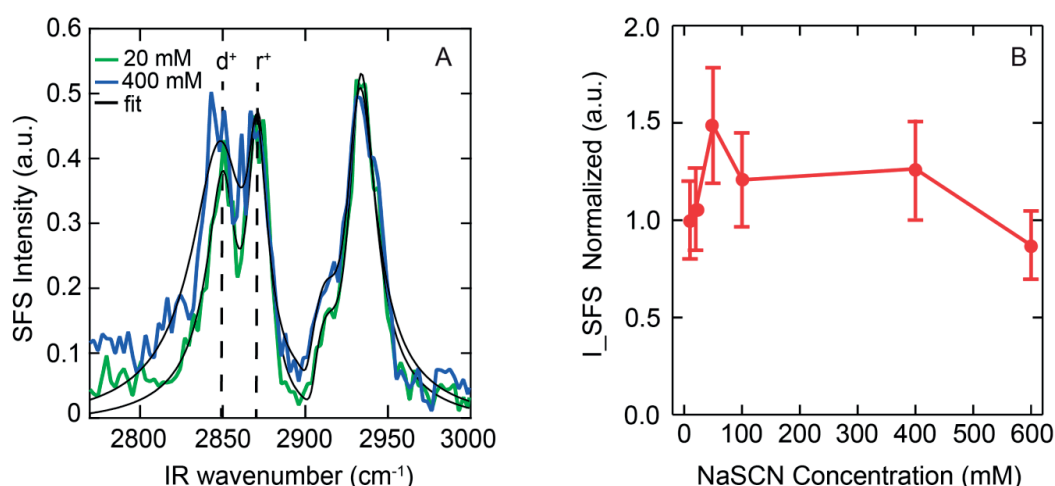


**Figure 6.5: Surface structure of DTA<sup>+</sup>.** Measurements of hexadecane nanodroplets ( $R \sim 100$  nm, 1 vol % concentration) in D<sub>2</sub>O stabilized with 15 mM DTAB. (A) SFS spectra of the C-H stretch modes of DTA<sup>+</sup> cations at the hexadecane/water interface for 20 mM (green) and 400 mM (blue) bulk NaSCN concentrations. The spectra were recorded in the SSP polarization combination, i.e. the sum frequency and visible beams were polarized perpendicular with respect to the scattering plane, while the infrared beam was polarized parallel to it. The black lines are fits to the spectra, as explained analytically in the SI of Ref. <sup>1</sup>. The dashed lines indicate the central frequencies of the symmetric methylene (CH<sub>2</sub>) stretch mode ( $d^+$ , at  $\sim 2850$  cm<sup>-1</sup>) and the symmetric methyl (CH<sub>3</sub>) stretch mode ( $r^+$ , at  $\sim 2870$  cm<sup>-1</sup>). (B) Normalized integrated SFS amplitude over increasing bulk concentration of NaSCN calculated by integration of the area of the vibrational spectra between 2820 cm<sup>-1</sup> – 2970 cm<sup>-1</sup> followed by a division with the respective value for 0 mM NaSCN. The error bars presented are the standard deviation calculated based on measurements of a reference sample in-between the samples of interest.

As shown in Fig. 6.5A, and verified for all NaSCN concentrations, the value of the  $d^+/r^+$  amplitude ratio is  $\sim 0.5 - 1$  for addition of NaSCN, an indication that the orientation of the

alkyl chains of DTA<sup>+</sup> does not change considerably. Figure 6.5B displays the respective integrated SFS intensities of the C-H vibrational modes mentioned above for increasing bulk NaSCN concentrations. It can be seen that the change of the SFS intensity remains within the standard deviation of the measurement, pointing towards a constant surface density of interfacial DTA<sup>+</sup> cations upon interfacial adsorption of SCN<sup>-</sup> anions.

## 6.4.2 Spectral Lorentzian fittings

The SFS intensity spectra of the CN mode are fitted with the use of the program IGOR Pro 6 (Wavemetrics) employing Levenberg – Marquardt iterations. The fittings are obtained from a global fitting procedure<sup>64</sup> described by the formula

$$I_{SFS}(\omega) = \left| \left( A_{NR} e^{-i\varphi_{NR}} + \sum_n \frac{A_n \gamma_n e^{-i\varphi_n}}{\omega - \omega_n - i\gamma_n} \right) \right|^2, \quad (6.1)$$

which describes a superposition of  $n$  Lorentzian shaped vibrational modes, each with an amplitude  $A_n$ , phase  $\varphi_n$ , resonance frequency  $\omega_n$  and linewidth  $\gamma_n$ , on a non-resonant ( $NR$ ) background with amplitude  $A_{NR}$  and phase  $\varphi_{NR}$ . Table 6.1 presents the fitting parameters used for the fitting of  $I_{SFS}$  spectra of the CN vibrational mode(s).

As can be seen in Table 6.1, the fitting requires a maximum of three vibrational modes with vibrational frequencies of  $\sim 2045 \text{ cm}^{-1}$  (1<sup>st</sup>),  $\sim 2062 \text{ cm}^{-1}$  (2<sup>nd</sup>) and  $\sim 2110 \text{ cm}^{-1}$  (3<sup>rd</sup>) and phases  $0^\circ$ ,  $180^\circ$  and  $0^\circ$  respectively. Table 6.1 displays analytically the amplitudes and linewidths. As can be seen in Table 6.1, for bulk aqueous NaSCN concentration between 5 mM to 100 mM NaSCN only the first and the third mode are required while above 100 mM the second peak appears, with an opposite ( $180^\circ$ ) phase. The strength of each vibrational mode is proportional to its amplitude  $A_n$  and we observe the following trend:  $A_1$  (monotonically) increases from 0.8 to 1.7 between 5 mM and 200 mM, followed by a decrease to a plateau at  $\sim 0.8$  by 600 mM, a value similar to the one for NaSCN concentrations  $< 100 \text{ mM}$ .  $A_2$  is zero up to 100 mM, and levels off at its maximum value of  $\sim 1.7$  at 300-400 mM. Last,  $A_3$  fluctuates around a constant value of  $0.27 \pm 0.08$  over the whole concentration range.

As mentioned in the main text, the MD simulations have been crucial for recognizing the three vibrational modes as signatures of three distinguishable structural motifs that the SCN<sup>-</sup> ions exhibit in their interaction with the DTAB-stabilized nanodroplet interface. In detail, the peak at  $\sim 2045 \text{ cm}^{-1}$  is attributed to SCN<sup>-</sup> ions attached on the bare hexadecane/water interface with their sulphur (S) atom pointing towards the interface. The peak at  $\sim 2062 \text{ cm}^{-1}$  is attributed to SCN<sup>-</sup> in the proximity of the same, bare, hydrophobic interface, only with an opposite orientation, namely with their nitrogen (N)-atom pointing towards the interface. In

this second ‘bulk-like’ configuration, the anion is not in direct contact with the hydrophobic interface but a water layer mediates. Finally, the peak at  $\sim 2110 \text{ cm}^{-1}$  corresponds to  $\text{SCN}^-$  anions at the proximity of interfacial  $\text{DTA}^+$ , with their S-atom pointing always towards the cation/interface. MD simulation is in direct agreement with the fitting parameters as the phase values ( $\varphi_i, i = 1,2,3$ ) of the three modes estimated by the fitting reflect the different anionic orientation described above: The modes with the highest and lowest vibrational frequencies correspond to  $\text{SCN}^-$  orientation with the S-atom towards the interface and can be fitted with Lorentzian curves with  $\varphi_1 = \varphi_3 = 0^\circ$  while the mode of intermediate frequency corresponds to an opposite interfacial  $\text{SCN}^-$  orientation and can be fitted with  $\varphi_2 = 180^\circ$ .

**Table 6.1: Fitting parameters for  $\text{SCN}^-$  spectra.** Amplitudes  $A_n$  used for the fitting of SFS intensity spectra, according to Eq. (6.1), of the CN mode of  $\text{SCN}^-$  anions at the interface of hexadecane nanodroplets stabilized with 15 mM DTAB in  $\text{D}_2\text{O}$ .

NaSCN Aqueous concentration [mM]	1 <sup>st</sup> mode Hydrophobic patch $\omega_1 \sim 2045 \text{ cm}^{-1}$ $\varphi_1 = 0^\circ, \gamma_1 = 26 \text{ cm}^{-1}$	2 <sup>nd</sup> mode Bulk-like hydration $\omega_2 \sim 2062 \text{ cm}^{-1}$ $\varphi_2 = 180^\circ, \gamma_2 = 21 \text{ cm}^{-1}$	3 <sup>rd</sup> mode Proximity of $\text{DTA}^+$ $\omega_3 \sim 2110 \text{ cm}^{-1}$ $\varphi_3 = 0^\circ, \gamma_3 = 35 \text{ cm}^{-1}$
-	$A_1$	$A_2$	$A_3$
5	0.81	0	0.19
25	0.88	0	0.24
50	0.79	0	0.16
75	0.89	0	0.28
100	0.93	0	0.18
200	1.68	0.9	0.27
300	1.47	1.66	0.3
400	1.04	1.69	0.31
500	0.83	1.34	0.39
600	0.77	1.18	0.39

### 6.4.3 Orientation of $\text{SCN}^-$ at the surface

Figure 6.6 depicts the probability distribution of the CN-bond vector  $\alpha$  with respect to the surface normal for the four independent molecules in the QM simulations for the whole

simulation time. Both independently run simulations relax the orientation and local solvation structure for the  $\text{SCN}^-$  close to the  $\text{DTA}^+$  to the same average, orienting the CN-bond vector about 12 degrees with respect to the surface normal for the last third of the simulation, shifting the distribution to larger angles. For the  $\text{SCN}^-$  next to the purely hydrophobic surface on the other hand, the initial orientation is a major influence. The  $\text{SCN}^-$  oriented with the nitrogen to the interface does not stay in the vicinity but detaches and forms a solvation layer between the interface while exhibit bulk-like behaviour. The other one persists associated with the hydrophobic interface being oriented about 30 degrees with respect to the surface normal, consistent with an earlier finding for the air/water interface.

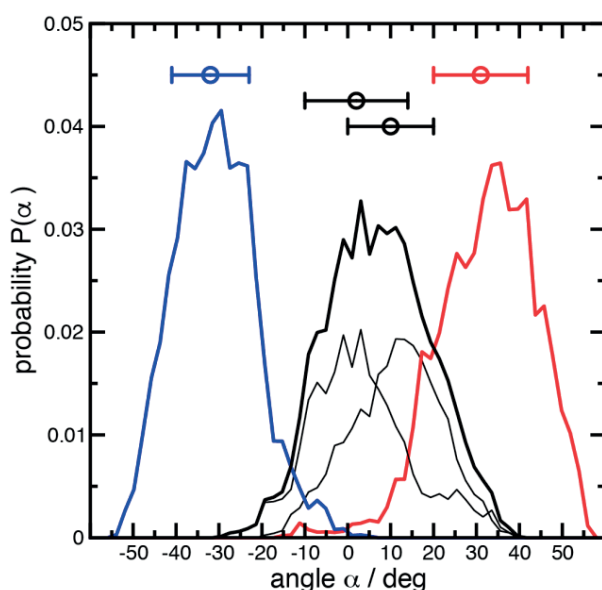


**Figure 6.6: Probability distribution of the CN-bond vector  $\alpha$  with the surface normal.** for the  $\text{SCN}^-$  associated with the  $\text{DTA}^+$  (black), next to the hydrophobic patch (red) and the bulk-like  $\text{SCN}^-$  (blue). Circles with horizontal error bars indicate the average and standard deviation of the angles.

#### 6.4.4 Validation of QM/MM approach

The calculation of the harmonic frequencies for the CN-stretch mode of the  $\text{SCN}^-$  molecule along the molecular dynamics simulation for the large interfacial system is validated with three model bulk systems for which along a trajectory both the QM and QM/MM harmonic frequencies can be calculated. The model systems are 1)  $\text{NaSCN}$  in 97 water molecules in a  $14.4 \times 14.4 \times 14.4 \text{ \AA}^3$  box, 2)  $\text{TMA}^+$  and  $\text{SCN}^-$  in 211 water molecules, and 3) neopentane in a  $18.873 \times 18.873 \times 18.873 \text{ \AA}^3$  box,  $\text{Na}^+$  and  $\text{SCN}^-$  in 210 water molecules in a  $18.834 \times 18.834 \times 18.834 \text{ \AA}^3$  box. All DFT simulations were performed using the CP2K ([www.cp2k.org](http://www.cp2k.org)) simulation suite within the QUICKSTEP module<sup>52</sup>, which contains an accurate and efficient implementation of DFT that employs dual basis sets of Gaussian-type orbitals (molopt-DZV2P) and plane waves (expanded to 400 Ry) for the electron density<sup>53</sup>.



The core electrons were represented using Goedecker-Teter-Hutter pseudopotentials<sup>53</sup> in conjunction with the revised Perdew, Burke and Ernzerhof (revPBE)<sup>55,56</sup> functional with empirical dispersion correction D3, introduced by Grimme<sup>57-59</sup>. A Nose-Hoover thermostat chain<sup>60</sup> of length 3 was coupled to every molecule to maintain a temperature of 300K with an integration time step of 0.5 fs.

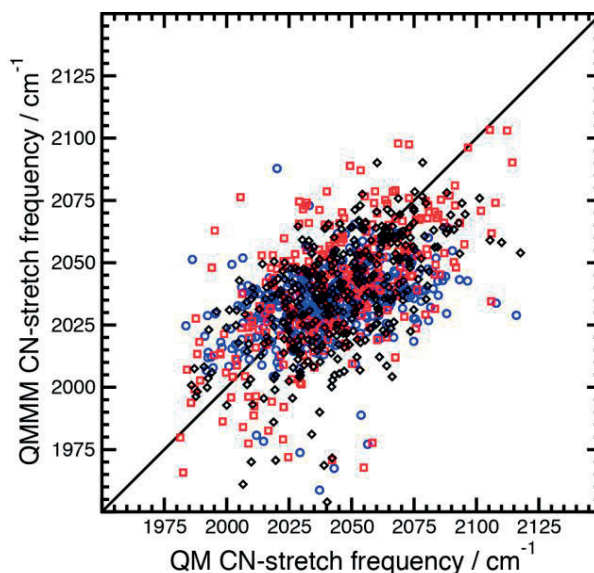


**Figure 6.7: Correlation between QM and QM/MM harmonic frequencies** for bulk  $\text{SCN}^-$  (blue),  $\text{SCN}^-$  bound to  $\text{TMA}^+$  (black) and neopentane (red).

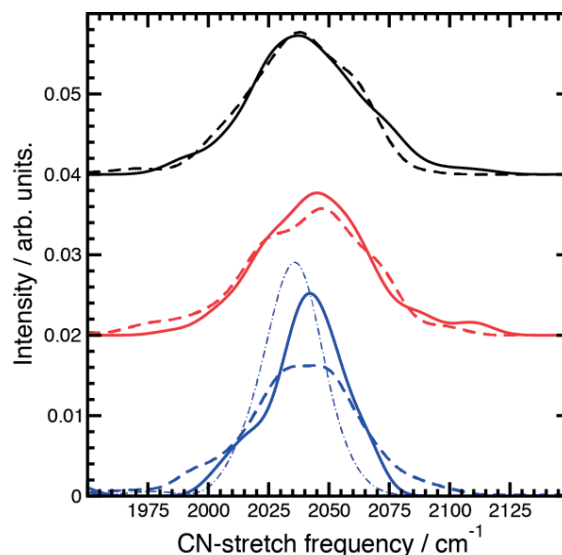


**Figure 6.8: Comparison of averaged harmonic spectra** for QM (solid lines) and QM/MM (dashed lines) approach for bulk  $\text{SCN}^-$  (blue),  $\text{SCN}^-$  bound to  $\text{TMA}^+$  (blue) and neopentane (red).

The frequency of the CN-stretch mode was calculated using either the QS module or the QM/MM module in cp2k for configurations along each trajectory. The harmonic frequencies

were calculated for the  $\text{SCN}^-$  molecule only by optimizing the molecule in the fixed field of all other atoms. For the QM/MM calculations point charges of +0.8e and -0.4e are assigned to each water oxygen and hydrogen not bound to a carbon, respectively and +0.08e to each hydrogen bound to a carbon atom. The charge on each carbon atom is calculated by the number of hydrogens within 1.0 Å multiplied by -0.08e and the  $\text{TMA}^+$  nitrogen is +1.0e. The correlation between the QM and QM/MM frequencies are shown in Fig. 6.7 and the averaged spectra are compared in Figure 6.8.

The overall good agreement between the QM/MM and QM method for these model systems that capture all relevant species in the large interfacial systems provides a viable path to calculate the spectra for the otherwise not tractable large system.

## 6.5 References

1. Alberts, B., Johnson, A., Lewis, J., Raff, M., Roberts, K. & Walter, P. *Molecular biology of the cell* (Oxford University Press, New York, 2002).
2. Israelachvili, J. N. *Intermolecular and surface forces* (Academic Press, San Diego, 2011).
3. Duignan, T. T., Baer, M. D. & Mundy, C. J. Ions interacting in solution: Moving from intrinsic to collective properties. *Curr. Opin. Colloid Interface Sci.* **23**, 58-65 (2016).
4. Baer, M. D., Fulton, J. L., Balasubramanian, M., Schenter, G. K. & Mundy, C. J. Persistent ion pairing in aqueous hydrochloric acid. *J. Phys. Chem. B* **118** (26), 7211-7220 (2014).
5. Baer, M. D. & Mundy, C. J. Local aqueous solvation structure around  $\text{Ca}^{2+}$  during  $\text{Ca}^{2+}\cdots\text{Cl}^-$  pair formation. *J. Phys. Chem. B* **120** (8), 1885-1893 (2016).
6. Bruneval, F., Donadio, D. & Parrinello, M. Molecular dynamics study of the solvation of calcium carbonate in water. *J. Phys. Chem. B* **111** (42), 12219-12227 (2007).
7. Daily, M. D., Baer, M. D. & Mundy, C. J. Divalent ion parameterization strongly affects conformation and interactions of an anionic biomimetic polymer. *J. Phys. Chem. B* **120** (9), 2198-2208 (2016).
8. Kahlen, J., Salimi, L., Sulpizi, M., Peter, C. & Donadio, D. Interaction of charged amino-acid side chains with ions: An optimization strategy for classical force fields. *J. Phys. Chem. B* **118** (14), 3960-3972 (2014).
9. Pluharova, E., Baer, M. D., Schenter, G. K., Jungwirth, P. & Mundy, C. J. Dependence of the rate of lif ion-pairing on the description of molecular interaction. *J. Phys. Chem. B* **120** (8), 1749-1758 (2016).
10. Pluharova, E., Marsalek, O., Schmidt, B. & Jungwirth, P. Ab initio molecular dynamics approach to a quantitative description of ion pairing in water. *J. Phys. Chem. Lett.* **4** (23), 4177-4181 (2013).
11. Buchner, R., Chen, T. & Hefter, G. Complexity in “simple” electrolyte solutions: Ion pairing in  $\text{MgSO}_4(\text{aq})$ . *J. Phys. Chem. B* **108** (7), 2365-2375 (2004).
12. Chen, D. M., Zhang, Y. H., He, T. J. & Liu, F. C. Raman and UV–visible absorption spectra of ion-paired aggregates of copper porphyrins. *Spectrochim. Acta, Part A* **58** (10), 2291-2297 (2002).
13. Van Der Post, S. T., Scheidelaar, S. & Bakker, H. J. Water dynamics in aqueous solutions of tetra-n-alkylammonium salts: Hydrophobic and Coulomb interactions disentangled. *J. Phys. Chem. B* **117** (48), 15101-15110 (2013).

14. Kuroda, D. G. & Hochstrasser, R. M. Dynamic structures of aqueous oxalate and the effects of counterions seen by 2D IR. *Phys. Chem. Chem. Phys.* **14** (18), 6219-6224 (2012).
15. Shih, O., England, A. H., Dallinger, G. C., Smith, J. W., Duffey, K. C., Cohen, R. C., Prendergast, D. & Saykally, R. J. Cation-cation contact pairing in water: Guanidinium. *J. Chem. Phys.* **139** (3), (2013).
16. Antonio, M. R., Nyman, M. & Anderson, T. M. Direct observation of contact ion-pair formation in aqueous solution. *Angew. Chem. Int. Ed.* **48** (33), 6136-6140 (2009).
17. Zhang, Y. & Cremer, P. S. Chemistry of Hofmeister anions and osmolytes. *Annu. Rev. Phys. Chem.* **61** (1), 63-83 (2010).
18. Plath, K. L., Valley, N. A. & Richmond, G. L. Ion-induced reorientation and distribution of pentanone in the air–water boundary layer. *J. Phys. Chem. A* **117** (45), 11514-11527 (2013).
19. Hua, W., Verreault, D., Huang, Z., Adams, E. M. & Allen, H. C. Cation effects on interfacial water organization of aqueous chloride solutions. I. Monovalent cations:  $\text{Li}^+$ ,  $\text{Na}^+$ ,  $\text{K}^+$ , and  $\text{nh}_4^+$ . *J. Phys. Chem. B* **118** (28), 8433-8440 (2014).
20. Carrier, O., Backus, E. H. G., Shahidzadeh, N., Franz, J., Wagner, M., Nagata, Y., Bonn, M. & Bonn, D. Oppositely charged ions at water–air and water–oil interfaces: Contrasting the molecular picture with thermodynamics. *J. Phys. Chem. Lett.* **7** (5), 825-830 (2016).
21. Van Der Vegt, N. F. A., Haldrup, K., Roke, S., Zheng, J., Lund, M. & Bakker, H. J. Water-mediated ion pairing: Occurrence and relevance. *Chem. Rev.* **116** (13), 7626-7641 (2016).
22. Viswanath, P. & Motschmann, H. Effect of interfacial presence of oriented thiocyanate on water structure. *J. Phys. Chem. C* **112** (6), 2099-2103 (2008).
23. Casillas-Iltuarte, N., Chen, X., Castada, H. & Allen, H. C.  $\text{Na}^+$  and  $\text{Ca}^{2+}$  effect on the hydration and orientation of the phosphate group of DPPC at air-water and air-hydrated silica interfaces. *J. Phys. Chem. B* **114** (29), 9485-9495 (2010).
24. Jubb, A. M. & Allen, H. C. Sulfate adsorption at the buried fluorite-solution interface revealed by vibrational sum frequency generation spectroscopy. *J. Phys. Chem. C* **116** (16), 9085-9091 (2012).
25. Scheu, R., Chen, Y. X., Subinya, M. & Roke, S. Stern layer formation induced by hydrophobic interactions: A molecular level study. *J. Am. Chem. Soc.* **135** (51), 19330-19335 (2013).
26. Perera, G. S., Nettles, C. B., Zhou, Y., Zou, S., Hollis, T. K. & Zhang, D. Direct observation of ion pairing at the liquid/solid interfaces by surface enhanced Raman spectroscopy. *Langmuir* **31** (33), 8998-9005 (2015).

27. Smolentsev, N., Smit, W. J., Bakker, H. J. & Roke, S. The interfacial structure of water droplets in a hydrophobic liquid. *Nat. Commun.* **8**, 15548 (2017).
28. Cederquist, K. B. & Keating, C. D. Curvature effects in DNA: Au nanoparticle conjugates. *ACS Nano* **3** (2), 256-260 (2009).
29. Zdrali, E., Chen, Y., Okur, H. I., Wilkins, D. M. & Roke, S. The molecular mechanism of nanodroplet stability. *ACS Nano* **11** (12), 12111-12120 (2017).
30. Okur, H. I., Chen, Y., Smolentsev, N., Zdrali, E. & Roke, S. Interfacial structure and hydration of 3d lipid monolayers in aqueous solution. *J. Phys. Chem. B* **121** (13), 2808-2813 (2017).
31. Roke, S., Roeterdink, W. G., Wijnhoven, J. E. G. J., Petukhov, A. V., Kleyn, A. W. & Bonn, M. Vibrational sum frequency scattering from a submicron suspension. *Phys. Rev. Lett.* **91** (25), 258302 (2003).
32. Roke, S. & Gonella, G. Nonlinear light scattering and spectroscopy of particles and droplets in liquids. *Annu. Rev. Phys. Chem.* **63**, 353-378 (2012).
33. Schürer, B., Wunderlich, S., Sauerbeck, C., Peschel, U. & Peukert, W. Probing colloidal interfaces by angle-resolved second harmonic light scattering. *Phys. Rev. B* **82** (24), 241404-241404 (2010).
34. Wang, H., Yan, E. C. Y., Borguet, E. & Eisenthal, K. B. Second harmonic generation from the surface of centrosymmetric particles in bulk solution. *Chem. Phys. Lett.* **259** (1-2), 15-20 (1996).
35. Petersen, P. B. & Saykally, R. J. Probing the interfacial structure of aqueous electrolytes with femtosecond second harmonic generation spectroscopy. *J. Phys. Chem. B* **110** (29), 14060-14073 (2006).
36. Kinell, P. O. & Strandberg, B. Infrared and Raman spectra of some systems containing thiocyanate groups. *Acta Chem. Scand.* **13** (8), 1607-1622 (1959).
37. Bian, H., Chen, H., Zhang, Q., Li, J., Wen, X., Zhuang, W. & Zheng, J. Cation effects on rotational dynamics of anions and water molecules in alkali ( $\text{Li}^+$ ,  $\text{Na}^+$ ,  $\text{K}^+$ ,  $\text{Cs}^+$ ) thiocyanate ( $\text{SCN}^-$ ) aqueous solutions. *J. Phys. Chem. B* **117** (26), 7972-7984 (2013).
38. Viswanath, P. & Motschmann, H. Oriented thiocyanate anions at the air-electrolyte interface and its implications on interfacial water - a vibrational sum frequency spectroscopy study. *J. Phys. Chem. C* **111** (12), 4484-4486 (2007).
39. Roke, S., Kleyn, A. W. & Bonn, M. Femtosecond sum frequency generation at the metal-liquid interface. *Surf. Sci.* **593** (1), 79-88 (2005).
40. Duffy, D. C., Ward, R. N., Davies, P. B. & Bain, C. D. Direct observation of counterions bound to a charged surfactant monolayer by sum-frequency vibrational spectroscopy. *J. Am. Chem. Soc.* **116** (3), 1125-1126 (1994).

41. Dreier, L. B., Nagata, Y., Lutz, H., Gonella, G., Hunger, J., Backus, E. H. G. & Bonn, M. Saturation of charge-induced water alignment at model membrane surfaces. *Science Advances* **4** (3), (2018).
42. Viswanath, P., Aroti, A., Motschmann, H. & Leontidis, E. Vibrational sum frequency generation spectroscopic investigation of the interaction of thiocyanate ions with zwitterionic phospholipid monolayers at the air-water interface. *J. Phys. Chem. B* **113** (44), 14816-14823 (2009).
43. Baer, M. D. & Mundy, C. J. An ab initio approach to understanding the specific ion effect. *Faraday Discuss.* **160** (0), 89-101 (2013).
44. Hunter, R. J. *Zeta potential in colloid science: Principles and applications* (Academic Press, London, 1981).
45. De Beer, A. G. F. & Roke, S. Obtaining molecular orientation from second harmonic and sum frequency scattering experiments in water: Angular distribution and polarization dependence. *J. Chem. Phys.* **132** (23), 234702 (2010).
46. Scheu, R., Chen, Y. X., De Aguiar, H. B., Rankin, B. M., Ben-Amotz, D. & Roke, S. Specific ion effects in amphiphile hydration and interface stabilization. *J. Am. Chem. Soc.* **136** (5), 2040-2047 (2014).
47. Okur, H. I., Hladílková, J., Rembert, K. B., Cho, Y., Heyda, J., Dzubiella, J., Cremer, P. S. & Jungwirth, P. Beyond the Hofmeister series: Ion-specific effects on proteins and their biological functions. *J. Phys. Chem. B* **121** (9), 1997-2014 (2017).
48. Johnson, C. M. & Baldelli, S. Vibrational sum frequency spectroscopy studies of the influence of solutes and phospholipids at vapor/water interfaces relevant to biological and environmental systems. *Chem. Rev.* **114** (17), 8416-8446 (2014).
49. De Aguiar, H. B., Strader, M. L., De Beer, A. G. F. & Roke, S. Surface structure of sodium dodecyl sulfate surfactant and oil at the oil-in-water droplet liquid/liquid interface: A manifestation of a non-equilibrium surface state. *J. Phys. Chem. B* **115**, 2970-2978 (2011).
50. Baer, M. D., Kuo, I. F. W., Tobias, D. J. & Mundy, C. J. Toward a unified picture of the water self-ions at the air-water interface: A density functional theory perspective. *J. Phys. Chem. B* **118** (28), 8364-8372 (2014).
51. Galib, M., Duignan, T. T., Misteli, Y., Baer, M. D., Schenter, G. K., Hutter, J. & Mundy, C. J. Mass density fluctuations in quantum and classical descriptions of liquid water. *J. Chem. Phys.* **146** (24), 244501 (2017).
52. Vandevondele, J., Krack, M., Mohamed, F., Parrinello, M., Chassaing, T. & Hutter, J. Quickstep: Fast and accurate density functional calculations using a mixed gaussian and plane waves approach. *Comput. Phys. Commun.* **167** (2), 103-128 (2005).

53. Vandevondede, J. & Hutter, J. Gaussian basis sets for accurate calculations on molecular systems in gas and condensed phases. *J. Chem. Phys.* **127** (11), (2007).
54. Goedecker, S., Teter, M. & Hutter, J. Separable dual-space gaussian pseudopotentials. *Phys. Rev. B* **54** (3), 1703-1710 (1996).
55. Perdew, J. P., Burke, K. & Ernzerhof, M. Local and gradient-corrected density functionals. *Chemical Applications of Density-Functional Theory* **629**, 453-462 (1996).
56. Zhang, Y. K. & Yang, W. T. Comment on "generalized gradient approximation made simple". *Phys. Rev. Lett.* **80** (4), 890-890 (1998).
57. Antony, J. & Grimme, S. Density functional theory including dispersion corrections for intermolecular interactions in a large benchmark set of biologically relevant molecules. *Phys. Chem. Chem. Phys.* **8** (45), 5287-5293 (2006).
58. Grimme, S. Accurate description of van der waals complexes by density functional theory including empirical corrections. *J. Comput. Chem.* **25** (12), 1463-1473 (2004).
59. Grimme, S., Antony, J., Ehrlich, S. & Krieg, H. A consistent and accurate ab initio parametrization of density functional dispersion correction (DFT-D) for the 94 elements H-Pu. *J. Chem. Phys.* **132** (15), (2010).
60. Martyna, G. J., Klein, M. L. & Tuckerman, M. Nose-hoover chains - the canonical ensemble via continuous dynamics. *J. Chem. Phys.* **97** (4), 2635-2643 (1992).
61. De Aguiar, H. B., De Beer, A. G. F., Strader, M. L. & Roke, S. The interfacial tension of nanoscopic oil droplets in water is hardly affected by SDS surfactant. *J. Am. Chem. Soc.* **132**, 2122-2123 (2010).
62. Gomopoulos, N., Lutgebaucks, C., Sun, Q. C., Macias-Romero, C. & Roke, S. Label-free second harmonic and hyper rayleigh scattering with high efficiency. *Opt. Express* **21** (1), 815-821 (2013).
63. De Aguiar, H. B., Scheu, R., Jena, K. C., De Beer, A. G. F. & Roke, S. Comparison of scattering and reflection SFG: A question of phase-matching. *Phys. Chem. Chem. Phys.* **14**, 6826-6832 (2012).
64. Chen, Y. X., Jena, K. C. & Roke, S. From hydrophobic to hydrophilic: The structure and density of the hexadecane droplet/alkanol/water interface. *J. Phys. Chem. C* **119** (31), 17725-17734 (2015).





# Chapter 7: Summary and Outlook

## 7.1 Summary

In this thesis, we used nonlinear optical scattering techniques to study the oil/water interface of nanometer-sized emulsions in molecular level detail. At the beginning, in Chapter 1, we introduced the state-of-the-art in the field, and pointed out the open questions that motivated this work. Then, in Chapter 2, the theoretical background of the techniques, and the employed experimental setups were presented, followed by our results, in Chapters 3-6. This work represents the first systematic in situ molecular level study of the stabilization mechanism of the interface of emulsion nanodroplets, as well as of specific anionic effects there. The results obtained bring about new knowledge for the molecular interactions at the nanointerface, which are of great importance both in biological and industrial systems.

Chapter 3 describes SHS and SFS experiments performed on oil nanodroplets in water stabilized with negatively charged (SDS), positively charged (DTAB), neutral (hexanol), or zwitterionic (DPPC) amphiphilic molecules/surfactants. Surprisingly, we find that the stability of the nanodroplets is not correlated with surfactant surface density, but rather depends on the charge of the surfactant, and interfacial water ordering: Charged surfactants are better stabilizers than neutral and zwitterionic ones. Additionally, the ability of a surfactant to increase interfacial water ordering through charge-dipole and/or hydrogen-bonding interactions reinforces stability. The lower surface density of charged surfactants (by an order of magnitude) at nanoscale interfaces, as compared to extended planar interfaces, is caused by a difference in charge-charge screening interactions on the sub-micrometer length scale. For small droplet systems there is less screening in the oil phase, resulting in repulsion of like charges at opposing sides of the droplets, thus in a lower surface density of free charges.

In Chapter 4, we applied SFS and microscopy to study the effect of the inversion of the two phases on the stability and surface structure of nanometer- and micrometer-sized oil/water emulsions stabilized with an oil-soluble neutral surfactant (Span80), a water-soluble anionic surfactant (SDS) or with a combination of the two. We find that micro-emulsions and water-in-oil nanoemulsions are, as expected, stabilized only with surfactants soluble in their continuous phase. Interestingly, though, oil-in-water nanoemulsions can be stabilized with an oil-soluble surfactant that adapts a different configuration than in the water-in-oil system. The present study reinforces the state-of-the art research, suggesting that the stability of nano-emulsions does not necessarily follow the rules that have been developed for interfaces that are flat on a molecular scale.

In Chapter 5,  $\zeta$ -potential measurements, SFS and SHS were employed to compare the interaction of anions with different hydration structures and dipole moments ( $\text{SCN}^-$ ,  $\text{NO}_3^-$ ,  $\text{Cl}^-$  and  $\text{SO}_4^{2-}$ ) with the positively charged (stabilized with  $\text{DTA}^+$ ) interface of oil nanodroplets in water. All anions approach the positively charged interface, however each with a unique adsorption pattern, even the well-hydrated  $\text{SO}_4^{2-}$ . For the polyatomic anions, complex multi-regime behaviour is observed over increasing bulk anionic concentrations, reflecting a change in the orientation with which they adsorb at the interface, and/or in the binding interfacial sites (hydrophobic/charged).

Last, in Chapter 6 we continued our study from Chapter 5, and employed additionally *ab-initio* molecular dynamics simulations to further study the speciation of  $\text{SCN}^-$  at the  $\text{DTA}^+$  stabilized nanointerface. We found  $\text{DTA}^+$ - $\text{SCN}^-$  ion pairing at concentrations as low as 5 millimolar. A variety of ionic species emerged at different ionic strengths, with differently oriented  $\text{SCN}^-$  groups adsorbed on hydrophilic or hydrophobic parts of the surface. This diverse and heterogeneous chemical environment is surprisingly different from the behaviour at extended liquid planar interfaces, where ion pairing is typically detected at molar concentrations and nanoscale system stability is no requirement.

## 7.2 Outlook

In the first part of this work, we dealt with the stability of the aqueous hydrophobic interface in the nanoscale, and showed that it does not necessarily follow the rules that have been developed for planar interfaces. We attributed the difference in surface densities of surfactants between nanodroplets and planar interfaces to differences in charge–charge screening interactions on the sub-micrometer length scale: For small droplet systems, the very low screening in the oil phase allows repulsive interactions between charges of the same sign that are situated at diametrically opposite sites on the surface. As a result, lower surface density of free charges at the interface is observed. This behaviour is particularly important as it should extend up to the micrometer-scale, and is expected to occur for any type of dielectric particles in water. It is also expected to occur for the inverse system of water droplets in oil.

Based on our findings, it would be very interesting to further study parameters that are of importance in the suggested mechanism, namely the size of the droplets, the value of the dielectric constant of the hydrophobic phase, and the inversion of the two phases. Specifically, the study of larger droplets would allow the quantification of the size limit at which the change in the adsorption behaviour of surfactants takes place, as compared to planar interfaces. Moreover, the employment of dielectric materials of high dielectric value, that screen the dielectric repulsion between charges on the opposite sites of the nanodroplets, would shed more light on the applicability of the suggested stabilization mechanism. Last, a start in the study of the inversion of the two phases was made in Chapter 4 of the present work. There, it was shown that the same surfactant can adopt different configuration on the oil/water interface, depending on whether it is soluble in the dispersed or the continuous phase. This new insight might facilitate the choice of appropriate surfactants, which could greatly facilitate the use of emulsions in research and industry. As such, further systematic study of surfactants with different molecular structure would add valuable information.

In the second part of this thesis, anionic interactions with charged and hydrophobic groups in the nanoscale were studied. Ion specific interactions were detected, even at concentrations much lower than in planar interfaces and bulk solutions, like the formation of interfacial ion-pairs already at 5 mM. Moreover, unexpected changes in the interfacial configuration on the nanoscale were revealed for biologically relevant (~100 mM) salt concentrations. This diverse and heterogeneous chemical environment, and the interactions thereat, is of great importance for biological systems. Given that ion specific phenomena are still not fully understood, further studies employing the nanodroplet platform could reveal

more unexpected adsorption patterns of ions at the hydrophobic interface. A step further, oil nanodroplets can be replaced with more biologically relevant systems, like micelles and liposomes in aqueous electrolyte solutions, so that ion binding to specific sites can be directly studied in a system that is much closer to reality than planar model membranes.

## List of publications

The present thesis is based on the following publications/manuscripts:

- Zdrali, E., Chen, Y., Okur, H. I., Wilkins, D. M. & Roke, S. *The molecular mechanism of nanodroplet stability*. ACS Nano **11**(12), 12111-12120 (2017).
- Zdrali, E., Etienne G., Smolentsev, N., Amstad E. & Roke, S. *The interfacial structure of nanometer- and micrometer-sized oil and water droplets stabilized with SDS and Span80*, submitted to J. Phys. Chem. C (2018)
- Zdrali, E., Okur, H. I. & Roke, S. *Specific ion effects at the interface of nanometer-sized oil droplets in water*, in preparation
- Zdrali, E., Marcel, D. B., Okur, H. I., Mundy, C. M. & Roke, S. *The diverse nature of ion speciation at the nanoscale hydrophobic/water interface*, under review in J. Phys. Chem. B

Other publications not described within this thesis:

- Okur, H. I., Chen, Y., Smolentsev, N., Zdrali, E. & Roke, S. *Interfacial structure and hydration of 3d lipid monolayers in aqueous solution*. J. Phys. Chem. B **121**(13), 2808-2813 (2017).



# Curriculum Vitae

**Evangelia ZDRALI** (Ευαγγελία Ζδράλη)

E-mail: [evangelia.zdrali@epfl.com](mailto:evangelia.zdrali@epfl.com), [ezdrali@gmail.com](mailto:ezdrali@gmail.com)

Address: Chemin des Côtes 74, 1020 Renens, Switzerland

Date and place of birth: 25.06.1988, Thessaloniki, Greece

Nationality: Greek

## EDUCATION

Ph.D. in photonics, EPFL, Lausanne 2018

Diploma in Electrical and Computer Eng., Aristotle Uni., Thessaloniki, Greece 2013

## WORK EXPERIENCE

*École polytechnique fédérale de Lausanne* 2014-2018

Ph.D. student in Laboratory for fundamental BioPhotonics (under supervision of prof. S. Roke) Operation and alignment of TiSa lasers (SpecraPhysics SpitFire and Quantronix Integra-C and ADD-ON) and OPAs (TOPAS, Light Conversion, old and new generations, ORPHEUS)

Sum frequency scattering and second harmonic scattering measurements of colloids

Data analysis using Mathematica, Matlab, and IgorPro software

FTIR, dynamic light scattering and UV-VIS measurements

Wet lab experience: preparation of oil-in-water emulsions

## SELECTED CONFERENCES

Swiss Chemical Society Fall Meeting, Lausanne, Switzerland, oral 2018

89<sup>th</sup> ACS Colloid and Surface Science Symposium, Pittsburgh, USA, oral 2015

Sum Frequency Spectroscopy Workshop, Wiesbaden, Germany 2015

## COMPUTER SKILLS

Mathematica, Matlab, Igor Pro, Adobe Illustrator, MS Office

## TEACHING EXPERIENCE

Teaching assistant of Prof. Sylvie Roke for

Interfaces for biology and nanoscience, Nonlinear optics, Nonlinear spectroscopy

**LANGUAGES**

English: Advanced (C2)

French: Intermediate (B1)

German: Intermediate (B1)

Greek: Native

**HOBBIES**

Piano, capoeira





